



**HAL**  
open science

# Impact of photon-number coherence on the performance and energetics of quantum optics protocols

Ilse Maillette de Buy Wenniger

## ► To cite this version:

Ilse Maillette de Buy Wenniger. Impact of photon-number coherence on the performance and energetics of quantum optics protocols. Quantum Physics [quant-ph]. Université Paris-Saclay, 2023. English. NNT : 2023UPASP039 . tel-04128680

**HAL Id: tel-04128680**

**<https://theses.hal.science/tel-04128680v1>**

Submitted on 14 Jun 2023

**HAL** is a multi-disciplinary open access archive for the deposit and dissemination of scientific research documents, whether they are published or not. The documents may come from teaching and research institutions in France or abroad, or from public or private research centers.

L'archive ouverte pluridisciplinaire **HAL**, est destinée au dépôt et à la diffusion de documents scientifiques de niveau recherche, publiés ou non, émanant des établissements d'enseignement et de recherche français ou étrangers, des laboratoires publics ou privés.

Impact of photon-number coherence on  
the performance and energetics of  
quantum optics protocols  
*Impact de la cohérence dans la base d'états de nombre de  
photons sur les performances et aspects énergétiques des  
protocoles d'optique quantique*

**Thèse de doctorat de l'université Paris-Saclay**

École Doctorale n°572 Ondes et Matière (EDOM)

Spécialité de doctorat : Physique

Graduate school : Physique

Référent : Faculté des sciences d'Orsay

Thèse préparée dans l'unité de recherche **Centre de Nanosciences et de Nanotechnologies (Université Paris-Saclay, CNRS)**, sous la direction de **Pascale SENELLART-MARDON**, Directrice de Recherche

Thèse soutenue à Paris-Saclay, le 11 Avril 2023, par

**Ilse MAILLETTE DE BUY WENNIGER**

**Composition du jury**

Membres du jury avec voix délibérative

<b>Rosa TUALLE BROURI</b> Professeure, Laboratoire Charles Fabry, Université Paris Saclay	Présidente
<b>Janet ANDERS</b> Professeure, Physics and Astronomy, University of Exeter	Rapporteur & Examinatrice
<b>Benjamin HUARD</b> Professeur, Laboratoire de Physique, ENS LYON	Rapporteur & Examineur
<b>Alexia AUFFÈVES</b> Directrice de Recherche, Université Côte d'Azur, Sorbonne Université, National University of Singapore, Nanyang Technological University	Examinatrice
<b>Julien CLAUDON</b> Directeur de Recherche, Laboratoire Photonique Electronique et Ingénierie Quantiques, CEA, Université Grenoble Alpes	Examineur

**Titre** : Impact de la cohérence dans la base d'états de nombre de photons sur les performances et aspects énergétiques des protocoles d'optique quantique

**Mots clés** : superposition d'état du nombre de photon, thermodynamique quantique, optique quantique, échanges d'énergie, cohérence

**Résumé** : Les émetteurs quantiques sont des sources de photons uniques intéressantes pour les technologies quantiques, pouvant théoriquement émettre un photon unique sur demande. En 2019, il a été démontré que sous excitation résonnante, la cohérence imprimée entre l'état fondamental et l'état excité de l'émetteur quantique est transférée lors de l'émission spontanée en cohérence dans la base d'états de nombre de photons, créant une superposition cohérente de zéro et un photon. Cette démonstration a conduit à de nouvelles études théoriques sur le rôle de la cohérence en nombre de photons en optique quantique et en thermodynamique quantique. Dans cette thèse, nous étudions expérimentalement l'impact de la cohérence en nombre de photons sur certains fondamentaux de l'optique quantique – par exemple l'effet Hong-Ou-Mandel et les interférences de Ramsey – du point de vue de l'optique quantique et de la thermodynamique quantique. Nous démontrons que la cohérence en nombre de photons doit être prise en compte lors de la réalisation de mesures d'indiscernabilité et peut conduire à de nouveaux phénomènes d'interférence quantique qui peuvent altérer

considérablement les performances de portes quantiques annoncées. Par ailleurs, nous démontrons que la cohérence occupe non seulement une place centrale en optique quantique, mais aussi dans le domaine de la thermodynamique quantique en proposant et mettant en œuvre des protocoles expérimentaux afin de mesurer les échanges énergétiques entre un émetteur quantique et la lumière. Nous montrons que la génération de cohérence dans un émetteur quantique peut conduire à un transfert spontané de travail vers le champ électromagnétique, qui est réduite par la décohérence de l'émetteur ainsi que par intrication cumulée émetteur-champ lors de l'émission spontanée. Cette dernière observation est approfondie en étudiant les transferts énergétiques entre un émetteur quantique et le vide du champ électromagnétique lors de l'interférence de Ramsey. Cette thèse pose ainsi les bases pour de nombreuses autres études expérimentales sur l'impact et l'utilisation des états de superposition en nombre de photons dans les protocoles d'optique quantique et l'énergétique de l'informatique quantique optique.

**Title** : Impact of photon-number coherence on the performance and energetics of quantum optics protocols

**Keywords** : Photon-number superpositions, quantum thermodynamics, quantum optics, energy exchanges, coherence, quantum dots

**Abstract** : Quantum emitters are interesting single-photon sources for quantum technologies that can theoretically emit a single-photon on-demand. In 2019 it was shown that when resonantly excited, the coherence imprinted on the quantum emitter in the energy basis is mapped upon spontaneous emission onto coherence in the photon-number basis, creating a coherent photon-number superposition of zero- and one-photon. This demonstration led to new theoretical investigations on the role of photon-number coherence in quantum optics and quantum thermodynamics. In this thesis we experimentally study the impact of photon-number coherence on pillars of quantum optics – e.g. the Hong-Ou-Mandel effect and the Ramsey sequence – from a quantum optics and quantum thermodynamics perspective. We demonstrate that photon-number coherence has to be considered when performing indistinguishability measurements and can lead to new quantum interference phenomena that can substantially alter

the performances of heralded quantum gates. Additionally, we demonstrate that coherence not only takes a pivotal place in quantum optics, but also in the field of quantum thermodynamics by proposing and implementing experimental protocols to measure energetic exchanges between a quantum emitter and light fields. We show that the generation of coherence in a quantum emitter can lead to the spontaneous release of work in the electromagnetic field, which is reduced by decoherence and the build-up of emitter-field entanglement during spontaneous emission. The latter observation is further exploited by studying the energetic transfers between a quantum emitter and the vacuum of the electromagnetic field along the Ramsey sequence. This thesis serves as the first steps to hopefully many more experimental studies into the impact and use of photon-number superposition states and photon-number coherence in quantum optics protocols and the energetics of optical quantum computing.



## Synthèse en français

Les émetteurs quantiques sont des sources de photons uniques intéressantes pour les technologies quantiques, pouvant théoriquement émettre un photon unique sur demande. En 2019, il a été démontré que sous excitation résonnante, la cohérence imprimée entre l'état fondamental et l'état excité de l'émetteur quantique est transférée lors de l'émission spontanée en cohérence dans la base d'états de nombre de photons, créant une superposition cohérente de zéro et un photon. Cette démonstration a conduit à de nouvelles études théoriques sur le rôle de la cohérence en nombre de photons en optique quantique et en thermodynamique quantique. Dans cette thèse, nous étudions expérimentalement l'impact de la cohérence en nombre de photons sur certains aspects fondamentaux de vue de l'optique quantique et de la thermodynamique quantique.

Après un chapitre d'introduction des concepts, nous montrons dans le chapitre 3 que la présence éventuelle de la cohérence en nombre de photons affecte le traitement quantique de l'information. Nous étudions explicitement l'impact de la cohérence en nombre de photons sur une expérience pionnière de l'optique quantique : l'effet Hong-Ou-Mandel. Nous démontrons théoriquement et expérimentalement que lors de l'excitation d'un émetteur quantique en dessous de l'inversion totale de population avec un laser pulsé, la cohérence en nombre de photons qui en résulte doit être soigneusement prise en compte. Plus précisément, la procédure de normalisation des mesures de corrélation doit être revue afin de ne pas sous-estimer les paramètres de l'état quantique tels que l'indiscernabilité du paquet d'ondes et la cohérence en nombre de photons.

Lorsqu'elles sont correctement normalisées, les mesures de corrélation révèlent également un nouveau phénomène d'interférence quantique en présence de cohérence en nombre de photons. Si l'entrée d'un interféromètre de Mach-Zehnder est un train d'impulsions contenant des superpositions de nombres de photons, la mesure de coïncidences séparées par une impulsion - c'est-à-dire deux clics retardés dans le temps - enchevêtre trois impulsions. Cette intrication se manifeste par une dépendance de phase des pics du premier retard dans les histogrammes de coïncidence.

Nous démontrons que ce type d'interférence quantique affecte les performances et le taux d'erreur de portes quantiques bien connues dans l'informatique quantique optique en considérant à la fois la porte CNOT post-sélectionnée et la porte CNOT annoncée. Le fait que dans une porte CNOT annoncée, seuls deux photons sur quatre sont détectés donne lieu à des interférences quantiques qui ont un impact important sur le taux d'erreur de la porte. Ces deux exemples démontrent l'impact préjudiciable de la cohérence en nombre de photons sur les schémas de calcul quantique si elle n'est pas prise en compte.

Dans les chapitres 4 et 5, nous étudions l'impact de la cohérence en nombre de photons sur l'énergétique des éléments constitutifs du traitement de l'information quantique par la lumière. Dans le chapitre 4, nous proposons et mettons en œuvre un protocole expérimental pour mesurer les échanges énergétiques au niveau le plus fondamental : entre un qubit et le vide du champ électromagnétique par émission spontanée, et entre un champ quantique et un champ cohérent classique. En thermodynamique quantique, ces étapes sont équivalentes à la charge et à la décharge d'une batterie quantique, ici le mode de champ électromagnétique dans lequel émet le qubit. Les protocoles des deux étapes de l'étude reposent sur des mesures de type homodyne, par lesquelles nous extrayons la visibilité de l'interférence, que nous pouvons à son tour relier directement aux quantités énergétiques impliquées dans le processus. Nous démontrons que nous sommes en mesure de mesurer directement le travail et la chaleur transférés du qubit au électromagnétique, qui sont affectés par la présence d'un déphasage pur.

Dans la deuxième étape, nous montrons que l'interférence entre le champ de la batterie et un champ classique. Là encore, nous sommes capables de séparer les différentes contributions énergétiques : le travail et l'énergie thermique. Cependant, nous démontrons que, contrairement à la première étape (chargement de la batterie quantique), le transfert de travail est ici limité et que nous produisons même un flux de travail indésirable du champ classique vers le champ de la batterie.

Dans le chapitre 5, nous revisitons l'excitation d'un système à quatre niveaux avec des séquences de Ramsey en termes de thermodynamique quantique. Tout d'abord, nous examinons comment l'excitation avec des séquences de Ramsey peut conduire à une absorption de travail accrue lorsque deux impulsions sont séparées dans le temps par un délai spécifique. Des mesures ultérieures avec notre système à quatre niveaux révèlent en effet cette augmentation de l'absorption travail, comme en témoigne l'augmentation de l'intensité d'émission de notre qubit par rapport à l'énergie émise lorsqu'on conduit un qubit jusqu'à l'inversion totale de population.

Pour comprendre la nature de l'énergie émise par le qubit, nous effectuons des mesures homodynes avec les paquets d'ondes résultant des séquences de Ramsey pour deux délais différents, un délai proche du délai d'absorption de travail maximale et l'autre où nous n'attendons pas d'amélioration de l'absorption de travail. Après l'interférence, nous calculons la visibilité à partir des intensités d'émission résolues dans le temps (c'est-à-dire les profils de désintégration). Les visibilités obtenues nous permettent de résoudre temporellement le travail et le transfert de chaleur du qubit vers le vide du champ électromagnétique pendant l'émission spontanée. Cette procédure nous donne non seulement un outil puissant pour comprendre l'énergétique résolue dans le temps de l'émission spontanée, mais elle nous donne aussi potentiellement une nouvelle méthode pour mesurer le taux de déphasage d'un émetteur quantique. Les transferts de travail et de chaleur résolus dans

le temps indiquent que l'énergie émise par le qubit est principalement de nature thermique. De plus, quel que soit le délai, la chaleur est la seule quantité qui soit affectée par la phase relative entre les deux impulsions d'excitation. Le transfert de travail, quant à lui, n'est pas affecté par cette phase et reste plus ou moins constant entre les impulsions d'excitation.

Enfin, nous soulignons que les scénarios étudiés ici dans le cadre de la thermodynamique quantique sont des processus importants dans de nombreuses technologies quantiques, qu'il s'agisse de générer des mémoires quantiques à base d'atomes, de réaliser des portes optiques linéaires ou des mesures de l'état de Bell. En tant que telle, notre étude peut servir de point de départ à des études expérimentales sur l'énergétique de l'informatique quantique.



## Acknowledgments

Although it is my name on the front page, the work presented in this thesis could not have been done without the help and support of so many others. I wish I could write a document the size of my thesis to show how thankful I am<sup>1</sup>. Even then, it would probably not come close to what I actually want to say. Regardless, I will try my best to convey the message – and limit myself to three pages.

To **Pascale**. For welcoming me into the group back in April 2019. You have been a great mentor and an amazing role model, who not only knows so much about physics, but is also a great person. You taught me an incredible amount, and you still do. I hope we will continue working together in the future on many (new) projects, and perhaps one day, go and visit your family's vineyard and discuss physics (or other topics) over a glass of wine! To **Alexia**. For introducing me to the field of Quantum Thermodynamics and guiding all our experiments from the theoretical side. I am very happy to have been able to work with such an amazing scientist and person these past four years (and hopefully will continue to a bit longer). Thank you so much for all your support and all the things you taught me! To **Nadia**, my fairy scientific god mother of some sort. You have been – and still are – a great support, and made me often take a step back from my work to help me put things into perspective. Thank you so much for all your support and the discussions. It was so nice working with you, and I am already missing our daily interaction!

To my dear friend and former/present (yeah!) colleague **Sarah**, who arrived at C2N shortly after me, and became a partner in crime, both in- and outside of the lab! I am not just thankful for all the things you taught me in the lab (and you still do), but also for all our other adventures outside of it! My time in Paris would not have been half as fun, if it was not for you!

**Nathan**, this is going to seem out of character for a minute, but bare with me. Thank you for being there these four years (despite the number of times you threw Joey at me). Especially during lockdown, when we were the only ones in the lab (with Pascale and Sarah luckily on remote), trying to get experiments up and running – but feeling way out of our depths and a bit alone. I think the laughs we had together in the lab is what got me through that period, and where an enemy turned into a frenemy – even though I know you would deny the latter. That does not matter, I will miss working and sharing an office with you, regardless!

---

1. Just consider the amount of exclamation marks I would need to express my feelings!

To **Stephen** and **Maria**, my theory rocks since day one. I really enjoy(ed) working with you. You taught me so much and had the patience to answer every (silly) question I had! Most importantly, regardless of the question, you were always up for the challenge, which led in many occasions to projects that seemed "easy" at first, but then quickly expanded to such complex projects that we had to decide where to stop. You made me understand (or at least, I think I understand now) so many things and discover so many new parts of quantum physics!

To **Carlos**, who introduced me to the lab on my very first day at C2N, and helped me get acquainted with all the setups, procedures, and physics. You are a great teacher and friend and I was very lucky to be able to work together again on the final project for my thesis (full circle). Not only in the lab, but together with **Ioanna** and **Titta**, you also played a huge role in getting me through the pandemic with our Wednesday evening Zoom meetings that would last for hours! They really helped to forget about the lockdown for a few hours. I don't think I have managed to break the record of our longest Zoom meeting yet – over 6 hours?

To **Dario**. Thank you for all your help in the lab, and for being my sparring partner in the gym! You made the lab a lot of fun with your humor, philosophy and physics discussions (or philosophical discussions on physics), energy (even after dance marathons), and your support!

To **Elham & Anne**. My dear yoga retreat friends (well, we did a couple of yoga sessions together in the first year of our PhD, but the friends part remained). Sometimes we did not even need a lot of words to support each other, it could also be a picture of *Aki* or of *Taemin*, for example. I am so grateful that I was able to spend these four years with you here at the C2N, together it felt like a family of some sorts. Thank you for always being there! Now, it is time for the yoga retreat world tour edition! To **Hélène**. I had a lot of fun with you discovering in the lab that every time we thought something went right, something else probably had gone wrong. Thankfully, we had "Walk of Life" on full volume to cheer us up every time something in the experiment broke down (or I erased a crucial bit of the data at the last second). You are an amazing friend! To **Marie & Clément**, for our time at C2N and in and outside of Paris! Especially all those great castle tours, with wine tastings at ungodly hours! I had a lot of fun and discovered amazing parts of France and Paris with you!

To all the people in the GOSS team (a huge team of incredible people). Thank you to **Loïc, Olivier, Daniel, Jacqueline & Sylvain**. Together you really create such an incredible working and learning environment, and you taught me a lot through discussions and chats! To my office mates **Antoine & Tim**. It was such a pleasure working and discussing with you! I am going to miss having you as my office mates. **Hubert**, although our overlap in the actual lab was rather short (you soon got the hang of it!), I really enjoyed working with you. To **Chushuang**.

It was really nice having you in the group, together with Anne and Elham we formed a great (support) team! To **Manuel**. For all the laughs and (high-speed) mind reading games – loved the competitiveness and dubious tendencies to want to annihilate all your competitors – in game situations! Thank you **Valentin & Prashant**. You probably thought you would never hear this from me : I really enjoyed all our interactions/discussions in and outside of the lab environment (often on stuff totally unrelated to physics I am afraid). Thank you to **Mathias**, without whom some of the data would not have looked half as nice as they look now! **Hélio & George**, despite our very limited overlap, it was great getting to know you and work with you. Thank you, **Priya, Edson, Martin & Rita** and the rest of the GOSS team, it was great working and interacting with you.

Of course, all this could not have been done without the support from my family and friends outside the lab. **Mama & Papa, Tessa**, thank you for everything, and so much more – *ik houd van jullie*. Thank you dear **Heleen & Arnold**, for all the support and text messages filled with love and enthusiasm, which always felt like such great comfort ; and all the great discussions and talks about physics and life. Thank you **Pé**, for all the support both during my Master thesis back in Amsterdam and my PhD here in Paris! Finally, I would like to thank my entire family and of course my dear friends : **Anne, Arlette**, my Martinus volleyball family **Lara & Tessel** ; **Laura, Mathilde**, the showpony's **Senna, Felicia & Dana**, and the Expat-isseries **Katie, Elena, Hannah & Edith**, for all the love and support and all the fun times.

*Thank you for these incredible years here in Paris!*



# Table des matières

<b>1</b>	<b>Introduction</b>	<b>17</b>
<b>2</b>	<b>Basics of a quantum dot-cavity system and photon-number coherence</b>	<b>23</b>
2.1	Introduction	23
2.2	Quantum dots as artificial atoms	24
2.2.1	Growth of self-assembled quantum dots	24
2.2.2	Electron and hole confinement	24
2.2.3	Charge configurations	26
2.2.4	Energy levels of neutral and charged quantum dots	27
2.2.5	Tuning the charge state	31
2.3	Spontaneous emission of a quantum dot in a cavity	32
2.3.1	Spontaneous emission in the bulk	32
2.3.2	Enhancing the spontaneous emission : the Purcell effect	35
2.3.3	Deterministic QD-cavity assembling	38
2.3.4	Controlling the QD charge state in a cavity	40
2.4	Properties of single-photon wavepackets	41
2.4.1	Temporal profile photonic field	41
2.4.2	Single-photon purity	42
2.4.3	Indistinguishability : the Hong-Ou-Mandel effect	45
2.5	Coherent control and energy coherence	51
2.5.1	Coherent control of a two-level system	51
2.5.2	Resonant excitation of a QD in a cavity	56
2.5.3	Excitation pulse shaping	60
2.5.4	Example of measured Rabi oscillations	61
2.5.5	Energy coherence in the emitted light field	62
<b>3</b>	<b>Quantum interference with photon-number superpositions</b>	<b>67</b>
3.1	Introduction	67
3.2	Generation of photon-number coherence under resonant excitation	69
3.2.1	First-order coherence	70
3.2.2	Re-excitation and first-order coherence	71
3.2.3	First-order coherence and correlation measurements	74
3.3	Measuring indistinguishability in the presence of photon-number coherence	76
3.3.1	Normalization revisited	77
3.3.2	Experimentally resolving phase-dependence long delay peaks	80
3.3.3	Error in wavepacket indistinguishability	82
3.4	Quantum interference between temporally separated wavepackets	86
3.4.1	New quantum interference phenomena	86

3.4.2	Phase-dependence first delay correlation peaks . . . . .	87
3.4.3	A witness for photon-number coherence in correlation histograms . . . . .	88
3.5	Errors in heralded quantum gates . . . . .	92
3.5.1	Post-selected CNOT gate . . . . .	92
3.5.2	Heralded CNOT gate . . . . .	95
3.6	Conclusion and perspectives . . . . .	98
<b>4</b>	<b>Experimental study of the energetic exchanges between a qubit and light fields</b>	<b>101</b>
4.1	Introduction . . . . .	101
4.2	Defining work and heat in the quantum regime . . . . .	103
4.2.1	Defining work and heat in a closed quantum system . . . . .	106
4.2.2	Predicted energetic exchanges between an atom and light fields . . . . .	107
4.2.3	Energetic exchanges between a qubit and a driving field . . . . .	107
4.2.4	Impact of quantum coherence on energetic exchanges between a qubit and the electromagnetic field . . . . .	109
4.3	Coherence-powered energy and work exchange during spontaneous emission . . . . .	113
4.3.1	Protocol to measure the energetic transfers . . . . .	113
4.3.2	Energetic exchanges for a pure battery field . . . . .	119
4.3.3	Energetic exchanges in presence of decoherence . . . . .	121
4.3.4	Measuring the impact of decoherence . . . . .	124
4.4	Coherence-powered energy and work exchange between light fields . . . . .	127
4.4.1	Theory : Energy transfers in quantum battery discharge . . . . .	127
4.4.2	Experimental implementation . . . . .	130
4.4.3	Study on mechanical vibrations in measurements . . . . .	131
4.4.4	Energetic exchanges between two light fields . . . . .	135
4.4.5	Limitations to discharging energy . . . . .	137
4.5	Conclusion and outlook . . . . .	140
<b>5</b>	<b>Temporally resolved energetic exchanges in the Ramsey sequence</b>	<b>143</b>
5.1	Introduction . . . . .	143
5.2	Work and heat transfers in Ramsey sequences . . . . .	145
5.2.1	A Ramsey sequence . . . . .	145
5.2.2	Time bin entanglement with Ramsey sequences . . . . .	147
5.3	Experimental study of enhancement in work absorption . . . . .	149
5.4	Experimental study of temporally resolved energetic exchanges during spontaneous emission	153
5.4.1	Locking the Ramsey phase . . . . .	153
5.4.2	Experimental protocol . . . . .	156
5.4.3	Heat and work transfer during spontaneous emission . . . . .	158
5.5	Signatures of memory effects . . . . .	163
5.6	Conclusion and perspectives . . . . .	165

<b>6</b>	<b>General conclusion and perspectives</b>	<b>167</b>
6.1	On the use of photon-number superpositions . . . . .	168
6.1.1	Twin-field quantum key distribution . . . . .	168
6.1.2	Compensating for photon-number coherence in quantum gates . . . . .	170
6.1.3	Towards continuous variable quantum computation . . . . .	170
6.2	On the energetics of optical quantum computing . . . . .	172
6.2.1	Energetic exchanges at a beam splitter . . . . .	172
6.2.2	Energetics of entangling states . . . . .	172
<b>7</b>	<b>Appendix : Hong-Ou-Mandel interference with photon-number superpositions – theory</b>	<b>189</b>
7.1	General description . . . . .	189
7.1.1	Zero delay peak . . . . .	191
7.1.2	First delay peak . . . . .	193
7.1.3	Far delay peaks . . . . .	194
7.2	Normalization second-order correlation histograms . . . . .	195
<b>8</b>	<b>Appendix : Photonic field</b>	<b>197</b>
8.1	General form of the emitted field . . . . .	197
8.2	Purely dephased emitter . . . . .	198
8.3	Relation between $M_s$ and $\mathcal{C}$ . . . . .	199
<b>9</b>	<b>Appendix : Discharging a quantum battery – theory</b>	<b>201</b>
9.1	Energy transfers in discharging . . . . .	201
9.2	Relating visibility of interference and energetic exchanges . . . . .	202
9.3	Pure dephasing in energy transfer . . . . .	203
9.3.1	Work and heat equations in presence of pure dephasing . . . . .	203
9.3.2	Relation between $M_{b,c}$ and $\mathcal{C}_{b,c}$ . . . . .	205
9.4	Field amplitude and work transfer . . . . .	205



# 1 - Introduction

In the last decades, quantum technologies have made incredible progress. These technologies make use of quantum physics and all its quirks, with subtle **quantum phenomena such as *superpositions***, where a particle can be in two or more states simultaneously, **or *entanglement***, where the state of a particle is directly and instantaneously related to the state of another particle. The latter phenomenon, entanglement, so-called “*spooky action at a distance*”, was recently celebrated in the 2022 Nobel prize (1). Besides practical applications in the fields of quantum key distribution (2; 3), quantum networks (4; 5), quantum metrology (6–8), and quantum computation (9) for example, these advancements also allow to further delve into the world of quantum physics and use the technologies as test beds.

To develop these applications and further study the fundamentals of quantum superpositions and entanglement, requires to encode information in a physical support. An optical approach is the use of single-photons as information carriers. It ideally relies on quantum light sources that generate on-demand a single quanta of light : a single-photon of high quantum purity. In the last two decades two different approaches to single-photon sources have emerged : sources based on **spontaneous parametric down conversion (SPDC)** technology (10; 11), and sources based on quantum emitters (12–14). SPDC sources make use of a nonlinear birefringent crystal which converts an intense pump field into two low intensity fields : a signal and an idler field, where the detection of one heralds the presence of the other. Despite great progress in the field, SPDC sources suffer from limited efficiencies caused by their probabilistic nature. This efficiency is even further reduced when considering that to produce a single-photon with high quantum purity, i.e. indistinguishable photons, requires operating at low photon pair generation probability in the first place, making scalability a real challenge.

The other approach to light-based devices, is the use of **quantum emitters** – diamond defects (15–18), molecules (19–21), atoms (22–24) or semiconductor quantum dots (13; 14; 25; 26) for example – as the single-photon source. Here, the quantum emitter ideally functions as a two-level system, an (artificial) atom with a ground  $|g\rangle$  and excited state  $|e\rangle$ . This two-level system inherently can only emit up to a single photon  $|1\rangle$  at a time. Unlike SPDC sources, single-photon generation with quantum emitters is a **deterministic process** at a rate dictated by the repetition rate of the driving field. When non-radiative processes are negligible, the (artificial) atom emits a photon with near-unity probability per excitation pulse. However, this single-photon is emitted in all directions of space. Fortunately, it was proposed in 1946 by Purcell that an atom coupled to a cavity allows for **control over the emission dynamics** (27), leading to enhanced emission into

the cavity mode. Such scheme was used to efficiently collect the emitted single-photons (14; 28–30), a necessity for many quantum technologies and research.

Because photons have no charge and no mass, they hardly couple to their environment and do not suffer from decoherence. However, implementing photon-photon gates is a real challenge for precisely the same reason. An initial solution to this challenge relies on the use of **the Hong-Ou-Mandel effect**, as proposed by the Knill-Laflamme-Milburn (KLM) linear quantum computation scheme (31). The Hong-Ou-Mandel (HOM) effect, named after the researchers who first experimentally demonstrated it in 1987 (32), occurs when two single-photon Fock states ( $|1\rangle$ ), identical in every degree of freedom and thus indistinguishable, impinge on either side of a beam splitter. As a result, the photons get entangled, resulting in a path-entangled two-photon state of the form  $|20\rangle + |02\rangle$ , a two-photon *NOON* state (7; 33) where both photons exit through the same output port of the beam splitter.

To produce **indistinguishable** single-photons from a quantum emitter, most schemes use **coherent control techniques such as resonant excitation** or two-photon excitation (34) to fully control the time at which the emitter is brought into its excited state and to reduce time jitter of the photon emission. These schemes rely on the interaction between an intense laser field and the atom, giving rise to atom population oscillations between the ground ( $p_g$ ) and the excited ( $p_e$ ) state with Rabi frequency  $\Omega_R$  (35). Besides the creation of populations, coherent control of the atom also generates coherences between the ground and excited state, called **energy coherence** and whose maximum amplitude is given by  $\sqrt{p_g p_e}$ .

Until 2019, the fact that a driving excitation pulse was not producing a photon each time, was thought as "limited brightness" of the source – i.e. probability of having a photon per pulse on-demand is below one – and the emitted field is a mixed state in the form of

$$\rho = p_0 |0\rangle \langle 0| + p_1 |1\rangle \langle 1|, \quad (1.1)$$

with Fock state population probabilities  $p_0$  and  $p_1$ . Such image appears correct under incoherent excitation, for instance non-resonant excitation. However, in 2019 – for the first time in the optical domain – it was shown by our group that under **resonant excitation** the emitted field is a photon-number superposition state of the

$$|\Psi\rangle = p_0 |0\rangle + e^{i\alpha} p_1 |1\rangle,$$

with  $p_0 + p_1 = 1$  and  $\alpha$  a phase in the Fock state basis. This demonstration revealed that **coherence in the energy basis was transferred from the atom to the electromagnetic field. Spontaneous emission should not be considered**

a “**decoherence**” process, instead one should consider the atom and the one-dimensional electromagnetic field it couples to, as a closed system. This publication triggered a very original proposal for photon-number entanglement, exploiting the entanglement between the atom and the emitted field (36), and theoretical studies into the energetics of atom-field coupling (37; 38), and the use of photon-number superpositions for quantum computing applications (39).

In this PhD work, we **experimentally explored the impact of photon-number superpositions on the building blocks of quantum optics, in terms of energetics and quantum protocols**. To do so, we study semiconductor quantum dots, artificial atoms comprised of  $\approx 10^4$  atoms, that can act as three- or four-level systems, generating single-photons upon resonant and off-resonant excitation (40). Since the first demonstration of control over the spontaneous emission of the QD through coupling to a (micro-pillar) cavity (28; 29; 41), the field has made significant advances in terms of efficiency of quantum light generation, with photon collection efficiencies reaching as high as 57% and near-unity single-photon indistinguishability (13; 14; 30). Moreover, our group at the Center for Nanosciences and Nanotechnologies (C2N) developed a technology to deterministically couple a QD to a cavity, a unique tool that allows for further studies (13; 42; 43).

To present our investigation of the role of photon-number superpositions in the fields of quantum thermodynamics, and quantum optics, we need first to explain the basics of the quantum dot cavity platform. This thesis is therefore ordered as follows :

- We present in Chapter 2 the **quantum dot-cavity system**. We first explain in Section 2.2 how quantum dots (QDs) can act as artificial atoms and be described as three- and four-level systems, generating single-photons. In Section 2.3, we show that coupling a QD to a micropillar cavity enhances the spontaneous emission rate into a desired photonic mode, thereby increasing the efficiency of light collection and the possibility to produce highly indistinguishable photonic fields. We then explain in Section 2.4 some experimental techniques used to benchmark single-photon sources, and explain in Section 2.5 how **resonant excitation allows us to coherently control the photonic state** of light generated by the QD-cavity systems. This latter section forms the starting point for my PhD thesis : we present the 2019 work by our group where it was shown that **energy coherence** imprinted by a laser on the QD-cavity system, transfers to the spontaneously emitted field in the form of **photon-number coherence**.

- In Chapter 3 we examine the impact of photon-number coherence on a cornerstone of optical quantum computing : the **Hong-Ou-Mandel interference**. We formerly introduce the notion of **first-order coherence in the photon-number basis** and explain how resonant excitation under realistic settings inevitably results in the presence of this photon-number coherence in Section 3.2. We explore the consequences of this observation by studying the phase-dependence of two-photon correlation measurements and show in Section 3.3 that commonly used normalization procedures break down in presence of photon-number coherence and can result in the underestimation of wavepacket indistinguishabilities. Moreover, we show in Section 3.4 that photon-number coherence in correlation measurements can result in **new quantum interference phenomena**, and, in turn, as we show in Section 3.5 can lead to errors in heralded quantum gates.
- In Chapter 4 and 5 we use photon-number coherence to study the **energetics of building blocks of quantum information processing with light**. Importantly, we first introduce some basics of **quantum thermodynamics** in Section 4.2 and define concepts of work and heat in a **closed quantum system**, where two coupled quantum systems interact, but are otherwise isolated from the environment. This framework allows us to study in Chapter 4 the **energetic exchanges between a qubit and light fields**. We propose an experimental protocol to measure work directly in the spontaneously emitted photonic field in Section 4.3 and subsequently implement the protocol whereby we validate previously published theory. We then go beyond theory by deliberately introducing decoherence to our qubit. In a second step of our protocol, Section 4.4, we show how one can measure the work and heat exchanged between two light fields interfering on a beam splitter.
- In Chapter 5 we study the energetics of **the Ramsey sequence**, used to study the free evolution of a qubit by applying two excitation pulses shortly separated in time. We break down the well-known Ramsey sequence in terms of work and heat transferred from the qubit to the electromagnetic field in spontaneous emission in Section 5.2 and predict an enhancement in work absorption by the qubit. This latter prediction is then experimentally evidenced in Section 5.3. In Section 5.4 we endeavor on temporally resolving the energetics in a Ramsey sequence, and show that we can determine the nature of the energy emitted by the qubit during and in between excitation pulses. The experimental results presented in this chapter have been obtained at the end of my PhD, hence we conclude with questions standing that we will address in the coming weeks.

- Finally, we give a general conclusion and outlook in Chapter 6. Here we anticipate on possible new lines of research exploiting photon-number coherence, and implications of the results presented in this thesis.



## 2 - Basics of a quantum dot-cavity system and photon-number coherence

### 2.1 . Introduction

Over the past couple of decades semiconductor quantum dots (QDs) coupled to micropillar cavities have proven to be very promising systems as single-photon sources (14; 25; 30; 44; 45) for quantum technologies such as quantum computation, quantum networks and quantum cryptography (2; 5; 46; 47). Ongoing research into quantum dots-cavity systems have matured the platform making them close to the ideal artificial atom at cryogenic temperatures (13; 42; 48–50). These advances in the technology also bring new opportunities to study previously uncharted territory in quantum physics. In this thesis, we use III-IV InGaAs/GaAs quantum dot-cavity systems as two-level systems to investigate the role of energy coherence in the energetic exchanges and in quantum light generation.

In this chapter, we explain how these semiconductor quantum dot-cavity systems are fabricated and how they can act as an artificial atom – or qubit – mostly isolated from their solid-state environment and coupled to a single mode of the electromagnetic field. We then explain how one can imprint coherence between the ground and excited state of the artificial atom - also called *energy coherence* - and how this coherence can be transferred onto a photonic field in the form of *photon-number coherence*. These properties make QD-cavity systems ideal platforms to experimentally investigate the impact of energy coherence on energy transfers in the context of quantum thermodynamics, and quantum light generation.

## 2.2 . Quantum dots as artificial atoms

### 2.2.1 . Growth of self-assembled quantum dots

The quantum dots we study are self-assembled indium gallium arsenide (InGaAs) and gallium arsenide (GaAs) QDs where nanostructures are fabricated by stacking layers of atoms with molecular beam epitaxy (MBE). GaAs, acting as the host material, is first deposited, followed by layers of InAs material. Because of lattice mismatch of 7% between the two materials (51), depositing layers of these materials will eventually induce lattice strain. When the InAs layer reaches a threshold of 1.7 monolayers, randomly distributed three-dimensional (3D) InAs islands will form through Stranski-Krastanov (SK) transition (52). This formation of 3D islands reduces the strain in the crystal, making the process energetically favorable. The growth proceeds with GaAs deposition, thereby obtaining InGaAs clusters mostly free from nonradiative defects (53). A large band gap difference between GaAs and InAs QDs of  $\Delta E_g = 1.1$  eV (at  $\simeq 300$  K) (53; 54) results in the QDs forming 3D confinement potential wells for charge carriers, both electrons  $e^-$  and holes  $h^+$ . This process leads to discrete electronic energy levels, making the QDs mimic a natural atom despite the fact that the islands are made out of  $\simeq 10^4$  atoms. In this work, the process is followed by annealing of the QDs at high temperatures ( $850 - 950^\circ$ ) to adjust their energy as it leads to interdiffusion of GaAs and InAs materials (55). This step in the growth of QDs lowers the potential barrier between the islands and the bulk material and affects the shape of the QDs. Across QDs, the shapes will be more homogeneous and the size larger than under pre-annealing conditions. Depending on the fabrication conditions, the InAs density and size of the QDs can differ (56). Typically they will form nano-lenses, elongated in the transverse plane, with a diameter on the order of 10 – 20 nm and heights of approximately 3.5 nm. The remainder of the InAs layer constitutes the wetting layer where carriers are confined in a 2D potential well with an energy gap of approximately 1.45 eV (855 nm), larger than the typical fundamental energy level of the QDs, 1.34 eV (925 nm) at 5 K for the samples studied here (55).

### 2.2.2 . Electron and hole confinement

Modelling the QD energy levels in such structures is complex and the core of a dedicated research field (57–59). However, we can get a “back of the envelop” estimation of the energy level structure of a quantum dot by using the effective mass approximation and reducing the system to a single conduction and single valence band (60).

Let us consider a 3D potential well with dimensions  $L_x, L_y, L_z$ . A charge carrier in the QD will be described by the electronic wavefunction  $\Psi(x, y, z)$ , which in the

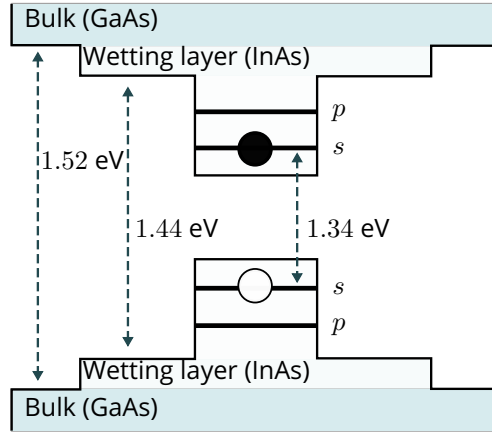


Figure 2.1 – **Schematic of the energy level structure of an InAs quantum dot.** The  $s$  and  $p$  shells for the electron (black circle) and hole (white) are indicated together with the energy band gap of the wetting layer and bulk GaAs.

effective mass approximation is a solution of the Schrödinger equation :

$$\left( \frac{\hbar^2}{2m_{e,h}^*} \nabla^2 + V(x, y, z) \right) \Psi(x, y, z) = E\Psi(x, y, z), \quad (2.1)$$

where  $m_{e,h}^*$  is the effective mass of the charge carrier ( $e^-$  or  $h^+$ ) and  $V$  the potential boundary conditions in  $x, y, z$ . If we further simplify and consider our potential well to be of infinite depth so that :

$$V_j = \begin{cases} 0, & 0 \leq j \leq L_j \quad \forall j = (x, y, z) \\ \infty, & \text{otherwise.} \end{cases} \quad (2.2)$$

We can then separate the energy into  $E = E_x + E_y + E_z$  and  $\Psi(x, y, z) = \Psi_x(x)\Psi_y(y)\Psi_z(z)$  which must verify the second order differential equation

$$\Psi''(j) + k_j^2 \Psi(j) = 0, \quad (2.3)$$

with  $k_j^2 = \frac{1}{\hbar^2} 2m^* E_j$ . Under the boundary conditions given in Eq. 2.2 we find for the energy levels as seen by the charge carriers :

$$E_{e,h} = \frac{\hbar^2 \pi^2}{2m_{e,h}^*} \left( \frac{n_x^2}{L_x^2} + \frac{n_y^2}{L_y^2} + \frac{n_z^2}{L_z^2} \right), \quad (2.4)$$

where  $n_x, n_y, n_z \geq 0$  and integers. The confinement of charge carriers in a 3D infinite potential well results in discrete energy levels for electrons and holes referred to as the  $s$ -shell and  $p$ -shell in analogy to the physics of an atom – considering the symmetry of the envelop function – see Fig. 2.1. Because of the nanometer

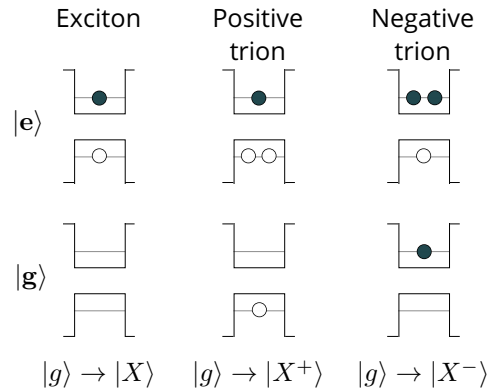


Figure 2.2 – **Occupancy states of a QD.** The QDs used in this thesis support different charge configurations. Excitation brings an electron into the excited state  $|e\rangle$  and leaves a hole in the ground state  $|g\rangle$ , the exciton state. If the conduction (valence) band contains an additional charge carrier, we refer to the excited state as a negatively (positively) charged trion state :  $X^- (X^+)$ .

height of the QDs there is only one confined state in the  $z$ -direction. In contrast, the in-plane directions supports several states. However, in this thesis we consider only the lowest energy levels for both electrons and holes. We will consider the ground state and first excited state to describe optical properties of the QDs. As such, a QD will be considered as a three- or four-level system when considering the ground state occupation and spin degrees of freedom.

### 2.2.3 . Charge configurations

The QD supports different ground and excited states considering the spin degree of freedom and the Pauli exclusion principle. In this thesis we consider two types of QD states comprising the ground and excited state levels : the trion and exciton. Fig. 2.2 shows three of the possible electron-hole configurations, constituting different transitions from the ground  $|g\rangle$  to the excited state  $|e\rangle$ . Generally, upon excitation of the QD, an electron is transferred to the conduction band, leaving a hole in the valence band. This neutral state of the QD is referred to as an *exciton* ( $X$ ) state. The electron and hole are oppositely charged, resulting in Coulomb interaction and limited lifetime of the state, with the emission of a single-photon upon decay, i.e. recombination of the electron and hole. If the QD contains an extra hole in the valence band (or electron in the conduction band) we refer to the excited QD state as a positively (negatively) charged *trion*  $X^+$  ( $X^-$ ) state. We show in Section 2.2.5 how we can control the charge state of the QD when it is inserted in a diode structure.

### 2.2.4 . Energy levels of neutral and charged quantum dots

We can describe the energy levels of both the neutral and charged QDs by considering the interaction between the electrons and holes involved in the optical transition. The energy levels result from both the direct Coulomb interaction induced by particles of opposite charge (electron and hole), and the exchange Coulomb interaction. The exchange Coulomb interaction can be divided into two contributions : the *long-range*, and the *short-range* exchange interaction. The long-range contribution in quantum dots arises from monopole-monopole coupling between different bulk unit cells, and is often neglected as it is screened by the bulk dielectric tensor (61). On the other hand, the short-range contribution emanates from Coulomb attraction between an electron and hole in the same bulk unit cell, and effectively couples the electron and hole spins (62). The balance between the short- and long-range exchange interaction depends on the dimensions of the QD, where the contribution of the short-range exchange interaction increases with quantum confinement. This latter interaction is responsible for the exciton fine-structure splitting (62; 63), (see section below). Contrastingly, the trion state, or charged exciton state, does not exhibit effects of fine-structure splitting and can be described through spin parity considerations. To explain how energy levels are determined by these Coulomb forces and considerations we summarize the discussion given in details in the PhD manuscript of Dr. Helène Ollivier (64).

#### Energy levels in neutral QDs

##### *Direct Coulomb interaction*

We first consider the simplest situation where we have a hole and an electron, corresponding to an exciton state. In such a bipartite system, two oppositely charged carriers  $q_i, q_j$  at position  $\mathbf{r}_i, \mathbf{r}_j$ , respectively, exhibit a direct Coulomb interaction as a function of their relative distance :

$$V_{ij}(\mathbf{r}_i, \mathbf{r}_j) = \frac{1}{4\pi\epsilon_r\epsilon_0} \frac{q_i q_j}{|\mathbf{r}_i - \mathbf{r}_j|} \quad (2.5)$$

This Coulomb direct interaction binds the electron and hole, whose energy is lower than the sum of energies arising from a confined electron and hole individually. The energy levels of a excitonic state are mainly dictated by the spatial confinement of the carriers, as the QD size is smaller than the exciton radius in bulk. From Eq. 2.5 we see that the interaction goes as  $1/R$  with  $R = |\mathbf{r}_i - \mathbf{r}_j|$ , whereas a particle in a box model results in discrete energy level spacing proportional to  $1/R^2$ . As a result, the size of the QD dominantly dictates the confinement of the charge carriers.

##### *Exchange Coulomb interaction*

For our semiconductor quantum dot sources we consider the holes to be heavy holes (64), whose spin can be written as  $|\uparrow\rangle$  or  $|\downarrow\rangle$ , and its angular momentum – along growth axis  $z$  – is  $J_h = \pm 3/2$ . The electron has spin  $|\uparrow\rangle$  or  $|\downarrow\rangle$  and angular momenta  $S_e = \pm 1/2$ . These angular momenta and the their projections  $m_J, m_S$

give rise to four possible excitonic states given by  $|J, m_J\rangle_h \otimes |m_S\rangle_e$  :

$$\begin{aligned} | +1 \rangle &= \left| \frac{3}{2}, +\frac{3}{2} \right\rangle_{\text{hole}} \otimes \left| -\frac{1}{2} \right\rangle_{\text{electron}} & | +2 \rangle &= \left| \frac{3}{2}, +\frac{3}{2} \right\rangle_{\text{hole}} \otimes \left| +\frac{1}{2} \right\rangle_{\text{electron}} \\ | -1 \rangle &= \left| \frac{3}{2}, -\frac{3}{2} \right\rangle_{\text{hole}} \otimes \left| +\frac{1}{2} \right\rangle_{\text{electron}} & | -2 \rangle &= \left| \frac{3}{2}, -\frac{3}{2} \right\rangle_{\text{hole}} \otimes \left| -\frac{1}{2} \right\rangle_{\text{electron}}, \end{aligned} \quad (2.6)$$

with total angular momentum projection  $F = S_e + J_h = \pm 1$  or  $\pm 2$ .

Not all states correspond to an optically active state. We can see this by considering  $F$ , and considering that when an electron and hole recombine, the QD returns to its ground state with zero angular momentum. The  $F = \pm 2$  states are optically inactive since conservation of angular momentum is not compatible with photon emission. As such, these  $F = \pm 2$  states are called *dark* excitonic states. Contrastingly, the  $F = \pm 1$  states are called *bright* excitonic states, and have dipole transitions coupled to left  $|L\rangle$  and right  $|R\rangle$  circular (i.e. polarized) photons.

We write the short-range part of the exchange interaction between an electron and a hole as :

$$\hat{H}_{\text{exchange}} = - \sum_{i=x,y,z} (a_i J_{h,i} \cdot S_{e,i} + b_i J_{h,i}^3 \cdot S_{e,i}), \quad (2.7)$$

with spin coupling constants  $a_i, b_i$  along axis  $i$ , and where the  $z$ -axis corresponds to the growth axis of the QD, and  $x, y$  correspond to the in-plane axes. The exchange interaction Hamiltonian in the eigenbasis of the exciton angular momentum ( $|+1\rangle, |-1\rangle, |+2\rangle, |-2\rangle$ ), is given by (55) :

$$\hat{H}_{\text{exchange}} = \frac{1}{2} \begin{pmatrix} \delta_0 & \delta_1 & 0 & 0 \\ \delta_1 & \delta_0 & 0 & 0 \\ 0 & 0 & -\delta_0 & \delta_2 \\ 0 & 0 & \delta_2 & -\delta_0 \end{pmatrix} \quad (2.8)$$

where  $\delta_i$  are parameters dependent on spin coupling constants  $a_i, b_i$ , and can be written as

$$\begin{aligned} \delta_0 &= -\frac{3}{4} \left( a_z + \frac{9}{4} b_z \right) \\ \delta_1 &= \frac{3}{8} (b_x - b_y) \\ \delta_2 &= \frac{3}{8} (b_x + b_y). \end{aligned} \quad (2.9)$$

The diagonal of the matrix in Eq. 2.8 reveals that the bright and dark states are split by energy  $\delta_0$  (typically  $\approx 500 \mu\text{eV}$ ). The terms  $\delta_2$  refer to mixing and splitting of the dark states, whereas  $\delta_1$  corresponds to mixing and splitting of

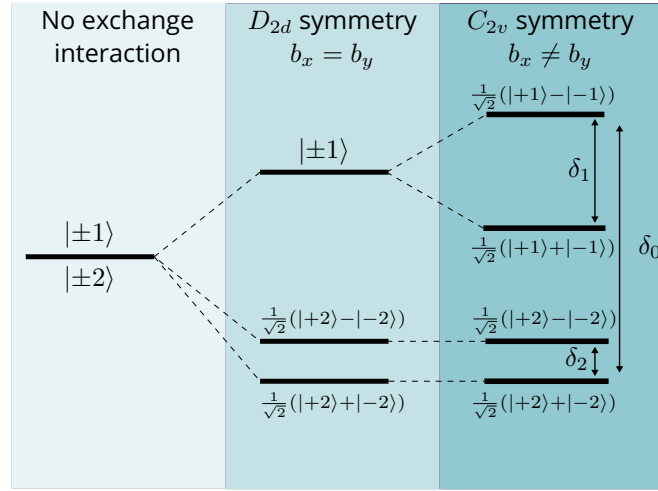


Figure 2.3 – **Exciton energy level diagram and degeneracies arising from asymmetries.** Depending on the exchange interaction and spin coupling constants  $a_i$  and  $b_i$  in the  $i = x, y, z$  direction, the in-plane symmetry can be broken, giving rise to the exciton fine-structure splitting  $\delta_1$  when  $b_x \neq b_y$ .

the bright states whenever  $b_x \neq b_y$ , which is called the exciton fine-structure splitting (FSS) (65). This latter condition happens when there is an asymmetry in the  $x, y$ -plane. We summarize the influence of (a-)symmetry considerations and interactions on the energy level structure of the excitonic manifold in Fig. 2.3 where the different symmetries correspond to a tetrahedral point symmetry of the bulk semiconductor ( $T_d$ ), a symmetry caused by z-confinement ( $D_{2d}$ ), and no in-plane symmetry ( $C_{2v}$ ). Typical values for the degeneracy breaking of bright and dark excitons are  $\delta_1 \sim 1 - 100 \mu\text{eV}$  and  $\delta_2 \sim 1 \mu\text{eV}$ , respectively (60).

If we now consider only the bright excitonic states in absence of in-plane symmetry ( $C_{2v}$ ), the eigenstates of the exchange Hamiltonian become  $|X\rangle = (|+1\rangle + |-1\rangle)/\sqrt{2}$  and  $|Y\rangle = (|+1\rangle - |-1\rangle)/\sqrt{2}$ , split by energy  $\delta_1 = \Delta_{\text{FSS}}$ . These two states are optically coupled to a single ground state  $|g\rangle$  where the QD embeds no carrier (empty QD), resulting in a "V"-type optical system, see Fig. 2.4. The corresponding optical selection rules dictate that both exciton states  $|X\rangle$  and  $|Y\rangle$  are coupled to the ground state through a combination of circularly polarized photons  $(|R\rangle - |L\rangle)\sqrt{2}$  and  $(|R\rangle + |L\rangle)\sqrt{2}$ .

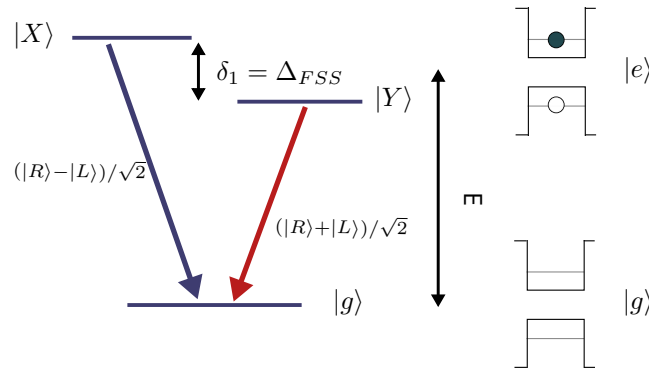


Figure 2.4 – **Energy levels in a neutral quantum dot.** Two excited states  $|e\rangle$  of an exciton,  $|X\rangle$  and  $|Y\rangle$ , are separated by the fine-structure splitting energy  $\Delta_{FSS}$  and coupled to the ground state  $|g\rangle$  through a combination of circularly polarized photons  $|R\rangle$  and  $|L\rangle$ .

#### Energy levels in charged QDs

The charged excitonic state, or trion, is composed out of an electron-hole pair with an additional charge carrier. Two carriers of the same nature must have opposite parity, as these charge carriers are fermions and therefore obey Pauli's exclusion principle (60). As a result, the exchange interaction – present when we have a single electron and hole pair – cancels, and, therefore, so does the fine-structure splitting. The energy of a trion transition is the combination of the energy of the charge carriers forming an exciton and the extra charge carrier, and the binding energy from direct Coulomb interaction whose sign and magnitude are dictated by the shape and size of the QD. As such, a single-photon emitted by a source based on a trion transition will have a different energy compared to a single-photon coming from an exciton source.

The energy level diagram of the trion transition is a four-level system containing hole and electron spins. We show an example for a positively charged trion under resonant excitation in absence of a magnetic field in Fig. 2.5, where we have the degenerate ground state levels composed out of hole spin states  $|\uparrow\rangle_Z$  and  $|\downarrow\rangle_Z$  aligned along the axis  $z$ , perpendicular to the growth plane. The excited state is similarly degenerate and corresponds to the contribution of two holes with opposite spin states and a single electron, either in electron spin state  $|\uparrow\rangle$  or  $|\downarrow\rangle$ . The ground and excited states are coupled through optical selection rules, where excitation with circularly right-  $|R\rangle$  or left-handed  $|L\rangle$  light determines the excited electron hole spin state.

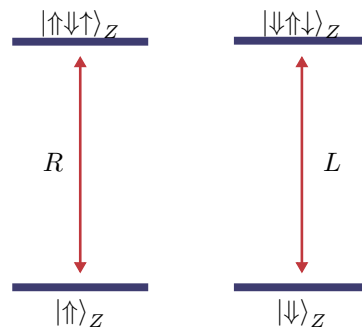


Figure 2.5 – **Energy level diagram of a quantum dot source based on the trion transition.** The degenerate ground and excited state levels of a positively charged trion state, composed of hole spin states  $|\uparrow\rangle_z$ ,  $|\downarrow\rangle_z$ , and electron spin states  $|\uparrow\rangle_z$ ,  $|\downarrow\rangle_z$ , in absence of a magnetic field. The ground and excited states are coupled through circularly polarized photons  $|R\rangle$  and  $|L\rangle$ .

### 2.2.5 . Tuning the charge state

The charge state of a QD can be tuned by inserting the QD in a p-i-n structure. Fig. 2.6 illustrates a p-i-n diode structure used to trap a hole inside the QD (66; 67) introducing proper doping structure and barriers. In the structure under study,  $n$ -doping is brought close to the QD, which in turn experiences a local electric field that allows, once the QD is excited, the electron to tunnel out. Conversely, an  $\text{Al}_{0.1}\text{Ga}_{0.9}\text{As}$  barrier prevents the remaining hole from tunneling outward. A sufficient trapping time of the hole then allows to generate a positive trion state with a second laser pulse.

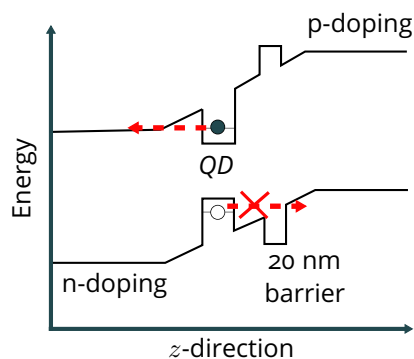


Figure 2.6 – **Trapping charge carriers.** The doping structure used to trap charge carriers inside a QD, here a hole. An  $n$ -doping is brought close to the QD, which as a result experiences a local electric field, allowing for the electron to tunnel out. An  $\text{Al}_{0.1}\text{Ga}_{0.9}\text{As}$  barrier traps the hole. Taken from Ref. (66).

## 2.3 . Spontaneous emission of a quantum dot in a cavity

When the QD is brought into an excited state, light-matter interaction gives rise to relaxation to the ground state through spontaneous emission of a photonic field. The QD, however, acts as a point emitter radiating over a wide range of angles, thereby reducing the light collection efficiency. This light collection efficiency is further reduced by another phenomenon in the bulk semiconductor, total internal reflection of light : light is reflected at the boundary of GaAs and air because of the difference in refractive index between the two materials. These two factors combined result in a poor photon collection efficiency which at best reaches  $\approx 2\%$  in the bulk.

While the photon collection efficiency is not a property that is fundamentally critical for the experimental studies conducted within this PhD work, it turns out to be pivotal to enable the experiments. We studied samples where the QD is coupled to a single cavity mode, thereby realizing important enabling features for our studies. First, this coupling leads to an efficient collection of the QD emission and allows high detection rates that are critical to make most studies presented here feasible. Second, by forcing the QD to emit in a well-defined mode of the electromagnetic field, our system is close to textbook situation of the so-called one-dimensional atom (13; 14). Finally, by accelerating the spontaneous emission, interaction with the QD environment is strongly suppressed - and the coherence which is at the core of our studies strongly enhanced.

In Section 2.3.1 we describe how light-matter interaction gives rise to **spontaneous emission**, initially for QDs in bulk material. Then, we will discuss how by coupling the QD to a cavity, one can control the direction of spontaneous emission and thereby enhance the collection efficiency.

### 2.3.1 . Spontaneous emission in the bulk

To understand how coupling a QD to a cavity alters the emission dynamics, we first discuss spontaneous emission from quantum dots in bulk material. For this section and the following, we follow the explanation found in Refs. (64; 68; 69). In a general picture, let us consider a two-level system, a point dipole, located at  $\mathbf{r} = 0$  and surrounded by a continuous homogeneous dielectric material, here GaAs. With an optical pulse we resonantly excite the two-level system with frequency  $\omega_0$  such that population inversion takes place, thereby populating the excited state. Once the QD is excited, the optical excitation pulse is instantaneously switched off, leaving the electromagnetic field surrounding the QD in a vacuum state. After a certain amount of time, the excited state population of the QD starts to decay back to the ground state. The population is transferred via spontaneous emission onto the electromagnetic field, generating a photonic field – an excited state of the electromagnetic field – with wave vector  $\mathbf{k}$  and polarization  $\mathbf{p}$ . The transition rate,

or decay rate, can be calculated using perturbation theory, making use of Fermi's Golden Rule :

$$\Gamma_{i \rightarrow [f]} = \frac{\pi}{2} \sum_f \frac{|(\hat{H}_{\text{pert.}})_{fi}|^2}{\hbar^2} \delta(\omega - \omega_{fi}), \quad (2.10)$$

where  $i$  denotes the initial state  $|i\rangle = |e, 0\rangle$  (atom in excited state, no photon) and  $f$  the accessible final state  $|f\rangle = |g, \mathbf{k}, \mathbf{p}\rangle$  (atom in ground state, photon in mode  $\mathbf{k}, \mathbf{p}$ ),  $\hat{H}_{\text{pert.}}$  the perturbation Hamiltonian,  $\omega$  the frequency of radiation, and  $\omega_{fi}$  the atomic transition frequency. Summing over the possible final states of the QD-bulk system results in a spontaneous emission rate  $\Gamma_{\text{sp}}^{\text{bulk}}$ .

The perturbation Hamiltonian introduced in Eq. 2.10 in the dipole approximation reads :

$$\hat{H}_{\text{pert.}} = -\hat{\mathbf{d}} \cdot \hat{\mathbf{E}}, \quad (2.11)$$

with dipole  $\hat{\mathbf{d}}$  and electric field operators in the second quantization framework given by

$$\hat{\mathbf{E}}(\mathbf{r}, t) = i \left( \frac{\hbar\omega}{2n^2\varepsilon_0V} \right)^{1/2} \mathbf{p}(\hat{a}_{\mathbf{k},\mathbf{p}}e^{i\mathbf{k}\cdot\mathbf{r}} - \hat{a}_{\mathbf{k},\mathbf{p}}^\dagger e^{-i\mathbf{k}\cdot\mathbf{r}}), \quad (2.12)$$

where  $\hat{a}_{\mathbf{k},\mathbf{p}}$  and  $\hat{a}_{\mathbf{k},\mathbf{p}}^\dagger$  are the annihilation and creation operators in mode  $\{\mathbf{k}, \mathbf{p}\}$ . Moreover, we have the material specific parameters  $\varepsilon_0, n$  which are the dielectric permittivity and refractive index of a medium, respectively. We also recognize the quantization volume  $V = L^3$ .

We obtain

$$\Gamma_{i \rightarrow f} = \frac{2\pi}{\hbar} \frac{E_f}{2|n|^2\varepsilon_0V} d^2 |\mathbf{e}_z \cdot \mathbf{p}|^2 \delta(E_f - E_i), \quad (2.13)$$

with  $d = |\langle g | \hat{\mathbf{d}} | e \rangle|$ ,  $E_f = \hbar\omega$  and  $\mathbf{e}_z$  is the unit vector pointing along the dipole direction. We can simplify this transition rate by noting that the real part of the refractive index of GaAs for 900 nm is 3.5, whereas the imaginary part is close to zero. Moreover, we know that each wavevector  $\mathbf{k}$  has two possible orthogonal polarization states  $\mathbf{p}_1, \mathbf{p}_2$ , but we can choose them such that one is orthogonal to the orientation of the dipole, resulting in a single polarization state contributing to the emitted field :  $|\mathbf{e}_z \cdot \mathbf{p}|^2 = \sin^2 \theta$ , with  $\theta$  being the angle between the dipole and the wavevector, see Fig. 2.7 where a dipole is situated at the origin pointing along  $z$ .

As mentioned before, the sum of the spontaneous emission rates gives rise to the bulk spontaneous emission rate. More accurately, the sum should be replaced by an integral over all possible energies and solid angles  $\Omega$ , weighted by the density of states  $\rho(\Omega, E)$  which is defined by :

$$dN = \rho(\Omega, E) dE d\Omega, \quad (2.14)$$

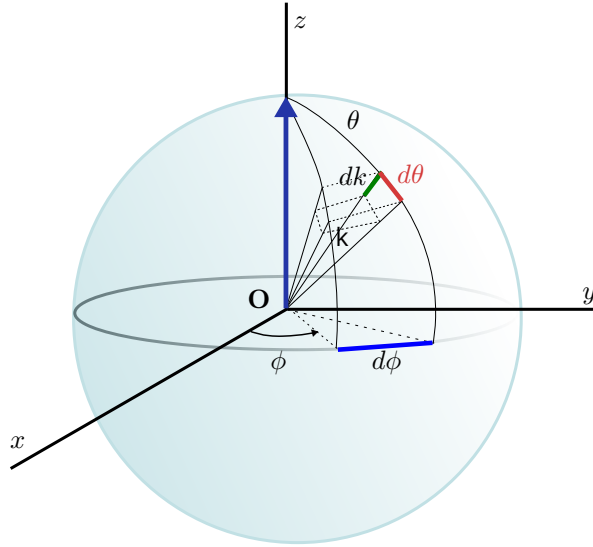


Figure 2.7 – **Integration volume in a sphere.** Integration angles with a dipole positioned at  $r = 0$ . The colored lines indicate the integration slices and the arrow at the origin points into the direction of the dipole orientation.

with the number of states  $dN$  within energy range  $[E, E + dE]$ , and whose wavevectors  $\mathbf{k}$  point along the solid angle  $d\Omega$ .

The volume over which to integrate in terms of polar coordinates ( $\mathbf{k} = k(\sin \theta \cos \phi, \sin \theta \sin \phi, \cos \theta)$ ) to obtain the total spontaneous emission rate in all the possible emission modes is given by  $d^3k = k^2 dk d\Omega$ , with  $d\Omega = \sin \theta d\theta d\phi$  the element of solid angle around the direction of  $\mathbf{k}$ .

Inside volume  $d^3k$  we find the number of modes by choosing a quantization volume  $L^3$  :

$$dN = \frac{d^3k}{\left(\frac{2\pi}{L}\right)^3} = \rho dE d\Omega. \quad (2.15)$$

The discrete energies are given by  $E = \hbar\omega = \hbar\frac{kc}{n}$  which allows us to write :

$$d^3k = \frac{n^3 E^2}{(\hbar c)^3} dE d\Omega. \quad (2.16)$$

The number of modes inside  $d^3k$  is then found by dividing Eq. 2.16 by the volume of a single mode  $(2\pi/L)^3$ , obtaining

$$dN = \left(\frac{L}{2\pi}\right)^3 \frac{n^3 E^2}{(\hbar c)^3} dE d\Omega \quad (2.17)$$

which results in the density of states :

$$\rho(\Omega, E) = \left( \frac{L}{2\pi} \right)^3 \frac{n^3 E^2}{(\hbar c)^3}. \quad (2.18)$$

Finally, we find the bulk spontaneous emission rate by integrating over all accessible final states :

$$\Gamma_{\text{sp}}^{\text{bulk}} = \int_f \Gamma_{i \rightarrow f} dN = \int \int \Gamma_{i \rightarrow f} \rho(\Omega, E_f) dE_f d\Omega. \quad (2.19)$$

Inserting our previously found expressions, noting  $E_i = E_e - E_g = \hbar\omega$ , we get :

$$\Gamma_{\text{sp}}^{\text{bulk}} = \frac{n\omega^3 d^2}{3\pi\epsilon_0 \hbar c^3}, \quad (2.20)$$

from which we also obtain the radiative lifetime of the exciton in the bulk  $T = (\Gamma_{\text{sp}}^{\text{bulk}})^{-1}$ , which for an InGaAs QD in GaAs is approximately 1 ns at 930 nm.

### 2.3.2 . Enhancing the spontaneous emission : the Purcell effect

For application purposes it is highly desirable to control the emission of the QD. A solution is offered by cavity quantum electrodynamics (cQED), from which we know that coupling a two-level system to a cavity will modify the emission rate into the cavity mode (70). In this section we discuss how coupling a QD to a cavity strongly alters the emission dynamics and can lead to a drastic increase in the spontaneous emission rate, the so-called *Purcell effect* (27; 68).

#### Enhancement spontaneous emission rate

We consider a two-level system inside the cavity, see Fig. 2.8. The coupling constant between the two-level system and the cavity mode is noted by the parameter  $g$ . Other important QD-cavity parameters are the cavity damping rate  $\kappa$ , describing the photon escape rate out of the cavity, and the total dephasing rate of the emitter  $\Gamma$ . The latter is the sum of the spontaneous emission decay rate  $\gamma$  into all modes (including outside the cavity mode), and the pure dephasing rate  $\gamma^*$  :  $\Gamma = \frac{\gamma}{2} + \gamma^*$ .

In terms of coupling strength, we can discern between two regimes : the strong coupling regime, where  $g > |\kappa - \gamma|/4$  and the spontaneous emission will happen at two distinct frequencies, or the weak coupling regime, where  $g < |\kappa - \gamma|/4$  (71; 72). The first scenario entails that once excited, a two-level system can emit and absorb a photon for several cycles until the photon exits the cavity : the system exhibits vacuum Rabi oscillations. Contrastingly, in the weak coupling regime the emitted photon escapes faster from the cavity than the time scale of the re-absorption and emission cycle. In such regime the excited state population of a QD will decay exponentially and thereby spontaneously emit a photon in a dissipative process. Our

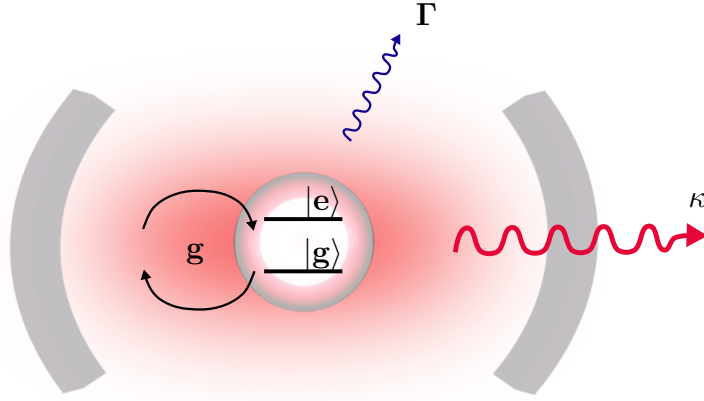


Figure 2.8 – **Different contributions to emission rate.** A two-level system coupled to a cavity (indicated by two bent mirrors) mode with coupling strength  $g$ . The cavity damping rate is given by  $\kappa$  and the total dephasing rate of the emitter by  $\Gamma$ .

devices operate in the weak coupling regime where  $g < |\kappa - \gamma|/4$  with typical values on the order of  $\hbar g \approx 10 - 20 \mu\text{eV}$ ,  $\hbar \kappa \approx 100 - 300 \mu\text{eV}$ , and  $\hbar \gamma \approx 1 - 4 \mu\text{eV}$ .

In the weak coupling regime the spontaneous emission regime is still dictated by Fermi's golden rule (41). The cavity effectively alters the density of electromagnetic modes coupled to the two-level system. If we consider the two-level system of frequency  $\omega$  coupled to the cavity ( $\omega_c$  with linewidth  $\kappa$ ), the density of modes seen by the QD is given by (70) :

$$\rho_{\text{cav}}(\omega) = \frac{2}{\pi \kappa} \frac{\kappa^2}{4(\omega - \omega_c)^2 + \kappa^2}, \quad (2.21)$$

which at the frequency of the cavity becomes :

$$\rho_{\text{cav}}(\omega_c) = \frac{2}{\pi \kappa} = \frac{2Q}{\pi \omega_c}, \quad (2.22)$$

where we introduce another important parameter of the system : the cavity quality factor  $Q = \omega_c/\kappa$ .

Applying Fermi's golden rule (Eq. 2.10), we find the spontaneous emission rate

$$\Gamma_{\text{sp}}^{\text{cav}} = \frac{2Qd^2}{n^2 \hbar \epsilon_0 V}, \quad (2.23)$$

for  $\omega = \omega_c$ . Finally, we can define the Purcell factor as being the ratio between the spontaneous emission rate of the emitter optically coupled to the cavity mode and of the emitter in bulk :

$$F_P = \frac{\Gamma_{\text{sp}}^{\text{cav}}}{\Gamma_{\text{sp}}^{\text{bulk}}} = \frac{3}{4\pi^2} \frac{Q\lambda_0^3}{n^3 V} = \frac{4g^2}{\kappa \Gamma_{\text{sp}}^{\text{bulk}}}, \quad (2.24)$$

where  $\lambda_0 = 2\pi c/\omega$ . This Purcell factor quantifies the enhancement of the spontaneous emission rate into the mode of the cavity, and as can be seen from Eq. 2.24 is proportional to the ratio of the quality factor and the mode volume (27). As such, a cavity with a high quality factor and low mode volume is desirable for efficient photon emission into the cavity mode.

In most situations, because the cavity presents some angular acceptances, the two-level system can still emit in other directions. The total lifetime of the emitter is actually given by the sum of the emission in the cavity mode and the emission into the continuum of modes outside the cavity :  $(T_1)^{-1} = \Gamma_{\text{sp}}^{\text{cav}} + \Gamma_{\text{sp}}^{\text{other}}$ . We can define a parameter  $\beta$  which will be the fraction of photons emitted in the cavity mode, or the *mode coupling* :

$$\beta = \frac{\Gamma_{\text{sp}}^{\text{cav}}}{\Gamma_{\text{sp}}^{\text{cav}} + \Gamma_{\text{sp}}^{\text{other}}}. \quad (2.25)$$

For the cavities studied during this PhD, it has been shown that  $\Gamma_{\text{sp}}^{\text{other}} \approx F_{\text{sp}}^{\text{bulk}}$  (41). In such case we have :

$$\beta \approx \frac{F_P}{F_P + 1}. \quad (2.26)$$

This latter expression shows that the larger the Purcell factor, or enhancement of spontaneous emission, the more photons are emitted into the desired mode (cavity mode).

Fig. 2.9 sketches a typical pillar structure used in our team where a layer of self-assembled InGaAs QDs is embedded into a  $\lambda/n$  thick GaAs layer – with  $\lambda$  the emission wavelength of the QD and  $n$  the material index of the layer. Bragg mirrors made out of 34 pairs of  $\lambda/(4n)$  GaAs/Al<sub>0.9</sub>Ga<sub>0.1</sub>As layers at the bottom and 16 other pairs at the top of this QD layer confine the light in the vertical direction and the etching of a cylindrical shape of the cavity induces confinement in the other directions. The typical height of one such pillar is around 13  $\mu\text{m}$  and its radius on the order of a couple of micrometers. To obtain maximum coupling between the pillar and the quantum dot, the latter should be positioned at the absolute center of the pillar in the  $x, y$  plane, where the cavity electric field of the fundamental pillar mode is maximum, and in the  $z$  direction at the position of the antinode of the cavity mode. This latter requirement is obtained thanks to the QD atomic layer deposition during the molecular beam epitaxy (MBE) growth process.

Also shown in Fig. 2.9 are the different escape channels a photon can take to exit the cavity : via the top mirror, the bottom mirror, or absorption and sidewall losses. The rate at which the photon escapes the cavity is thus given by :  $\kappa = \kappa_{\text{top}} + \kappa_{\text{bottom}} + \kappa_{\text{loss}}$ . Once the QD emits a photon into the cavity mode

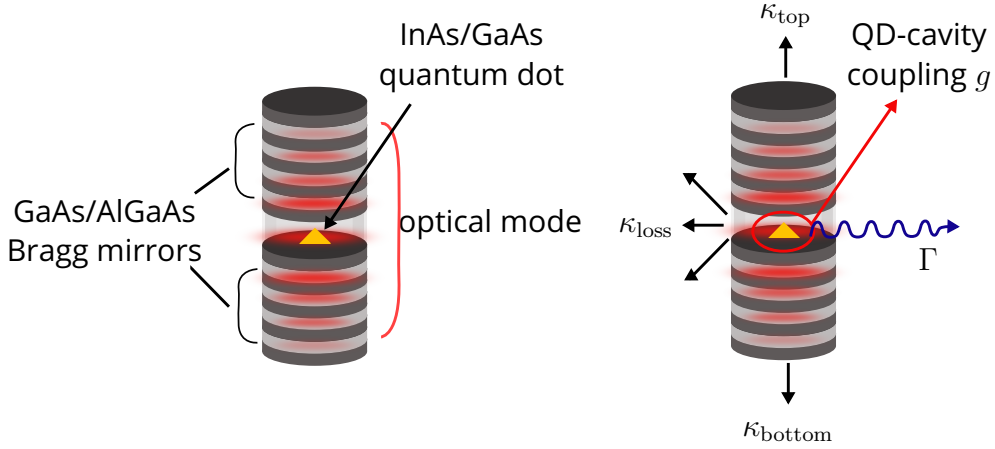


Figure 2.9 – **The studied quantum dot micropillar cavity system.** Left : A typical pillar structure for the QD-cavity systems studied in this thesis. A layer of self-assembled InGaAs QDs is embedded into a GaAs layer and surrounded by Bragg mirrors made out of 34 and 16 pairs of  $\lambda/(4n)$  GaAs/Al<sub>0.9</sub>Ga<sub>0.1</sub>As layers on the top and on the bottom (not to scale here), respectively, confining light. Right : The different channels through which photons can escape the cavity, either via the top mirror at rate  $\kappa_{\text{top}}$ , via the bottom mirror  $\kappa_{\text{bottom}}$ , or via the sidewalls  $\kappa_{\text{loss}}$ . The QD emits photons outside the cavity mode at decoherence rate  $\Gamma$ .

through the Purcell effect, the fraction leaving the cavity through the top mirror is given by  $\kappa_{\text{top}}/\kappa$ . Efficiently collecting the photons from the top of the cavity, is equivalent to  $\kappa \approx \kappa_{\text{top}}$ .

As a final note, we can write the total dephasing rate of our emitter in terms of the found spontaneous emission rates :  $\Gamma = \frac{\Gamma_{\text{sp}}^{\text{cav}} + \Gamma_{\text{sp}}^{\text{bulk}}}{2} + \gamma^*$ , with  $\gamma = \Gamma_{\text{sp}}^{\text{cav}} + \Gamma_{\text{sp}}^{\text{bulk}}$ .

### 2.3.3 . Deterministic QD-cavity assembling

The Purcell effect is maximal if the QD is centered in the pillar cavity and spectrally matched to the cavity mode. However, in the  $x, y$  plane this condition is a challenge since QDs grow at random spatial positions, and therefore regularly spaced pillars often contain more than one or no QDs. Moreover, QDs present different emission energies. Here we explain the technique used in the lab to solve these difficulties and deterministically couple self-assembled quantum dots to cavities, using the cryogenic *in situ* lithography technique developed in our group since 2008 (73). This technique allows for precise positioning of a quantum dot within a pillar microcavity with up to 50 nm accuracy. We briefly explain here the main steps of this lithography technique, for more details, we refer the reader to Ref. (73).

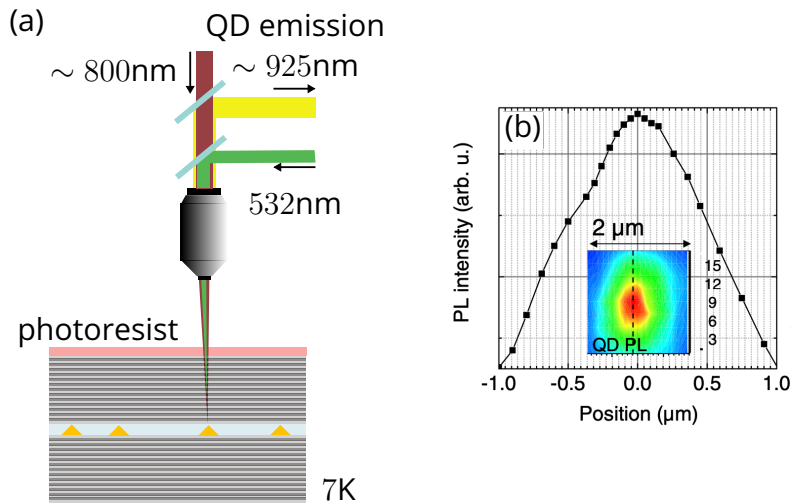


Figure 2.10 – **In-situ lithography for deterministic quantum dot microcavity pillar assembly.** (a) An excitation laser ( $\sim 800$  nm) off-resonantly excites QDs. The resulting QD emission (PL) is detected by a spectrometer and CCD camera. If the QD emission is at the right wavelength ( $\sim 925$  nm), the center of the QD position is obtained by scanning the photoluminescence as a function of position. A second laser at  $\sim 532$  nm then exposes the photoresist, creating a circular mask centered around the QD. (b) QD PL intensity as a function of sample position. Taken from Ref. (73).

To produce optimally coupled QD-cavity system, our group proposed an “in-situ” lithography method. The process starts by spin coating a planar cavity embedding the QD in the two-dimensional Bragg cavity structure with a positive photoresist. The resulting samples are placed inside a cryostat operating at 7K where the sample is mounted on piezoelectric actuators which allow for precise positioning of the sample with up to 10 nm accuracy. A microscope objective focuses an excitation laser ( $750 \text{ nm} < \lambda < 830 \text{ nm}$ ) onto the sample without affecting the photoresist layer, see Fig. 2.10(a). This laser off-resonantly excites a QD, which in turn results in photoluminescence (PL). The photoluminescence is detected by a spectrometer and a CCD camera. If a QD with the desired wavelength is detected, the PL is scanned as a function of sample position, see Fig. 2.10(b). A spatial PL map is obtained with a spatial distribution reflecting roughly the profile of the focused laser ( $\text{FWHM} \approx 1 \mu\text{m}$ ), allowing us to attribute the coordinates of maximum PL intensity to the center of the QD position. A second laser at 532 nm then exposes the photoresist, creating a circular mask centered on the QD  $x, y$ -coordinates. The circular mask is later used as a mask for the pillar etching. This method allows to position the QD at the maximum of

the pillar fundamental mode with  $\pm 50$  nm accuracy.

The in situ technique also allows to spectrally match the microcavity fundamental mode to the QD frequency by adjusting the radius of the pillar which dictates the wavelength of the cavity (73). The radius is a function of the exposure time and intensity of the 532 nm laser where a longer exposure time and higher intensity result in a larger pillar radius. By choosing the right parameters, a QD-cavity system with the desired parameters is obtained. Finally, the sample is removed from the cryostation and the photoresist is developed to obtain a mask suitable for the etching of micropillar cavities.

#### 2.3.4 . Controlling the QD charge state in a cavity

In 2014 (74), our group demonstrated the ability to create pillar patterns with an advanced *in-situ* lithography technique, allowing for electrical control of the device, see Fig. 2.11. Here the pillar is connected to a circular outer edge through four bridges creating a cross-like pattern. The outer edge is then electrically contacted with the ground. This electrical contact is especially useful as it provides a tool to control the charge state of the quantum dot, corresponding to the exciton or trion transition introduced in Section 2.2.3, and tune the QD into resonance with the cavity through the Stark effect.

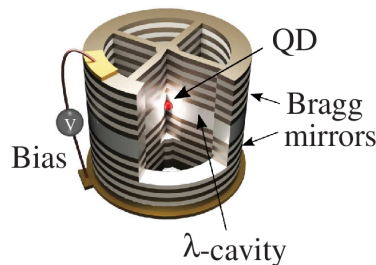


Figure 2.11 – **A schematic of an electrically contacted QD-cavity device.** A pillar is connected to a circular outer edge through four bridges, forming a cross pattern. The outer edge, in turn, is electrically contacted to apply a bias. Taken from Ref. (75).

In order to create these electrically contacted pillars, the top and bottom Bragg mirrors are *p*- and *n*-doped respectively, forming together with the QD layer a *p-i-n* type band structure. During the in-situ lithography step, the full connected pillar shape is defined and centered around the QD. After resist development, metallic deposition and bonding is done to define the *p*-contact on top of the pillar, with the *n*-contact defined at the bottom of the pillar. This electrical connection allows for

fine-tuning of the QD-cavity resonance after fabrication through the Stark effect, which shifts the electron and hole states. Specifically, when applying a negative (positive) bias, the band gap energy decreases (increases), resulting in a red (blue) shifted emission wavelength. We show in Chapter 3 that applying an electrical field to our QD-cavity system allows to maintain QD-cavity resonance when increasing the temperature of the sample.

## 2.4 . Properties of single-photon wavepackets

All along this PhD thesis, we study the properties of the single-photon wavepackets emitted by the QD. In particular, we characterize our generated photonic states in terms of temporal profile, purity and indistinguishability. These parameters reveal information on the QD emission dynamics, on the number of photons emitted, and on the spectral quantum purity of the emitted state. In this section we will describe how we experimentally measure these characteristics. All measurements are performed under pulsed excitation of the QD with a laser operating at a repetition rate of 81 MHz.

### 2.4.1 . Temporal profile photonic field

A temporal profile, or lifetime measurement, is dictated by the spontaneous decay rate  $\gamma = T_1^{-1}$ , and shows the temporal distribution of photons emitted by the QD. To measure such a profile, we directly send the emitted signal through a fiber to a superconducting nanowire single-photon detector (SNSPD, Single Quantum) connected to a time-to-digital converter (TDC) used for correlation measurements.

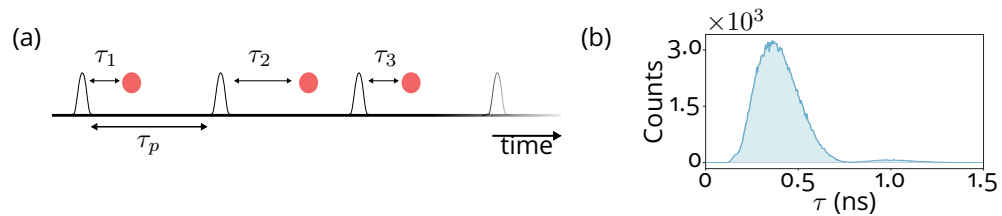


Figure 2.12 – **Measuring temporal distribution QD emission.** (a) A clock signal (black pulses) of the laser with repetition rate  $1/\tau_p$  is sent to a correlator. Every time the correlator receives a clock signal, it starts the internal clock and saves the time stamp  $\tau_i$  of the next incoming photonic field from the QD (red). (b) Measuring the arrival times with respect to the clock of the laser allows building a histogram of arrival times, or lifetime measurement of the QD.

The correlator is connected to the clock signal of the laser sending pulses at 81MHz, equivalent to a pulse separation of  $\tau_p = 12.3$  ns. In Fig. 2.12(a) we show a simplified image of how the temporal profile of the QD emission is reconstructed.

Every time the correlator receives a signal from the laser clock (black pulse) it will start the internal clock. As soon as an incoming photon is detected (red circles), the correlator saves the relative delay between the laser clock and photon signal :  $\tau_i$ . By repeating this procedure over a period of time, sufficient statistics are gathered, resulting in a histogram of arrival times, see Fig. 2.12(b) showing an example of such a decay curve.

The histogram is created by measuring the average photon number per unit time. From a formal point of view, we can write this intensity as  $I(t) = \langle \hat{a}^\dagger(t)\hat{a}(t) \rangle$  where we introduce the quantum operators  $\hat{a}(\hat{a}^\dagger)$  as creating (annihilating) photons in the propagating modes into which light is emitted.

### 2.4.2 . Single-photon purity

An important figure of merit for single-photon sources is the single-photon purity, used to quantify the probability of the photonic wavepacket to contain more than a single-photon Fock state. We quantify this probability with a Hanbury Brown - Twiss (HBT) setup, see Fig. 2.13(a). Photonic wavepackets separated in time by  $\tau_p$  (with pulse repetition rate  $(\tau_p)^{-1}$ ) enter the interferometer (input mode  $\hat{a}_1$ ) where they impinge on a beam splitter (BS) of reflectivity  $R$  and transmission  $T$  (input mode  $\hat{a}_2$  is in an uncorrelated vacuum state).

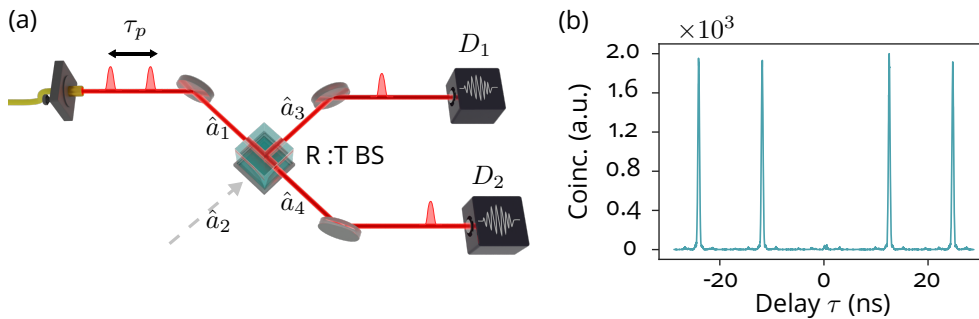


Figure 2.13 – **Hanbury Brown - Twiss setup for measuring the purity of a photonic state.** (a) Schematic of the optical setup (see main text). (b) A coincidence histogram as a function of delay computed by measuring detector clicks with the setup in (a). The absence of coincidence clicks at zero delay ( $\tau = 0$ ) indicates the input photonic state consists only of up to a single-photon Fock state. Peaks are separated in time set by the laser repetition rate  $(\tau_p)^{-1}$ .

If the wavepacket contains up to a single photon, it can either be reflected or transmitted by the beam splitter into output mode  $\hat{a}_3$  or  $\hat{a}_4$ , respectively. Depending on the path taken by the photonic state, detector  $D_1$  or  $D_2$  (with detection efficiencies  $\eta_1, \eta_2$ , respectively) will click once a photon is detected.

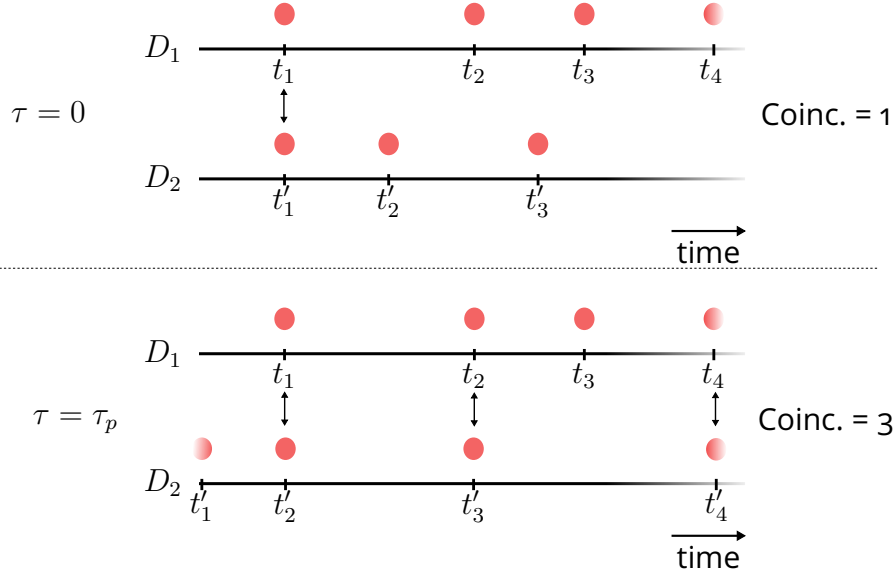


Figure 2.14 – **Measuring coincidences with arrival time photons.** Detectors  $D_1, D_2$  in a HBT setup register the arrival time of photon (red) detection events, resulting in two lists with time tags :  $\{t_i\}$  and  $\{t'_i\}$ , respectively. Comparing the lists for relative delays  $\tau$  results in coincidences as a function of delay, where  $\tau = 0$  corresponds to simultaneous events.

Alternatively, if the photonic state consists of higher dimension Fock states there is a chance of  $D_1$  and  $D_2$  to click simultaneously.

A cross-correlation histogram is built by comparing lists of photon arrival times (time tags) registered by  $D_1$  and  $D_2$  over a period of time,  $t = \{t_1, \dots, t_i\}$  and  $t' = \{t'_1, \dots, t'_i\}$ , respectively. The principle is shown in the upper panel of Fig. 2.14 with relative delay (offset)  $\tau = 0$  between the lists. The coincidences between the two lists are counted (here : one), and repeated for different relative delays  $\tau$  between the two event lists. In the lower panel of Fig. 2.14 the event list of  $D_2$  is offset by delay  $\tau_p$  with respect to  $D_1$ , resulting in three coincidences for the events pictured here. Fig. 2.13(b) shows a typical coincidence histogram for pulsed input states separated by  $\tau_p$  where the peak at zero delay shows the non-zero probability of having more than one photon in a single input state. Formally, the plotted histogram is described by the time integral over the coincidences for delay  $\tau$  :

$$G_{34}^{(2)}(\tau) = \int G_{34}^{(2)}(t, \tau) dt \quad (2.27)$$

where we introduce the unnormalized second-order correlation function  $G_{34}^{(2)}$  (76). This correlation function, in terms of interferometer output modes  $\hat{a}_3, \hat{a}_4$ , is given

by

$$G_{34}^{(2)}(t, \tau) = \eta_1 \eta_2 \langle \hat{a}_3^\dagger(t) \hat{a}_4^\dagger(t + \tau) \hat{a}_4(t + \tau) \hat{a}_3(t) \rangle, \quad (2.28)$$

where, again,  $t$  and  $t'$  are the arrival times of photons at detector  $D_1$  and  $D_2$ , and  $\tau$  the delay introduced between lists of events from detectors  $\tau = |t - t'|$ . We can express the unnormalized second-order correlation function in terms of its input state  $\hat{a}_1$  by using the beam splitter relations :

$$\begin{pmatrix} \hat{a}_3(t) \\ \hat{a}_4(t) \end{pmatrix} = \begin{pmatrix} T & -R \\ R & T \end{pmatrix} \begin{pmatrix} \hat{a}_1(t) \\ \hat{a}_2(t) \end{pmatrix}, \quad (2.29)$$

with  $\hat{a}_2$  a vacuum state and  $R^2 + T^2 = 1$ , and we find for a 50 : 50 BS ( $R = T = 1/\sqrt{2}$ ) :

$$G_{34}^{(2)}(t, \tau) = R^2 T^2 \eta_1 \eta_2 \langle \hat{a}_1^\dagger(t) \hat{a}_1^\dagger(t + \tau) \hat{a}_1(t + \tau) \hat{a}_1(t) \rangle = \frac{1}{4} G_{11}^{(2)}(t, \tau), \quad (2.30)$$

where  $G_{11}^{(2)}(t, \tau)$  is the correlation function in terms of the input state  $\hat{a}_1(t)$ . Thus, measuring coincidence clicks between output mode  $\hat{a}_3$  and  $\hat{a}_4$  gives us direct access to the unnormalized second-order autocorrelation of the input state and therefore how likely it is that the wavepacket contains more than one photon.

To benchmark our generated photonic state we need to be able to compare single-photon purities across different measurements (with different  $R, T, \eta_1, \eta_2$ ). A common method to normalize coincidence histograms uses uncorrelated coincidence counts for large delay  $\tau$ . For pulsed input states this entails extracting peak areas at large delay  $\tau$ . For a pulse separation  $\tau_p$ , these peak areas are given by

$$G_{n\tau_p}^{(2)} = \int_{-\tau_p/2}^{\tau_p/2} G^{(2)}(\tau + n\tau_p) d\tau. \quad (2.31)$$

In the limit of  $\tau_p \gg \gamma$ , with  $\gamma$  the decay rate of a single pulse, i.e. when the correlation peaks do not temporally overlap, Eq. 2.30 for  $n \geq 1$  can be written as :

$$\begin{aligned} G_{34}^{(2)}(t, \tau > \tau_p) &= R^2 T^2 \eta_1 \eta_2 \langle \hat{a}_1^\dagger(t) \hat{a}_1(t) \rangle \langle \hat{a}_1^\dagger(t + \tau) \hat{a}_1(t + \tau) \rangle \\ &= R^2 T^2 \eta_1 \eta_2 I(t) I(t + \tau), \end{aligned} \quad (2.32)$$

with the input intensity

$$I(t) = \langle \hat{a}_1^\dagger(t) \hat{a}_1(t) \rangle. \quad (2.33)$$

Using the uncorrelated peak areas therefore provides a way to remove the unwanted prefactors  $R^2 T^2 \eta_1 \eta_2$  from Eq. 2.30, and the normalized peak area at zero delay becomes :

$$\frac{G_{34}^{(2)}(t, \tau = 0)}{G_{34}^{(2)}(t, \tau > \tau_p)} = g^{(2)} = \frac{1}{\mu^2} \int \int \langle \hat{a}_1^\dagger(t) \hat{a}_1^\dagger(t + \tau) \hat{a}_1(t + \tau) \hat{a}_1(t) \rangle dt d\tau, \quad (2.34)$$

where  $\mu = \int I(t) dt$  is the mean photon number of a single pulse. This normalization allows us to thus extract a single-photon purity given by :  $1 - g^{(2)}$ .

### 2.4.3 . Indistinguishability : the Hong-Ou-Mandel effect

Another important figure of merit of the emitted wavepackets is the indistinguishability. It measures the purity of the quantum state in the temporal domain. This property is quantified by the mean wavepacket overlap  $M$ , with  $M = 1$  if the emitted state is pure in the temporal domain. This indistinguishability is an important requisite for performing any quantum gates in the Knill-Laflamme-Milburn (KLM) scheme (see Section 3.5.2 and Refs. (31; 77; 78)). In this PhD work, this quantity is also critical as it carries information on the coherence of the QD during spontaneous emission. The indistinguishability of a photonic wavepacket can be quantified using an unbalanced Mach-Zehnder interferometer, which we refer to as a Hong-Ou-Mandel interferometer henceforth, see Fig. 2.15.

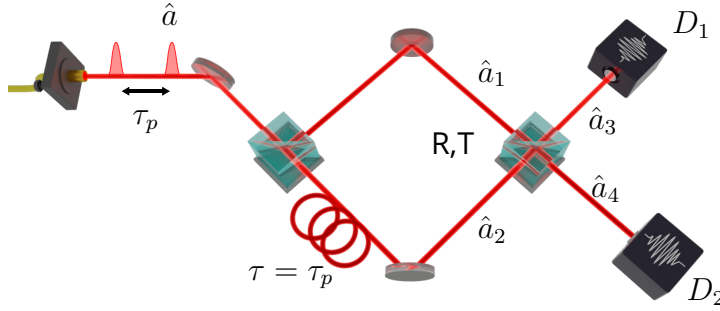


Figure 2.15 – **Hong-Ou-Mandel interferometer.** A pulsed field  $\hat{a}$  is input to an unbalanced Mach-Zehnder interferometer where it is temporally overlapped, using a delay line and a beam splitter, with a second pulse separated by  $\tau_p$ . The beam splitters have similar transmission and reflection coefficients  $R \approx T$ . Two detectors  $D_1$  and  $D_2$  register photon detection events at the output of the second beam splitter.

To measure the indistinguishability we temporally overlap two consecutively emitted photonic fields at the second beam splitter ( $R : T = 50 : 50$ ) by inserting a temporal delay equal to the pulse separation  $\tau_p$  in one arm of the interferometer. We then quantify the mean wavepacket overlap, or purity in the temporal domain, according to :

$$M = \frac{1}{\mu^2} \int \int |G^{(1)}(t, \tau)|^2 dt d\tau = \frac{1}{\mu^2} \int \int |\langle \hat{a}^\dagger(t + \tau) \hat{a}(t) \rangle|^2 dt d\tau \quad (2.35)$$

where we introduce the first-order (amplitude) correlation function

$$G^{(1)}(t, \tau) = \langle \hat{a}^\dagger(t + \tau) \hat{a}(t) \rangle \quad (2.36)$$

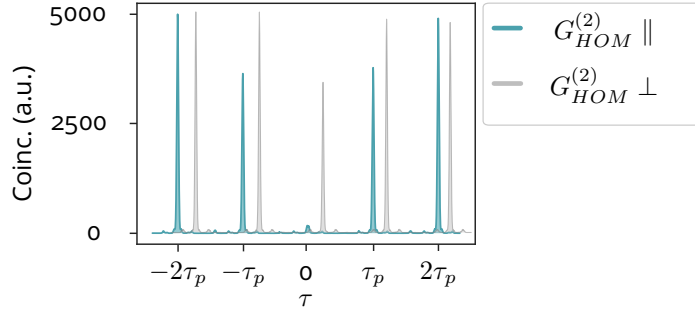


Figure 2.16 – **Hong-Ou-Mandel coincidence histogram**. Coincidences as a function of relative delay  $\tau$  for pulsed excitation in parallel ( $\parallel$ ) polarization and perpendicular ( $\perp$ ) polarization configuration. Peaks are separated by pulse repetition rate  $\tau_p$ .

in terms of the propagating input mode  $\hat{a}(t)$ .

In our setup, both beam splitters have very similar transmission and reflection coefficients ( $R \approx T$ ). Two superconducting nanowire single photon detectors ( $D_1, D_2$ ) at the outputs of the second beam splitter monitor output modes  $\hat{a}_3$  and  $\hat{a}_4$ , where we omit the time dependence for simplicity. If the consecutively emitted wavepackets are indistinguishable, they will bunch together at the second beam splitter. This effect is referred to as the Hong-Ou-Mandel effect, named after the researchers who first experimentally reported on this phenomenon in 1987 (32). Qualitatively, this phenomenon means that if you measure simultaneous events (coincidences) with the detectors monitoring outputs  $\hat{a}_3$  and  $\hat{a}_4$  that the two input fields share limited or no wavepacket overlap.

In practice, similar to measuring the single-photon purity, one can compute a coincidence histogram measuring coincidence clicks over a period of time, resulting in a time integrated histogram such as the one shown in Fig. 2.16. This histogram contains two measurements : a coincidence histogram for wavepackets that share same polarization ( $G_{HOM,\parallel}^{(2)}$ ), and wavepackets that have perpendicular polarization ( $G_{HOM,\perp}^{(2)}$ ) making them distinguishable<sup>1</sup>. This second measurement, where no interference is expected, is used as a reference to  $G_{HOM,\parallel}^{(2)}$ . The second-order correlation function in terms of output mode operators describing this measurement is given by

$$G_{HOM}^{(2)}(t, \tau) = \langle \hat{a}_3^\dagger(t) \hat{a}_4^\dagger(t + \tau) \hat{a}_3(t) \hat{a}_4(t + \tau) \rangle, \quad (2.37)$$

and similar to the correlation function describing a HBT measurement, we have

1. For example by adding a half wave plate ( $\lambda/2$ ) in one of the arms of the interferometer in Fig. 2.15.

the time integral over the coincidences for delay  $\tau$

$$G_{\text{HOM}}^{(2)}(\tau) = \int G_{\text{HOM}}^{(2)}(t, \tau) dt, \quad (2.38)$$

describing the histogram in Fig. 2.16.

We apply the beam splitter relations in Eq. 2.29 giving us  $G_{\text{HOM}}^{(2)}$  in terms of  $\hat{a}_1, \hat{a}_2$ . To simplify the resulting expression we assume again that the emitted pulse length ( $1/\gamma$ ) is much shorter than  $\tau_p$ . We then have :

$$\begin{aligned} 4G_{\text{HOM}}^{(2)}(t, \tau) = & \langle \hat{a}_1^\dagger(t) \hat{a}_1^\dagger(t + \tau) \hat{a}_1(t + \tau) \hat{a}_1(t) \rangle \\ & + \langle \hat{a}_1^\dagger(t) \hat{a}_1(t) \rangle \langle \hat{a}_2^\dagger(t + \tau) \hat{a}_2(t + \tau) \rangle \\ & + \langle \hat{a}_1^\dagger(t + \tau) \hat{a}_1(t + \tau) \rangle \langle \hat{a}_2^\dagger(t) \hat{a}_2(t) \rangle \\ & + \langle \hat{a}_2^\dagger(t) \hat{a}_2^\dagger(t + \tau) \hat{a}_2(t + \tau) \hat{a}_2(t) \rangle \\ & - 2\text{Re} \left( \langle \hat{a}_1^\dagger(t) \hat{a}_1(t + \tau) \rangle \langle \hat{a}_2^\dagger(t) \hat{a}_2(t + \tau) \rangle \right). \end{aligned} \quad (2.39)$$

We then apply the beam splitter relations a second time. In terms of input state  $\hat{a}$  we find

$$8G_{\text{HOM}}^{(2)}(t, \tau) = I(t)I(t + \tau) + G^{(2)}(t, \tau) - |G^{(1)}(t, \tau)|^2 \quad (2.40)$$

with  $G^{(2)}(t, \tau) = \langle \hat{a}^\dagger(t) \hat{a}^\dagger(t + \tau) \hat{a}(t + \tau) \hat{a}(t) \rangle$ , the second-order correlation from measuring intensity correlations with the Hanbury Brown - Twiss setup and  $G^{(1)}(t, \tau)$  containing the information on the indistinguishability  $M$ , see Eq. 2.35.

Similarly to the Hanbury-Brown and Twiss normalization procedure, the far delay peaks  $\tau = |t - t'|$  with  $t' \gg t$  serve as a reference for normalization. Indeed, for single-photon input states these coincidences are uncorrelated, and Eq. 2.40 becomes :

$$\begin{aligned} 4G_{\text{HOM}}^{(2)}(t, t' \gg t) = & \eta_1 \eta_2 \langle \hat{a}_3^\dagger(t) \hat{a}_4^\dagger(t') \hat{a}_3(t) \hat{a}_4(t') \rangle \\ = & \eta_1 \eta_2 I_3 I_4 = \eta_1 \eta_2 I^2. \end{aligned} \quad (2.41)$$

We define the normalized second-order correlation function according to :

$$g_{\text{HOM}}^{(2)}(\tau) = \frac{\int G_{\text{HOM}}^{(2)}(t, \tau) dt}{2\eta_1 \eta_2 \mu^2}, \quad (2.42)$$

with  $\mu_3 = \int I_3 dt$  and  $\mu_4 = \int I_4 dt$ . The peak at zero delay  $g_{\text{HOM}}^{(2)}(0)$  contains the coincidences measured with zero delay between the detectors. This peak area increases with simultaneous detection of photons, a sign of imperfect wavepacket overlap  $M$  between the interfering states. To solve for  $M$ , one can use zero delay coincidences measured in cross-polarization configuration where photons are

made perfectly distinguishable, and thus serve as a benchmark where no interference is expected. In such case, the second-order correlation function measured in orthogonal polarization and for zero delay ( $\tau = 0$ ) is given by :

$$\int G_{\text{HOM},\perp}^{(2)}(t, \tau = 0)dt = \int \frac{1}{4}\eta_1\eta_2 I(t)I(t + \tau)dt = \frac{1}{4}\eta_1\eta_2\mu^2 \quad (2.43)$$

Because generally, the detector efficiencies in parallel and in orthogonal polarization are not equal,  $\eta_{i,\parallel} \neq \eta_{i,\perp}$ , we define the the visibility of HOM interference, giving access to  $M$ , through the normalized second-order correlation functions :

$$V_{\text{HOM}} = \frac{g_{\text{HOM},\perp}^{(2)}(0) - g_{\text{HOM},\parallel}^{(2)}(0)}{g_{\text{HOM},\perp}^{(2)}(0)} = 1 - \frac{g_{\text{HOM},\parallel}^{(2)}(0)}{g_{\text{HOM},\perp}^{(2)}(0)}. \quad (2.44)$$

Considering Eq. 2.42 and Eq. 2.43, we have  $g_{\text{HOM},\perp}^{(2)} = 1/2$ . As a result, the visibility of Hong-Ou-Mandel interference reduces to :  $V_{\text{HOM}} = M$  with  $M$  defined in Eq. 2.35. It was previously shown that in presence of multi-photon components, spectrally and temporally identical to the wanted single-photon component, the HOM visibility in Eq. 2.44 can be written as :  $V_{\text{HOM}} = M - g^{(2)}$  (79; 80). However, multi-photon components can arise from different sources, and as such share no to limited overlap (i.e. temporally, spectrally) with the single-photon component. Below we show how to account for such separable noise in indistinguishability measurements.

### Indistinguishability measurement of an imperfect source

As part of this PhD work, we conducted a study on how the mean wavepacket indistinguishability (and thus HOM visibility) is affected by the nature of unwanted multi-photon components (64; 81). We therefore differentiate between the total mean wavepacket overlap  $M$ , which corresponds to the whole state after losses, and the mean wavepacket overlap of the single-photon component at the source  $M_s$ . The latter parameter is important as it reveals the impact of different dephasing mechanisms on the single-photon source and is mostly independent from the phenomena resulting in  $g^{(2)} \neq 0$ .

Multi-photon components can be classified as either distinguishable from, or identical to the wanted single-photon component. In Ref. (81) we take these differences into account and show that the visibility of HOM interference for an imperfect single-photon source is given by (for  $R = T = 1/\sqrt{2}$ ) :

$$V_{\text{HOM}} = M_s - \left( \frac{1 + M_s}{1 + M_{\text{sn}}} \right) g^{(2)}, \quad (2.45)$$

where  $M_{\text{sn}}$  is the mean wavepacket overlap between the single-photon component and the noise photon, with  $0 \leq M_{\text{sn}} \leq M_s$ . We studied two limiting cases of this

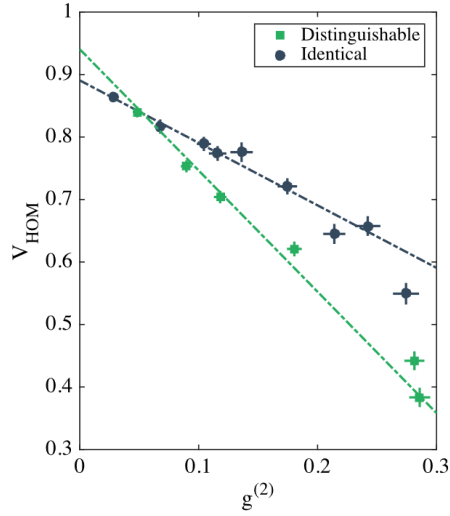


Figure 2.17 – **The impact of different types of noise photons on the visibility of HOM interference.** The visibility of HOM interference as a function of single-photon purity for distinguishable (green squares) noise photons and identical (black circles) noise photons. Taken from Ref. (81).

expression :  $M_s = M_{\text{sn}}$ , when the noise photon is identical to the single-photon, and  $M_{\text{sn}} = 0$ , when the noise photon shares no overlap with the single-photon. An experimental study of these two limiting cases shows that indeed the nature of the noise photon impacts the HOM visibility differently. In Fig. 2.17 we plot the visibility of HOM interference as a function of single-photon purity for distinguishable (green squares) and identical (black circles) noise sources. Here we add noise, increase  $g^{(2)}$ , by either increasingly adding laser photons (distinguishable) or single-photons from the same QD source (identical) to the light field. The fits correspond to Eq. 2.45 considering  $M_{\text{sn}} = 0$  (green) and  $M_s = M_{\text{sn}}$  (blue).

When considering the origin of noise in our QD sources, we can distinguish between trion-based sources and exciton-based sources. For trion-based sources, the multi-photon component arises from re-excitation during the excitation pulse (81; 82). The photon can get emitted by the QD before the end of the excitation pulse, leaving the possibility to emit a second photon. These photons are therefore temporally distinguishable from each other, and as such deemed as separable noise. Exciton-based sources on the other hand, do not suffer from re-excitation. The fine-structure splitting and optical selection rules imply that single-photon emission most likely occurs once the excitation pulse is over, see Ref. (43). Therefore, noise contributing to a non-zero  $g^{(2)}$  is dominantly caused by imperfect laser rejection, and as such also considered as separable noise. We

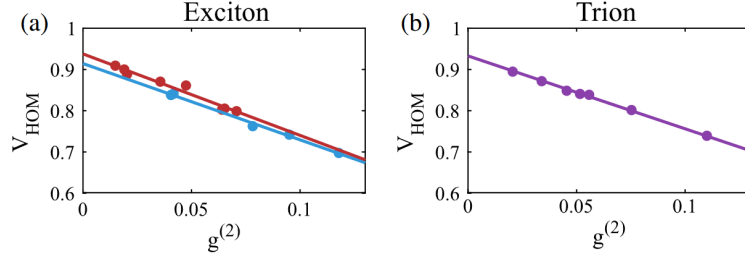


Figure 2.18 – **Influence of the photon noise in exciton- and trion-based sources.** The visibility of HOM interference as a function of single-photon purity for (a) an exciton-based source where we increase  $g^{(2)}$  by either increasing the pulse duration causing re-excitation (blue) or decreasing the laser rejection (red), and for (b) a trion-based source where we increase the pulse duration. Taken from Ref. (81).

thus expect, despite the different origins of multi-photon components, that in both cases we can treat the multi-photon component in trion- and exciton-based sources as uncorrelated – distinguishable – noise.

Subsequent measurements support this hypothesis, as shown in Fig. 2.18. Here again we measure the HOM visibility as a function single-photon purity now for an exciton- and a trion-based source. For both sources we increase the  $g^{(2)}$  by either increasing the pulse duration of the excitation pulse (exciton : red ; trion : purple), or decreasing the suppression of the excitation laser (exciton : blue). The data is fit with Eq. 2.45, from which we extract  $M_{sn} = 0$ , indicating indeed that despite that we can treat noise as separable for both trion- and exciton-based sources. Hence, in the limit of low  $g^{(2)}$  ( $g^{(2)} < 0.15$ ), the single-photon indistinguishability is given by :

$$M_s = \frac{V_{\text{HOM}} + g^{(2)}}{1 - g^{(2)}}, \quad (2.46)$$

for  $R = T = 1/\sqrt{2}$ . This equation is altered when compensating for imbalance in the final beam splitter :

$$M_s = \frac{V_{\text{HOM}} + 4RT(1 + g^{(2)}) - 1}{4RT(1 - g^{(2)})}. \quad (2.47)$$

These formulas, Eq. 2.46 and Eq. 2.47, presented here and in Ref. (81) thus allow to extract an upper bound (before losses) on the indistinguishability through HOM measurements, knowing the single-photon purity of the wavepacket, and are used in this thesis to quantify the wavepacket indistinguishability.

## 2.5 . Coherent control and energy coherence

In this section, we discuss how we can coherently control the state of our QD through resonant excitation of the transition. This technique is central for the present PhD work : it allows to create a quantum superposition of the QD ground and excited state. We then recall an important result published in 2019 by our group showing for the first time how this coherence in the QD energy basis is transferred to the electromagnetic field upon spontaneous emission (83).

### 2.5.1 . Coherent control of a two-level system

In this section we use the optical Bloch equations (OBE) in the Schrödinger picture to describe the dynamics of a coherently driven two-level system. This set of equations also describes the decay of the excited state population of an atom, thereby populating the ground state, as well as the decay of coherences (68).

Let us start by considering the Hamiltonian describing the quantized qubit-cavity system under coherent driving :

$$\hat{H} = \hat{H}_{\text{atom}} + \hat{H}_{\text{cavity}} + \hat{H}_{\text{int}}, \quad (2.48)$$

with  $\hat{H}_{\text{atom}}$  the Hamiltonian describing the qubit dynamics,  $\hat{H}_{\text{cavity}}$  the field Hamiltonian inside the cavity, and  $\hat{H}_{\text{int}}$  the interaction Hamiltonian describing the coupling between the two quantized systems. The atom Hamiltonian is given by

$$\hat{H}_{\text{atom}} = \hbar\omega_0\hat{\sigma}_+\hat{\sigma}_- \quad (2.49)$$

with  $\omega_0$  the transition frequency between the ground and excited state, and with the raising and lowering operators :

$$\begin{aligned} \hat{\sigma}_+ &= |e\rangle\langle g| \\ \hat{\sigma}_- &= |g\rangle\langle e|, \end{aligned}$$

respectively, and where

$$|g\rangle = \begin{bmatrix} 1 \\ 0 \end{bmatrix} \quad |e\rangle = \begin{bmatrix} 0 \\ 1 \end{bmatrix}.$$

We can also introduce the inversion operator

$$\hat{\sigma}_3 = |e\rangle\langle e| - |g\rangle\langle g|, \quad (2.50)$$

where the introduced operators obey

$$\begin{aligned} [\hat{\sigma}_+, \hat{\sigma}_-] &= \hat{\sigma}_3 \\ [\hat{\sigma}_3, \hat{\sigma}_\pm] &= \pm 2\hat{\sigma}_\pm. \end{aligned} \quad (2.51)$$

The Hamiltonian of the quantized electromagnetic field in the cavity, approximated as a single mode field, is written as

$$\hat{H}_{\text{cavity}} = \hbar\omega\hat{a}^\dagger\hat{a}, \quad (2.52)$$

and the interaction Hamiltonian as :

$$\hat{H}_{\text{int}} = -\hat{\mathbf{d}} \cdot \hat{\mathbf{E}},$$

with dipole operator :

$$\hat{\mathbf{d}} = \mathbf{d}_{ge}(\sigma_- + \sigma_+). \quad (2.53)$$

The electric field at the position of the QD ( $\mathbf{r}_0$ ) is given by, see Section 2.3 :

$$\hat{\mathbf{E}}(\mathbf{r}_0) = \sqrt{\frac{\hbar\omega}{2n^2\epsilon_0 V}} \mathbf{p}(\mathbf{r}_0)(\hat{a} + \hat{a}^\dagger), \quad (2.54)$$

where  $\mathbf{p}(\mathbf{r}_0)$  is the real part of the normalized spatial mode profile (polarization mode), and we recall  $V$  is the quantization volume. We can now write the interaction Hamiltonian as

$$\hat{H}_{\text{int}} = \hbar g(\hat{\sigma}_+ + \hat{\sigma}_-)(\hat{a} + \hat{a}^\dagger). \quad (2.55)$$

Here we recognize the coupling strength  $g$ , previously introduced, whose definition can be written as

$$\hbar g = \sqrt{\frac{\hbar\omega}{2n^2\epsilon_0 V}} \mathbf{d}_{ge} \cdot \mathbf{p}(\mathbf{r}_0), \quad (2.56)$$

If we assume the field is maximum at  $\mathbf{r}_0$  and the polarization of the field is aligned to the dipole (i.e.  $\mathbf{d}_{ge} \cdot \mathbf{p}(\mathbf{r}_0) = d$ ), the coupling strength can be written as :

$$\hbar g = d \sqrt{\frac{\hbar\omega}{2n^2\epsilon_0 V}}, \quad (2.57)$$

where we assume  $d$  is real.

When driving the QD on-resonance ( $\omega \approx \omega_0$ ), this parameter  $g$  is related to the Rabi frequency  $\Omega_R$  through  $\Omega_R = 2g\alpha$  (84). This is the frequency, dependent on the coupling strength and field amplitude  $\alpha = \sqrt{I}$  (with  $I$  the field intensity), at which the populations of the combined QD-cavity system oscillate, known as Rabi oscillations. If the field is initially in a vacuum state, then we have  $\Omega_R = 2g$ .

Combining the three Hamiltonians, we obtain the total Hamiltonian of the two-body system :

$$\begin{aligned} \hat{H} &= \hat{H}_{\text{atom}} + \hat{H}_{\text{cavity}} + \hat{H}_{\text{int}} \\ &= \hbar\omega_0\hat{\sigma}_+\hat{\sigma}_- + \hbar\omega\hat{a}^\dagger\hat{a} + \frac{\Omega_R\hbar}{2}(\hat{\sigma}_+ + \hat{\sigma}_-)(\hat{a} + \hat{a}^\dagger). \end{aligned} \quad (2.58)$$

We simplify this Hamiltonian by expressing the operators in terms of their explicit time dependence :

$$\hat{a}(t) = \hat{a}(0)e^{-i\omega t}, \quad \hat{a}^\dagger(t) = \hat{a}^\dagger(0)e^{i\omega t}, \quad \hat{\sigma}_\pm(t) = \hat{\sigma}_\pm(0)e^{\pm i\omega_0 t}. \quad (2.59)$$

Then the products of the operators in Eq. 2.58 become

$$\begin{aligned}\hat{\sigma}_+\hat{a} &\sim e^{i(\omega_0-\omega)t}, & \hat{\sigma}_-\hat{a}^\dagger &\sim e^{-i(\omega_0-\omega)t}, \\ \hat{\sigma}_+\hat{a}^\dagger &\sim e^{i(\omega_0+\omega)t}, & \hat{\sigma}_-\hat{a} &\sim e^{-i(\omega_0+\omega)t}.\end{aligned}$$

For  $\omega_0 \approx \omega$ , the two terms containing the sum of frequencies (bottom line) will vary faster than the other two terms. The last two terms  $\hat{\sigma}_+\hat{a}^\dagger, \hat{\sigma}_-\hat{a}$  do not uphold energy conservation, and correspond to the emission of a photon as the atom transitions from the ground to the excited state, and to the absorption of a photon as the atom goes from the excited state to the ground state, respectively. These non-energy conserving terms cancel under the rotating wave approximation, where we use the fact that the fast evolving terms containing  $\omega_0 + \omega$  average to zero when time integrating. This allows us to write the total Hamiltonian as :

$$\hat{H} = \hbar\omega_0\hat{\sigma}_+\hat{\sigma}_- + \hbar\omega\hat{a}^\dagger\hat{a} + \frac{\Omega_R\hbar}{2}(\hat{\sigma}_+\hat{a} + \hat{\sigma}_-\hat{a}^\dagger), \quad (2.60)$$

which is referred to as the Jaynes-Cummings model, and describes the interaction between a two-level system and a single-mode electromagnetic field (68; 85).

We now turn to the semi-classical representation of the electromagnetic field to describe the dynamics of a coherently driven QD using the optical Bloch equations in the Schrödinger picture. The density matrix describing our two-level system in the energy basis is given by :

$$\rho = \begin{bmatrix} \rho_{ee} & \rho_{eg} \\ \rho_{ge} & \rho_{gg} \end{bmatrix},$$

with  $\rho_{ij} = \langle i|\rho|j\rangle$ . The diagonal entries correspond to the *populations* of the ground and excited state, and the off-diagonal terms contain **coherences**, also called energy coherence. We can write the master equation for a dissipative process, describing the evolution of the two-level system upon interaction with the driving field as (83; 86; 87) :

$$\begin{aligned}\frac{d}{dt}\rho(t) &= -\frac{i}{\hbar}[\hat{H}, \rho] + \frac{\gamma}{2}([\hat{\sigma}_-, \rho\hat{\sigma}_+] + [\hat{\sigma}_-\rho, \hat{\sigma}_+]) \\ &+ \gamma^*([\hat{\sigma}_-\hat{\sigma}_+, \rho\hat{\sigma}_-\hat{\sigma}_+] + [\hat{\sigma}_-\hat{\sigma}_+\rho, \hat{\sigma}_-\hat{\sigma}_+]),\end{aligned} \quad (2.61)$$

with **total decoherence rate**  $\Gamma = \gamma/2 + \gamma^*$ , where  $\gamma$  is the **spontaneous decay rate** and  $\gamma^*$  the **dephasing rate of the two-level system**. We can discard the bare cavity Hamiltonian as it does not contribute to the dynamics of the system in the weak coupling regime, thus leaving the effective Hamiltonian :

$$\hat{H}_{\text{eff}} = \hat{H}_{\text{atom}} + \hat{H}_{\text{int}} = \hbar\omega_0\hat{\sigma}_+\hat{\sigma}_- + \frac{\Omega_R\hbar}{2}(\hat{\sigma}_+e^{i\omega t} + \hat{\sigma}_-e^{-i\omega t}). \quad (2.62)$$

To solve the equation of motion for any of the density matrix elements, one can compute  $\langle i|\rho|j\rangle$ . For example, let us consider the off-diagonal elements of the density matrix, the first part of the master equation becomes :

$$\frac{d}{dt}\rho_{eg} = -\frac{i}{\hbar}\langle e|[\hat{H}_{\text{eff}}, \rho]|g\rangle \quad (2.63)$$

When substituting  $\hat{H}_{\text{eff}}$  for Eq. 2.62, we can divide the equation into three parts. Using  $\sigma_-|e\rangle = |g\rangle$ ,  $\sigma_-|g\rangle = 0$ ,  $\sigma_+|e\rangle = 0$  and  $\sigma_+|g\rangle = |e\rangle$ , the evolution of the two-level system gives

$$-\frac{i}{\hbar}\langle e|[\hat{H}_{\text{atom}}, \rho]|g\rangle = -i\omega_0\langle e|(\sigma_+\sigma_-\rho - \rho\sigma_+\sigma_-)|g\rangle = -i\omega_0\rho_{eg}. \quad (2.64)$$

The second part, containing the interaction Hamiltonian, leads to

$$\begin{aligned} -\frac{i}{\hbar}\langle e|[\hat{H}_{\text{int}}, \rho]|g\rangle &= -i\frac{\Omega_R}{2}\langle e|(\sigma_-e^{i\omega t} + \sigma_+e^{-i\omega t})\rho - \rho(\sigma_-e^{i\omega t} + \sigma_+e^{-i\omega t})|g\rangle \\ &= -i\frac{\Omega_R}{2}\langle g|e^{-i\omega t}\rho|g\rangle + i\frac{\Omega_R}{2}\langle e|e^{-i\omega t}\rho|e\rangle \\ &= i\frac{\Omega_R}{2}(\rho_{ee} - \rho_{gg})e^{-i\omega t}, \end{aligned} \quad (2.65)$$

and the dissipative term in Eq. 2.62 becomes  $-\gamma^*\rho_{eg}$ . Combining the three elements, we obtain the evolution of density matrix element  $\rho_{eg}$  (energy coherence term) :

$$\frac{d}{dt}\rho_{eg} = -\gamma^*\rho_{eg} - i\omega_0\rho_{eg} + i\frac{\Omega_R}{2}(\rho_{ee} - \rho_{gg})e^{-i\omega t}. \quad (2.66)$$

Finally, we simplify the expression by moving into the rotating frame, thereby obtaining :

$$\frac{d}{dt}\rho_{eg} = \frac{d}{dt}\rho_{ge}^* = -\gamma^*\rho_{eg} + i\Delta\rho_{eg} + i\frac{\Omega_R}{2}(\rho_{gg} - \rho_{ee}), \quad (2.67)$$

where  $\Delta = \omega_0 - \omega$ . In a similar fashion, we obtain expressions for the ground and excited state population dynamics. We then write the coupled optical Bloch equations describing the dynamics of a two-level system upon resonant excitation :

$$\begin{pmatrix} \dot{\rho}_{ee} \\ \dot{\rho}_{gg} \\ \dot{\rho}_{ge} \\ \dot{\rho}_{eg} \end{pmatrix} = \begin{pmatrix} -\gamma & 0 & \frac{i\Omega_R}{2} & \frac{-i\Omega_R}{2} \\ \gamma & 0 & \frac{-i\Omega_R}{2} & \frac{i\Omega_R}{2} \\ \frac{i\Omega_R}{2} & \frac{-i\Omega_R}{2} & -i\Delta - \gamma^* & 0 \\ \frac{-i\Omega_R}{2} & \frac{i\Omega_R}{2} & 0 & i\Delta - \gamma^* \end{pmatrix} \begin{pmatrix} \rho_{ee} \\ \rho_{gg} \\ \rho_{ge} \\ \rho_{eg} \end{pmatrix}, \quad (2.68)$$

where we take for on-resonance conditions  $\Delta = 0$ . We can see from the coupled Bloch equations that the density matrix elements  $\rho_{gg}$  and  $\rho_{ee}$  decay with spontaneous emission rate  $\gamma$ , whereas the coherences are affected by dephasing of the system.

We can solve these coupled equations for some particular cases, such as for purely coherent dynamics ( $\Gamma = 0$ ). If we assume an atom initially in the ground state and  $\Delta = 0$ , we get the coupled equations :

$$\frac{d}{dt}\rho_{ee} = -\frac{d}{dt}\rho_{gg} = \frac{i\Omega_R}{2}(\rho_{eg} - \rho_{ge}) \quad (2.69)$$

$$\frac{d}{dt}\rho_{eg} = \frac{d}{dt}\rho_{ge}^* = \frac{i\Omega_R}{2}(\rho_{gg} - \rho_{ee}) \quad (2.70)$$

Solving these differential equations for  $\rho$  results in :

$$\rho_{ee} = \sin^2\left(\frac{\Omega_R t}{2}\right) \quad (2.71)$$

$$\rho_{ge} = i \sin\left(\frac{\Omega_R t}{2}\right) \cos\left(\frac{\Omega_R t}{2}\right), \quad (2.72)$$

which describe the evolution of the density matrix for a closed quantum system. The populations at time  $t$ , or probability of finding the atom in the ground state  $|g\rangle$  or excited state  $|e\rangle$  with the atom initially in the ground state, are given by

$$P_g = \cos^2\left(\frac{\Omega_R t}{2}\right) \quad (2.73)$$

$$P_e = \sin^2\left(\frac{\Omega_R t}{2}\right), \quad (2.74)$$

respectively. For a pulse duration equal to  $t = \pi/\Omega_R$ , these equations predict full population inversion and no coherences. In Fig. 2.19 we plot different solutions to the optical Bloch equations in Eq. 2.68, population oscillations as a function of time for  $\Delta = 0$ . We plot the excited state population as a function of time where we assume the driving field stays on after time  $t = 0$ . The dephasing rate  $\gamma^*$  affects the time it takes to reduce the oscillations to a steady-state. Whereas the Rabi frequency  $\Omega_R = 2g\sqrt{I}$  impacts the probability of reaching the excited state, and the oscillation frequency. For an ideal emitter, we have  $\gamma^* = 0$ , or  $\Gamma = \gamma/2$ . Under the latter condition, we call the emitter a lifetime-limited quantum emitter.

Measuring population oscillations (Rabi oscillations) in emission, whether in absence or presence of damping, are an indication of coherent control over the qubit state whereby the light field and the qubit periodically exchange energy at frequency  $\Omega_R$ . We show in Section 2.5.4 how we measure these Rabi oscillations, which attest for coherent control over the QD states, and as we will show in Section 2.5.5, in our system also leads to the generation of photon-number superpositions with coherence in the photon-number basis.

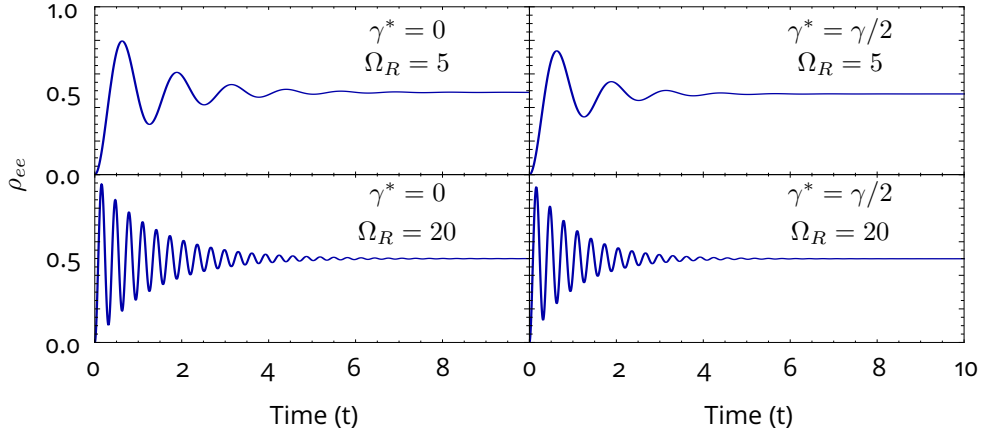


Figure 2.19 – **Solutions to optical Bloch equations.** The excited state population  $\rho_{ee}$  as a function of time when driving with resonant laser field  $\Delta = 0$ . For different Rabi frequencies  $\Omega_R$  (intensity of the driving field) and dephasing rates  $\gamma^*$ .

### 2.5.2 . Resonant excitation of a QD in a cavity

To resonantly excite our QD source and reject the excitation laser that is at the same wavelength as the single-photons, we use a cross-polarization configuration, Fig 2.20. We resonantly ( $\approx 925$  nm) excite our QD inside a cryostation with a pulsed laser with a pulse duration between 3 – 7 ps. The excitation laser has a polarization dictated by the first polarizer and polarizing beam splitter (PBS) in Fig. 2.20. The polarization is set to the transmission axis of the PBS. By aligning the quarter- ( $\lambda/4$ ) and half-wave ( $\lambda/2$ ) plate we can control the linear polarization of the light entering the cavity and we can compensate for distortions in polarization due to ellipticity in our setup. We set the polarization of the excitation field along one of the cavity axes so not to collect reflected laser light whose polarization is rotated by the cavity birefringence. As a result, the laser light reflected from the pillar and the emission from the QD are cross-polarized. This orthogonal polarization in combination with the PBS leads to rejection of the laser field in the collection path. The remaining field, containing the emission from the QD, is then either sent to other optical setups, to a spectrometer (Horiba, 35 pixels/nanometer), or to superconducting nanowire single-photon detectors (SNSPDs, Single Quantum) for characterization or other measurements.

Note that, although the pillar cavity is mostly of circular shaped, the cavity still presents some birefringence caused by slight asymmetries in the cylindrical geometry arising from anisotropy present during the etching step of the fabrication process. As a result, the cavity supports two perpendicular linearly polarized cavity modes  $H$  and  $V$  split by energy. This cavity birefringence puts constraints on the resonant excitation of exciton and trion states coupled to micropillar cavities as we summarize below.

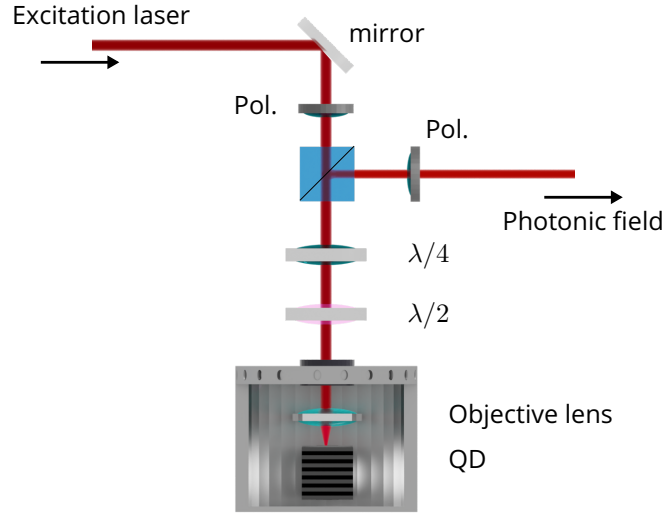


Figure 2.20 – **Cross-polarization configuration for resonant excitation of the QD.** The polarization of the resonant excitation laser is set in cross-polarization with respect to the emission of the QD through a set of polarizers, waveplates and a polarizing beam splitter (PBS). An objective lens placed inside the cryostat focuses the laser onto the sample. The emitted field is reflected from the PBS and sent towards other parts of the setup.

### Resonant fluorescence of a neutral QD

The energy level diagram of a neutral QD consists of three levels, Fig. 2.4. The three levels constitute a ground state  $|g\rangle$  and two excited states  $|X\rangle, |Y\rangle$ , separated by the fine-structure splitting  $\Delta_{FSS} = E_x - E_y$ . The neutral exciton states couple to the cavity modes  $|V\rangle$  and  $|H\rangle$  according to :

$$\begin{aligned}
 |V\rangle &= -\sin(\theta) |X\rangle + \cos(\theta) |Y\rangle \\
 |H\rangle &= \cos(\theta) |X\rangle + \sin(\theta) |Y\rangle,
 \end{aligned}$$

where  $\theta$  is the angle between the  $X$ -dipole and  $H$ -polarization axis, see Fig. 2.21. This angle  $\theta$  is determined randomly during the fabrication process as a result of cavity (a-)symmetry.

In cross-polarization configuration we align the polarization of the excitation laser to the polarization of the PBS in Fig. 2.20,  $V_{exc}$ , at  $90^\circ$  angle with respect to the polarization of the collected photons,  $H_{coll}$ . Whenever  $V_{exc}$  and  $H_{coll}$  are not aligned to the cavity axes  $V$  and  $H$  ( $\phi \neq 0$  in Fig. 2.20(a)), cavity birefringence – effectively acting as a wave plate – causes the excitation light to rotate to  $H_{coll}$ . This laser leakage causes serious degrading of the collected single-photon purity and indistinguishability. As such, it is necessary to **align the excitation and**

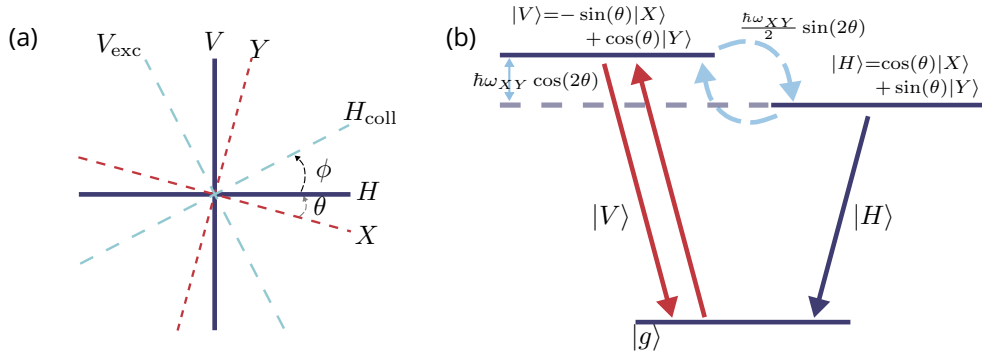


Figure 2.21 – **Energy level diagram of a neutral QD.**(a) Orientation of QD dipole axes  $X, Y$ , cavity polarization axes  $V, H$ , and polarization axes of the excitation laser  $V_{exc}$  and collection polarization  $H_{coll}$ , with  $\theta$  the angle between the  $X$ -dipole and  $H$ -polarization axis, and  $\phi$  the angle between the cavity  $H$  axis and the collection polarization  $H_{coll}$ . (b) Energy level diagram of an exciton based quantum dot source in the cavity mode bases with ground  $|g\rangle$  and excited states  $|V\rangle, |H\rangle$ , and where  $\theta$  is directly linked to the fine-structure splitting according to  $\Delta_{FSS} = \hbar\omega_{XY} \sin(2\theta)/2$ .

collection axes along the cavity axes such that  $\phi = 0$  and  $V = V_{exc}, H = H_{coll}$ .

In the cavity polarization basis, the energy level diagram of a neutral QD can be described by Fig. 2.21(b). We see that under resonant excitation the coupling between the excited states  $|V\rangle$  and  $|H\rangle$ , proportional to the fine-structure splitting  $\Delta_{FSS} = \hbar\omega_{XY} \sin(2\theta)/2$ , gives rise to an oscillation in excited state populations whenever  $\theta \neq 0$ . As a result, the emission of a photon will have a time-dependent probability of being  $H$ -polarized. Using a cross-polarization configuration to excite in  $V$ -polarization and collect photons in  $H$ -polarization will thus lead to the rejection of any photon emitted in  $V$ . Contrastingly, if  $\theta = 0$  or  $\pi/2$  – equivalent to excitation in  $|X\rangle$  or  $|Y\rangle$  – the emitted photons have the same polarization as the driving field. In such case, cross-polarization configuration cannot be used to measure single-photons.

### Resonant fluorescence of a charged QD

In the case of a charged QD, the resonant excitation scheme is much simpler. Indeed, as shown in Fig. 2.22, in absence of an in-plane magnetic field, the optical selection rules can be rewritten in the cavity polarization basis with  $H$  and  $V$ .

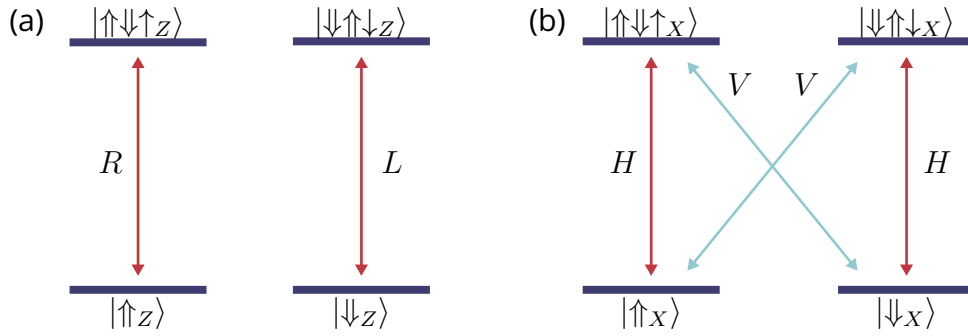


Figure 2.22 – **Energy level diagram trion.** (a) The degenerate ground and excited state levels of a positively charged trion state, composed of hole spin states  $|\uparrow\rangle_z, |\downarrow\rangle_z$ , and electron spin states  $|\uparrow\rangle_z, |\downarrow\rangle_z$ , in absence of a magnetic field. (b) Same as in for (a), but rewritten in the cavity polarization basis  $H$  and  $V$ .

Defining

$$|\uparrow_x\rangle = \frac{1}{\sqrt{2}}(|\uparrow_z\rangle + |\downarrow_z\rangle)$$

$$|\downarrow_x\rangle = \frac{1}{\sqrt{2}}(|\uparrow_z\rangle - |\downarrow_z\rangle),$$

and similar expressions for the excited states, we can write the linearly polarized optical transitions connecting the ground and excited states :

$$|H\rangle = \frac{1}{\sqrt{2}}(|R\rangle + |L\rangle)$$

$$|V\rangle = \frac{-i}{\sqrt{2}}(|R\rangle - |L\rangle),$$

which leads to the energy level diagram in the cavity polarization basis in Fig. 2.5(b). There we see that a linearly polarized  $V$  excitation pulse populates both excited states, which in turn both radiate  $H$  polarized light with a 50% probability.

### 2.5.3 . Excitation pulse shaping

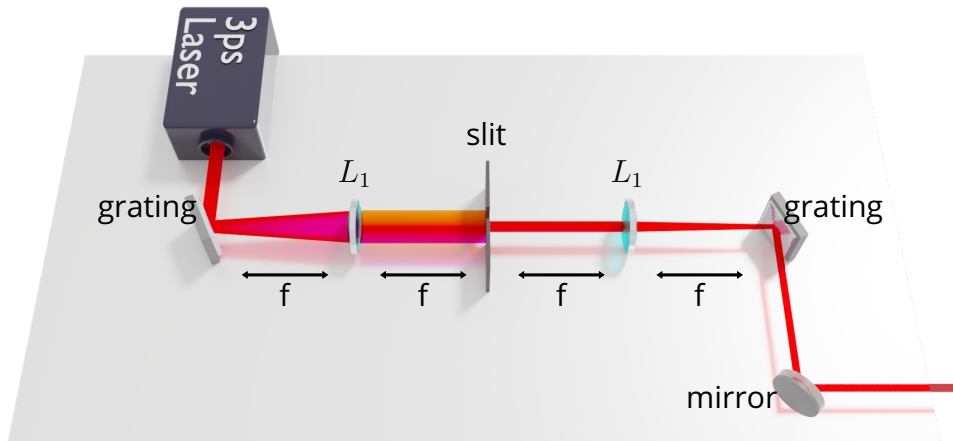


Figure 2.23 – **A 4f-system to control the temporal shape of a coherent field.** Two gratings, two lenses  $L_1$  with focal length  $f$  and a slit are all placed at distance  $f$  from each other. A slit allows for selecting wavelengths of the 3 ps pulsed laser, thereby temporally shaping the excitation laser.

In our experiments we use mode-locked Ti :Sapphire wavelength-tunable driving lasers (Mira from Coherent, and Tsunami from SpectraPhysics) which produce 3 ps pulses at a repetition rate of 81MHz. For the experiments in this thesis we need to control the pulse duration, or temporal shape, of the driving laser. In order to alter the pulse duration we use a 4f-system as depicted in Fig. 2.23. The setup consists of 2 gratings with 1200 lines/mm, 2 lenses  $L_1$  of focal length  $f$ , and a slit, all equidistantly placed at distance  $f$  of each other. The laser pulse is spectrally dispersed by the first diffraction grating. Next, a convex lens with focal length  $f$  makes the different spectral components of the beam parallel. A slit placed in the Fourier plane (at the shared focal point of the two lenses) allows to select a spectral component of the beam, cutting out the unwanted components. A second lens converges the beam onto a second grating which collapses the remaining components into a coherent beam. This technique allows us to adjust the pulse duration from 3 ps up to 15 ps. To achieve longer pulse durations we can insert multiple etalons in the path of the shaped laser pulse. The combination of 4f-line and etalons allows us to reach pulses with durations up to the lifetime of a single photon (around 180 ps). Moreover, shaping the spectral or temporal profile of our driving laser also allows us to increase the mode matching between the laser field and the QD-micropillar cavity to increase the excitation efficiency.

### 2.5.4 . Example of measured Rabi oscillations

We present here an example of measured Rabi oscillations when we resonantly drive our QD with a pulsed laser with constant pulse duration  $t = \tau_{\text{exc}}$  (here 3ps) while varying the laser power. We measure the QD emission intensity  $I_{\text{QD}}$  as a function of laser power  $P$ . During the excitation pulse, the ground and excited state populations of the QD oscillate with Rabi frequency  $\Omega_R$ . The Rabi frequency is proportional to the electric field amplitude, and thus to  $\sqrt{P}$ . After the pulse, the QD returns to the ground state, emitting a single-photon. The probability of emitting a single-photon is proportional to the probability of the QD being in the excited state,  $P_e = \sin^2(\theta/2)$  (Eq. 2.74) where we define pulse area  $\theta = \int \Omega_R(t)dt$ , not to be confused with the angle previously used to define the fine-structure splitting in Section 2.5.2.

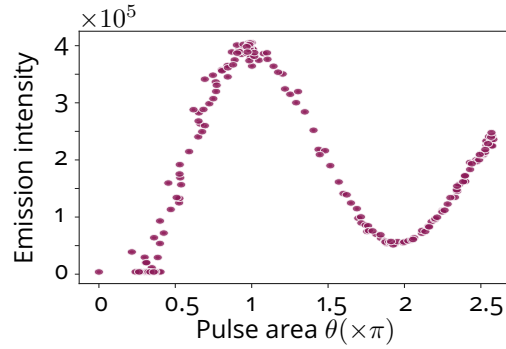


Figure 2.24 – **Example of measured Rabi oscillations.** The measured emission intensity of a quantum dot as a function of pulse area  $\theta$  of the driving laser, where  $\theta = 2 \arcsin(\sqrt{P})$ . By varying the pulse area we can see a periodic increase and decrease of emission intensity of our QD.

The relation between Rabi frequency and laser power ( $\Omega_R = 2g\sqrt{I}$ ) reveals that the emission intensity  $I_{\text{QD}}$  of a two-level system oscillating with phase  $\Omega_R\tau_{\text{exc}}$  is directly related to  $\sqrt{P}$ , and proportional to :

$$I_{\text{QD}} \propto \sin^2\left(\frac{\theta}{2}\right). \quad (2.75)$$

Fig. 2.24 shows a typical Rabi oscillation measurement from our two-level system, where we plot the unnormalized emission intensity as a function of the effective pulse area  $\theta = 2\arcsin(\sqrt{P})$  in units of  $\pi$ , from  $\theta = 0$  to  $2.5\pi$ . We observe that as we increase the excitation power, the probability of the QD being in the excited state, increases. We can define the pulse area for which the QD emission is maximum :  $\theta = \pi$ , with an excitation probability approaching unity. This pulse area is referred to as  $\pi$ -pulse and equal to the power necessary to generate a single-photon Fock state.

### 2.5.5 . Energy coherence in the emitted light field

In 2019, our group demonstrated in Ref. (83) that the coherently driven QD-cavity systems produce quantum superpositions of zero and one photons, in other words : **coherence in the photon-number basis**. In this section we recall these results that are the core of my PhD studies.

As mentioned in Section 2.5.4 we have coherent control over the atomic state of our QD through resonant pulsed excitation. To simplify, we consider the case of a two-level system composed of a ground  $|g\rangle$  and excited  $|e\rangle$  state. As we resonantly drive our QD, we generate a superposition in the two-level system basis :

$$|\Psi_{\text{atom}}\rangle = \sqrt{p_g}|g\rangle + \sqrt{p_e}e^{i\alpha}|e\rangle, \quad (2.76)$$

where we use  $p_g$  and  $p_e$  to indicate the ground and excited state populations, given by  $\cos(\theta/2)$  and  $\sin(\theta/2)$ , respectively. Moreover, this coherent driving also imprints its classical phase  $\alpha$  onto the atomic state, and brings energy coherence to the qubit as seen in the off-diagonal terms of the density matrix describing the state :

$$\rho = \begin{bmatrix} p_g & e^{-i\alpha}\sqrt{p_g p_e} \\ e^{i\alpha}\sqrt{p_e p_g} & p_e \end{bmatrix}.$$

Thus, we can write the energy coherence initially given to the qubit as :

$$s(0) = e^{i\alpha}\sqrt{p_g p_e} = e^{i\alpha} \cos\left(\frac{\theta}{2}\right) \sin\left(\frac{\theta}{2}\right). \quad (2.77)$$

Upon spontaneous decay, Ref. (83) demonstrated experimentally that the coherence present in the atom is transferred onto the photonic field, generating a photonic field according to :

$$|\Psi_a\rangle = \sqrt{p_0}|0\rangle + \sqrt{p_1}e^{i\alpha}|1\rangle, \quad (2.78)$$

where  $p_0 = p_g$  and  $p_1 = p_e$ .

To demonstrate this phenomena, the authors performed homodyne measurements with the emitted photonic fields using an unbalanced Mach-Zehnder interferometer as described in Section 2.4.3 and seen in Fig. 2.25 from Ref. (83). Here the HOM interference takes place at a 50 : 50 fibered beam splitter (FBS) between two consecutively emitted fields, one described by Eq. 2.78, and the other only differing by a relative phase  $\phi$  between the states :

$$|\Psi_b\rangle = \sqrt{p_0}|0\rangle + \sqrt{p_1}e^{i(\alpha+\phi)}|1\rangle, \quad (2.79)$$

where  $\phi$  arises from path length differences between the two arms of the MZI.

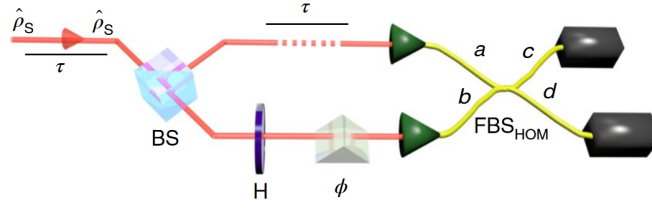


Figure 2.25 – **Measuring photon-number coherence.** A pulsed state  $\hat{\rho}_s$  comprising a photon-number superposition is input to a HOM interferometer. A temporal delay  $\tau$ , matched to the repetition rate of the pulses, temporally overlaps two consecutively entering states  $\hat{\rho}_s$  at a 50 :50 fiber beam splitter. Detectors monitoring the outputs of the FBS register the coincidence clicks. Taken from Ref. (83).

The output state resulting from interference is :

$$\begin{aligned}
 |\Psi_{\text{out}}\rangle = & p_0 |0, 0\rangle + \frac{p_1}{\sqrt{2}} e^{i(2\alpha+\phi)} (|2, 0\rangle - |0, 2\rangle) \\
 & + \sqrt{2p_0p_1} e^{i(\alpha+\frac{\phi}{2})} \left( \cos\left(\frac{\phi}{2}\right) |1, 0\rangle - i \sin\left(\frac{\phi}{2}\right) |0, 1\rangle \right), \quad (2.80)
 \end{aligned}$$

where we find the  $N00N$  ( $N = 2$ ) state for  $p_0 = 0$ . In contrast, whenever  $p_0 \neq 0$  we obtain an oscillation in the single counts  $|1, 0\rangle, |0, 1\rangle$  as a function of the interferometer phase  $\phi$  :  $\mu_{c,d} = p_1(1 \pm p_0 \cos(\phi))$ . Defining the visibility of single counts :

$$v_{\text{max}} = \max_{\phi} \frac{\mu_c - \mu_d}{\mu_c + \mu_d}, \quad (2.81)$$

one can show  $v_{\text{max}} = p_0$  for pure states in the photon-number basis, as described in Eq. 2.79.

To describe the more general situation where the light fields can no longer be described by a pure photonic state, the authors of Ref. (83) defined a density matrix in the form of :

$$\rho_S = \lambda \rho_{\text{pure}} + (1 - \lambda) \rho_{\text{mixed}}, \quad (2.82)$$

with  $\rho_{\text{pure}} = |\Psi_i\rangle \langle \Psi_i|$  and  $\rho_{\text{mixed}} = \text{diag}\{p_0, p_1\}$  a diagonal matrix, and  $\lambda$  a **parameter tuning the photon-number purity**. The density matrix of the pure state is given by :

$$\rho_{\text{pure}} = \begin{pmatrix} p_0 & \sqrt{p_0p_1} \\ \sqrt{p_1p_0} & p_1 \end{pmatrix}, \quad (2.83)$$

with photon-number coherence given by the off-diagonal elements  $\rho_{01} = \rho_{10}^* = \sqrt{p_0p_1}$ .

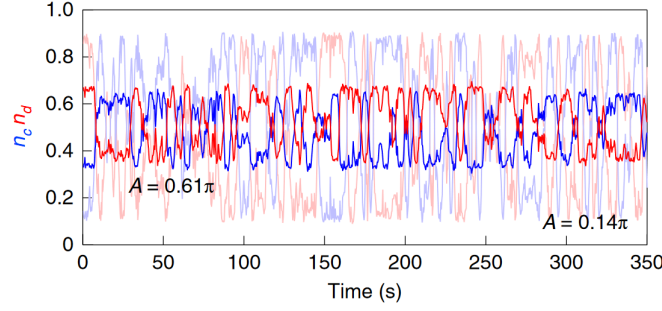


Figure 2.26 – **Signature of photon-number coherence.** Normalized intensities measured by detectors (here  $c, d$ ) as a function of time when driving a QD below  $\pi$ -pulse, here for pulse areas  $A = \theta$  of  $0.14\pi$  and  $0.61\pi$ . The anticorrelated oscillations evidence the generation of quantum coherence in the photon-number basis and temporal domain. Taken from Ref. (83)

The visibility amplitude for a general state described by  $\rho_S$  is given by :

$$v_{\max} = \lambda^2 p_0 \sqrt{M_s}, \quad (2.84)$$

with the photon indistinguishability (or purity in the temporal domain)  $M_s$  given previously in Section 2.4.3. Importantly, indistinguishability and photon-number purity both affect the visibility amplitude. As a result, **observing  $v_{\max} \neq 0$  means that the light field contains quantum coherences both in the photon-number basis and temporal domain.**

To demonstrate that the coherence of the atomic state is transferred onto the photonic field, the authors of Ref. (83) registered the single counts over 350sec with the setup in Fig. 2.25 for different values of  $p_0$  (or pulse area  $\theta$ , here  $A$ ). Two resulting timetraces are given in Fig. 2.26, where they observe anticorrelated oscillations as a function of freely evolving phase  $\phi$ , evidence the generation of quantum coherence in the photon-number basis and temporal domain. Moreover, the amplitude of these anticorrelated oscillations increases with lower pulse areas, as predicted. From these measurements, they extract the visibility as a function of pulse area  $v_{\max}$ , see Fig. 2.27. By fitting the data to  $v_{\max} = \lambda^2 p_0 \sqrt{M_s}$ , they were able to deduce the purity in photon-number basis  $\lambda = 0.965 \pm 0.018$  for a mean wavepacket overlap  $M_s = 0.903 \pm 0.008$  that is measured at  $\theta = \pi$  from standard HOM measurements (see Section 2.4.3), where  $\lambda \approx 1$  indicates a pure state in the photon-number basis.

This paper is the starting point of my thesis in which we use the ability to generate any arbitrary photon-number superposition up to a single-photon Fock

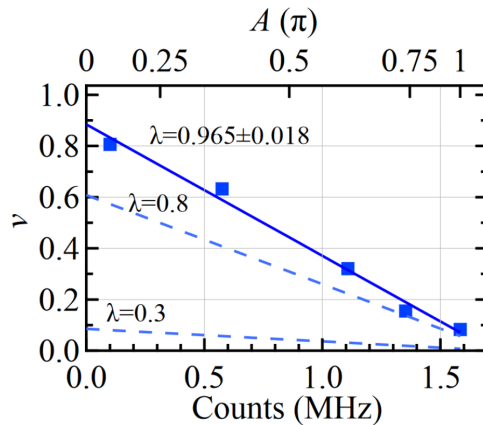


Figure 2.27 – **Extracting purity in the photon-number basis.** The visibility of single counts as a function of pulse area  $A = \theta$  (or emission intensity in MHz), where the experimental data is indicated by the squares. The fit to the data is given by  $v_{\max} = \lambda^2 p_0 \sqrt{M}$ , from which the purity in the photon-number basis  $\lambda$  is extracted. Taken from Ref. (83).

state with high purity in the photon-number basis to investigate the influence of first-order coherence, or quantum coherence, on energetic transfers and quantum measurements.

#### Conclusion Chapter 2 – Basics of a quantum dot-cavity system and photon-number coherence

In this chapter we have introduced all the tools necessary to present the main results of my PhD work. With these tools, we first study Chapter 3 the impact of photon-number coherence on basic quantum protocols, such as the cornerstone of linear optical quantum computing : Hong-Ou-Mandel interference. By extension, we then show that this result has implications for certain types of quantum gates. In Chapter 4 and 5 we show that photon-number coherence plays an important role in the energetics of basic quantum optics schemes. Specifically, we investigate the energetics of three key building blocks in quantum information processing : quantum light generation, two field interference, and Ramsey interferometry.



## 3 - Quantum interference with photon-number superpositions

### 3.1 . Introduction

Over the past few decades, quantum computing based on single-photon sources has emerged as a promising platform (14; 47; 88; 89). The underlying principle of many quantum technologies such as linear optical quantum computing (9), quantum networks (4; 5), and quantum key distribution (2; 3), is **the Hong-Ou-Mandel effect** (32) where two identical single-photons impinging on a beam splitter get entangled (see Section 2.4.3).

To fully exploit this feature, these technologies require single-photon sources, which ideally generate highly indistinguishable single-photons on demand. Over the years several quantum emitter platforms have been developed and optimized in parallel of which semiconductor quantum dot-cavity systems are one example (14; 74; 88; 90; 91). To create highly indistinguishable photons with these quantum emitters, requires bringing the two-level system in the excited state with minimal time jitter. A common method to bring a quantum emitter into the excited state is using coherent excitation techniques such as resonant excitation (see Section 2.5.2) or two-photon excitation schemes (92–94). With these techniques quantum dot-cavity systems are able to produce single-photons of high indistinguishability (13; 14; 25), making them excellent building blocks for optical quantum technologies.

With the work of Loredó et al. (see Section 2.5.5) it was evidenced that under coherent excitation, a two-level system generates quantum superpositions of vacuum and one-photon Fock states : the energy coherence initially imprinted on the driven qubit is transferred onto the electromagnetic field through spontaneous emission (83). Changing the drive power and optical phase  $\phi$  allows to tune the vacuum and one-photon component of the emitted field and the coherence in photon-number basis. This demonstration opens up new pathways to encode information in quantum states of light (36), and already led to new quantum sampling schemes such as superposition Boson sampling (39), and theoretical proposals for twin-field quantum key distribution (95).

Despite the potential applications of quantum superpositions, common quantum protocols so far have been based on single-photon inputs. However, physical limitations and experimental inaccuracies – as we show in this chapter – often result in the generation of unwanted photon-number coherence. Here we study

the effect of photon-number coherence on core building blocks of optical quantum technologies. We first study the impact of photon-number coherence on the Hong-Ou-Mandel (HOM) interference, and show that considering photon-number coherence forces to rethink commonly used normalization methods to extract single-photon indistinguishability. We show that because it was overlooked, this effect has led to improper indistinguishability measurements in the past. Secondly, we observe new physical phenomena when interfering trains of photon-number superpositions with an unbalanced Mach-Zehnder interferometer : the presence of quantum interference between temporally separated photonic fields when partially measuring the qubits. We explore the consequences of this new effect in quantum computing schemes relying on partial qubit measurements such as heralded CNOT gates. The results we report here, demonstrate a sample of the wide range of possibilities and complications arising from performing quantum protocols with photon-number superpositions.

The work presented in this chapter has been developed in close collaboration with Jean Senellart<sup>1</sup> and Dr. Stephen Wein<sup>2</sup> who provided the theory for the research.

---

1. Quandela SAS, 7 Rue Léonard de Vinci, 91300 Massy, France.

2. Previously : Université Grenoble Alpes, CNRS, Grenoble INP, Institut Néel, 38000 Grenoble, France.

Currently : Quandela SAS, 7 Rue Léonard de Vinci, 91300 Massy, France.

### 3.2 . Generation of photon-number coherence under resonant excitation

Optical quantum protocols frequently require photonic fields of high brightness and high single-photon purity,  $g^{(2)} = 0$  (Section 2.4.2). However, finding the right conditions for particular measurements is generally a trade-off between these two requirements. Indeed, as discussed for instance in Refs. (96; 97), **re-excitation of the QD during the drive pulse decreases the single-photon purity**, an effect that increases with the pulse area  $\theta$ . Experimentalists often choose to operate below  $\theta = \pi$  to minimize re-excitation effects that reduce the single-photon purity. As a result, following our discussion in Section 2.5.5, the photonic field emitted by the two-level system is of the form :

$$|\Psi\rangle = \sqrt{p_0} |0\rangle + e^{i\phi} \sqrt{p_1} |1\rangle, \quad (3.1)$$

presenting photon-number coherence attested by the off-diagonal density matrix elements  $\rho_{01} = \sqrt{p_0 p_1}$ , and where  $p_0 = \cos^2(\theta/2)$  and  $p_1 = \sin^2(\theta/2)$ . Consequently, when performing Hong-Ou-Mandel measurements using an unbalanced Mach-Zehnder interferometer, oscillations in single counts are expected – as a function of the optical phase  $\phi$  – between the two arms of the interferometer (83).

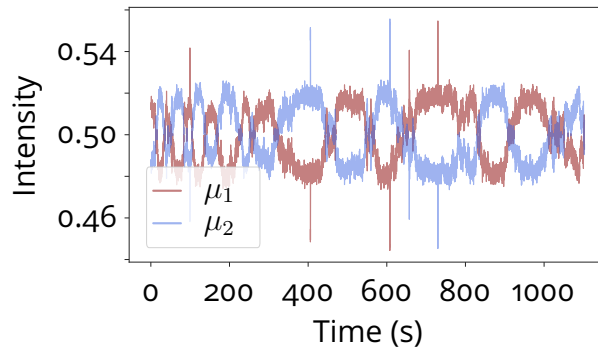


Figure 3.1 – **Photon-number coherence for  $\pi$ -pulse.** The intensities  $\mu_1$  and  $\mu_2$  measured with two detectors in a Hong-Ou-Mandel interferometer as a function of time for  $\theta \approx \pi$ . The presence of anti-correlated oscillations as a function of  $\phi$  indicates the presence of photon-number coherence.

On the other hand, to increase brightness and reducing the vacuum component in the field, requires driving the quantum emitter with  $\theta = \pi$  at the potential cost of reducing the single-photon purity, i.e. **the addition of a two-photon component in the field**. Yet, even when operating close to  $\theta = \pi$  with a temporally short pulse (7 ps), we experimentally observe single counts oscillations in HOM measurements when driving a QD source resonantly as shown in Fig. 3.1,

which presents a typical intensity time trace recorded with two detectors part of the HOM setup presented in Fig. 2.15. These anti-correlated oscillations indicate the presence of photon-number coherences, despite driving the quantum emitter close to population inversion.

### 3.2.1 . First-order coherence

At this point, we need to introduce the notion of first-order coherence, describing the coherence in photon-number basis between  $|n\rangle$  and  $|n+1\rangle$  Fock states. We first generalize the study of Ref. (83) by considering a more general photonic state comprising the  $|0\rangle$  and  $|1\rangle$  Fock state in the pulse operator formalism (98) :

$$\begin{aligned}\hat{\rho} &= p_0 |0\rangle \langle 0| + p_1 \iint dt dt' \xi(t, t') \hat{a}^\dagger(t) |0\rangle \langle 0| \hat{a}(t') \\ &+ \sqrt{p_0 p_1} \int dt \zeta(t) \hat{a}^\dagger(t) |0\rangle \langle 0| + \text{h.c.} \\ &= p_0 \hat{\rho}_0 + p_1 \hat{\rho}_1 + \sqrt{p_0 p_1} (\hat{\rho}_{01} + \hat{\rho}_{10}),\end{aligned}\quad (3.2)$$

where  $\hat{\rho}_{i(j)} = |i\rangle \langle i(j)|$  is the photonic density operator, and  $\hat{a}(t)$  is the propagating mode, and the photon-number probabilities  $p_0, p_1$  satisfy  $p_0 + p_1 = 1$ . Additionally, we introduce two parameters : the Hermitian function  $\xi(t, t') = \xi^*(t', t)$  describing the temporal shape and coherence of the pulse, and the complex amplitude  $\zeta(t)$  describing the temporal dynamics of the photon-number coherence. Thus, if the photonic field  $\hat{\rho}$  is a pure field,  $\text{Tr}[\hat{\rho}] = 1$  we have  $\int \xi(t, t) dt = 1$ .

For a state described by Eq. 3.2 the total purity (i.e. in photon-number and temporal domain) of the state is given by

$$\mathcal{P} = \text{Tr}[\hat{\rho}^2] = p_0^2 + p_1^2 M_s + 2p_0 p_1 \mathcal{C} \quad (3.3)$$

with the single-photon indistinguishability, or purity in the temporal domain :

$$M_s = \text{Tr}[\hat{\rho}_1^2] = \iint |\xi(t, t')|^2 dt dt'. \quad (3.4)$$

The parameter  $\mathcal{C}$  is to define the **purity in the number coherence between the vacuum and the single photon Fock state** :

$$\mathcal{C} = \text{Tr}[\hat{\rho}_{01} \hat{\rho}_{10}] = \int |\zeta(t)|^2 dt. \quad (3.5)$$

We note that if we consider a quantum emitter affected by pure dephasing, we obtain (Appendix 8.2) :

$$M_s = \frac{\gamma}{\gamma + 2\gamma^*} \quad (3.6)$$

$$\mathcal{C} = \lambda^2 \left( \frac{\gamma}{\gamma + 2\gamma^*} \right) = \lambda^2 M_s, \quad (3.7)$$

with  $\gamma$  the spontaneous decay rate,  $\gamma^*$  the dephasing rate (Section 2.5.1), and  $\lambda$  a parameter tuning the purity in photon-number basis (Section 2.5.5 and Ref. (83)). Thus, for a quantum emitter subject to pure dephasing we find  $M_s = \mathcal{C}$ . However, when considering other dephasing mechanisms, we have  $\mathcal{C} \leq \sqrt{M_s}$ , see Appendix 8.3.

We define the first-order coherence between the  $|n\rangle$  and  $|n+1\rangle$  photon-number states present in the field as :

$$c^{(1)} = \frac{1}{\mu} \int |\langle \hat{a}(t) \rangle|^2 dt, \quad (3.8)$$

In the case of the state described by Eq. 3.2, limited to zero and one-photon, the first-order coherence is given by :

$$c^{(1)} = \cos^2\left(\frac{\theta}{2}\right) \mathcal{C}. \quad (3.9)$$

As we show below, in case of a light state comprising zero, one-, and two-photon Fock states, the same definition holds. Generally speaking, this first-order coherence  $c^{(1)}$  is related to the single counts visibility in the Mach-Zehnder-based Hong-Ou-Mandel interference, where the visibility is given by :

$$v(t) = \frac{\mu_1(t) - \mu_2(t)}{\mu_1(t) + \mu_2(t)}, \quad (3.10)$$

with average photon-number  $\mu_i = \int \langle \hat{a}_i^\dagger(t) \hat{a}_i(t) \rangle dt$  measured by detector  $D_i$ . We then find the visibility is related to the first-order coherence between  $|0\rangle$  and  $|1\rangle$  according to :

$$v = \cos(\phi) c^{(1)}, \quad (3.11)$$

see Section 4.3.1 for explicit derivation.

### 3.2.2 . Re-excitation and first-order coherence

The observation of a non-zero visibility at  $\theta = \pi$  is thus a signature of first-order coherence. The presence of first-order coherence for  $\theta = \pi$  can be explained by considering light-matter interaction between a temporally finite excitation pulse and the quantum emitter, whereby the emitter undergoes stimulated emission and absorption during the pulse (96; 97). As a result, there is a possibility that a second photon is emitted at the end of the pulse. Indeed, a simulation in Fig. 3.2(a) for 7 ps pulses shows that as we move towards pulse area  $\theta = \pi$ , the probability of emitting a second photon ( $p_2$ ) becomes non-zero and steadily increases with pulse area.

The probability of generating a two-photon component at  $\theta = \pi$  is further affected by increasing the pulse duration. Fig. 3.2(b) shows for several pulse durations the probabilities of generating a photonic field containing vacuum ( $p_0$ ) and

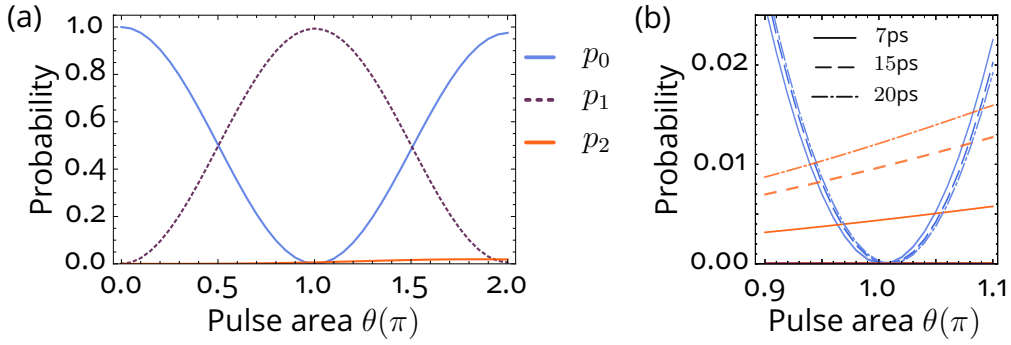


Figure 3.2 – **Photon-number populations.** (a) The probability of generating vacuum  $p_0$ , one-photon  $p_1$ , and two-photon  $p_2$  populations as a function of pulse area, for resonant excitation with a 7 ps pulse. (b) The  $p_0$  (blue) and  $p_2$  (orange) population as a function of pulse area for several pulse durations (7 ps, 15 ps, and 20 ps). Simulations by Dr. Stephen Wein.

two-photon ( $p_2$ ) components for pulse areas close to  $\theta = \pi$ . Operating close to  $\pi$ -pulse in the ideal case creates a photon-number superposition of the form :

$$|\Psi\rangle = \sqrt{p_0}|0\rangle + \sqrt{p_1}|1\rangle + e^{i\phi}\sqrt{p_2}|2\rangle, \quad (3.12)$$

where we note  $|2\rangle = |1\rangle_e|1\rangle_l$  in time bin basis, indicating a photon emitted during the pulse ( $e$ ) and another one at the end of the pulse ( $l$ ) (36; 81).

A state such as the one given in Eq. 3.12 exhibits not only first-order coherence between the vacuum and one-photon component, but also between the one- and two-photon component of the emitted field (83). In the general case of a mixed state containing vacuum, one- and two-photon components, it can be shown that the first-order coherence  $c^{(1)}$  contains contributions from the off-diagonal density matrix elements  $\rho_{01}$  and  $\rho_{12}$  :

$$c^{(1)} \simeq \frac{|\rho_{01} + e^{i\phi}\rho_{12}|^2}{p_1 + 2p_2}. \quad (3.13)$$

To gain insight into the different contributions to the first-order coherence, we plot Eq. 3.13 (in absence of decoherence) for  $\phi = \pi/2$  and  $\gamma\tau = 0.1$  in Fig. 3.3 as a function of pulse area together with the coherences  $\rho_{01} = \sqrt{p_0 p_1}$  and  $\rho_{12} = \sqrt{p_1 p_2}$ . Indeed, in line with Fig. 3.2, we observe that the first-order coherence at  $\theta = \pi$  is expected to stem from the prevailing coherence between one- and two-photon Fock state. As such, although the vacuum component of the field vanishes for  $\theta \rightarrow \pi$ , the first-order coherence  $c^{(1)}$  does not.

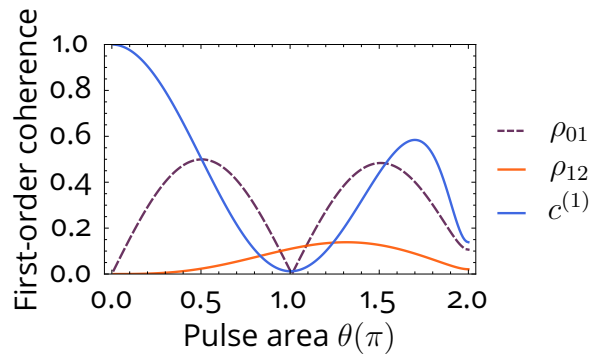


Figure 3.3 – **Contributions to first-order coherence.** The first-order coherence as a function of pulse area, together with the density matrix elements  $\rho_{01}$  and  $\rho_{12}$  contributing to the first-order coherence. See main text for details. Simulations by Dr. Stephen Wein.

The observations in Fig. 3.2 and Fig. 3.3 thus suggest that completely removing photon-number coherence would require driving the qubit with temporally infinitely short pulses of exactly  $\theta = \pi$ . However, a calculation of the first-order coherence as a function of pulse duration  $\gamma\tau$  and pulse area in Fig. 3.4 demonstrates that for  $\theta = \pi$  the first-order coherence does not vanish. Hence, resonantly driving a two-level system – with a finite pulse – inevitably results in the generation of first-order coherence whatever the pulse area  $\theta$ .

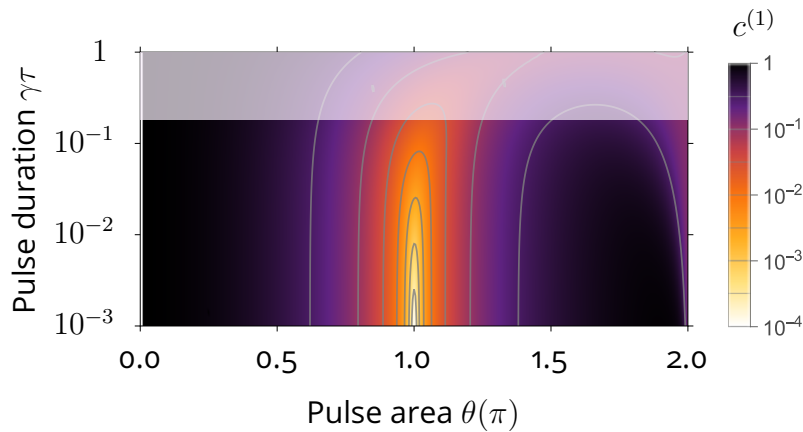


Figure 3.4 – **First-order coherence and pulse duration.** The first-order coherence  $c^{(1)}$  as a function of pulse area  $\theta$  in units  $\pi$  and pulse duration  $\gamma\tau$ , with  $\gamma$  the decay rate of the emitter. Pulse durations commonly used in experiments lay outside the shaded area. Simulations by Dr. Stephen Wein.

### 3.2.3 . First-order coherence and correlation measurements

As seen in the previous sections, first-order coherence gives rise to oscillations in the single counts measured in a Mach-Zehnder-based HOM interferometer. Here we show that number coherence also leads to other effects in multi-photon correlations. We exemplify this by measuring the second-order intensity correlation curves from a Hong-Ou-Mandel interference (Section 2.4.3) with wavepackets generated with pulse areas  $\theta = \pi$  and  $\theta = 0.22\pi$ . The subsequent correlation histograms are shown in Fig. 3.5, where we also plot the correlation histogram for perfectly distinguishable wavepackets obtained with  $\theta = \pi$ , Fig. 3.5(a) lower panel. The latter histogram is obtained by setting the polarization of interfering wavepackets at orthogonal angles, see Section 2.4.1.

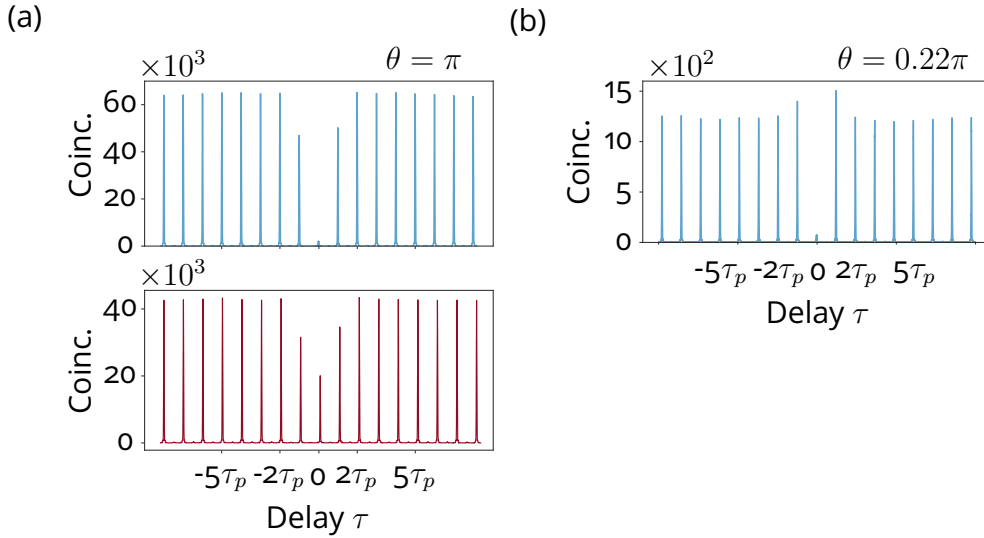


Figure 3.5 – **Effect of photon-number superpositions on correlation measurements.** Coincidence histograms obtained through Hong-Ou-Mandel measurements where the input field is in a photon-number superposition, for (a)  $\theta = \pi$  and (b) with  $\theta = 0.22\pi$ . The lower panel in (a) shows the coincidence histogram obtained for  $\theta = \pi$  when the photons are perfectly distinguishable.

The peaks in Fig. 3.5(b) show different behavior compared to driving with a pulse area close to  $\pi$ . In such histograms, the peaks correspond to intensity correlation measurements with respect to different delays :  $\tau_k = k\tau_p$  with  $\tau_p \simeq 12.3$  ns and  $k \in \mathbb{Z}$ . We observe different relative peak heights depending on pulse area  $\theta$ . For  $\theta = \pi$ , the  $|k| = 1$  peaks are roughly  $3/4$  of the  $|k| > 2$  peaks. This ratio arises from statistical considerations, as is explained in Ref. (99) where they show that the different possible paths leading to coincidences at delay  $\tau_k$ , corresponding to the delay of the Mach-Zehnder interferometer, result in  $\mathcal{A}_1/\mathcal{A}_2 = 3/4$  for input state  $|1\rangle$ , where  $\mathcal{A}_k$  is the area of coincidence peak

$\tau_k$ . However, as shown in Fig. 3.5(b), for  $\theta = 0.22\pi$  this ratio no longer holds, suggesting that photon-number coherence also affects two-photon correlations.

In the following of the chapter, we study the impact of first-order photon-number coherence on the Hong-Ou-Mandel interference. We limit our study to the case where we can neglect  $p_2$ , hence  $\theta < \pi$ . We explain the phenomena behind the observations mentioned in this section by deliberately increasing the photon-number coherence in the photonic field (i.e. decreasing pulse areas  $\theta$ ). In Sec. 3.3 we show that the way correlation histograms are normalized should be revised in presence of photon-number coherence, and leads to wrong assessment of wavepacket indistinguishability  $M_s$  if photon-number coherence is disregarded. Next, in Sec. 3.4, we explain how photon-number coherence gives rise to new quantum interference phenomena in particular correlation measurements, witnessed in Fig. 3.5 in correlation peaks  $\tau_k$  for  $|k| = 1$ . Finally, in Sec. 3.5 we discuss how photon-number coherence impacts the performance and error rates in optical quantum gates.

#### Conclusion Section 3.2 – Resonant excitation and photon-number coherence

In this section we explained how resonant excitation of a quantum emitter inevitably leads to the generation of a photonic field containing photon-number coherence. This coherence is first-order coherence  $c^{(1)}$  either between the vacuum and one-photon component of the emitted field for  $\theta < \pi$ , or between the one- and two-photon component for  $\theta \approx \pi$ , where the latter arises from re-excitation effects during the drive pulse. We have shown that under realistic conditions, the photon-number coherence does not vanish. The first-order coherence between the vacuum and one-photon component of the field ( $\theta < \pi$ ), can be directly related to the single counts visibility measured in Mach-Zehnder-based Hong-Ou-Mandel measurements :

$$c^{(1)} = \cos^2\left(\frac{\theta}{2}\right) \mathcal{C} = v_{\max},$$

where we also introduced  $\mathcal{C}$  to capture the purity in photon-number coherence between the vacuum and single-photon Fock state. Finally, we predict that this first-order coherence affects two-photon correlations, as suggested by initial measurements.

### 3.3 . Measuring indistinguishability in the presence of photon-number coherence

As explained in Section 2.4.3, the Hong-Ou-Mandel interferometer is commonly used to measure wavepacket indistinguishability through analysis of coincidence (i.e. correlation) histograms. To obtain the indistinguishability requires quantifying the visibility of HOM interference :  $V_{\text{HOM}}$ . This visibility is extracted by performing two coincidence measurements : one measurement with a train of photonic fields with parallel polarization  $G_{\text{HOM},\parallel}^{(2)}$ , and one measurement where the interfering fields are orthogonally (or cross-) polarized  $G_{\text{HOM},\perp}^{(2)}$ . The latter measurement serves as a benchmark where no interference of photons is expected. The visibility is defined through :

$$V_{\text{HOM}} = 1 - \frac{g_{\text{HOM},\parallel}^{(2)}(0)}{g_{\text{HOM},\perp}^{(2)}(0)}, \quad (3.14)$$

where the normalized second-order intensity correlations  $g_{\text{HOM},\parallel,\perp}^{(2)}(0)$  at zero delay ( $k = 0$ ) are deduced from the area of the zero delay peaks in correlation histograms,  $\mathcal{A}_{0,\parallel/\perp}$ , after proper normalization. These zero delay areas are given by :

$$\mathcal{A}_{0,\parallel/\perp} = \frac{1}{4}\eta_1\eta_2 \iint G_{D_1,D_2}^{(2)}(t_1, t_2)dt_1dt_2, \quad (3.15)$$

with  $t_1 - t_2 = 0$ ,  $G_{D_1,D_2}^{(2)}$  **being the second-order cross-correlation function** experimentally obtained with detector  $D_1$  and detector  $D_2$  of efficiencies  $\eta_1$  and  $\eta_2$ , respectively, in a HOM setup, and where the integrals are taken over the duration of a single pulse. In this chapter, henceforth, we use the subscript  $D_1, D_2$  instead of HOM whenever we refer to a second-order cross-correlation function  $g^{(2)}$  or  $G^{(2)}$ .

The normalized cross-correlation for zero delay is then given by :

$$g_{D_1,D_2,\parallel(\perp)}^{(2)}(0) = \frac{4\mathcal{A}_{0,\parallel(\perp)}}{\eta_1\eta_2\mu^2},$$

with average photon-number  $\mu = \int I dt$  in a single input pulse. It was previously assumed that the average photon-number can be extracted from correlation peak areas  $|k| \geq 2$ , considering that :

$$\mathcal{A}_{\perp}(k) = \mathcal{A}_{\parallel}(k) = \iint I(t_1)I(t_2)dt_1dt_2 = \eta_1\eta_2\frac{\mu^2}{4}. \quad (3.16)$$

This is a commonly used method for normalization, and even seen as standard in commercially available correlators (Swabian TimeTagger). However, as we show in this section, this normalization method is no longer valid in the presence of photon-number coherence.

### 3.3.1 . Normalization revisited

As discussed in Sec. 2.5.5 and in Sec. 3.2- 3.2.2, first-order photon-number coherence leads to phase-dependent single counts in the standard Mach-Zehnder-based HOM interferometer. This phase-dependence in single counts measured by detector  $D_1$  and  $D_2$  translates to phase-dependent coincidence counts :  $\mu_1(\phi)\mu_2(\phi)$  with  $\mu_{1,2} = \eta_{1,2}\mu(1 \pm c^{(1)} \cos(\phi))/2$  and  $\mu_1 + \mu_2 = \mu$ . Generally, the areas of the  $k \geq 2$  peaks in parallel polarization configuration are thus proportional to

$$\mathcal{A}_{|k| \geq 2, \parallel} = \eta_1 \eta_2 \frac{\mu^2}{4} \left( 1 - \left( c^{(1)} \cos(\phi) \right)^2 \right), \quad (3.17)$$

with first-order coherence  $c^{(1)}$ . In the general case described by Eq. 3.2,  $\mathcal{C} = \text{Tr}[\hat{\rho}_{01}\hat{\rho}_{10}]$  and  $c^{(1)} = \mathcal{C} \cos^2(\theta/2) = v_{\max}$  where  $\mathcal{C} = 1$  signals a pure state in the photon-number basis, see Appendix 8.1. As seen from Eq. 3.17, in presence of photon-number coherence the  $k \geq 2$  peaks for parallel polarization are no longer equal to  $\eta_1 \eta_2 \mu^2/4$ , reflecting that there are missing coincidence counts arising from the single-photon interference between two wavepackets.

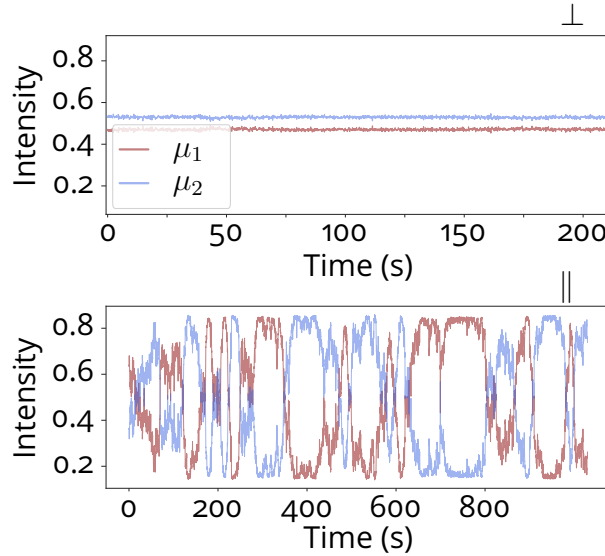


Figure 3.6 – **Phase-dependence single counts.** Normalized intensities  $\mu_1$  and  $\mu_2$  as a function of time for an HOM measurement when the wavepackets are made perfectly distinguishable through orthogonal polarization  $\perp$  (upper panel), or (partially) indistinguishable through parallel polarization  $\parallel$  (lower panel). Here  $\theta = 0.22\pi$ .

We can understand this by considering the single counts in parallel ( $\parallel$ ) and orthogonal ( $\perp$ ) polarization configuration in an HOM interferometer, see Fig. 3.6.

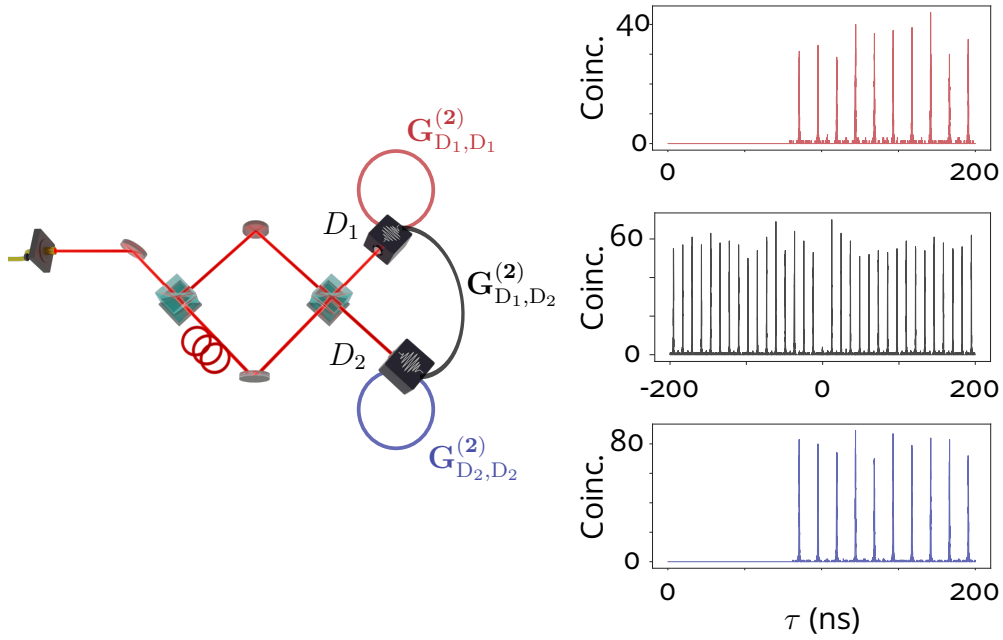


Figure 3.7 – **Cross- and auto-correlations.** Cross-correlation  $G_{D_1,D_2}^{(2)}$  obtained by comparing events between detector 1 and detector 2, and auto-correlations  $G_{D_i,D_i}^{(2)}$  obtained with events from a single detector  $D_i$ .

In orthogonal polarization, the wavepackets are fully distinguishable. As a result, there is no interference, and thus no phase-dependence on the single counts as can be seen in the upper panel, where a slight difference in intensities is caused by different detection efficiencies. This observation also translates to the coincidences at long delay  $|k| \geq 2$ , which are dependent on the product of the single counts only. In contrast, for parallel polarization we see a clear phase-dependence in the single counts (Fig. 3.6 lower panel). Hence, the coincidences at long delays  $|k| \geq 2$  are also affected. Therefore, one needs to revise the normalization procedure used in second-order correlation measurements.

When the overall detection efficiencies are identical ( $\eta_1 = \eta_2$ ), taking the sum  $(\mu_1 + \mu_2)^2/4$  instead of the product  $\mu_1\mu_2$  as was the case in Section 2.4.3), cancels the phase dependence and gives access to  $\eta_1\eta_2\mu^2/4$ . This factor not only **depends on the cross-correlation function  $G_{D_1,D_2}^{(2)}$ , but also on the auto-correlation function of each detector :  $G_{D_1,D_1}^{(2)}$  and  $G_{D_2,D_2}^{(2)}$ .** Generally, these functions can be experimentally accessed through the areas of long delay peaks ( $|k| \geq 2$ ) in **cross- and auto-correlation histograms** measured with both detectors.

In Fig. 3.7 we plot examples of raw coincidence histograms obtained from the auto-correlation and from the cross-correlation functions. In a similar fashion to

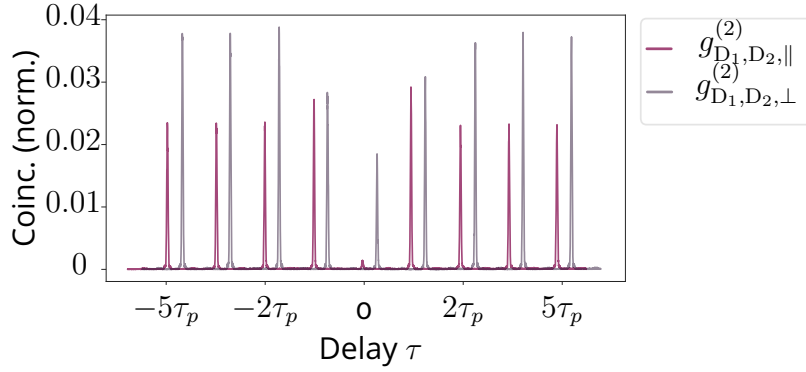


Figure 3.8 – **Normalization of correlation histograms using cross- and auto-correlation functions.** Coincidence histograms obtained with  $\theta = 0.22\pi$  for orthogonal and parallel polarization, where the curve for orthogonal polarization is shifted along the x-axis for clarity.

the cross-correlation histogram (see Section 2.4.2), an auto-correlation histogram is obtained by comparing the list of photon arrival times measured by detector  $D_i$  with a copy of itself. Distinctly different from the cross-correlation histogram in Fig. 3.7, is the fact that auto-correlation measurements suffer from electronic dead time (detectors and correlators), resulting in the absence of peaks in the  $0 - 85$  ns range. In the case of  $\eta_1 = \eta_2 = \eta$ , we have :

$$\eta^2 \frac{\mu^2}{4} = \frac{(\mu_1 + \mu_2)^2}{4} \eta^2 = \frac{1}{4} (\mathcal{A}_{D_1, D_1} + 2\mathcal{A}_{D_1, D_2} + \mathcal{A}_{D_2, D_2}), \quad (3.18)$$

where  $\mathcal{A}$  is the peak area extracted from correlation peaks  $k \geq 2$  in auto- ( $D_i, D_i$ ) and cross-correlation ( $D_i, D_j$ ) histograms in parallel polarization. Generally, when  $\eta_1 \neq \eta_2$ , Eq. 3.18 becomes (see Appendix 7.2) :

$$\frac{(\mu_1 + r_\eta \mu_2)^2}{4r_\eta} = \frac{1}{4r_\eta} (\mathcal{A}_{D_1, D_1} + 2r_\eta \mathcal{A}_{D_1, D_2} + r_\eta^2 \mathcal{A}_{D_2, D_2}), \quad (3.19)$$

where we have introduced  $r_\eta$ , a parameter accounting for differences in detection efficiencies :

$$r_\eta = \frac{\eta_1}{\eta_2}. \quad (3.20)$$

Fig. 3.8 shows two time-integrated coincidence histograms measured in orthogonal and parallel polarization configuration for  $\theta = 0.22\pi$ , normalized according to Eq. 3.19. The histogram in parallel configuration shows a stark contrast with the histogram obtained in orthogonal polarization with a strong suppression of the  $|k| \geq 2$  peak areas in parallel compared to the orthogonal polarization. This observation is consistent considering Eq. 3.17. However, it should be noted that these histograms correspond to time-integrated measurements, resulting in a

phase-averaging effect on the correlation histograms. In the next section we perform phase-resolved analysis to remove the effect of phase-averaging, allowing us to study the effect of phase on correlation measurements.

### 3.3.2 . Experimentally resolving phase-dependence long delay peaks

To evidence the phase-dependence of the  $|k| \geq 2$  peaks in coincidence histograms, we measure for different pulse areas the coincidence clicks with the Hong-Ou-Mandel setup shown in Section 2.4.3, and we use the corresponding single count oscillations to access the interferometer phase  $\phi$  at each point in time. More specifically, we perform time-tagged correlation measurements with two detectors  $D_1$  and  $D_2$  at the output of a beam splitter, and we acquire all arrival times of incoming photon clicks. For each pulse area  $\theta$  we acquire time stamps for approximately twenty minutes during which we let the relative phase  $\phi(t)$  freely evolve and explore the full phase space  $[0, \pi]$ . From the single counts time trace, see example Fig. 3.6 lower panel for  $\theta = 0.22\pi$ , we extract the visibility as a function of time  $v(t)$  (Eq. 3.10) and the maximum visibility  $v_{\max}$  given by

$$v_{\max} = \max_{\phi} \frac{\mu_1 - \mu_2}{\mu_1 + \mu_2}. \quad (3.21)$$

We can then assign to each time stamp an interferometer phase given by  $\phi(t) = \arccos(v(t)/v_{\max})$ .

For each measurement ( $\theta$ ) we acquire over a time span of 20 minutes two lists of photon arrival times measured with  $D_1$  and  $D_2$ . From these event lists we can build correlation histograms as discussed in Section 2.4.2. Each list is divided into one second time chunks, a time span over which the interferometer phase  $\phi$  is stable. We now have two lists of photon arrival times corresponding to detection events measured by  $D_1$  and  $D_2$  happening within the one second time chunk. For each time chunk we compute the corresponding auto- and cross-correlation functions. As a result, for a 20 minutes measurement we obtain approximately 1200 cross-correlation histograms, and  $\sim 2400$  corresponding auto-correlation histograms. Finally, the single counts time trace of  $D_1$  and  $D_2$  allow us to determine the optical phase corresponding to each time chunk.

Fig. 3.9 shows an example of a chunked raw histogram for pulse area  $\theta = 0.48\pi$  and interferometer phase at the time of acquisition  $\phi = 0.58\pi$ . We normalize each cross-correlation histogram according to Eq. 3.19, using the corresponding auto-correlation histograms. From the normalized histogram we then compute the  $k = \pm 2$  peak area, where the error in areas is given by the square root of the area and through error propagation. We repeat this measurement for six different pulse areas  $\theta$ .

Fig. 3.10 shows the theoretical expectation of the  $|k| \geq 2$  peak areas according

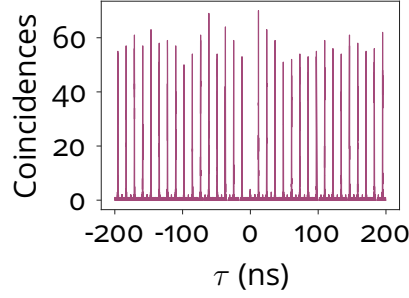


Figure 3.9 – **Time chunked coincidence histogram.** A raw chunked coincidence histogram where we plot the coincidences as a function of delay  $\tau$ , with measurement integration time 1s, for  $\theta = 0.48\pi$  and  $\phi = 0.58\pi$ .

to Eq. 3.17 as a function of optical phase  $\phi$  and  $\theta$ , where  $\theta = \arcsin \sqrt{I/I_\pi}$  with  $I_\pi$  the emission intensity at the first maximum of the Rabi curve ( $\pi$ -pulse, see Fig. 2.24). We predict and observe an increasing phase-dependence of the peak areas with increasing vacuum component,  $\theta \rightarrow 0$ . The phase-resolved intensity measurements in Fig. 3.10 show excellent agreement with theory, where we again observe an increasing phase-dependence with increasing vacuum population. The experimental data exhibits a slight offset with respect to the theory ( $-6\%$  offset), which we attribute to path-dependent losses in the interferometer. The results presented here, reveal for the first time the impact of first-order photon-number coherence on intensity correlation measurements in HOM experiments.

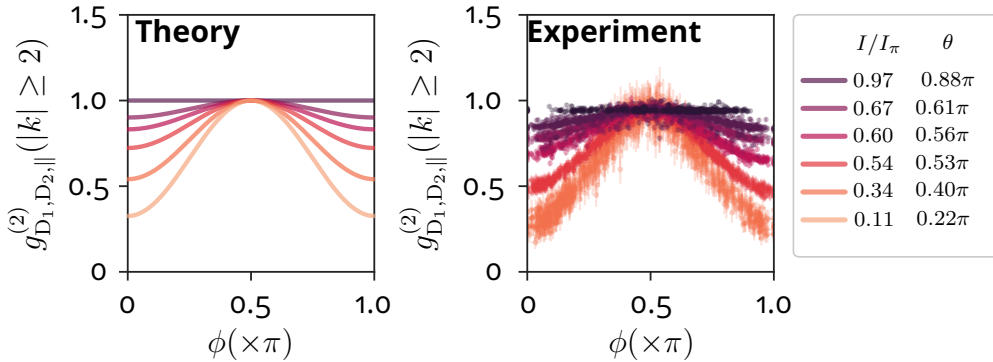


Figure 3.10 – **Phase-dependence long delay correlation peaks.** Average normalized area of the long delay ( $|k| = 2$ ) peaks as a function of optical phase  $\phi$  for different pulse areas, theory and experiment.

We fit the experimental data with the theory curves, Eq. 3.17 and extract the first-order coherence  $c^{(1)}$  as a function of pulse area. We plot the extracted first-order coherence together with the visibility  $v_{\max}$  obtained from single counts,

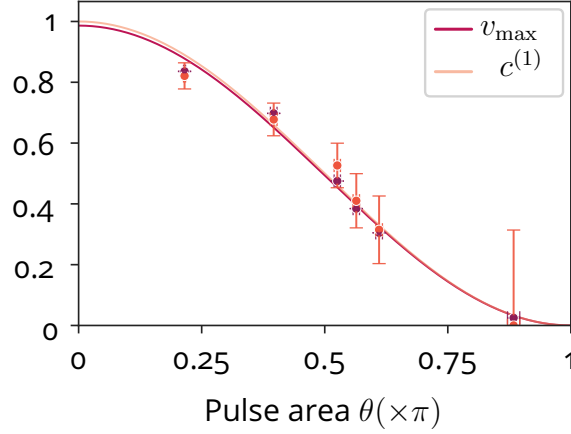


Figure 3.11 – **First-order coherence from coincidence measurements.** The single counts visibility  $v_{\max}$  and first-order coherence  $c^{(1)}$  as a function of pulse area  $\theta$ , where  $c^{(1)}$  is extracted from the fits to the uncorrelated peak areas in coincidence measurements.

see Section 2.5.5. As mentioned in Section 3.2.1, this latter quantity is directly related to the first-order coherence according to  $v_{\max} = c^{(1)}$ . We expect both parameters, although extracted via different types of measurements, thus to be identical. Indeed, Fig. 3.11 shows the comparable values obtained via either single counts visibility  $v_{\max}$ , or via coincidence counts  $c^{(1)}$ . In both cases we fit the data to  $\mathcal{C} \cos^2(\theta/2)$ , resulting in  $\mathcal{C} = (98.60 \pm 0.01)\%$  for the  $v_{\max}$  curve, and  $\mathcal{C} = (100.00 \pm 0.09)\%$  for  $c^{(1)}$  obtained from coincidence measurements, in close agreement with the single counts measurement.

### 3.3.3 . Error in wavepacket indistinguishability

To assess the consequences of ignoring the presence of photon-number coherence in indistinguishability measurements, we study the impact of a standard normalization procedure on the extracted indistinguishability  $M_s$ , as performed prior to the present study and discussed in Section 2.4.3. This normalization procedure relies on normalizing using the correlation peak areas  $|k| \geq 2$ , or making the assumption that  $\mathcal{A}_{\parallel}(|k| \geq 2) = \mathcal{A}_{\perp}(|k| \geq 2)$ . Both assumptions are equivalent to considering the product of the detector intensities :  $\mu_1 \mu_2 = \mu^2/4$ . However, taking the product leads to an underestimation of the actual wavepacket indistinguishability as we show in the following. This can be qualitatively understood by considering the effect of using a too small normalization factor. When the long delay peaks  $|k| \geq 2$  in cross-correlation functions are reduced due to photon-number coherence, normalization of coincidence histograms with these peaks as reference will artificially increase the zero delay peak containing information on the wavepacket indistinguishability  $M_s$ .

We consider two situations to estimate the error in the wavepacket indistinguishability. Firstly, we consider the case where the phase evolves faster than the measurement time so that there is an effect of phase averaging on the coincidence histograms. In such case, we have  $\cos^2(\phi) = 1/2$  and the normalized areas of the  $|k| \geq 2$  peaks become :

$$\begin{aligned} g_{D_1, D_2, \parallel}^{(2)}(|k| \geq 2) &= 1 - \frac{1}{2}(c^{(1)})^2 \\ &= 1 - \frac{1}{2}M_s(1 - p_1)^2, \end{aligned} \quad (3.22)$$

where we used the relation  $c^{(1)} = \sqrt{M_s}p_0$  for a state pure in the photon-number basis, see Section 3.2.1 and Ref. (83). Experimentally, to retrieve the indistinguishability from correlation histograms, one measures and normalizes the zero delay peak area ( $k = 0$ ). This peak in presence of photon-number coherence remains unaffected (see Appendix 7.1), and – when normalized properly – is given by :

$$g_{D_1, D_2, \parallel}^{(2)}(k = 0) = \frac{1}{2}(1 - M_s). \quad (3.23)$$

Properly normalized (using Eq. 3.19) time-tagged measurements also reflect this theoretical prediction, as shown in Fig. 3.12 where we plot the normalized zero delay peak areas as a function of pulse area.

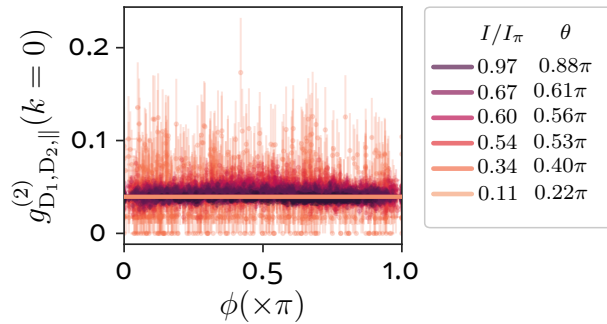


Figure 3.12 – **Zero delay peak area.** Average normalized area of the zero delay peak ( $k = 0$ ) peaks as a function of optical phase  $\phi$  for different pulse areas, theory (lines) and experiment (data).

With the newly introduced normalization, we thus have  $M_s = 1 - 2g_{D_1, D_2, \parallel}^{(2)}(k = 0)$ . This also corresponds to  $M_s = V_{\text{HOM}}$  for  $g_{D_1, D_2, \perp}^{(2)}(0) = 1/2$  (see Eq. 3.14), with or without photon-number coherence. As such, we fit Eq. 3.23 to each data set and **are able to directly retrieve  $M_s$  without needing an additional set**

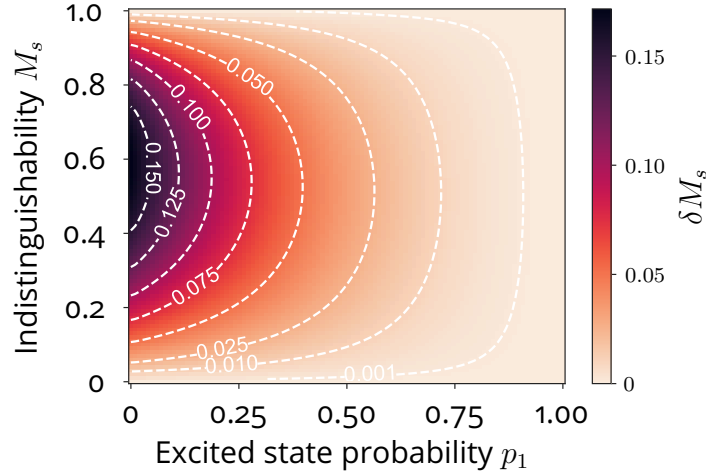


Figure 3.13 – **Effect of phase-averaging on indistinguishability measurements.** Underestimation of indistinguishability  $\delta M_s = M_s - V_{\text{HOM}}$  as a function of true indistinguishability  $M_s$  and excited state probability  $p_1$  for phase-averaged coincidence histograms.

of measurements in cross-polarization.

In contrast, **ignoring possible first-order coherence effects** and using the phase-averaged peak areas in Eq. 3.22 to define the HOM visibility through :

$$V_{\text{HOM}} = 1 - \frac{g_{D_1, D_2, \parallel}^{(2)}(0)}{g_{D_1, D_2, \perp}^{(2)}(0)} = 1 - \frac{2\mathcal{A}_0}{\mathcal{A}_{|k| \geq 2}}, \quad (3.24)$$

where  $g_{D_1, D_2, \parallel}^{(2)}(0)$  is taken as  $\mathcal{A}_0/\mathcal{A}_{|k| \geq 2}$ , and  $g_{\text{HOM}, \perp}^{(2)}(0) = 1/2$  following Section 2.4.3, **leads to an error in  $M_s$  defined as  $\delta M_s = M_s - V_{\text{HOM}}$** , with  $M_s$  the actual wavepacket indistinguishability. We find that  $\delta M_s > 0$  in presence of photon-number coherence and plot  $\delta M_s$  in Fig. 3.13 as a function of the actual  $M_s$  and excited state probability  $p_1$ . We observe for a pure state close to full population inversion, the error in  $M_s$  is less than 0.001. However, measuring the wavepacket indistinguishability for pure photon-number superpositions without proper normalization, can easily result in  $\delta M_s > 0.02$  under certain conditions. This effect worsens when interfering wavepackets of limited overlap  $M_s$ .

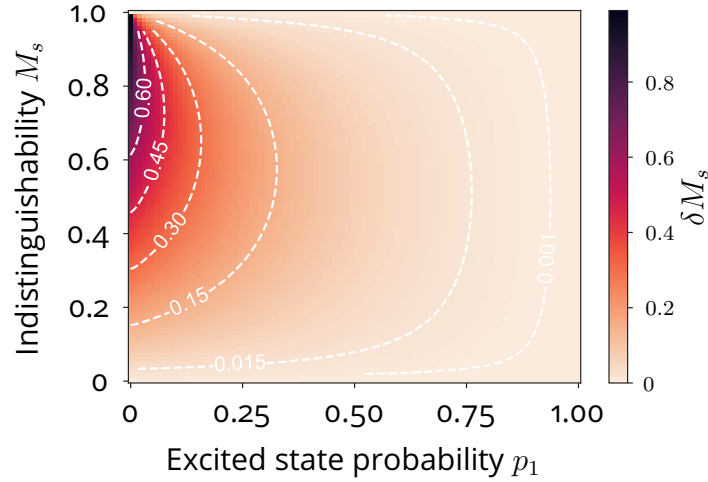


Figure 3.14 – **Effect of time integrating on indistinguishability measurements.** Underestimation of indistinguishability  $\delta M_s$  as a function of true indistinguishability  $M_s$  and excited state probability  $p_1$  for  $\phi = 0(\pi)$  for time-integrated coincidence histograms.

If instead, the Mach-Zehnder interferometer is stable over the correlation measurement, potentially one can obtain an integrated phase of  $\phi = 0$  or  $\pi$ , a phase where the peak areas are most affected by the photon-number coherence. Under such conditions,  $\cos^2(\phi) = 1$  and the peak areas of the  $|k| \geq 2$  peaks are given by :

$$\mathcal{A}_{|k| \geq 2} \propto 1 - M_s(1 - p_1)^2.$$

We plot the error  $\delta M_s$  again as a function of  $M_s$  and  $p_1$ , see Fig. 3.14. Similar to Fig. 3.13, we observe a decrease in extracted wavepacket indistinguishability with  $p_1$  and  $M_s$ . In such case, the error can be much higher, with the error  $\delta M_s$  quickly reaching values  $> 5\%$  for  $p_1 < 0.5$ .

### Conclusion Section 3.3 – Indistinguishability and photon-number coherence

In this section, we discussed the effect of first-order coherence on indistinguishability measurements. If not properly taken into account, i.e. not using the correct normalization method, photon-number coherence can lead to errors in the extracted wavepacket indistinguishability. This normalization method involves both auto- and cross-correlation functions, and allows to resolve the phase-dependence of correlation histograms. By performing time-tagged coincidence measurements and using the correct normalization method, we were able to – for the first time – experimentally demonstrate the phase-dependence of far delay peaks in correlation histograms, and show the impact of first-order coherence on coincidence measurements.

### 3.4 . Quantum interference between temporally separated wavepackets

Besides the impact on the  $|k| \geq 2$  peaks, the photon-number coherence also affects the first delay peak areas  $\mathcal{A}_{|k|=1}$ . In this section we demonstrate that these observations result from a new phenomenon coming from temporally distant interference effects.

#### 3.4.1 . New quantum interference phenomena

Let us consider three pulses input to a Mach-Zehnder interferometer and separated by delay  $\tau_p$ , see Fig. 3.15 where the subscripts indicate the order in which the pulses have been generated. All three pulses contain a photon-number superposition of the form  $\sqrt{p_0}|0\rangle + e^{i\alpha}\sqrt{p_1}|1\rangle$  with  $\alpha = 0$ , but for readability we omit the prefactors  $\sqrt{p_0}$  and  $\sqrt{p_1}$  in Fig. 3.15. The superposition of two scenarios leads to quantum interference signaled by the phase  $\phi$  dependence of the  $|k| = 1$  correlation peak areas. First, we consider the first and second pulse in Fig. 3.15(a) taking the long and short path, respectively, in a HOM interferometer. The first and second pulse arrive simultaneously at the 50 : 50 beam splitter where the one-photon components interfere – depending on indistinguishability  $M$  – and result in a detector click. The third pulse follows the same path as the second pulse, resulting in a detector click delayed by  $\tau_p$  with respect to the previous detection event. If these delayed clicks happen in two different detectors, in Fig. 3.15 indicated by early and late output port of the beam splitter, they contribute to the cross-correlation peak area  $|k| = 1$ .

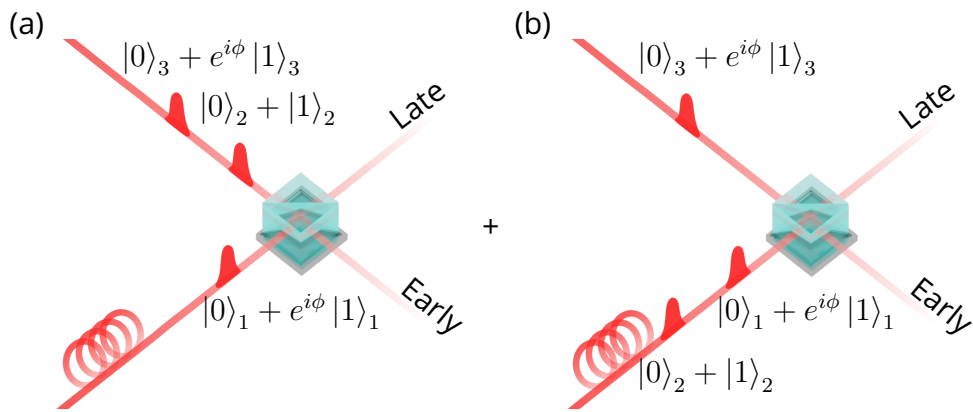


Figure 3.15 – **A new quantum interference phenomenon.** A quantum interference phenomenon arising from HOM measurements with a train of pulses containing photon-number superpositions. (a) The first pulse arrives simultaneously with the second pulse at the beam splitter. (b) Second pulse arrives simultaneously with the third pulse. See main text for details.

Secondly, we consider the scenario pictured in Fig. 3.15(b). Here the first and second pulse both follow the long path in the interferometer. As a result, the second pulse arrives at the beam splitter simultaneously with the third pulse. In such case, the one-photon component of the second and third pulse will interfere, and can contribute to the cross-correlation peak area  $|k| = 1$ . In such case, the coincidence clicks measured are indistinguishable from the first scenario. Indeed, the coincidence clicks can arise from the one-photon component in either the first two pulses or the latter two pulses, with a phase  $\phi$  difference. Thus, measuring two out of three pulses generates quantum interference. This quantum interference is dependent on both the first-order coherence present in the wavepackets as well as on the wavepacket indistinguishability, or spectral coherence.

### 3.4.2 . Phase-dependence first delay correlation peaks

This quantum interference phenomenon results in a  $\phi$ -dependence of the normalized areas of the first delay peaks given by (see Appendix 7.1) :

$$g_{D_1, D_2, ||}^{(2)}(|k| = 1) = \frac{3}{4} - \frac{1}{2} s_{\{1|M\}}^{(2)} \cos(2\phi), \quad (3.25)$$

for  $g^{(2)} = 0$ , and where we introduce a new parameter  $s_{\{1|M\}}^{(2)}$  : a parameter that quantifies the overlap between first-order coherence and temporal coherence, where the superscript indicates a two-photon process. This parameter, for a purely dephased emitter driven by an instantaneous pulse ( $\tau_{exc} \rightarrow 0$ ), is expected to be equal to :

$$s_{\{1|M\}}^{(2)} = c^{(1)} \left( \frac{2M}{1+M} \right), \quad (3.26)$$

with  $M = M_s$  if  $g^{(2)} = 0$ , see Appendix 8.2. Note that, in absence of photon-number coherence, Eq. 3.25 reduces to  $3/4$ , as expected from statistical considerations (99).

Using the same techniques as for the  $|k| \geq 2$  correlation peaks we extract the average  $|k| = 1$  peak areas as a function of  $\phi$ , Fig. 3.16 right panel. As expected for pulse areas close to  $\theta = \pi$ , we retrieve the normalized peak area  $g_{D_1, D_2, ||}^{(2)}(|k| = 1) = 3/4$ . We fit the data to the theoretical expectation given by Eq. 3.25, and see excellent agreement between theory and experiment with again an offset of 6% due to path-dependent losses. Moreover, from both the theory curves and the experimental data we notice an increasing amplitude with photon-number coherence, with normalized maximum peak areas reaching above one. This value is higher than the maximum achievable normalized area for the  $|k| \geq 2$  correlation peaks in orthogonal polarization.

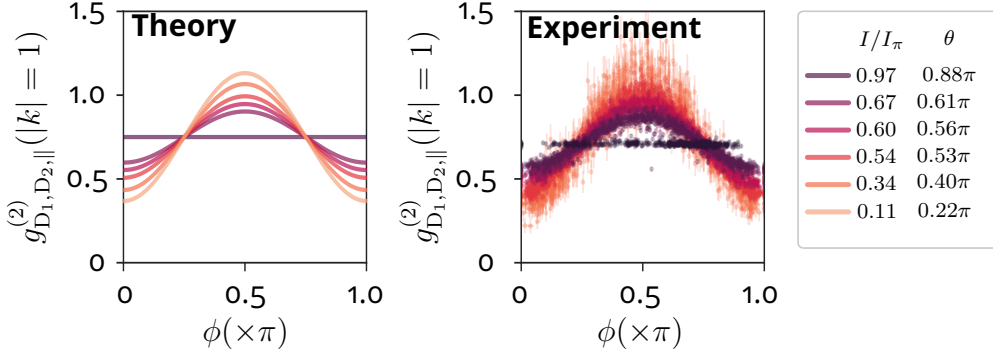


Figure 3.16 – **Phase-dependence**  $|k| = 1$  **peak area**. Average area of first delay ( $|k| = 1$ ) peaks as a function of optical phase  $\phi$  for different pulse areas, theory and experiment.

The theory curves in Fig. 3.16 allow us to retrieve the joint temporal photon-number coherence  $s_{\{1|M\}}^{(2)}$  as a function of pulse area. In Fig. 3.17 we plot this parameter together with the first-order coherence  $c^{(1)}$  obtained from the  $|k| \geq 2$  peaks with the corresponding theory curve :  $c^{(1)} = \mathcal{C} \cos^2(\theta/2)$ . In addition, we plot the wavepacket indistinguishability  $M_s$  obtained from the fits to the normalized zero delay peaks in Fig. 3.12. Combining  $M_s$  with the first-order coherence allows us to compare  $s_{\{1|M\}}^{(2)}$  and the expression given for an ideal quantum emitter, Eq. 3.26 (square points and dashed curve). We notice that for an emitter with a mean single-photon purity of  $g^{(2)} \approx (1.32 \pm 0.08)\%$  over the probed  $\theta$  range, the overlap in temporal coherence and first-order coherence is remarkably well approximated by the expression given in Eq. 3.26. Finally, we also note that the wavepacket indistinguishability is constant with increasing photon-number coherence, showing again the importance of proper normalization to source characterization.

### 3.4.3 . A witness for photon-number coherence in correlation histograms

As suggested in the previous section, the presence of photon-number coherence can be efficiently recognized considering the peak ratio  $|k| = 1$  over  $|k| \geq 2$ . We plot this ratio as a function of  $\phi$  in Fig. 3.18, both theory and experiment. We see that as we move away from  $\pi$  pulse and increase the vacuum component, the ratio between the first and the far delay peaks becomes phase-dependent, and the first delay peak areas even exceed the  $|k| \geq 2$  peaks. For even lower pulse areas, the first delay peak area is bigger than the  $|k| \geq 2$  peak areas for any value of  $\phi$ . The ratio between the first and second delay peaks (area or amplitude) thus carries with information on the amount of vacuum component of the interfering photonic fields. Only for photonic states prepared with a pulse area close to  $\pi$ -pulse do we

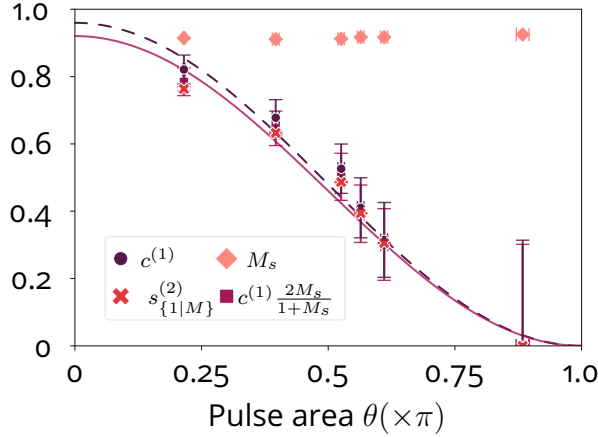


Figure 3.17 – **State parameters from coincidence measurements.** Quantum state parameters, first-order coherence  $c^{(1)}$ , indistinguishability  $M_s$ , and joint temporal photon-number coherence  $s_{\{1|M\}}^{(2)}$ , obtained from coincidence measurements and single counts measurements as a function of pulse area.

expect the ratio to be  $3/4$ . Under resonant excitation of a quantum emitter, any discrepancy thus reveals the presence of photon-number coherence.

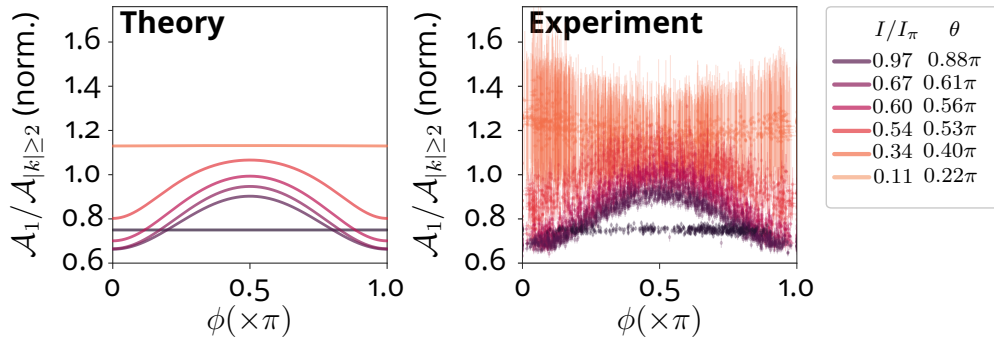


Figure 3.18 – **Identifying photon-number coherence.** Ratio of the  $|k| = 1$  and  $|k| \geq 2$  peak areas as a function of optical phase  $\phi$ , theory and experiment.

A search through papers performing HOM measurements with coherently driven quantum emitters, however, shows a large number of coincidence histograms where the ratio of the first and second delay peak is not equal to the expected  $3/4$ , indicating the presence of photon-number coherence, see a selection in Fig. 3.19 taken from Refs. (100–103) for several QD-based single-photon sources. The effect is very clear in Fig. 3.19(a,c,d) where the peak ratio indicates a suppression

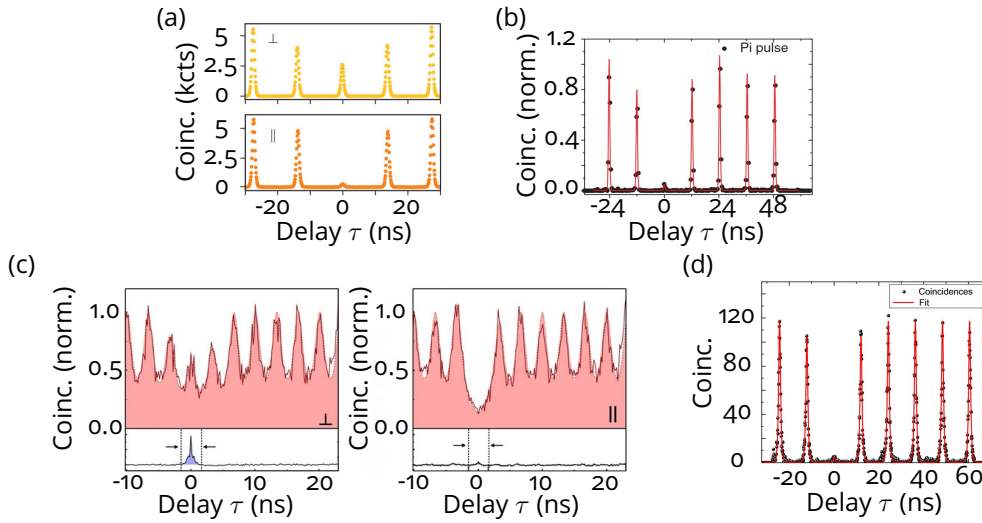


Figure 3.19 – **Photon-number coherence in coincidence histograms.** Coincidence histograms diverging from the  $\tau_1/\tau_2 = 3/4$  peak ratios (see main) : (a) in cross- and co-polarization for a QD single-photon source under resonant excitation, taken from Ref. (100); (b) for a QD in planar nanobeam waveguide, taken from Ref. (101); (c) in cross- and co-polarization for a QD embedded in a Schottky diode, taken from Ref. (102); (d) for a QD-cavity single-photon source, taken from Ref. (103). Red curves in (b,d) are fits to data (dots).

of long delay peaks due to coherence. There is thus a number of reports where the effect of photon-number coherence in HOM measurements has been overlooked. As discussed, this observation may indicate an underestimation in  $M_s$  and we expect that the high single-photon indistinguishability mentioned in the articles, probably are a lower limit on the actual single-photon indistinguishability based on our findings in this chapter. Considering the peak ratios in Fig. 3.19, it is highly likely that the wavepacket indistinguishability extracted from the histograms using side peak normalization resulted in an apparent value 1 – 5% below the actual  $M_s$ , indicating that at time of measurement, the source was not driven up to full population inversion, but rather around  $p_1 \simeq 0.7 - 0.8$ . Therefore, awareness should be raised to discrepancies in peak ratios or oscillations in single counts when characterizing coherently driven single-photon sources through HOM-type measurements.

### Conclusion Section 3.4 – Quantum interference between temporally separated wavepackets

In this section we have shown that – besides resulting in phase-dependence of far delay peaks – the first-order coherence also affects the first delay peaks in correlation histograms. More importantly, the presence of first-order coherence in Hong-Ou-Mandel-type measurements can also result in a new quantum interference phenomenon between temporally separated wavepackets when performing partial detection (i.e. detection of two out of three photons). In addition, we discussed how the ratio between first and far delay peaks in correlation histograms can be used as a witness for photon-number coherence. As we have shown, in the presence of first-order coherence this ratio is no longer equal to the ratio expected at pulse area  $\theta = \pi : 3/4$ . Using this observation, we argue how witnessing a discrepancy in the  $3/4$  ratio can potentially reveal an error in the measured wavepacket indistinguishability. Based on the examples used in this section, we suspect that the wavepacket indistinguishability in more published articles is actually higher than the reported value, showing the importance of proper normalization and awareness of the impact of photon-number coherence.

### 3.5 . Errors in heralded quantum gates

As we have shown in Sec. 3.4, measurements based on the Mach-Zehnder interferometer where the input is a train of pulses, can generate a new quantum interference phenomenon when detecting two photons out of three pulses which contain photon-number coherence. This observation suggests potential errors in quantum computation schemes when the input photon carries photon-number coherence. We demonstrate in this section using the Perceval framework (104) that when considering quantum gates, the use of quantum superpositions of zero- and one-photon – as expected when resonantly driving a quantum emitter – can impact both the performance of the gate and the error rate under certain conditions.

#### 3.5.1 . Post-selected CNOT gate

We first consider the linear optical quantum gate depicted in Fig. 3.20, the post-selected path-encoded CNOT gate proposed by Ralph et al. (77) comprising two control input modes  $c_{0_i}$  and  $c_{1_i}$ , two target input modes  $t_{0_i}, t_{1_i}$ , and two ancillary input modes in the vacuum state  $v_c, v_t$ . Fig. 3.20 presents the optical circuit of the proposed gate with four beam splitters of reflection ratios  $R = 1/3$  and  $R = 1/2$ . The control (target) input modes form the logical 0 or 1 bit with either a single-photon input in  $c_{0_i}$  ( $t_{0_i}$ ) or  $c_{1_i}$  ( $t_{0_i}$ ), respectively. **In this section, to distinguish  $|0\rangle \equiv |\text{vacuum}\rangle$  and  $|0\rangle \equiv |0_{\text{logical}}\rangle$ , we therefore note the  $|0\rangle \equiv |\text{vacuum}\rangle$  and  $|0_i\rangle \equiv |0_{\text{logical}}\rangle$ .**

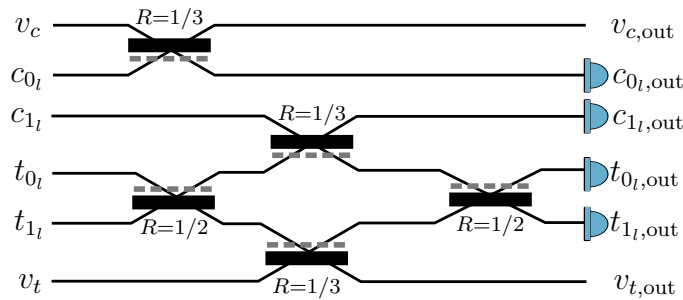


Figure 3.20 – **A post-selected CNOT gate.** The path-encoded configuration of a post-selected path-encoded CNOT gate, with control  $c_{i_i}$ , target  $t_{i_i}$  and vacuum  $v$  input modes.  $R$  corresponds to the beam splitter reflection coefficient (angle) with  $R \in [0, 1]$ .

The relations between the input and output modes in this circuit are given by

$$\begin{aligned}
c_{0l,\text{out}} &= \frac{1}{\sqrt{3}}(\sqrt{2}v_c + c_{0l}) \\
c_{1l,\text{out}} &= \frac{1}{\sqrt{3}}(-c_{1l} + t_{0l} + t_{1l}) \\
t_{0l,\text{out}} &= \frac{1}{\sqrt{3}}(c_{1l} + t_{0l} + v_t) \\
t_{1l,\text{out}} &= \frac{1}{\sqrt{3}}(c_{1l} + t_{1l} - v_t) \\
v_{c,\text{out}} &= \frac{1}{\sqrt{3}}(-v_c + \sqrt{2}c_{0l}) \\
v_{t,\text{out}} &= \frac{1}{\sqrt{3}}(t_{0l} + t_{1l} - v_t).
\end{aligned}$$

Conditional on the presence of a single-photon in the control input mode  $c_{1l}$  ( $|1_l\rangle_c$ ), a single-photon in one of the target input modes switches logical state (from  $|0_l\rangle_t$  to  $|1_l\rangle_t$  or vice versa). The gate performs as a CNOT gate when measuring coincidences between the control and target outputs ( $c_{i,\text{out}}$  and  $t_{i,\text{out}}$ , with  $i = 0$  or  $1$ ). The gate operates thus as a probabilistic gate where we post-select on the desired output, with the probability of a successful gate ideally  $1/9 \approx 11\%$ .

We write the truth table of the CNOT gate with in the first column the possible logical input states for the control and target input modes, and in the first row the possible logical outputs :

	$ 0\rangle_c  0\rangle_t$	$ 0\rangle_c  1\rangle_t$	$ 1\rangle_c  0\rangle_t$	$ 1\rangle_c  1\rangle_t$
$ 0\rangle_c  0\rangle_t$	$P_{0000}$	$\delta_1$	$\delta_2$	$\delta_3$
$ 0\rangle_c  1\rangle_t$	$\delta_4$	$P_{0101}$	$\delta_5$	$\delta_6$
$ 1\rangle_c  0\rangle_t$	$\delta_7$	$\delta_8$	$\delta_9$	$P_{1010}$
$ 1\rangle_c  1\rangle_t$	$\delta_{10}$	$\delta_{11}$	$P_{1101}$	$\delta_{12}$

The entries indicated by  $P_{ijkl}$  are in the ideal case equal and  $11\%$ . The other values  $\delta_m$  correspond to unwanted outputs, and thus can be related to an error rate. An ideal probabilistic Ralph CNOT gate would therefore have entries  $P_{ijkl} = 11\%$  and  $\delta_m = 0\%$ . However, errors in computation can be introduced due to limited indistinguishability and beam splitting ratios, for example. These sources of error potentially decrease the probability of the wanted outcomes,  $P_{ijkl}$ , and increase the probability of generating unwanted outcomes, referred to as the error rate  $\delta_m$ . We define for the quantum gates **the performance rate as determined by the lowest value of the four entries  $P_{ijkl}$** .

We test the fidelity of the gate considering the input logical state :

$$\frac{1}{\sqrt{2}} (|0_l\rangle_c + |1_l\rangle_c) \otimes |0_l\rangle_t.$$

The output state of the CNOT gate is then the post-selected Bell state :

$$|\Psi^+\rangle = \frac{1}{\sqrt{2}} (|0_l\rangle_c |0_l\rangle_t + |1_l\rangle_c |1_l\rangle_t). \quad (3.27)$$

We then plot **the state fidelity**, the overlap between the generated state  $|\Phi_{\text{out}}\rangle$  and the desired state  $|\Psi^+\rangle$ , as :

$$\mathcal{F} = |\langle \Phi_{\text{out}} | \Psi^+ \rangle|^2 \quad (3.28)$$

where  $\mathcal{F} = 1$  indicates a perfect overlap.

We study whether changing the input state into a photon-number superposition degrades the performance of quantum gates. These quantum gates are operated with single-photon input states  $|1\rangle$  on which we encode the logical bits. However, when inputting a photon-number superposition with zero- and one-photon component, the possible output state distribution changes. We can anticipate that this change also affects the performance of the gate. To investigate the effect of photon-number superpositions on the performance of the post-selected CNOT gate, we define a superposition input state (not in logical basis)

$$|\text{in}\rangle = \cos\left(\frac{\theta}{2}\right) |0\rangle + \sin\left(\frac{\theta}{2}\right) |1\rangle,$$

where we set global phase  $\alpha = 0$ , and we tune the angle  $\theta$  (pulse area) between  $0 - \pi$  in steps of 50. For each angle we compute the possible outcomes, and the resulting performance and fidelity.

Fig. 3.21 shows the performance and fidelity as a function of pulse area. At full population inversion the gate performs as expected with a  $\approx 11\%$  probability. However, as soon as we introduce vacuum population, the performance of the gate degrades as a result the lower probability to detect two photons : one for the control, and one for the target qubit. Interestingly, this performance degradation is not reflected in a change in fidelity, which remains 1 for all  $\theta$ . This observation can be understood by the fact that this CNOT gate is a post-selected gate. The probability of generating the wanted outcome, performance, decreases with pulse area. However, because of post-selection, we discard all outcomes that are of no interest in the computation, i.e. other generated states. Hence, the fidelity is unity and only drops in the limit of  $|\text{in}\rangle \equiv |0\rangle$ .

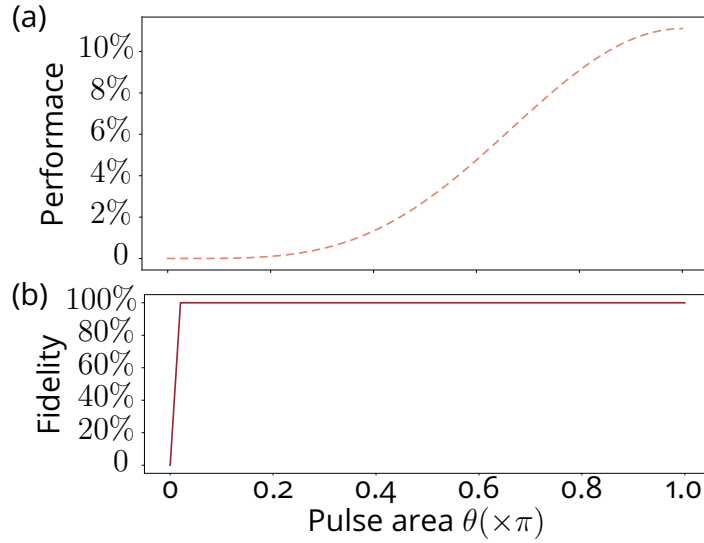


Figure 3.21 – **Performance and gate fidelity using a Ralph CNOT gate with photon-number superpositions.** (a) The performance of a post-selected CNOT gate as a function of pulse area  $\theta$ , where  $\theta = \pi$  corresponds to an ideal single-photon input state. (b) The gate fidelity of the post-selected CNOT gate as a function of pulse area. Because of post-selection, the fidelity only drops in the limit of  $\theta \rightarrow 0$ .

### 3.5.2 . Heralded CNOT gate

We now consider another important quantum gate in optical quantum computing, the Knill-Laflamme-Milburn (KLM) heralded CNOT gate (31; 105). The basic idea behind this scheme is the following : four logical bits formed by indistinguishable control  $c_{i_l}$ , target  $t_{i_l}$  and ancilla  $h_{i_l}$  photons are input to the quantum gate, see Fig. 3.22, where again  $R$  indicates the beam splitter ratios. Conditional on the simultaneous detection, i.e. heralding, of two output ancilla photons – one at either detector  $h_{0_l, \text{out}}$  or  $h_{1_l, \text{out}}$  and one at either detector  $h_{2_l, \text{out}}$  or  $h_{3_l, \text{out}}$  – a CNOT operation is performed whereby the target qubit switches mode (106). Similar to the post-selected CNOT gate, the gate we described here is probabilistic, although the protocol can be altered by using teleportation to create near-deterministic gates (105; 107). An advantage of heralded CNOT gates, is that the measurement is non-destructive, i.e. the generated states can be used in subsequent gates, unlike post-selected CNOT gates, where a successful operation is solely verified by measuring the output state a posteriori (106). However, as we show here, the operation of such of a heralded CNOT gate is affected when the input states contain photon-number coherence.

Here in Fig. 3.23 we study three different scenarios : where the heralding qubits are in a single-photon Fock state, and both the control and target qubit

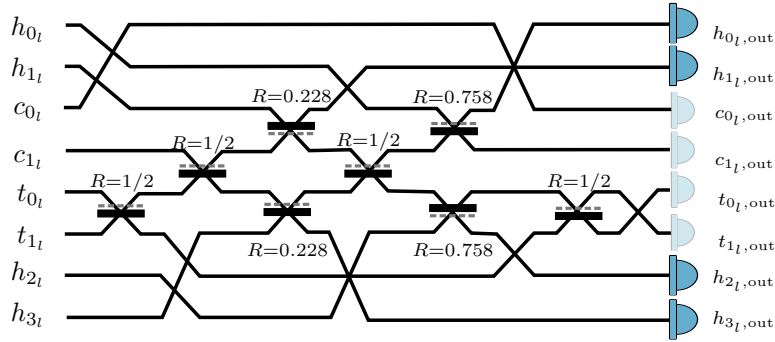


Figure 3.22 – **A heralded CNOT gate.** The path-encoded configuration of a heralded KLM CNOT gate, with control  $c_{i_i}$ , target  $t_{i_i}$  and ancilla  $h_{i_i}$  input modes.  $R$  corresponds to the beam splitter reflection coefficient with  $R \in [0, 1]$ .

are in a photon-number superposition state with vacuum component determined by  $\theta$  ("perfect herald"); where the heralding qubits are in a superposition state, and the target and control are in single-photon Fock states ("perfect data"); and where all qubits are in a photon-number superposition state according to Eq. 3.5.1 (" $\sqrt{p_0}|0\rangle + \sqrt{p_1}|1\rangle$ "). Analogous to the CNOT gate simulation, we plot the gate performance as a function of pulse area  $\theta$  and the overlap between the desired state and the output state, the state fidelity in Eq. 3.28.

Let us first consider Fig. 3.23(a). Similarly to the post-selected CNOT we witness a degradation in performance with smaller pulse area when all qubits contain photon-number coherence (dashed red), caused by the decreasing probability of detecting the two photons. However, if only the herald qubit, or target and control qubit, are in a superposition state, the slope observed in the performance as a function of  $\theta$  is less steep. This can be understood by considering for instance the case of an imperfect herald. Such an imperfect herald does not always herald a successful gate, but when it does, the gate is indeed successful because the target and control are in a single-photon Fock state. The same logic can be applied to the case of imperfect data.

Unlike the post-selected CNOT gate, the state fidelity of the heralded CNOT gate is heavily impacted by the presence of photon-number coherence, see Fig. 3.23(b) and (c). The working principle of the heralded CNOT gate is similar to the detection of coincidences separated by one pulse, corresponding to the first delay peak in coincidence histograms : the gate is performed based on the conditional detection of two out of four photons. This partial detection results in quantum interference phenomena similar to those discussed in Sec. 3.4 : if all input qubits are in a photon-number superposition, there will be phase-dependent

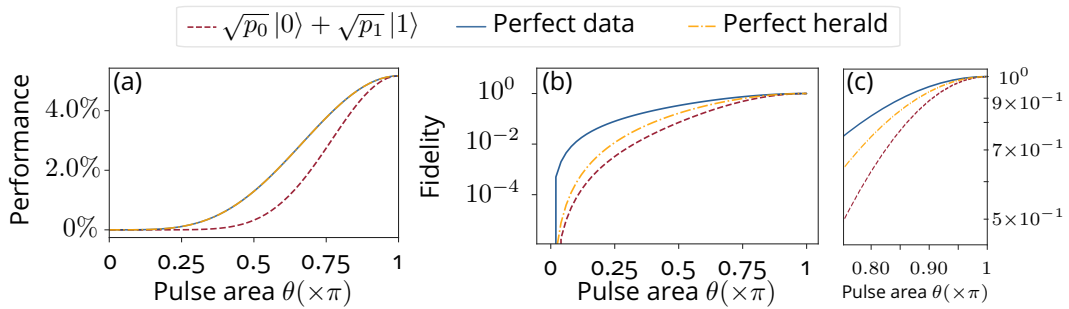


Figure 3.23 – **Effect of photon-number coherence in heralded CNOT gate.** (a) The performance of a heralded CNOT gate as a function of pulse area. (b) The fidelity as a function of pulse area. (c) A zoom-in of the fidelity in (b) for pulse areas close to  $\theta = \pi$ . (a-c) : dashed red corresponds to heralding, target and control qubits in a superposition state with vacuum population determined according to  $p_0 = \cos^2(\theta/2)$ ; solid blue corresponds to target and control qubits in a perfect single-photon Fock state, and herald in superposition state; dashed yellow corresponds to herald in a perfect single-photon Fock state, and target and control in superposition state.

interference between the one-photon components. The photon-number superpositions in the heralded CNOT gate therefore result in unwanted output states, which in turn affect subsequent quantum gates in the optical circuit, removing the benefit of using heralded CNOT gates.

#### Conclusion Section 3.5 – CNOT gates and photon-number coherence

We have shown that introducing photon-number superpositions does not only affect the probability of a successful gate (performance), but it can also change the output state due to interference effects. Hence, the input quantum state of light should be carefully considered and prepared when performing optical quantum computations based on Hong-Ou-Mandel-type interferometry. The two examples shown here, are common gates in optical quantum computing, and only present a small selection of gates based on the Hong-Ou-Mandel effect. As such, one can imagine that other quantum gates – specifically heralded gates – may similarly suffer from the presence of quantum coherence.

### 3.6 . Conclusion and perspectives

In this chapter we have shown that the possible presence of photon-number coherence affects quantum information processing in all its facets. We explicitly investigated the impact of photon-number coherence on the cornerstone of optical quantum computing : the Hong-Ou-Mandel effect. We demonstrate theoretically and experimentally that when exciting a quantum emitter below full population inversion with a pulsed laser, the resulting first-order coherence requires careful consideration. Specifically, the normalization procedure of correlation measurements based on uncorrelated peaks, needs to be revisited to not underestimate quantum state parameters such as wavepacket indistinguishability and first-order coherence. We demonstrated that one has to take into account auto-correlation functions to obtain a phase-robust normalization procedure.

When properly normalized, the coincidence histograms also reveal a new quantum interference phenomenon in presence of photon-number coherence. If the input to a Mach-Zehnder interferometer is a train of pulses containing photon-number superpositions, measuring coincidences separated by one pulse – i.e. two temporally delayed clicks – entangles three pulses. Indeed, we demonstrate that the coincidence click corresponding to delay  $\tau_k$  with  $|k| = 1$  can arise from coincidences between the first two pulses or the last two pulses. This entanglement manifests itself as a phase-dependence of the first delay peak areas in coincidence histograms, and is dependent on the overlap between the first-order coherence and temporal coherence : the joint temporal photon-number coherence  $s_{\{1|M\}}^{(2)}$ . Together with the phase-dependence of the uncorrelated peaks, the coincidence histograms thus reveal information on the first-order coherence, wavepacket indistinguishability, and  $s_{\{1|M\}}^{(2)}$ .

Finally, we have shown that this type of quantum interference affects the performance and error rate of well-known quantum gates in optical quantum computing by considering both the post-selected CNOT gate and the heralded CNOT gate. The fact that in a heralded CNOT gate only two out of four photons are detected, gives rise to quantum interference which strongly impacts the error rate of the gate. We show that photon-number coherence does not affect the error rate in a post-selected CNOT gate, but does affect the performance of the gate in a similar fashion to the heralded CNOT gate. These two examples demonstrate the detrimental impact of photon-number coherence on quantum computation schemes if disregarded.

### Overcoming computation errors

To overcome the negative effect of photon-number coherence in quantum computation schemes, one could therefore consider alternative excitation schemes which do not create photon-number coherence. In 2021 our group proposed an alternative to coherent excitation, making use of phonon assisted excitation (40). A spectrally blue-detuned driving laser ( $\Delta_{LA} = 0.4 - 0.8$  nm) dresses the ground and excited states of the QD. During the excitation pulse, the QD relaxes to the excited states through longitudinal-acoustic (LA) phonon emission.

The laser field is easily separated from the single-photons through spectral filtering, and as a result we obtain photonic fields of high single-photon purity and indistinguishability comparable to resonant excitation schemes.

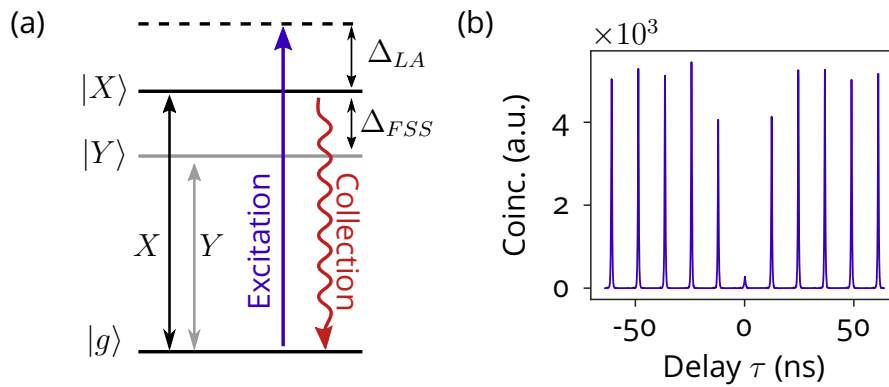


Figure 3.24 – (a) The principle of LA excitation, inspired by Ref. (40). (b) A coincidence histogram obtained using LA excitation.

However, because of the emission of acoustic phonon during the pulse, phonon assisted excitation does not produce any atomic coherence in the energy basis, and therefore no photon-number coherence. This absence of photon-number coherence is reflected in the coincidence histograms obtained with subsequent HOM measurements, Fig. 3.24(b). The peaks exhibit no phase-dependence, despite a maximum occupation probability of 85% for the presented experimental data (40; 108). This protocol thus offers an excellent solution to benefit from the high source performance for optical quantum computing.

### Perspectives

Finally, besides negative effects, one can also imagine new research opportunities with the quantum interference phenomenon discussed in this chapter. This quantum interference, present in any Mach-Zehnder-like interferometer when the input is a train of pulses containing photon-number coherence, could be further

investigated to understand how it could be turned into an asset for the generation of complex states of light showing photon-number superpositions (39), or time bin entanglement (36).

## 4 - Experimental study of the energetic exchanges between a qubit and light fields

### 4.1 . Introduction

The observation of energy coherence transfer between a QD and a light field (83) has triggered theoretical work to revisit this physical phenomenon in the framework of quantum thermodynamics. Indeed, coherence has been identified as a fundamental property in work exchange (109; 110). This chapter presents a major experimental effort conducted during this PhD, exploiting for the first time a QD in order to experimentally access heat and work in the energetic exchanges between two coupled systems. We thus validate a fundamental model for quantum thermodynamics and show experimentally how quantum features connect with energetics - i.e. ubiquitous thermodynamics.

The chapter is ordered as follows : in Sec. 4.2 we first explain **work and heat in the quantum regime** in the framework of two coupled systems, otherwise isolated. To understand how these definitions apply to our quantum dot-cavity system, we briefly set out the main results from previous works where the theoretical framework was applied to a more specific setting : a qubit coupled to the electromagnetic field (37; 38). The results presented there form the starting point and give predictions for Sec. 4.3 and Chapter 5.

In Sec. 4.3, we discuss the **experimental protocol** that we propose to access these energetic quantities and the results obtained in this framework of quantum thermodynamics with a qubit operating in the **spontaneous emission regime**. This step is energetically equivalent to the charging of a quantum battery : an energy storage device exploiting non-classical features such as coherence or entanglement (111). We therefore first apply the theory discussed in Sec. 4.2.2 to our specific quantum dot-cavity system, and show that we can measure the energetic exchanges in spontaneous emission through homodyne-type measurements with the spontaneously emitted photonic fields. We then extend the theory by **introducing decoherence** to our qubit system and experimentally measure its impact on the energetic transfers in spontaneous emission.

In a second step, Sec. 4.4, of our experimental protocol we develop a new experimental and theoretical framework to quantify and measure the **energetic exchanges between two light fields**, the photonic field emitted by the qubit and a classical coherent field interfering at a beam splitter. This step is a common operation in optical quantum computing, and energetically equivalent to the discharging of a quantum battery. Here again, we show how we can measure the energetic exchanges experimentally, and discuss our observations. We show that

measuring the energetic exchanges experimentally in this scenario can also be achieved by performing a homodyne measurement.

The theoretical work presented in this chapter, supporting and guiding our experimental research, has been developed by Prof. Alexia Auffèves<sup>1</sup>, Dr. Maria Maffei<sup>2</sup>, and Dr. Stephen Wein<sup>3</sup>.

---

1. Université Grenoble Alpes, CNRS, Grenoble INP, Institut Néel, 38000 Grenoble, France.

2. Université Grenoble Alpes, CNRS, Grenoble INP, Institut Néel, 38000 Grenoble, France.

3. Previously : Université Grenoble Alpes, CNRS, Grenoble INP, Institut Néel, 38000 Grenoble, France.

Currently : Quandela SAS, 7 Rue Léonard de Vinci, 91300 Massy, France.

## 4.2 . Defining work and heat in the quantum regime

Classical thermodynamics deals with energetic processes in the macroscopic world, where the relation with statistical physics holds because it describes many-body systems (112). In classical thermodynamics, a change in energy within a closed system can be decomposed into a heat and work contribution, giving rise to the first law of classical thermodynamics, a formulation of the conservation of energy :

$$\delta\mathcal{E} = \delta\mathcal{W} + \delta\mathcal{Q}, \quad (4.1)$$

where  $\delta\mathcal{W}$  is the amount of work exerted onto the system by another entity, and  $\delta\mathcal{Q}$  the heat transferred to the system. Work and heat are path-dependent statistical quantities and therefore are associated with a process (113; 114). These energetic transfers in the form of work and heat, are often also defined as reversible (useful) or irreversible (wasteful) processes, respectively. The internal energy change, however, is only a function of its initial and final state. With these definitions one can for example determine the efficiency of heat engines, where the system (for instance a gas) contains a manifold of molecules.

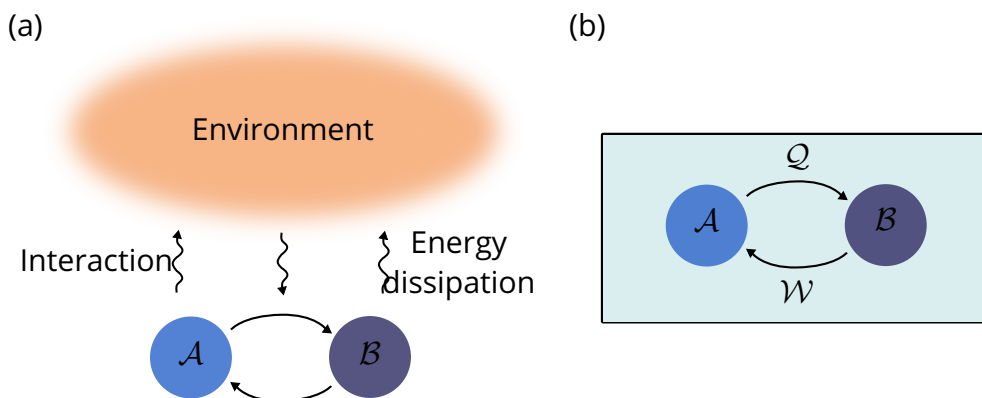


Figure 4.1 – **Two approaches to defining thermodynamic quantities in the quantum regime.** (a) An open system where two quantum bodies are coupled to each other and interact with the environment (several and different baths). (b) A closed quantum systems where two coupled quantum systems do not exchange energy with any external bath, and where we are able to define work and heat transfer.

One of the most important challenges in quantum thermodynamics addresses the question on how the field of classical thermodynamics, with concepts such as heat and work, translates to the level of a few, or even of a single particle : the quantum regime, where statistical physics does not hold and the systems are time-reversal invariant (114; 115). Over the past decades different approaches to defining these thermodynamic quantities in the quantum regime have been put forward,

with one of the first in a paper by R. Alicki in 1979 **defining work exchange in a quantum open system** (116). Such open quantum system can be seen as two quantum systems  $\mathcal{A}, \mathcal{B}$  coupled to each other and to the environment (a heat bath for example), see Fig. 4.1(a). In such a system, energy can dissipate into the environment through interaction. In the paper by Alicki, the author considers an open quantum system weakly coupled to two thermal reservoirs at different temperatures  $T_1$  and  $T_2$  (where  $T_1 \geq T_2$ ). Under the influence of **time-dependent** external conditions (e.g. switching on and off coupling with a classical field (117)), the heat engine *periodically* dissipates work into the environment, see Fig. 4.2.

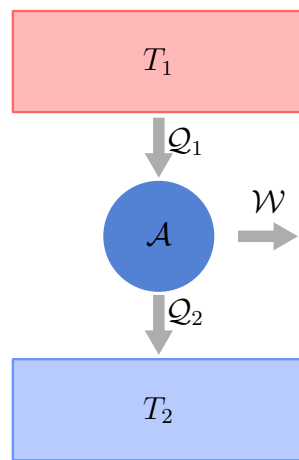


Figure 4.2 – **A quantum heat engine.** A quantum open system describing a heat engine where a quantum system  $\mathcal{A}$  is coupled to two thermal baths with temperatures  $T_1 \geq T_2$  that supply heat  $Q_i$  and induce mechanical work  $\mathcal{W}$ .

This periodically-driven open quantum system constitutes a heat engine and is described by a time-dependent Hamiltonian. Under the assumption that the external conditions during a cycle are slowly varying in time, heat can be defined as the sum of heat originating from the different heat baths. Combining this definition with the first law of thermodynamics, Eq. 4.1, the author finds that the sum of heat contributions is equal to the work performed by the system per cycle,  $\mathcal{W} = Q_1 + Q_2$ , which in turn allows to define an efficiency  $\eta$  of the heat engine :

$$\eta = \frac{\mathcal{W}}{Q_1} \leq \frac{T_1 - T_2}{T_1}.$$

This equation is actually identical to the famous Carnot inequality which holds in the classical limit of thermodynamics.

Other approaches have been put forward to account for work and heat transfer in *time-independent quantum open systems*. One such approach comprises a

system coupled to one or more thermal baths with temperatures  $T_i$  and a “work-storage” device in the form of a quantum system with mass  $m$  that can be raised or lowered, thereby storing work in the form of gravitational energy (118), see Fig. 4.3. Imposing the first law of thermodynamics – average total energy is preserved – allows to define the heat flow as the decrease in average energy of the bath, and the work exchange as the change in average (gravitational) energy of the weight. For a recent overview on other approaches to define work and heat in an open quantum system, we refer the reader to Ref. (114).

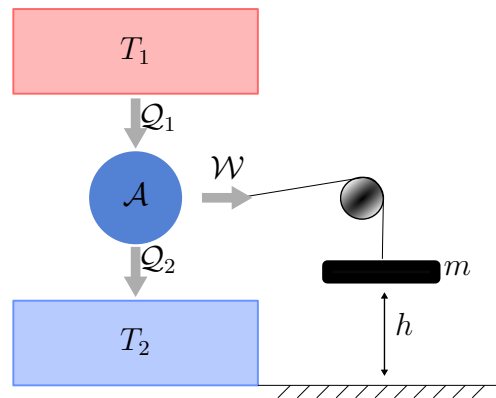


Figure 4.3 – **Storing work in a quantum system.** A quantum open system describing a heat engine with quantum system  $\mathcal{A}$  and a quantum system (weight) with mass  $m$  at height  $h$  which is used to store work in the form of gravitational energy.

The various approaches to describe thermodynamics in an open quantum system have put forward different definitions of work (114) : average work defined for an ensemble of experimental runs such as the one described in Fig. 4.3, fluctuating work for a single shot measurement (119), optimal single shot work (120), and work given by optimal thermodynamic resource theory (110). Despite the different approaches to defining work and heat in open quantum systems, the approaches seem not entirely consistent with one another leading to different values of work exchanged when evaluating the same system (114; 121–123). In addition, for an open quantum system *strongly* coupled to the environment, the possibility of a thermodynamically consistent definition for heat is still debated (124–126). Moreover, some approaches do not take into account the possible role played by genuine quantum features such as quantum correlations or coherences (121; 122). For all these reasons, the work conducted during this PhD, led on the theoretical side by Prof. A. Auffèves and collaborators, is positioned in a framework of closed systems : we will only consider situations where two quantum systems are coupled to, but do not exchange energy with baths.

### 4.2.1 . Defining work and heat in a closed quantum system

We study the notions of work and heat in the quantum regime within closed quantum systems where two coupled quantum systems  $\mathcal{A}$ ,  $\mathcal{B}$  are otherwise isolated, Fig. 4.1(b) (122; 127–129). The two systems interact, generating **classical and quantum correlations** such as entanglement, but do not dissipate energy to the environment.

In Ref. (122) the state of such a bipartite system in absence of correlations is described by the density matrix  $\rho(t) = \rho^{\mathcal{A}}(t) \otimes \rho^{\mathcal{B}}(t)$  with  $\rho^{\mathcal{A}(\mathcal{B})}(t) = \text{Tr}_{\mathcal{B}(\mathcal{A})}\{\rho(t)\}$ , and evolves under a total **time-independent** Hamiltonian :

$$H_{\text{tot}} = H_{\mathcal{A}} + H_{\mathcal{B}} + V_{\mathcal{A},\mathcal{B}}, \quad (4.2)$$

where the interaction Hamiltonian  $V_{\mathcal{A},\mathcal{B}}$  couples the two systems. In presence of correlations between the subsystems, the state is written as :

$$\rho(t) = \rho^{\mathcal{A}}(t) \otimes \rho^{\mathcal{B}}(t) + \chi_{\mathcal{A},\mathcal{B}}(t), \quad (4.3)$$

where the correlation matrix  $\chi_{\mathcal{A}\mathcal{B}}(t)$  quantifies all classical and quantum correlations. This separation of dynamics given in Eq. 4.3, allows us to define work and heat in terms of the bare Hamiltonians of the two systems :

$$\dot{\mathcal{W}}_{\mathcal{A}(\mathcal{B})} = -\frac{i}{\hbar} \text{Tr}_{\mathcal{A},\mathcal{B}} \{ [H_{\mathcal{A}(\mathcal{B})}, V_{\mathcal{A},\mathcal{B}}] \rho^{\mathcal{A}}(t) \otimes \rho^{\mathcal{B}}(t) \}, \quad (4.4)$$

$$\dot{\mathcal{Q}}_{\mathcal{A}(\mathcal{B})} = -\frac{i}{\hbar} \text{Tr}_{\mathcal{A},\mathcal{B}} \{ [H_{\mathcal{A}(\mathcal{B})}, V_{\mathcal{A},\mathcal{B}}] \chi_{\mathcal{A},\mathcal{B}}(t) \}. \quad (4.5)$$

These definitions combined form the **quantum version of the first law of thermodynamics**, where for each system undergoing a change in internal energy  $\Delta\mathcal{E}$  we can write :

$$\Delta\mathcal{E}_{\mathcal{A}(\mathcal{B})} = \mathcal{W}_{\mathcal{A}(\mathcal{B})} + \mathcal{Q}_{\mathcal{A}(\mathcal{B})}. \quad (4.6)$$

If the average coupling energy is constant, i.e.  $\frac{d}{dt} \text{Tr} \{ V_{\mathcal{A},\mathcal{B}} \rho(t) \} = 0$ , Refs. (38; 122) find that the **work and heat transfer from  $\mathcal{B}$  to  $\mathcal{A}$  are equal in amplitude, but opposite** :

$$\dot{\mathcal{W}}_{\mathcal{A}}(t) = -\dot{\mathcal{W}}_{\mathcal{B}}(t), \quad (4.7)$$

$$\dot{\mathcal{Q}}_{\mathcal{A}}(t) = -\dot{\mathcal{Q}}_{\mathcal{B}}(t), \quad (4.8)$$

where  $\mathcal{A}$  absorbs work (heat) and  $\mathcal{B}$  releases work (heat).

Thus, **correlations (classical and quantum) can be directly related to the heat transfer** between  $\mathcal{A}$  and  $\mathcal{B}$  in a closed quantum system, and **work exchange is defined as an effective unitary interaction between the two systems**. These definitions of work and heat therefore do not, unlike in open quantum systems, require the incorporation of any external driving forces or

coupling to an external bath. Importantly, this framework can be generalized to any pairs of systems  $\mathcal{A}$  and  $\mathcal{B}$

Another important feature of this framework is that whenever one of the subsystems becomes classical, these definitions of work and heat in a closed quantum system are consistent with the classical framework. This framework has established some consensus within the field of quantum thermodynamics. The presented theoretical framework does therefore provide a footing to experimentally investigate energetic flows at the quantum level for a qubit coupled to another quantum system (e.g. the electromagnetic field), but otherwise isolated from its environment.

#### 4.2.2 . Predicted energetic exchanges between an atom and light fields

Recently theorists started to apply the definitions for work and heat in closed quantum systems to more specific cases, such as that of a two-level system coupled to a reservoir of electromagnetic modes, and investigate the energy flows for such a coupled system in different scenarios (130–132). A particularly interesting scenario is a **qubit coupled to the vacuum of the electromagnetic field**. This is the regime of spontaneous emission, and is energetically equivalent to the charging of an empty quantum battery, an energy storage device exploiting quantum features. In the following we briefly review published results examining this regime of light-matter interaction in terms of work and heat flow to understand how we can apply this framework to our QD-cavity system and quantify the various energetic exchanges. The theoretical results presented here serve as a starting point for the first part of the chapter.

#### 4.2.3 . Energetic exchanges between a qubit and a driving field

The work by Maffei et al. (38), considers two quantum systems : a qubit  $q$  initially in the ground state and stationary at position  $x = 0$ , and a coherent field  $f$  propagating along  $x$  with speed  $v$ , see Fig. 4.4. At time  $t = t_0$ , both systems are brought into a pure state by Alice ( $A$ ) through unitary operations which have an energetic cost corresponding to work  $-\mathcal{W}_A = \Delta\mathcal{E}_q + \Delta\mathcal{E}_f$  (blue), where  $\Delta\mathcal{E}_i$  corresponds to the change in internal energy of system  $i$ . At time  $t = 0$ , Fig. 4.4(b), the field is resonant with the qubit and they interact whereby the two systems exchange work (blue) and heat (blue and red) in the form of correlation energy. Finally, at time  $t$  in Fig. 4.4(c), Bob ( $B$ ) attempts to extract work from the bipartite system using unitary operations.

In this framework, **energy conservation holds**, and the work flow between the qubit and the field at time  $t = 0$  is defined as :  $\dot{\mathcal{W}} = \dot{\mathcal{W}}_q = -\dot{\mathcal{W}}_f$ . In terms of the field operators, this **work flow is equal to the energy change of the field coherent component** :

$$\dot{\mathcal{W}} = \hbar\omega_0(|\langle\hat{a}_{\text{out}}(t)\rangle|^2 - |\langle\hat{a}_{\text{in}}(t)\rangle|^2), \quad (4.9)$$

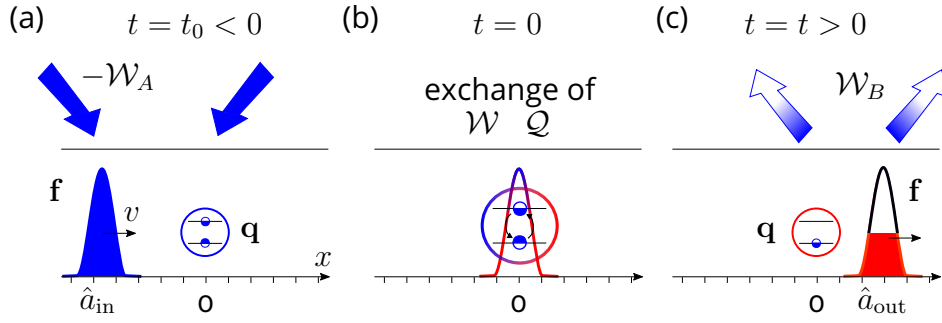


Figure 4.4 – **Energetic exchanges between a qubit and a propagating field.** (a) At time  $t = t_0$ , a qubit  $q$  stationary at  $x = 0$  and a propagating electromagnetic field  $f$ , described by input operator  $\hat{a}_{\text{in}}$ , are prepared in an initial state by Alice, at the expense of work  $-\mathcal{W}_A$  (blue). (b) At time  $t = 0$ , the two systems interact, exchanging work  $\mathcal{W}$  (blue) and correlation energy  $\mathcal{Q}$  arising from entanglement (blue and red). (c) At time  $t$ , Bob extracts work from the two systems  $\mathcal{W}_B$ . The energy arising from correlations is not extractable and remains inside the field and the qubit. The propagating output field is now described by output operator  $\hat{a}_{\text{out}}$ . Figure adapted from Ref. (38). See text for details.

where  $\omega_0$  is the frequency of the qubit, and  $\hat{a}_{\text{in}}(t)$  and  $\hat{a}_{\text{out}}(t)$  are the time-dependent input and output operators of the propagating field before and after time  $t = 0$ , respectively, see Fig. 4.5. Strikingly, even in the absence of an input field ( $\langle \hat{a}_{\text{in}}(t) \rangle = 0$ ), the qubit can spontaneously release work into the vacuum of the electromagnetic field (initially empty battery), a scenario corresponding to the spontaneous emission regime of light-matter interaction. In the absence of an input field, Eq. 4.9 then simply becomes :

$$\mathcal{W} = \hbar\omega_0 \int dt' |\langle \hat{a}_{\text{out}}(t') \rangle|^2, \quad (4.10)$$

where the work corresponds to the energy change of the coherent component of the output field. More precisely, Eq. 4.10 is the work provided by the qubit – i.e. originating from energy coherence, see Section 2.5.5 – to the vacuum of the electromagnetic field. The authors note that a change in coherence of the propagating field can be used as a witness for quantum correlations present at the time of interaction ( $t = 0$ ). **Correlations, built up during the interaction, reduce the total amount of work that can be extracted from the system at time  $t$ .** To extract all work initially given to the bipartite system  $\mathcal{W}_A$  would require one of the subsystems,  $f$  or  $q$ , to be initially prepared in a classical state, for example the driving field  $f$  being a high-intensity coherent field. This is a scenario corresponding to the stimulated emission regime of light-matter interaction, where thus work extraction from the qubit is possible, but comes at a high energetic cost.

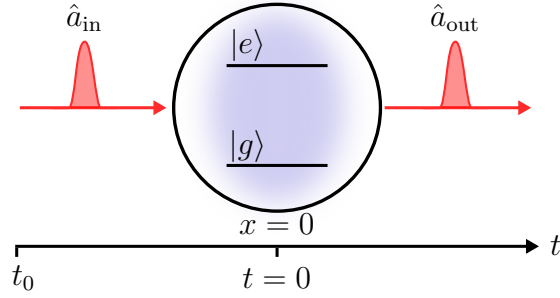


Figure 4.5 – **Input-output formalism.** Input  $\hat{a}_{\text{in}}(t)$  and output  $\hat{a}_{\text{out}}(t)$  operators of a propagating field where wavepackets travel without deformation before and after interaction ( $t = 0$ ) with a qubit at position  $x = 0$  composed of a ground and excited state.

#### 4.2.4 . Impact of quantum coherence on energetic exchanges between a qubit and the electromagnetic field

Similar to the previous section, Monsel et al. (37) also investigate work exchange between a qubit and light fields. Inspired by the experimental evidence brought by Ref. (83) (see Section 2.5.5), the authors assume all energy coherence initially present in the qubit is transferred to the coherence in photon-number basis upon spontaneous emission. Under this assumption, they demonstrate that work exchange in spontaneous emission is equal to the change in energy coherence in the output field, Eq. 4.10.

The aim of Ref. (37) is to maximize work transfer from the qubit to the electromagnetic field, thus reducing the amount of quantum correlations built up during interaction between the two systems. More specifically, they study how work extraction from a qubit is affected by the presence of initial qubit coherence in the energy basis, and by the initial energy carried by the electromagnetic field. A simplistic sketch of the framework is given in Fig. 4.6, where a qubit is constantly coupled to a mode of the electromagnetic field, here depicted as a quantum battery and initially empty.

The authors consider a qubit initially ( $t = 0$ ) prepared by a laser with pulse area  $\theta$  in the pure quantum state :

$$|\Psi_q\rangle = \cos\left(\frac{\theta}{2}\right)|g\rangle + \sin\left(\frac{\theta}{2}\right)|e\rangle,$$

This state preparation also brings energy to the qubit  $\mathcal{E}_q(0) = \hbar\omega_0 \sin^2(\theta/2)$ , with  $\omega_0$  the frequency of the qubit. Additionally, this state preparation creates coherence in the energy basis of the qubit according to  $s(t = 0) = \cos(\theta/2)\sin(\theta/2)$ . By choosing the initial state of the battery (e.g. vacuum, charged) and the coupling

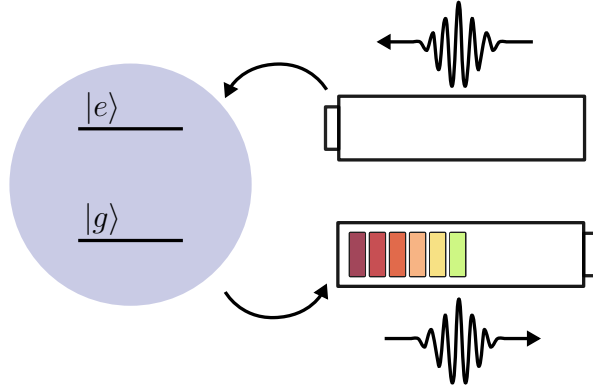


Figure 4.6 – **Energetics of spontaneous emission.** A qubit coupled to the vacuum of the electromagnetic field, here depicted as an empty battery field. A pulsed laser excites the qubit, which subsequently spontaneously decays and transfers work (coherence) to the battery field. Inspired by Ref. (37).

duration between the qubit and the battery carefully, work extraction from the qubit is optimized. As discussed previously, work is defined as the coherent fraction of energy radiated by the qubit in the battery (Eq. 4.9), whereas heat corresponds to the incoherent part, making up the energy balance previously introduced in Eq. 4.1.

First, the authors consider a qubit-battery coupling duration which maximizes the work transfer from the qubit to the field. For a given initial state of the qubit, the amount of work transfer increases with initial energy contained inside the battery and reaches a maximum value in the limit where the input photon rate is  $\dot{N} \gg \gamma$ , with  $\gamma$  being the spontaneous emission rate of the qubit. This is equivalent to **the stimulated emission regime of light-matter interaction**, where spontaneous emission is negligible. In this regime, the qubit-battery interaction is unitary and thus the heat flow becomes  $\dot{Q} = 0$ . However, this limit requires heavy energetic resources as the required input photon rate in the battery is high.

A second scenario assumes an initially empty battery. This scenario corresponds to **the spontaneous emission regime of light-matter interaction**. After spontaneous emission (time  $t$ ) the energy is transferred to the battery (b) field :

$$\begin{aligned} \Delta\mathcal{E}_q &= \mathcal{E}_q(t) - \mathcal{E}_q(0) = 0 - \mathcal{E}_q(0) \\ &= -\hbar\omega_0\mu_b = -\hbar\omega_0 \sin^2\left(\frac{\theta}{2}\right), \end{aligned} \quad (4.11)$$

where we have the average photon-number  $\mu_b = \int \langle \hat{a}_b^\dagger(t)\hat{a}_b(t) \rangle dt$  and  $-\Delta\mathcal{E}_q = \Delta\mathcal{E}_b$ . In the transfer, the energy coherence is mapped onto the photon-number

basis of the battery field that reads :

$$|\Psi_b\rangle = \cos\left(\frac{\theta}{2}\right)|0\rangle + \sin\left(\frac{\theta}{2}\right)|1\rangle.$$

In such case **the work transferred to the battery is shown to be directly proportional to the energy coherence** (see Section 2.5.5) initially present in the qubit :

$$\mathcal{W}_{q,b} = \hbar\omega_0 s^2(0) = \hbar\omega_0 \sin^2\left(\frac{\theta}{2}\right) \cos^2\left(\frac{\theta}{2}\right), \quad (4.12)$$

where we rewrite  $\mathcal{W}$  as  $\mathcal{W}_{q,b}$  to highlight that work is transferred from the qubit to the field. **The heat is then given by the incoherent part of the spontaneously emitted field** and is obtained by considering the energy balance in a closed quantum system :

$$\mathcal{Q}_{q,b} = \Delta\mathcal{E}_b - \mathcal{W}_{q,b} = \hbar\omega_0 \left[ \sin^2\left(\frac{\theta}{2}\right) - \cos^2\left(\frac{\theta}{2}\right) \sin^2\left(\frac{\theta}{2}\right) \right]. \quad (4.13)$$

This result implies that as soon as the qubit contains energy coherence,  $s(0) \neq 0$ , the qubit can spontaneously transfer work to the electromagnetic field, reaching a maximum when the qubit contains maximum energy coherence  $s(0) = \cos(\theta/2) \sin(\theta/2) = 0.5$ . This limit is reached when the qubit is initially brought into a pure and equal superposition ( $\theta = \pi/2$ ) between the ground and excited state :

$$|\Psi_q\rangle = \frac{1}{\sqrt{2}}(|g\rangle + |e\rangle).$$

The authors expand on this result by considering the case where the qubit is in a general state described by the density matrix :

$$\rho(0) = p|-\theta\rangle\langle-\theta| + (1-p)|+\theta\rangle\langle+\theta| \quad (4.14)$$

with  $|+\theta\rangle = \cos(\theta/2)|g\rangle + \sin(\theta/2)|e\rangle$ ,  $|-\theta\rangle = -\cos(\theta/2)|e\rangle + \sin(\theta/2)|g\rangle$ , and  $p$  a parameter tuning the purity of the field, ranging from  $p = 0$ , a pure state, to a fully mixed state for  $p = 1/2$ . For such a general state, they predict that **a degradation in purity decreases the maximum achievable work exchange between the qubit and the battery**, see Fig. 4.7 where the work transfer  $\mathcal{W}$  (blue, dashed), and initial energy of the qubit  $\mathcal{E}(0)$  (green) are plotted as a function of pulse area of the driving field for different values of  $p$ . Also shown is the qubit's ergotropy  $\mathcal{W}(0)$  (red, dashed) which is the maximum energy one can extract from the system through unitary actions (133). We can see from Fig. 4.7 that for a fully mixed state with  $p = 1/2$ , the qubit does not **spontaneously** transfer work to the battery, all energy contained inside the qubit is of incoherent nature. In contrast, work transfer is optimized for  $p = 0$  and  $\theta = \pi/2$ , corresponding to maximum initial qubit coherence  $s(0) = 1/2$ .

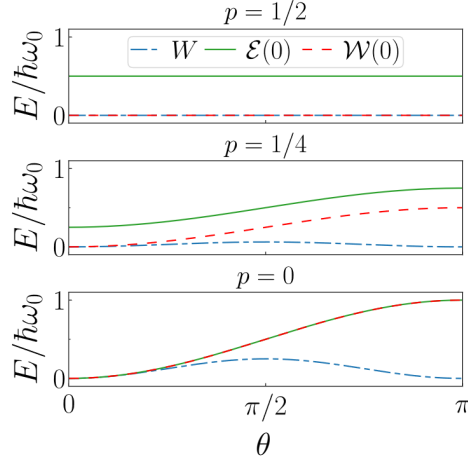


Figure 4.7 – **Impact of the qubit’s energy coherence on the work transfer.** Work transfer  $\mathcal{W}$  (blue, dashed) from a qubit to a battery field as a function of the pulse area  $\theta$  of the driving field. Also shown are the total energy  $\mathcal{E}(0)$  (green) and ergotropy  $\mathcal{W}(0)$  (red, dashed) transfer, where the ergotropy is defined as the maximum energy extractable through unitary actions. From Ref. (37).

The above theoretical studies, conducted in the group of Alexia Auffèves, were strongly inspired by the work of Loredó and Antón et al. (2019) where it was shown that upon resonant excitation of the QD-cavity system, the energy coherence  $s(0)$  is mapped onto the photon-number coherence of the spontaneously emitted photonic field, allowing for on-demand generation of photon-number superposition states with coherence in the photon-number basis with near-unity photon-number purity, see Section 2.5.5 and Ref. (83). In this PhD, we experimentally studied the energetics of spontaneous emission in a QD-cavity system, whereby we propose protocols to measure the work and heat in a closed quantum system. Moreover, we extend the theory to include scenarios where the qubit is subject to pure dephasing.

### 4.3 . Coherence-powered energy and work exchange during spontaneous emission

We experimentally study the energetic exchange during spontaneous emission with our QD-cavity platform described in Chapter 2 and test the previously described theory. From a quantum thermodynamics point of view, the qubit acts as a work provider, and the vacuum of the electromagnetic field as an empty quantum battery at the beginning of the process, see a sketch of the equivalent energy protocol in Fig. 4.8. Here the qubit is initially brought into an atomic state by a classical drive through coherent control, before it spontaneously decays and provides work to the battery.

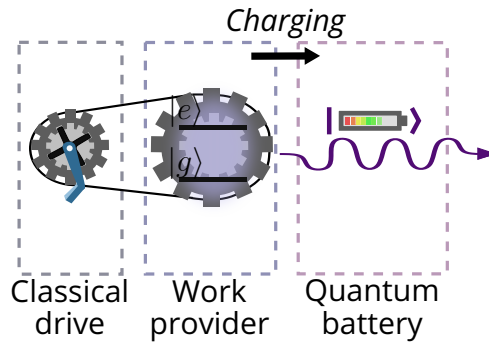


Figure 4.8 – **Quantum battery charging.** A sketch of the quantum battery charging protocol where a classical drive resonantly excites a two-level system, acting as a work provider. The qubit is coupled to the vacuum of the electromagnetic field, presented here as a battery, and transfers work to it through spontaneous emission, thereby charging the initially empty battery.

#### 4.3.1 . Protocol to measure the energetic transfers

At the beginning of this PhD work, we proposed an experimental protocol to measure heat and work exchanges between the qubit and the electromagnetic field during spontaneous emission. This protocol is inspired by work performed in our group in 2019 (83) where the authors performed self-homodyne measurements with two consecutively emitted photonic wavepackets temporally overlapped at a beam splitter, and extract the maximum visibility of interference  $v_{\max}$  as a function of pulse area  $\theta$  (see Section 2.5.5). Similarly, here we resonantly excite the qubit with a pulsed laser and interfere successively emitted battery fields at a beam splitter in a Mach-Zehnder interferometer, Fig. 4.9. The visibility of interference is given by

$$v = \frac{\mu_3 - \mu_4}{\mu_3 + \mu_4}, \quad (4.15)$$

with average photon numbers  $\mu_i = \int \langle \hat{a}_i^\dagger(t) \hat{a}_i(t) \rangle dt$  in output mode  $i$  of a 50 : 50 beam splitter.

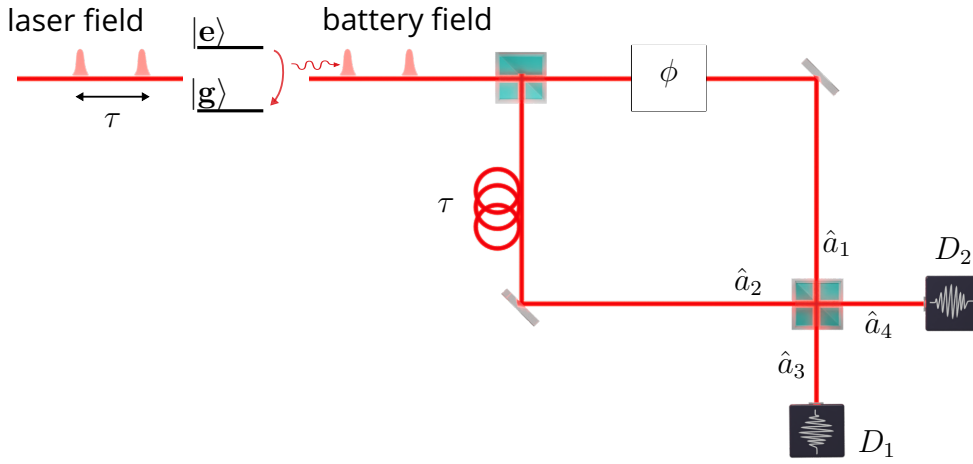


Figure 4.9 – **Experimental protocol to measure energetic exchanges.** A two-level system is resonantly excited by a pulsed laser field with repetition rate  $\tau^{-1}$ . The qubit spontaneously decays, thereby emitting a photonic field (the battery field), containing photon-number coherence. The battery field is input to an unbalanced Mach-Zehnder interferometer where two consecutively emitted battery fields, with a relative phase  $\phi$  caused by path differences, interfere at a second 50 : 50 beam splitter. By measuring the output intensities with two detectors  $D_1$  and  $D_2$ , we can extract the amount of photon-number coherence present in the battery field.

The beam splitter equation relating the output modes to the input modes, are given by :

$$\begin{pmatrix} \hat{a}_3(t) \\ \hat{a}_4(t) \end{pmatrix} = \frac{1}{\sqrt{2}} \begin{pmatrix} 1 & 1 \\ -1 & 1 \end{pmatrix} \begin{pmatrix} \hat{a}_1(t) \\ \hat{a}_2(t) \end{pmatrix}. \quad (4.16)$$

Two wavepackets taking different paths in the Mach-Zehnder interferometer will experience different path lengths. As a result, the two wavepackets arriving in input modes  $\hat{a}_1$  and  $\hat{a}_2$  of the final beam splitter **obtain a relative phase  $\phi$  in the Fock state basis**. This phase changes with differences in optical paths, and leads to constructive and destructive interference at output ports  $\hat{a}_3$  and  $\hat{a}_4$  of the final beam splitter. We can absorb the phase arising from the MZI interferometer into Eq. 4.16 to relate the input and output ports of the final beam splitter in this specific setup :

$$\begin{pmatrix} \hat{a}_3(t) \\ \hat{a}_4(t) \end{pmatrix} = \frac{1}{\sqrt{2}} \begin{pmatrix} 1 & e^{i\phi} \\ -e^{i\phi} & 1 \end{pmatrix} \begin{pmatrix} \hat{a}_1(t) \\ \hat{a}_2(t) \end{pmatrix}. \quad (4.17)$$

This protocol corresponds to a self-homodyne measurement where we interfere a battery field with a copy of itself. In this first part, we **assume that the qubit**

is not subject to any source of decoherence. Thus we have  $\hat{a}_1(t)$  and  $\hat{a}_2(t)$  corresponding to battery fields  $\hat{a}_{b1}(t)$  and  $\hat{a}_{b2}(t)$ , respectively, where the two input fields are identical except for the relative phase  $\phi$ . Evaluating Eq. 4.15 for these input states, we find the numerator can be written in terms of input modes :

$$\begin{aligned} 2\text{Re} \left[ \int dt \langle e^{i\phi} \hat{a}_{b1}^\dagger(t) \hat{a}_{b2}(t) \rangle \right] &= 2\text{Re} \left[ \int dt e^{i\phi} \langle \hat{a}_{b1}^\dagger(t) \hat{a}_{b2}(t) \rangle \right] \\ &= 2 \cos(\phi) \int dt |\langle \hat{a}_b(t) \rangle|^2 \end{aligned} \quad (4.18)$$

considering that  $\langle \hat{a}_{b1} \rangle = \langle \hat{a}_{b2} \rangle = \langle \hat{a}_b \rangle$ . Since the input intensities are equal,  $\mu_1 = \mu_2 = \mu_b$ , and considering energy conservation rules,  $\mu_1 + \mu_2 = \mu_3 + \mu_4$ , Eq. 4.15 becomes

$$v = \cos(\phi) \frac{\int dt |\langle \hat{a}_b(t) \rangle|^2}{\mu_b} \quad (4.19)$$

Considering Eq. 4.10, Eq. 4.12, and  $2\mu_b = 2\mathcal{E}_b/\hbar\omega_0$ , we find :

$$v = \cos(\phi) \frac{\mathcal{W}_{q,b}}{\mathcal{E}_b} = \cos(\phi) \cos^2\left(\frac{\theta}{2}\right). \quad (4.20)$$

We see that the visibility of interference is equal to the fraction of energy corresponding to work transferred from the qubit to the battery. We can thus simply access the work transfer efficiency  $\eta = \mathcal{W}_{q,b}/\mathcal{E}_b$  from the visibility. The visibility also depends on the cosine of the interferometer phase  $\phi$ , which means that we will have maximum (minimum) work transfer efficiency for  $\phi = 0(\pi)$ . Thus, **measuring the maximum visibility of interference  $v_{\max}$  for a given pulse area  $\theta$  allows to quantify the energetic exchanges between a qubit and the vacuum of the electromagnetic field.**

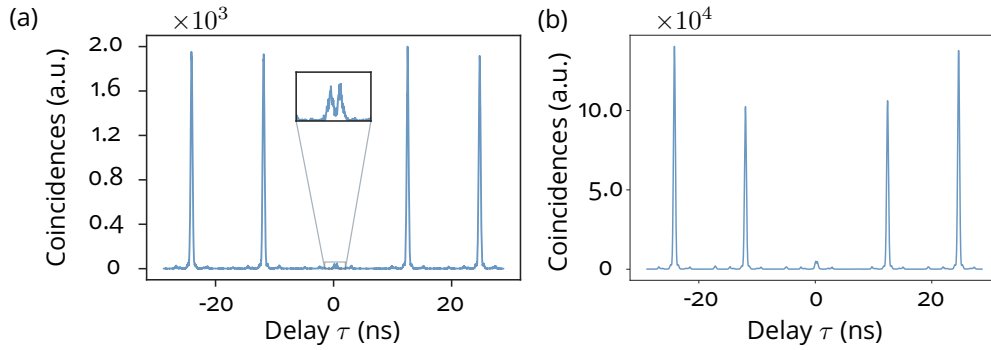


Figure 4.10 – **Quantum battery performance.** (a) The single-photon purity, and (b) single-photon indistinguishability measurements with a battery field. For  $\theta = \pi$  at 5K normalized to the average amplitude of large delay peaks. We extract values of (a)  $g^{(2)} = (2.84 \pm 0.08)\%$  and (b)  $M_s = (92.6 \pm 0.1)\%$ .

We first implement this protocol with our InGaAs QD-cavity system inside a cryostat kept at 5K. At this temperature, **our emitter acts close to the ideal two-level system**, which can produce photon-number superpositions with high single-photon purity and near-unity indistinguishability (13; 83). For our measurements we use a neutral QD, exciton, as a work provider which we drive resonantly with a pulsed laser (see Section 2.5.2). Coincidence measurements for  $\theta = \pi$  reveal a high single-photon purity of  $g^{(2)} = (2.84 \pm 0.08)\%$ , allowing us to neglect two-photon emission from the QD, and a single-photon indistinguishability of  $M_s = (92.6 \pm 0.1)\%$ , see Fig. 4.10. These high values allow us to consider that our qubit system is well isolated from its solid state environment and thus will be approximated as a **closed quantum system coupled to the electromagnetic field** in the first part of our study.

The experimental setup is shown in Fig. 4.11, where we resonantly excite our qubit with a Ti :Sapphire pulsed laser at 81 MHz repetition rate with a pulse duration of 7 ps which is focused onto the QD with a lens  $L$ , bringing the qubit into a pure quantum superposition state depending on the pulse area  $\theta$ . We separate the spontaneously emitted battery field from the excitation laser with a cross-polarization configuration at the polarizing beam splitter (PBS). The remaining battery field is then sent to a Mach-Zehnder interferometer where we perform self-homodyne measurements. A beam splitter and a temporal delay ( $\tau = \tau_p$ ) matched to the repetition rate of the laser are placed in the optical setup to temporally overlap two consecutively emitted battery fields at the final beam splitter  $BS_2$ . Here the coherent parts of the field will interfere constructively or destructively depending on the relative phase  $\phi$  between the two fields. Two superconducting nanowire single photon detectors (SNSPDs),  $D_1, D_2$  at the output of  $BS_2$  record

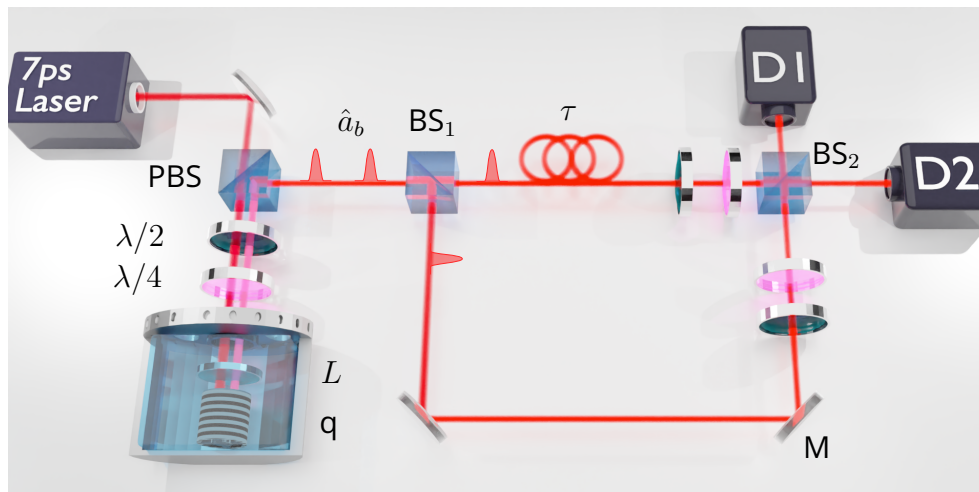


Figure 4.11 – **Experimental setup to study energetic exchanges between a qubit and light fields.** The qubit (q) is placed inside a cryostat operating at 5 – 20 K. We resonantly excite our qubit, generating a quantum battery field. A cross-polarization configuration (PBS,  $\lambda/2$ ,  $\lambda/4$ ) suppresses the reflected driving field. The battery field enters a Mach-Zehnder interferometer where we perform self-homodyne measurements with two consecutively emitted battery fields  $\hat{a}_b$ . They are temporally overlapped at the  $BS_2$  by inserting a delay line  $\tau$  matched to the repetition rate of the laser. Two SNSPDs  $D_1$  and  $D_2$  at the output of  $BS_2$  register the photon clicks as a function of time.

the single counts over a period of up to 20 minutes, allowing us to extract the visibility of interference and thus access the photon-number coherence.

Initial measurements of the emission intensity as a function of pulse area of the driving laser show the onset of Rabi oscillations (Fig. 4.12) demonstrating **coherent control over the atomic state and transfer of energy** to the battery field through spontaneous emission. This measurement allows us to access the energy transferred to the battery field :  $\mathcal{E}_b = \hbar\omega_0\mu_b$ , where we take  $\mu_b \propto I_b$  as the sum of intensities measured by the two detectors in Fig. 4.11 :  $I_b = I_1 + I_2$ .

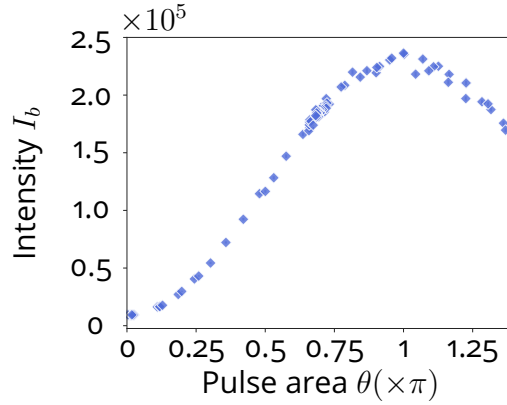


Figure 4.12 – **Rabi oscillations.** The measured emission intensity from a resonantly driven QD-cavity system as a function of pulse area  $\theta$ .

The **single counts show phase-dependent anti-correlated oscillations** whose amplitudes grow with decreasing pulse area. An example data set for  $\theta = 0.20\pi$  is shown in Fig. 4.13. For each pulse area  $\theta$  we extract the maximum visibility of interference  $v_{\max}$  from the normalized intensity time traces in Fig. 4.13(a). Such time traces are normalized to compensate for differences in detection efficiencies : we normalize each point in time  $I_1(t_i)$  (or  $I_2(t_i)$ ) by the sum of the two detectors :  $I_1(t_i) + I_2(t_i)$ . From these normalized intensity traces we can compute the visibility time trace in Fig. 4.13(b) according to Eq. 4.15 with  $I_1(t_i) \propto \mu_3$  and  $I_2(t_i) \propto \mu_4$ .

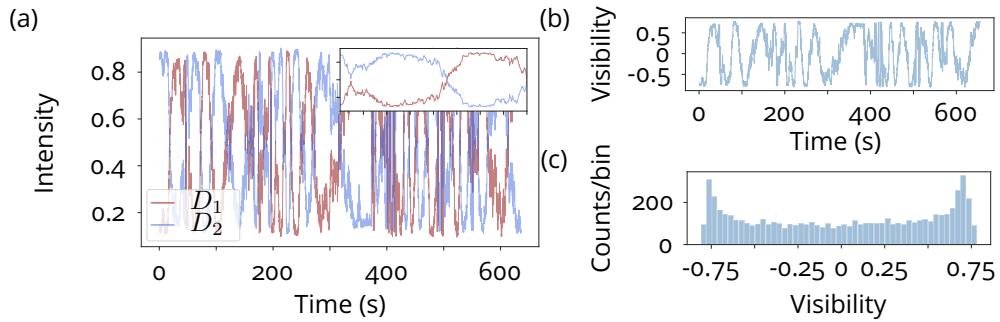


Figure 4.13 – **Extracting visibility.** Example data set for self-homodyne measurements performed at 5K for  $\theta = 0.21\pi$ . (a) QD emission intensity recorded over the duration of 20 minutes, where two signals  $I_1(t)$  and  $I_2(t)$ , measured by detectors  $D_1$  and  $D_2$ , respectively, show phase-dependent anticorrelated oscillations (see inset). (b) The visibility time trace corresponding to measurement in (a). (c) A histogram of the visibility values measured over time. The visibility distribution follows an arccos dependency since  $v \propto \cos(\phi)$ .

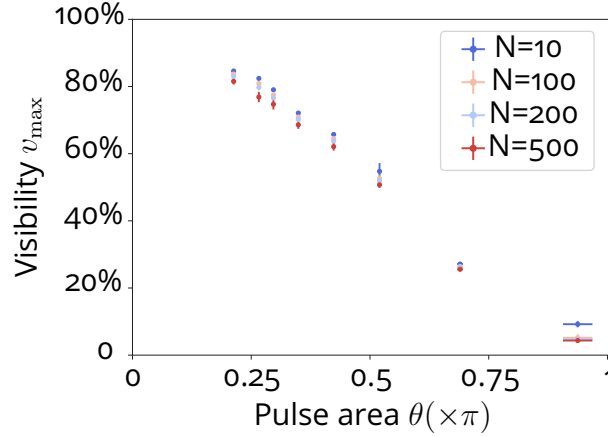


Figure 4.14 – **Standard deviation in visibility.** The average visibility of interference  $v_{\max}$  as a function of pulse area  $\theta$ , where the mean is taken by considering the  $N$  highest and  $N$  lowest visibilities, with  $N \in [10, 100, 200, 500]$ .

From the visibility time trace in Fig. 4.13(b) we construct a histogram, revealing the visibility distribution over the duration of the measurement, Fig. 4.13(c). This distribution shows a typical arccos dependence expected from the relation between the visibility and the optical phase  $\phi$  :  $\phi(t) = \arccos(v(t)/v_{\max})$  (see Eq. 4.20). This arccos distribution reveals that the phase  $\phi$  fully explores the phase space  $\phi \in [0, \pi]$ . We extract  $v_{\max}$  from the histograms by taking the average of the absolute value of the  $N$  highest, and  $N$  lowest visibility data points. We choose here a value of  $N = 100$  as we want to capture the edges of the visibility histogram in Fig. 4.13(c), but do not wish to underestimate or overestimate  $v_{\max}$  : if  $N$  is too small random counting error dominates, but if  $N$  is too high we underestimate the visibility by including lower visibility values. A study on  $v_{\max}$  as a function of  $N$  shows that for  $N \in [100, 200, 500]$  there is little variation in  $v_{\max}$ , see Fig. 4.14 where we also plot  $N = 10$ , but discard it as this value overestimates the visibility. The error in  $v_{\max}$  is determined by the variation and by the standard counting error. For the data set shown in Fig. 4.13 we obtain a visibility of  $0.775 \pm 0.016$ .

### 4.3.2 . Energetic exchanges for a pure battery field

Following the procedure described in Sec. 4.3.1 we extract the visibility of interference  $v_{\max}$  as a function of the driving pulse area  $\theta$ , see Fig. 4.15(a). We can see that the visibility increases with decreasing pulse area, as expected (see Section 2.5.5). The data is well accounted for by the theory without considering any decoherence of the qubit, as can be seen by comparing the data to the fitted curve :  $v_{\max} = \cos^2(\theta/2)$  from Eq. 4.20.

From the measured Rabi oscillations in Fig. 4.12 we extract **the total energy transferred from the qubit to the battery field** normalized to the

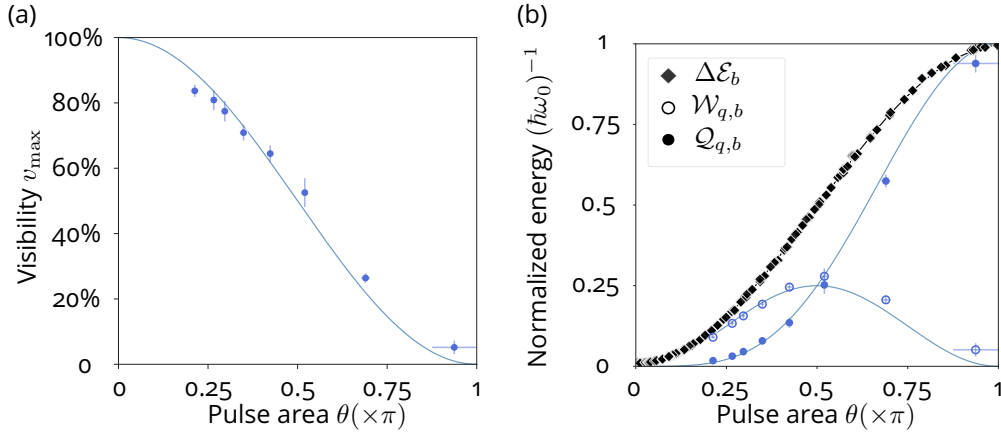


Figure 4.15 – **Quantum battery charging.**(a) Measured visibility of interference  $v_{\max}$  as a function of  $\theta$  from self-homodyne measurements with the battery field. (b) The total energy  $\Delta\mathcal{E}_b$ , work  $\mathcal{W}_{q,b}$ , and heat  $\mathcal{Q}_{q,b}$  transferred from the qubit  $q$  to the battery  $b$  upon spontaneous excitation. All theoretical curves are fitted to the data, assuming no decoherence.

transition energy of the qubit, Fig. 4.15(b) (diamonds). We fit the data to  $\Delta\mathcal{E}_b/(\hbar\omega_0) = \mu_b = \sin^2(\theta/2)$  (black curve). The visibility measurements combined with the Rabi oscillation fit allow us to deduce the thermodynamic quantities plotted in Fig. 4.15(b). We obtain the work and heat charged into the battery field :  $\mathcal{W}_{q,b}/(\hbar\omega_0) = \Delta\mathcal{E}_b \times v_{\max}$  (open circles) and  $\mathcal{Q}_{q,b}/(\hbar\omega_0) = \Delta\mathcal{E}_b \times (1 - v_{\max})$  (solid circles), respectively.

From the curves in Fig. 4.15(b) we see that, as predicted in Ref. (37), the fraction of work in the energy transfer is highest for low pulse areas. This high efficiency can be understood by considering that **all the emission originates from the qubit dipole only in the low power limit** : no entanglement takes place between the qubit and the electromagnetic field. Moreover, for small  $\theta$  the quantum battery field's amplitude is close to that of a coherent field, which has unity first-order coherence  $c^{(1)} = 1$ , truncated for photon number components above 1 :  $|\alpha\rangle \approx e^{-|\alpha|^2/2}(|0\rangle + \alpha|1\rangle)$ . Work transfer from the qubit to the vacuum is therefore most efficient in this limit.

As we move towards higher values for  $\theta$  Fig. 4.15(b), the work contribution of the battery field drops. We can understand this effect by considering light-matter interaction between the qubit and the electromagnetic field : as we build qubit population with increasing  $\theta$ , entanglement takes place between the qubit and the electromagnetic field, lasting until the end of the spontaneous emission process. The resulting **quantum correlations during the emission process reduce the work transfer** to the battery field, which in the limit of  $\theta \rightarrow \pi$  actually

results in net zero work transfer. In this limit, the qubit acts as a single-photon source that only spontaneously emits energy in the form of heat. At 5K we see that maximum work transfer is highest at  $\theta = \pi/2$  as predicted, a situation where the emitted field is in an equal superposition between zero and one photon Fock state and therefore contains highest possible first-order coherence  $c^{(1)} \approx 1/2$ .

Even though the work transfer for a fully inverted qubit acting as a perfect single-photon source is zero, Ref. (37; 38) predicts that **one can still extract work if the battery is not in the vacuum state**. Indeed, in Ref. (37) the authors predict that more work can be exchanged with growing energy contained in the electromagnetic field at the beginning of the interaction. This work transfer scenario corresponds to the regime of stimulated emission.

### 4.3.3 . Energetic exchanges in presence of decoherence

In a second step of this study, we went **beyond the theoretical framework** introduced and studied in Sec. 4.2 by deliberately introducing decoherence to the qubit, which we achieve by increasing its environment temperature. As we raise the temperature the QD couples to acoustic phonons with growing strength (134–136). As a result, the zero-phonon line starts to broaden with pure dephasing, and phonon sidebands appear where phonon-assisted emission can occur. These phonons affect the indistinguishability of generated photons by producing frequency-detuned photons in the sideband through interaction with the QD, and by dephasing of the zero phonon line (137). In 2019, however, Thomas et al. (40) demonstrated that the phonon sideband emission in our QD-cavity system is strongly suppressed by the Purcell effect : the cavity accelerates the zero-phonon line emission by many orders of magnitude more than the phonon sideband emission. Therefore, we can neglect the effect of phonon sidebands, and can assume that the **qubit is subject to pure dephasing**, and does not exchange energy with the phonon bath. We will provide in Sec. 4.3.4 clear experimental proof that the QD does not exchange energy with the phonon bath during the excitation and emission process since we show that the amount of energy emitted in the field at higher temperature remains unchanged with respect to the emitted energy at 5K.

Although the QD is observed not to exchange energy with the phonon bath during spontaneous emission, it does undergo pure dephasing. To evidence this, we carry out an initial measurement to investigate the effect of increasing temperature on photon indistinguishability. We heat up the environment by changing the target temperature of the cryostation. As we increase the environment temperature of the qubit, the QD red shifts caused by a change in band gap energy. For each probed temperature we excite the qubit with a  $\pi$ -pulse, and apply a suitable voltage to maintain qubit-cavity resonance through Stark shift. We perform Hong-Ou-Mandel measurements with the generated single-photon field to extract

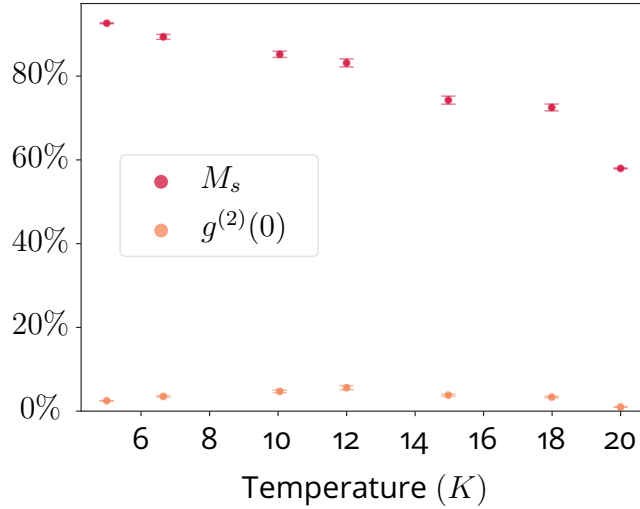


Figure 4.16 – **Single-photon purity  $g^{(2)}$  and indistinguishability  $M_s$  versus temperature.** As we increase the qubit environment temperature, the measured single-photon indistinguishability  $M_s$  decreases. The indistinguishability is corrected for an imperfect single-photon purity. Within the range 5–20 K we maintain QD-cavity resonance through Stark shift using a voltage source.

the visibility of interference  $V_{\text{HOM}}$  (using side peak normalization since  $\theta = \pi$ ). Subsequent Hanbury-Brown and Twiss measurements with the single-photon field (blocking one arm of the HOM interferometer) allow us to correct for a non-zero multiphonon component (81). Fig. 4.16 shows the single-photon indistinguishability  $M_s$  as function of temperature. We see that the corrected wavepacket indistinguishability decreases from  $M_s(\pi) = (92.6 \pm 0.1)\%$  at 5 K to  $M_s(\pi) = (58.0 \pm 0.1)\%$  at 20 K, while still maintaining QD-cavity resonance. Note that **we limit our study to  $\approx 20$  K** since above this temperature we are not able to keep the QD in resonance with the cavity.

At 20 K the qubit is prone to pure dephasing effects, but does not exchange energy with the phonon bath. Moreover, the phonon bath does not couple to the electromagnetic field. As such, the phonon bath does not exchange energy with the two systems and we can **consider the bipartite subsystem as an energetically closed quantum system**, allowing us to adopt the same framework as in Sec. 4.3.2 where work and heat transferred between qubit and field are equal and opposite, see full proof developed by the theory team in Appendix 9.3.1. However, pure dephasing degrades the performance of the qubit which is reflected in the single-photon indistinguishability at 20 K. We can thus no longer describe our battery field as a pure state, but rather have to consider a mixed state described by the

density matrix operator :

$$\hat{\rho}_b = \cos^2(\theta/2)\hat{\rho}_0 + \sin^2(\theta/2)\hat{\rho}_1 + \cos(\theta/2)\sin(\theta/2)(\hat{\rho}_{01} + \hat{\rho}_{10}), \quad (4.21)$$

where the subscripts 0,1 indicate the vacuum or one-photon component of the battery field. For this battery field, we can write the single-photon indistinguishability, or purity in the temporal domain, in terms of the density matrix operator as  $M_s = \text{Tr}[\hat{\rho}_1^2]$ . Considering the case where the qubit is subject to pure dephasing we have :

$$M_s = \frac{\gamma}{\gamma + 2\gamma^*}, \quad (4.22)$$

where  $\gamma + 2\gamma^* = 2/T_2$ , with  $T_2$  the total decoherence rate creating the homogeneous broadening of the emission line width. Moreover, if there is a slow fluctuation in the QD solid state environment (spectral diffusion), the emission energy of the QD varies with  $\delta\omega$ . In this case, the indistinguishability is given by :

$$M_s(\delta\omega) = \frac{\gamma(\gamma + 2\gamma^*)}{(\gamma + 2\gamma^*)^2 + \delta\omega^2}, \quad (4.23)$$

see Appendix 8.3.

In contrast to the battery field at 5 K described in Sec. 4.3, the first-order coherence between the zero and one-photon component is now reduced. The theoretical framework is extended to capture this reduction by introducing the parameter (Appendix 8.1) :

$$\mathcal{C} = \text{Tr}[\hat{\rho}_{01}\hat{\rho}_{10}]. \quad (4.24)$$

In terms of the density matrix describing the state given in Eq. 4.21, the reduction in quantum coherence is given by the off-diagonal terms (see the general density matrix for a state with up to one-photon component in Section 2.5.5).

Evaluating the definition for work transfer in spontaneous emission Eq. 4.10 on the general battery state in Eq. 4.21 results in the equations for energetic transfers :

$$\mathcal{W}_{q,b} = \hbar\omega_0 \cos^2\left(\frac{\theta}{2}\right) \sin^2\left(\frac{\theta}{2}\right) \mathcal{C} \quad (4.25)$$

$$\mathcal{Q}_{q,b} = \Delta\mathcal{E}_b - \mathcal{W}_{q,b} = \hbar\omega_0 \left[ \sin^2\left(\frac{\theta}{2}\right) - \cos^2\left(\frac{\theta}{2}\right) \sin^2\left(\frac{\theta}{2}\right) \mathcal{C} \right]. \quad (4.26)$$

The maximum visibility of interference is now reduced to :  $v_{\max} = \mathcal{C} \cos^2(\theta/2)$ . As shown in Appendix 8.3, in the presence of pure dephasing, **the reduction in quantum coherence is related to the temporal purity** according to :  $\mathcal{C} = M_s$ , posing an important bound on the maximum coherence present in the field.

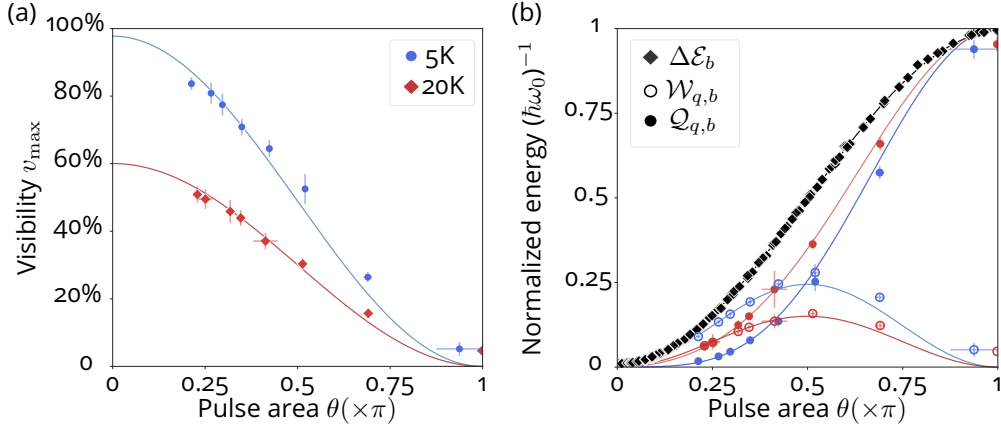


Figure 4.17 – **Quantum battery charging.**(a) Measured visibility of interference  $v_{\max}$  as a function of  $\theta$  from self-homodyne measurements with the battery field. (b) The total energy  $\Delta\mathcal{E}_b$ , work  $\mathcal{W}_{q,b}$ , and heat  $Q_{q,b}$  transferred from the qubit (q) to the battery (b) upon spontaneous excitation.

#### 4.3.4 . Measuring the impact of decoherence

We repeat the same measurements as for the 5K case described in Sec. 4.3.1 and extract the visibility as function of pulse area. We show the results of the self-homodyne measurements at both temperatures in Fig. 4.17(a), where we see that the work transfer efficiency is significantly decreased with higher temperature. We fit both data sets to  $v_{\max} = C \cos^2(\theta/2)$ , taking into account the possible reduction in quantum coherence. We extract  $C(5 \text{ K}) = 0.975 \pm 0.007$ , showing indeed that the battery field at 5 K is close to a pure state, and  $C(20 \text{ K}) = 0.594 \pm 0.007$ , revealing a mixed state.

The clean proof that the QD does no exchange energy with the phonon bath at 20K is found by comparing the Rabi oscillation curves at both 5K and 20K. Fig. 4.18(a) shows the raw measured QD intensity as a function of pulse area where we see that the maximum intensity ( $\theta = \pi$ ) remains similar when increasing temperature. From these raw intensities we can **estimate the occupation probability of the excited state**  $p_1$  as a function of pulse area for the two different temperatures. We estimate  $p_1$  for  $\theta = \pi$  through the measured visibility of interference according to

$$p_1(\pi) = 1 - \frac{v_{\max}(\pi)}{C}, \quad (4.27)$$

see Section 3.2, and where we use the values for  $C$  extracted from the fits in Fig. 4.17(a) at 5 K and 20 K. We scale the intensity measurements in Fig. 4.18(a) for 5 K and 20 K by the obtained values for  $p_1(\pi)$  :  $0.95 \pm 0.19$  and  $0.92 \pm 0.02$ , respectively, resulting in Fig. 4.18(b). We can see that despite the introduced decoherence, the qubit operating at 20K still reaches an occupation close to unity

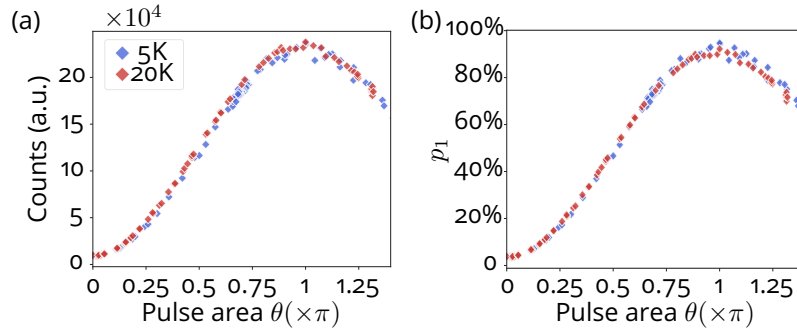


Figure 4.18 – **Probability of population inversion as a function of pulse area.** (a) The emission intensity as a function of pulse area for a resonantly driven qubit at 5 K (blue) and 20 K (red). (b) The corresponding excited state probability as a function of pulse area.

at  $\pi$  pulse and the total energy transferred to the electromagnetic field remains unchanged.

From these measurements and the Rabi oscillation data, we can deduce the work and heat transport between the qubit and the battery field at 20 K, red circles (open and solid, resp.) in Fig. 4.17(b). The maximum work transfer is still found at pulse areas close to  $\theta = \pi/2$ , but we can see that **the reduction in quantum coherence at 20 K significantly impacts the absolute amount of work transfer**, which reduces from  $\mathcal{W}_{q,b}/\hbar\omega_0 = (27.9 \pm 1.2)\%$  at 5 K to  $\mathcal{W}_{q,b}/\hbar\omega_0 = (15.8 \pm 0.6)\%$  at 20 K. In contrast, the proportion of heat exchanged has increased with temperature. This change in the nature of energy transfer is in agreement with the intuition that **decoherence reduces the effective unitary interaction between the qubit and the field**. Again, we fit both data sets using the values of  $\mathcal{C}$  obtained from the visibility measurements in Fig. 4.17(a) and see good agreement between the data and the theoretical curves.

Finally, we can also test the theoretical bound on  $\mathcal{C}$  mentioned in section 4.3.3 by measuring the mean wavepacket indistinguishability  $M_s$  of our battery fields at 5 K and 20 K. From Fig. 4.16 we know the single-photon indistinguishability at 5 K and 20 K :  $M_s(5\text{ K}) = (92.6 \pm 0.1)\%$  and  $M_s(20\text{ K}) = (58.0 \pm 1.0)\%$ . These values saturate the theoretical predicted bound  $\mathcal{C} \approx M_s$ , demonstrating maximum achievable work transfer at both temperatures.

### Conclusion Section 4.3 – Charging a quantum battery

In this section we proposed a protocol based on homodyne measurements to measure the work  $\mathcal{W}_{q,b}$  and heat  $\mathcal{Q}_{q,b}$  transfers between a qubit and the electromagnetic field in spontaneous emission. We implemented this protocol and measured for the first time these energetic quantities for a two-level system coupled to the vacuum of the electromagnetic field, energetically equivalent to charging a quantum battery. Our observations confirm theoretical predictions, where the amount of work transfer is predicted to be proportional to the initial quantum coherence present in the qubit. We pushed the framework further by introducing pure dephasing to our qubit system, both experimentally and theoretically, emphasizing the special role played by quantum coherence on the energetic exchanges between a two-level system and the vacuum of the electromagnetic field.

#### 4.4 . Coherence-powered energy and work exchange between light fields

In the last part of this study, we proposed to study the possibility to **discharge the battery field into a classical field**. To discharge the battery field we propose to interfere it with a classical field on a beam splitter. A sketch of the full protocol is given in Fig. 4.19. The use of a coherent field as a receiver illustrates the whole concept of the battery field : a laser (classical drive) gives energy to the qubit that in turn transfers the energy to the battery field. The battery is subsequently discharged towards a similar classical coherent field.

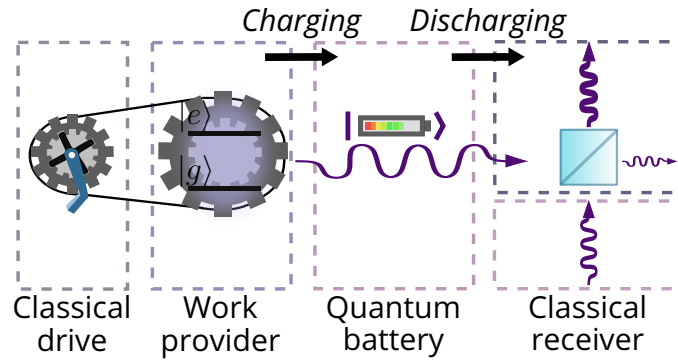


Figure 4.19 – **Charging and discharging a quantum battery.** In a two-step protocol we measure the energetic transfers between a work provider (resonantly driven by a classical drive) and the vacuum of the electromagnetic field (initially empty quantum battery), and between two light fields : the charged quantum battery field and a classical receiver interfering at a 50 : 50 beam splitter. The two steps in the protocol are equivalent to charging and discharging of a battery.

##### 4.4.1 . Theory : Energy transfers in quantum battery discharge

This discharging step is conceptually different from the charging step, and therefore required the development of a new theoretical framework, led by our colleagues at Institute Néel and Quandela - Alexia Auffèves, Maria Maffei, and Stephen Wein.

We consider the beam splitter in Fig. 4.20 where we now have two different input fields that we set to show equal intensities : the coherent field (c) in input port  $\hat{a}_1(t) = \hat{a}_c^{(in)}(t)$  and the battery field (b) in input port  $\hat{a}_2(t) = \hat{a}_b^{(in)}(t)$ . We define the discharged battery field as the field exiting through output port 4 :  $\hat{a}_4(t)$ . The energy received by the classical receiver in this output port is then given by (see Appendix 9.1) :

$$\Delta\mathcal{E}_c = \hbar\omega_0 \cos\left(\frac{\theta}{2}\right) \sin^2\left(\frac{\theta}{2}\right) C_{b,c} = -\Delta\mathcal{E}_b, \quad (4.28)$$

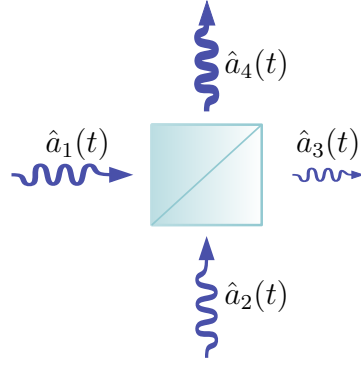


Figure 4.20 – **Homodyne interference at a 50 : 50 beam splitter.** Two input fields  $\hat{a}_1(t)$  and  $\hat{a}_2(t)$  interfere and exchange energy at a beam splitter and exit the beam splitter in output ports  $\hat{a}_3(t)$  and  $\hat{a}_4(t)$ .

where we see that an amount of the battery's energy is transferred to the classical field. **The amount of energy transferred to the classical field is limited by the parameter  $\mathcal{C}_{b,c}$ , a parameter which captures simultaneously the classical and quantum coherence exchanged in the process.** In the case of a qubit subject to pure dephasing, this parameter  $\mathcal{C}_{b,c}$  is equal to the mean wavepacket overlap between the battery field and the classical field :  $M_{b,c}$ . For a battery field and classical field with equal decay rate,  $\gamma_b = \gamma_c = \gamma$ , the mean wavepacket overlap is given by :

$$M_{b,c} = \frac{\gamma}{\gamma + \gamma^*}, \quad (4.29)$$

see Appendix 9.3.2. This expression is identical to the expression found for  $M_s$  except for a factor 2 in front of  $\gamma^*$ , which disappears when one of the two fields, the coherent field, is not subject to pure dephasing.

The visibility of interference  $v_{\max}$  is given by :

$$v_{\max} = \cos\left(\frac{\theta}{2}\right) \mathcal{C}_{b,c}, \quad (4.30)$$

see Appendix 9.2. Hence, measuring the maximum visibility of interference in homodyne-type measurements with a classical receiver and a battery field, allows us to determine the total energy transferred from the battery to the receiver in the process according to :

$$\Delta\mathcal{E}_c = v_{\max} \times \mathcal{E}_b^{(in)}. \quad (4.31)$$

We can split the energy exchanged in Eq. 4.28 into a work and heat contribution, similarly to the charging step :

$$\Delta\mathcal{E}_c = \mathcal{W}_{b,c} + \mathcal{Q}_{b,c}, \quad (4.32)$$

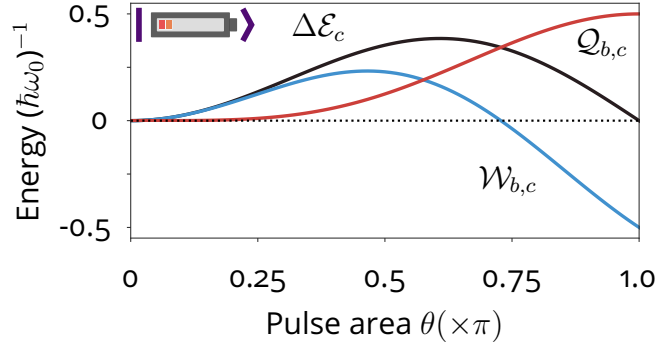


Figure 4.21 – **Theoretical predictions on energy exchange between two coupled light fields.** The predicted total energy transfer  $\Delta\mathcal{E}_c$ , the work  $\mathcal{W}_{b,c}$  and heat  $\mathcal{Q}_{b,c}$  from a pure battery field to a classical field as a function of pulse area  $\theta$  in the discharging step.

where the work component is equal to the coherent part of the field and the heat is equal to the incoherent part. Following the analysis method introduced in Refs. (38; 122; 127–129), it can be shown that

$$\mathcal{W}_{b,c} = \hbar\omega_0 \sin^2\left(\frac{\theta}{2}\right) \left[ \cos\left(\frac{\theta}{2}\right) \mathcal{C}_{b,c} + \frac{1}{2} \left( \cos^2\left(\frac{\theta}{2}\right) \mathcal{C} - 1 \right) \right], \quad (4.33)$$

see Appendix 9.1. Combining this expression for work with the energy balance in Eq. 4.32 we obtain the heat transfer in discharge :

$$\mathcal{Q}_{b,c} = \frac{1}{2} \hbar\omega_0 \sin^2\left(\frac{\theta}{2}\right) \left( 1 - \cos^2\left(\frac{\theta}{2}\right) \mathcal{C} \right) = \mathcal{Q}_{q,b}/2, \quad (4.34)$$

which, remarkably, is equal to half of the energy initially transferred from the qubit to the battery field in the charging process, see Eq. 4.26.

Fig. 4.21 shows the expected work, heat and total energy transferred to the classical field for a pure battery state. In the limit of  $\theta \rightarrow 0$  we expect the most efficient work discharge. In this limit, when intensities of both fields are matched, the battery field and the coherent field have the highest overlap, as explained in Sec. 4.3.2. Furthermore we can see that we expect most energy transfer  $\Delta\mathcal{E}_c$  for  $\pi/2 \leq \theta \leq \pi$ , resulting from an interplay of quantum coherence and classical coherence : the battery field has maximum quantum coherence  $\mathcal{C}$  for  $\theta = \pi/2$ , whereas the normalization condition  $\mathcal{E}_b^{(in)} = \mathcal{E}_c^{(in)} = \hbar\omega_0 \sin^2(\theta/2)$  results in an increase of classical coherence of the coherent field as  $\theta \rightarrow \pi$ . Another interesting feature arises at high values for  $\theta$ , where the work transfer becomes negative. This negative work flow indicates an **unexpected transfer of work from the classical receiver to the quantum battery** and reaches its minimum value for  $\theta = \pi$ , where it balances out with the positive maximal heat flow resulting in a

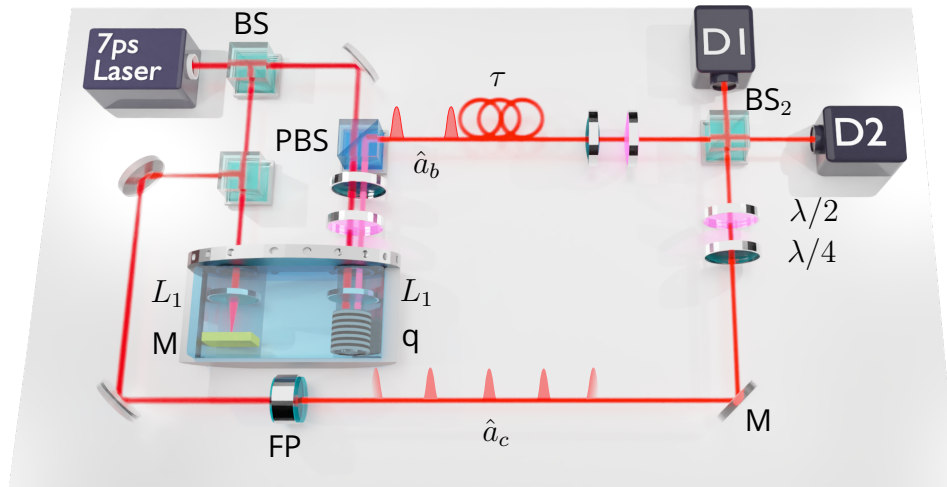


Figure 4.22 – **Experimental setup to study energetic transfers between light fields.** A 7ps pulsed laser is split into two paths : one excitation path towards the qubit (q), and one path towards a mirror (M), both placed inside a cryostation. The qubit is resonantly excited and emits a battery field  $\hat{a}_b$ , which is sent towards a beam splitter  $BS_2$ . The laser field sent towards the mirror inside the cryostation is reflected and sent towards  $BS_2$ . Two Fabry-Pérot etalons (one depicted) and an inserted delay line in both paths ensure the temporal overlap and simultaneous arrival, respectively, of the laser field and the qubit at  $BS_2$ , where they interfere. Detectors  $D_1$  and  $D_2$  monitor the output ports of  $BS_2$ , registering the single counts.

zero net energy transfer.

#### 4.4.2 . Experimental implementation

Experimentally we adopt the setup given in Fig. 4.22 where we interfere the quantum battery field  $\hat{a}_b$  generated by the QD with a coherent field  $\hat{a}_c$  at the beam splitter  $BS_2$ . The classical receiver is derived from the laser driving the QD, and temporally shaped by two Fabry-Pérot (FP) etalons to ensure temporal mode matching between the classical field and the battery field. We align the etalons to the central wavelength of the QD by first sending the QD emission through the etalons in the path of the classical receiver. We center the etalons by adjusting their angle with respect to the light path, maximizing the QD signal at the output. Once we have maximized the transmission of the QD signal through the etalons we redirect the laser field into the etalon and send the QD emission to the homodyne set-up, thereby obtaining the setup in Fig. 4.22.

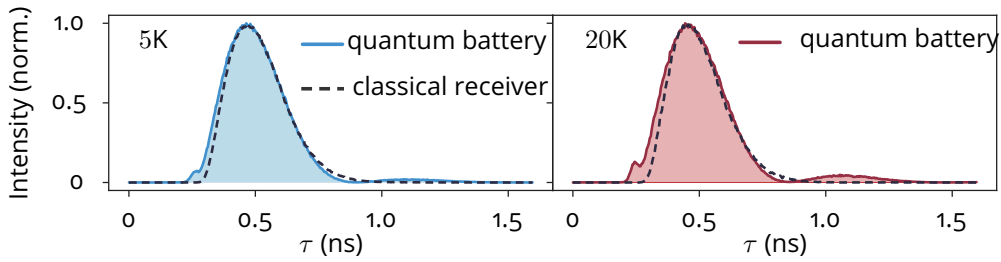


Figure 4.23 – **Temporal profiles battery fields and classical receiver.** We measure the temporal profile of our battery fields generated at 5 K and 20 K, and the temporal profile of the classical receiver (coherent laser) to ensure temporal mode matching.

With two detectors  $D_1, D_2$  at the output of the final beam splitter we can estimate the quality of temporal mode matching between the photonic field and the laser field. Fig. 4.23 shows the temporal profiles of the battery fields measured at 5 K and 20 K and the temporal profile of the classical receiver (dashed black). Because we measure the temporal profiles with the detectors  $D_1, D_2$  placed at the outputs of the final beam splitter in Fig. 4.22, this measurement also shows that by inserting the right delay  $\tau$  in the battery arm, the battery field and classical field arrive simultaneously at the beam splitter.

Similarly to the procedure for the charging step in our protocol, we register the single counts received by two SNSPDs for a period of time and extract the visibility of interference. Initial measurements at 5K where we interfere the QD light field with the classical receiver field bypassing the cryostation in Fig. 4.22, show fast oscillating intensity counts such as in Fig. 4.24(a) (for  $\theta = 0.39\pi$ ). These fast oscillating counts result in a visibility (phase space) distribution shown in Fig. 4.24(c), where we observe that  $\phi$  does not cover the entire  $[0, \pi]$  space. A visibility distribution such as the one shown in Fig. 4.24(c) does not allow for easy access to the maximum visibility of interference, crucial for quantifying work and heat. Fourier transposing the visibility time trace, see Fig. 4.25, shows principal frequencies in the low frequency range 35 – 75 Hz, probably associated with the mechanical pumping of the cryostation.

#### 4.4.3 . Study on mechanical vibrations in measurements

To test whether the visibility measurements are limited by vibrations originating from the cryostation, we perform a study with our laser field, using a setup displayed in Fig. 4.26. We send a pulsed laser field into an unbalanced Mach-Zehnder interferometer where the laser path is split into two branches. The laser field in the upper branch is sent through the same cryostation as the one containing the qubit.

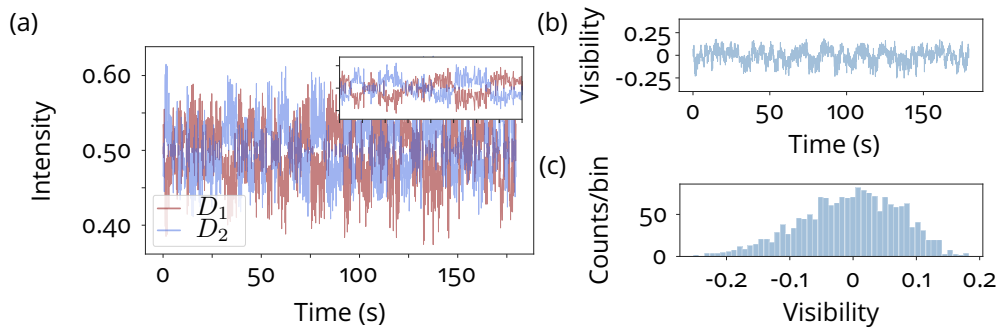


Figure 4.24 – **Extracting visibility for homodyne-type measurements from initial measurements.** Data set for QD-laser interference at 5K for  $\theta = 0.39\pi$  when the laser is not sent via the cryostation. (a) The intensity time trace shows fast oscillating counts. (b) The fast oscillations in (a) result in telegraph-like visibility time traces. (c) The histogram of the visibility distribution shows a maximum around zero.

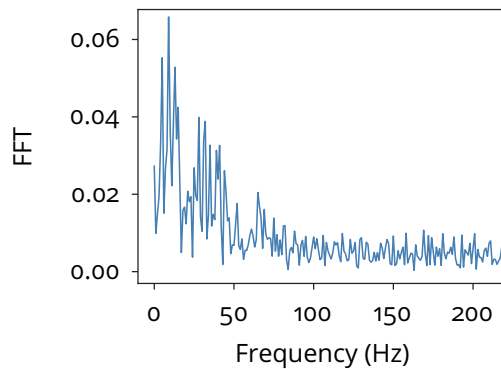


Figure 4.25 – **Mechanical noise.** Fast Fourier transform of the visibility time trace in Fig. 4.24(b) shows principal frequencies in range 35-75Hz.

A lens  $L_1$  in the cryostation focuses the laser onto a mirror which reflects the laser, see Fig. 4.22. In this configuration the laser field in the upper branch of Fig. 4.26 is subject to the similar vibrations as the qubit and battery field. The laser field in the lower branch does not enter the cryostation and instead is temporally delayed such that two consecutive pulses following the two different paths coincide at the final beam splitter. Two detectors at the output register single counts, allowing us to extract the visibility of interference.

The Cryostation s200 from Montana Instruments allows for operation at different compressor powers corresponding to different mechanical frequencies. We first perform the measurements at high compressor power and obtain the intensity time traces in Fig. 4.27(a). The corresponding visibility time trace shows the same telegraphic behavior as seen in Fig. 4.24. Subsequent measurements at

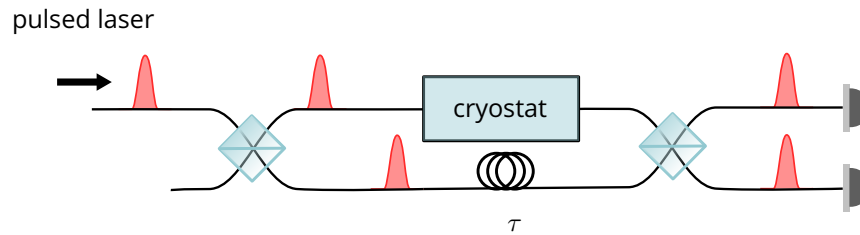


Figure 4.26 – **Testing effect mechanical vibrations on phase stability.** Self-interference with a laser field. A pulsed laser field is split into two paths : through a cryostation (upper branch) or via a time-delayed path (lower branch), after which they interfere at a second 50 : 50 beam splitter, where two SNSPDs at the outputs record the single counts.

low compressor power result in an increase in intensity (and visibility) oscillation amplitude (Fig. 4.28). The corresponding visibility histogram shows a distribution more similar to the expected  $\arccos$  shape. We note that both measurements do not show a fully explored phase space (askew histograms) which is caused by the relatively short integration time whereby we do not explore the full phase space.

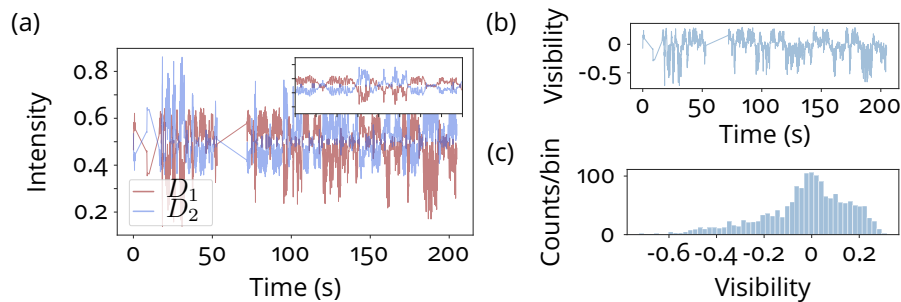


Figure 4.27 – **Laser interference through cryostation operating at high compressor power.** (a) Intensity time trace with fast anticorrelated oscillations. (b) Visibility time trace corresponding to (a). (c) Visibility distribution shows a spike around zero.

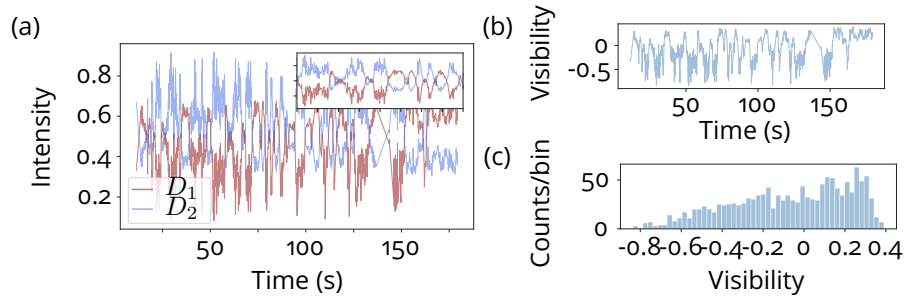


Figure 4.28 – **Laser interference through cryostation operating at low compressor power.** Intensity time trace shows increased amplitude of oscillations. (a) Intensity time trace, (b) visibility time trace, and (c) distribution.

To fully appreciate the effect of mechanical vibrations on the visibility distributions, we perform the same measurement but bypass the cryostation in the upper branch in Fig. 4.26. We see a drastic increase in oscillation amplitude, Fig. 4.29, with the normalized visibility reaching unity as expected for self-interference with a laser field with first-order coherence  $c^{(1)} = 1$ . These measurements show that the qubit and classical receiver are subject to different (mechanical) vibrations. The resulting fluctuating difference in path length introduces fast phase oscillations and suppresses the visibility of interference. As a result of these measurements, we perform the discharge measurements with the classical receiver focused onto, and reflected off a mirror  $M$  inside the cryostation as depicted in Fig. 4.22. Furthermore, we place waveplates ( $\lambda/2, \lambda/4$ ) in both paths leading to the final beam splitter to ensure parallel polarization of the two fields, and set the intensities of the two fields for each  $\theta$  to be equal at the final beam splitter in the setup :  $\mu_b = \mu_c$ .

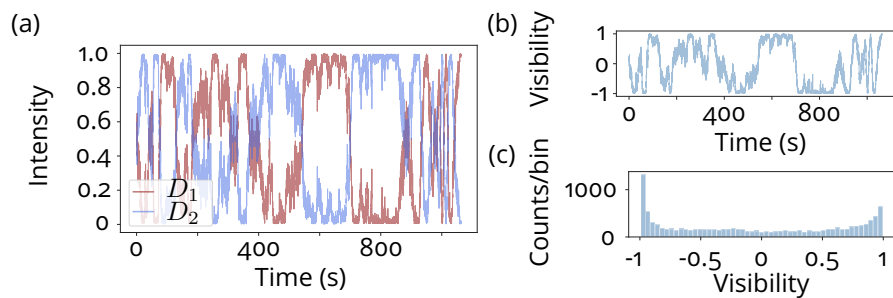


Figure 4.29 – **Laser interference in absence of cryostation vibrations.** (a) Intensity time trace of self-homodyne measurements with a coherent field containing maximum first-order coherence. (b) Visibility time trace, and (c) distribution.

#### 4.4.4 . Energetic exchanges between two light fields

We implement the protocol we propose to discharge the battery field, using the experimental conditions discussed above. We show an example data set in Fig. 4.30 where we drive our qubit with a  $\theta = 0.55\pi$  pulse area. Compared to the self-homodyne measurements, the optical phase changes at a faster rate. The inset in Fig. 4.30(a), however, clearly shows anticorrelated oscillations. The presence of anticorrelated oscillations is a clear indication that **we have achieved energy transfer from the battery field to the classical field**. However, the visibility histogram in Fig. 4.30(c) shows slightly less clear bounds to the visibility distribution compared to the self-homodyne measurements. Nevertheless, we can extract a maximum visibility of interference by again taking the mean absolute value of the  $N$  highest and  $N$  lowest visibilities, where we take  $N = 100$ . The error in visibility is given by the standard deviation in  $v_{\max}$  by comparing the results for  $N \in [10, 500]$ , and standard counting error. For the example data set in Fig. 4.30

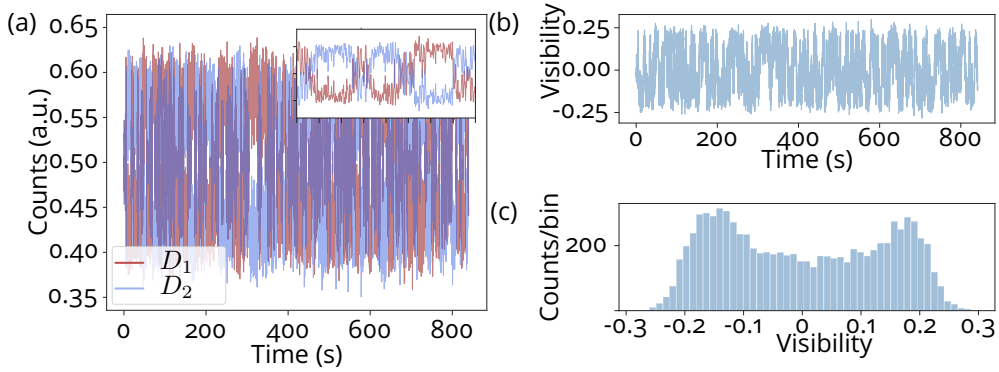


Figure 4.30 – **Visibility measurements with a battery field and classical receiver.** For  $\theta = 0.55\pi$ . (a) Intensity time trace, (b) visibility time trace, and (c) histogram showing the visibility distribution.

we find  $v_{\max} = 0.25 \pm 0.01$ . We repeat this measurement for different pulse areas at 5K and 20K.

We first examine the scenario where the qubit is kept at 5K and weakly couples to the phonon bath. Fig. 4.31(a) (blue) shows the results of the interference measurement. As in the battery charging step of the protocol, we can see an increase in visibility with decreasing  $\theta$  which corresponds to an increasing efficiency of discharge, albeit significantly reduced with respect to the charging step. From the fitted curve  $v_{\max} = C_{b,c} \cos(\theta/2)$  we extract  $C_{b,c}$  which captures the overall coherence between the two fields (classical and quantum). We find  $C_{b,c}(5K) = (36.3 \pm 0.4)\%$ . Next, we perform the same set of measurements at 20K, red data in Fig. 4.31(a), where now the total energy transfer is further reduced due to reduction in photon-number coherence of the battery field. From

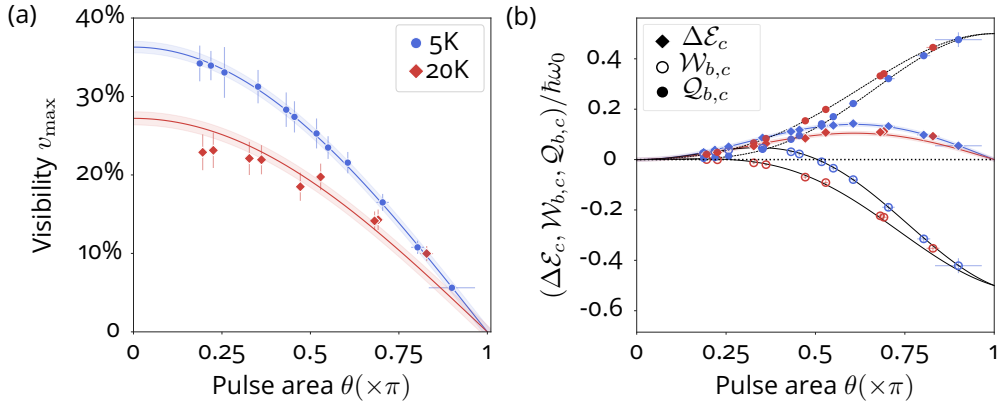


Figure 4.31 – **Discharging a quantum battery with a classical receiver.**(a) Visibility as a function of pulse area  $\theta$  for the interference of the battery field with a classical receiver, for a qubit operating at 5K (blue) and 20K (red). (b) The energetic transfers upon interference between a battery field and a classical receiver, with the total energy  $\Delta\mathcal{E}_c$  (diamonds), work  $\mathcal{W}_{b,c}$  (open circles), and heat  $\mathcal{Q}_{b,c}$  (circles) as a function of pulse area.

the fitted theory curve we extract  $\mathcal{C}_{b,c}(20\text{K}) = (27.2 \pm 0.4\%)$ .

In Fig. 4.31(b) we show the total energy exchanged between the battery field and the classical receiver (solid diamonds) where a positive value on the y-axis indicates a net energy transfer from the qubit towards the classical receiver. The other thermodynamic quantities can then be deduced from the visibility measurement where we highlight that the heat component of the energy exchanged  $\mathcal{Q}_{b,c}$  only originates from the quantum battery field as the classical receiver is a coherent field. As shown in the previous section we find the heat to be  $\mathcal{Q}_{b,c} = \mathcal{Q}_{q,b}/2$  and therefore the work component  $\mathcal{W}_{b,c} = \mathcal{E}_b^{(im)}v_{\max} - \mathcal{Q}_{q,b}/2$ .

The heat and work exchanged during the experiment are displayed in Fig. 4.31(b) as solid and open circles, respectively, and we fit the data to the theoretical predictions. We notice that although the net energy transfer is positive, the work transfer from the battery field is only positive for a small range of  $\theta$ , **indicating undesired work flow in the opposite direction**. This effect is amplified at 20K as a result of introducing pure dephasing to the qubit, which affects the charging of the battery field.

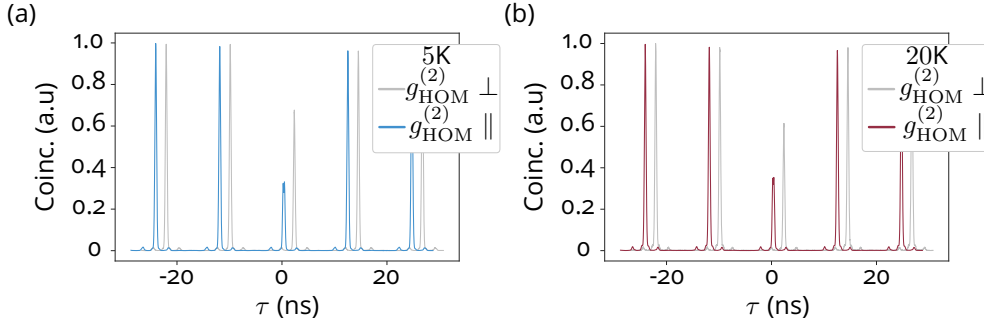


Figure 4.32 – **Mean wavepacket overlap between a quantum battery and a classical receiver.** (a) Second-order correlation histograms for a qubit operating at 5 K and  $\theta = \pi$  for co-polarization with the classical receiver (blue) and cross-polarization (gray). Histograms normalized by the amplitude of the uncorrelated peaks. (b) Same as in (a) but for the qubit operating at 20 K.

#### 4.4.5 . Limitations to discharging energy

To understand the limited energy exchange between the battery field and the classical receiver, we perform Hong-Ou-Mandel measurements to extract their mean wavepacket overlap at  $\theta = \pi$ . From the measurements, Fig. 4.32, we find  $M_{b,c}(5 \text{ K}) = (48.9 \pm 0.3)\%$  and  $M_{b,c}(20 \text{ K}) = (32.3 \pm 0.7)\%$  where we have taken into account the non-negligible classical intensity correlation  $g_c^{(2)} = 1$  from the classical receiver (see textbox). These values are lower than initially expected when observing the overlap in temporal profiles in Fig. 4.23, and the indistinguishability  $M_s$  of the battery field. This could indicate **the presence of spectral diffusion of the qubit resonance**. Indeed, the spectral diffusion takes place on timescales longer than the timescale at which we probe the indistinguishability of our battery field  $M_s$  (12.3 ns). As a result we do not capture the spectral diffusion with  $M_s$  but possibly see the effect of this when interfering the battery field and classical receiver. For a qubit prone to pure dephasing and spectral diffusion ( $\delta\omega$ ), the mean wavepacket overlap with the classical receiver is given by (Appendix 9.3.2) :

$$M_{b,c}(\delta\omega) = \frac{\gamma(\gamma + \gamma^*)}{(\gamma + \gamma^*)^2 + \delta\omega^2}, \quad (4.35)$$

where we consider  $\gamma_b = \gamma_c = \gamma$ , and we see that spectral diffusion over a range  $\delta\omega$  decreases the mean wavepacket overlap.

In contrast, we observe  $M_{b,c}$  only slightly higher than  $C_{b,c}$ , with  $C_{b,c}(5 \text{ K}) = (36.3 \pm 0.4)\%$  and  $C_{b,c}(20 \text{ K}) = (27.2 \pm 0.4\%)$ . We attribute this slight discrepancy to **blinking effects of the QD transition**, which affects the measurements for  $C_{b,c}$  and  $M_{b,c}$  differently. When we interfere the battery field with the classical field on the 50 : 50 beam splitter, we balance the intensities, or mean average photon-number. When a QD suffers from blinking, it switches between two different emission intensities "high" and "low" over long timescales. Whenever the QD emits at low intensity, the inputs to the beam splitter are no longer balanced, affecting the interference. Therefore, the extracted visibility and mean wavepacket overlap are limited by the amount of time the QD is in the "high" emission state, which could explain the slight discrepancy between the extracted values for  $C_{b,c}$  and  $M_{b,c}$ .

#### Extracting wavepacket overlap between a classical field and a quantum field

Let us consider two fields, a classical coherent field and a single-photon field, impinging on a 50 : 50 beam splitter. Coincidences at the outputs can be the result of :

1. Photon from classical source and quantum source do not bunch ; contribution :  $2\mu_b\mu_c(1 - M_{b,c})$ , where the factor two is taking into account the two ways this can happen (both photons reflected or transmitted).
2. Two photons originate from the same source, with the other input of the beam splitter in vacuum state ; contribution :  $\mu_c^2 g_c^{(2)}$  or  $\mu_b^2 g_b^{(2)}$ .

Assuming we drive our qubit close to  $\pi$ -pulse, the average uncorrelated peak area is  $\bar{A}_{\tau>0,\parallel} = 2\mu_c\mu_b$ , resulting in :

$$g_{\text{HOM},\parallel}^{(2)} = 1 - M_{b,c} + \bar{g}^{(2)},$$

with the weighted average input intensity correlation  $\bar{g}^{(2)} = (\mu_c/\mu_b)g_c^{(2)}/2 + (\mu_b/\mu_c)g_b^{(2)}/2$ .

Realising  $g_{\text{HOM},\perp}^{(2)} = 1 + \bar{g}^{(2)}$ , we obtain

$$M_{b,c} = \frac{g_{\text{HOM},\perp}^{(2)} - g_{\text{HOM},\parallel}^{(2)}}{g_{\text{HOM},\perp}^{(2)}} \left( 1 + \bar{g}^{(2)} \right) \quad (4.36)$$

For equal input intensities ( $\mu_b = \mu_c$ ) we get  $1 + \bar{g}^{(2)} = 1 + (g^{(2)} + 1)/2$ .

#### Conclusion Section 4.4 - Discharging a quantum battery with a classical field

In this section we proposed a protocol to discharge the charged quantum battery and measure the energetic exchanges during the process. This protocol is experimentally demonstrated whereby we discharge the battery through homodyne interference with a classical receiver, a coherent laser field. The energy transfer from the battery to the classical field is reduced by pure dephasing introduced to the qubit, which reduces the amount of work initially charged in the battery. Moreover, in terms of work transfer, we witness an unwanted work transfer from the receiver to the battery. Finally, in the protocol we chose to balance the input intensities at the beam splitter, which abets the perceptibility of the visibility of interference, and therefore maximizes the energy discharge.

## 4.5 . Conclusion and outlook

In this chapter we have proposed and implemented an experimental protocol to measure energetic exchanges on the most fundamental level : between a qubit and the vacuum of the electromagnetic field through spontaneous emission, and between a quantum field and a classical coherent field. In quantum thermodynamics these steps are equivalent to charging and discharging a quantum battery, here the photonic field emitted by the qubit.

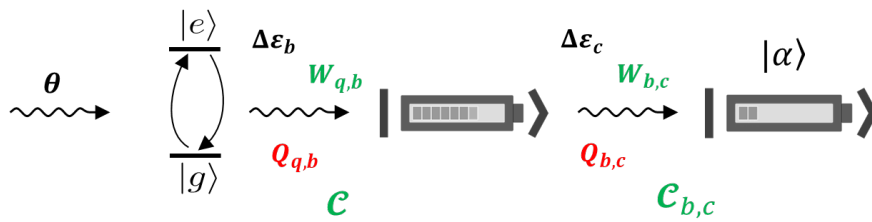


Figure 4.33 – **Summary energetic exchanges between a qubit and light fields** A two-level system resonantly excited by a pulsed laser field with pulse area  $\theta$ , spontaneously decays, thereby transferring energy  $\Delta\mathcal{E}_b$  in the form of work  $\mathcal{W}_{q,b}$  and heat  $Q_{q,b}$  to the vacuum of the electromagnetic field (a quantum battery). In the second step, the battery field is discharged through interference with a coherent field  $|\alpha\rangle$ , transferring work  $\mathcal{W}_{b,c}$  and heat  $Q_{b,c}$  to the field, leaving the battery field with less energy. In both steps the work transfer is reduced by dephasing, which affects the purity in photon-number basis  $\mathcal{C}$  and  $\mathcal{C}_{b,c}$ .

In the charging step of our protocol we extended previous theory by considering the effect of pure dephasing on the energetic transfers. However, more theory is needed to understand the energetics beyond the pure dephasing framework. Additionally, to fully understand the dephasing and decoherence mechanisms affecting the performance of the qubit presented in this chapter, assessment of the performance of the battery field at long delays should be considered. This would allow us to fully explain the energetic exchanges in discharging, and measure the effect of spectral wandering. This spectral wandering is hypothesized to arise from changes in the charge environment of the QD. As such, an important experimental improvement could be made by looking into ways to electrically isolate the QD from the environment.

In the discharging step of the protocol, improvements could be made by considering interference between the battery field and classical receiver under

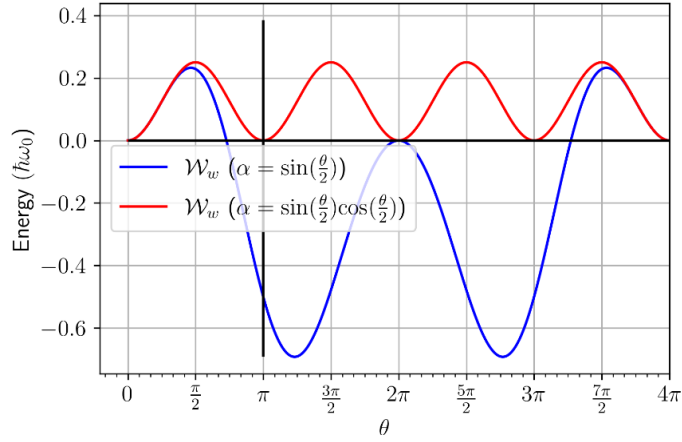


Figure 4.34 – **Optimizing work transfer.** The amount of work transfer from a battery field to a classical work receiver ( $w$ ) as a function of pulse area  $\theta$  when setting equal field intensities (blue), or setting equal field amplitudes (red). Simulations performed by Dr. M. Maffei, see Appendix 9.4.

different conditions. Here we chose to match the fields' input intensities, abetting the total energy transfer to the classical field. However, under this condition, we demonstrated that the energy transferred to the classical field is mostly of heat nature, and we see unwanted work transfer in the opposite direction. Instead of choosing to optimize the energy transfer, one could consider experimental and theoretical conditions whereby the work transfer from the battery field to the classical field in discharging is optimized. We mention that one possible solution to this could be matching of field amplitudes instead of intensities, see Fig. 4.34 where the subscript  $w$  indicates the energy received by the classical work receiver (Appendix 9.4). We see that when setting equal field intensities  $\mathcal{E}_b^{(in)} = \mathcal{E}_c^{(in)}$  (blue), the work flow is indeed as previously shown. However, if we were to set the amplitudes of the interfering fields equal (red), corresponding to  $\alpha = \sin(\theta/2)\cos(\theta/2)$ , the work is discharged into the classical field for all  $\theta$ , as desired for the discharging step in the protocol. Another important limitation to the total energy transfer, and therefore work transfer, is the presence of QD emission blinking. How much this blinking affects the energy flows could be investigated to fully understand under what conditions we can optimize discharge.

Finally, we underline that both steps in our protocol are important processes in many quantum technologies, from generating atom-based quantum memories, to performing linear optical gates or Bell state measurements. As such, our study can serve as the first steps to experimental studies on the energetics of quantum computing.



## 5 - Temporally resolved energetic exchanges in the Ramsey sequence

### 5.1 . Introduction

In the previous chapter we have seen how, in the framework of a closed bipartite quantum system, one can relate energy coherence and work transfer. We studied the spontaneous emission of an atom coherently driven. Our study showed in particular how the entanglement between the atom and the field arising during spontaneous emission led to heat in the energy exchange, see Sec. 4.2.

A Ramsey sequence where two pulses (both of pulse area  $\theta = \pi/2$ ) with a time delay are applied to a qubit after which the qubit decays, is a fundamental tool in quantum optics to determine the dephasing rate of a prepared state (138–140). In the present chapter, we revisit the Ramsey sequences in terms of the quantum thermodynamics framework introduced in Section 4 and study how generated correlations affect the energetic transfers between an atom and the emitted state of light.

First, in Sec. 5.2 we introduce the Ramsey sequence applied to a two-level system and explain the thermodynamic quantities relevant to each step in the protocol. Reconstruction of the output state of light at the end of a Ramsey sequence shows us that under certain conditions a qubit can actually absorb more energy from two  $\theta = \pi/2$  pulses than from a single  $\pi$ -pulse. This finding leads us to Sec. 5.3, where we experimentally study the dynamics of energy absorption as a function of pulse separation with a QD-cavity system, and experimentally find a range of delays for which the emission intensity exceeds the energy given by a single  $\pi$ -pulse. We propose an experimental protocol in Sec. 5.4 to temporally resolve energetic transfers during the Ramsey sequences. In line with the nature of Ramsey sequences, we show that the energy emitted by the emitter mostly originates from correlations (heat) : energy arising from entanglement between the field and the quantum emitter. Finally, we give some perspectives based on the results presented here in this chapter. We underline that the present study was still ongoing at the time of writing of the manuscript. We discuss some remaining open questions in Sec. 5.6 to give an outlook to future studies.

The theoretical work accompanying the results presented in this chapter is under development within the group of Prof. Alexia Auffèves<sup>1</sup> with Dr. Maria Maffei<sup>2</sup>, and with support of Dr. Stephen Wein<sup>3</sup>. The experiments performed for this chapter were done in collaboration with Dr. Carlos Antón-Solanas<sup>4</sup>.

---

1. Université Grenoble Alpes, CNRS, Grenoble INP, Institut Néel, 38000 Grenoble, France.

2. Université Grenoble Alpes, CNRS, Grenoble INP, Institut Néel, 38000 Grenoble, France.

3. Previously : Université Grenoble Alpes, CNRS, Grenoble INP, Institut Néel, 38000 Grenoble, France.

Currently : Quandela SAS, 7 Rue Léonard de Vinci, 91300 Massy, France.

4. Universidad Autónoma de Madrid, Facultad de Ciencias, Madrid, Spain.

## 5.2 . Work and heat transfers in Ramsey sequences

We are interested in understanding the Ramsey sequence from a quantum thermodynamic perspective, where we study the work and heat flow between a qubit, subject to two  $\pi/2$  excitation pulses, and the vacuum of the electromagnetic field, into which the energy is released through spontaneous emission. Again, we consider the qubit and the electromagnetic field as a closed quantum system where the energy released by the qubit (q) is equal to the energy received by the vacuum of the electromagnetic field – i.e.  $\dot{\mathcal{W}}_q = -\dot{\mathcal{W}}_f$ , and  $\dot{\mathcal{Q}}_q = -\dot{\mathcal{Q}}_f$ , see Section 4.2, and where the dot over  $\mathcal{W}$  and  $\mathcal{Q}$  represents a derivative with respect to time. In this section we use this framework to break down the Ramsey sequence in time bins with their corresponding energetic exchanges, and describe the output state of light.

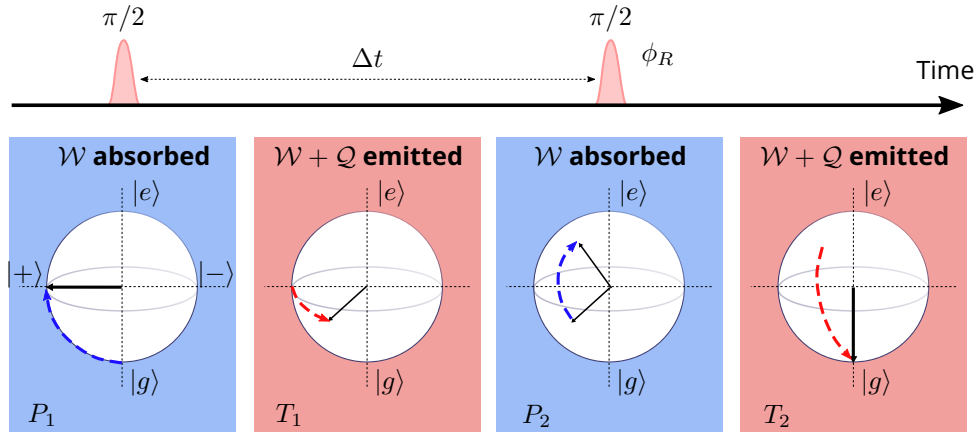


Figure 5.1 – **A Ramsey sequence.** A two-level system, represented by the Bloch sphere, is resonantly driven by two  $\theta = \pi/2$  pulses separated by time  $\Delta t$  and with relative Ramsey phase  $\phi_R$ . During each pulse (time bin  $P_1$  and  $P_2$ ) work is transferred to the qubit, where the first pulse brings it in an equal superposition between ground and excited state. Between the two pulses (time bin  $T_1$ ), the qubit spontaneously decays, thereby transferring energy to the vacuum of the electromagnetic field in the form of heat and work. After the second pulse (time bin  $T_2$ ), we let the system fully decay to the ground state.

### 5.2.1 . A Ramsey sequence

In a Ramsey sequence, a qubit is driven by two pulses of pulse area  $\theta = \pi/2$  separated in time by  $\Delta t$ , and repeated at laser repetition rate  $\tau_p^{-1}$  with  $\tau_p \gg \Delta t$ . Fig. 5.1 schematically depicts the procedure and the subsequent evolution of the qubit during one Ramsey sequence. In the first time bin ( $P_1$ ), a driving

field (pulse 1) with  $\theta = \pi/2$  provides energy to the qubit. As a result, the drive brings the qubit into an equal superposition between ground and excited state :  $|+\rangle = (|g\rangle + |e\rangle)/\sqrt{2}$ . The energy absorbed by the qubit in the process is of work  $\mathcal{W}$  nature, considering the driving field is a classical – i.e. coherent – field with classical coherence, and the entanglement between the field and the qubit is negligible during the excitation (38). The energy change of the drive is equal to the work absorbed by the qubit :  $\Delta\mathcal{E}_f = \mathcal{W}_{P_1}$ .

After the pulse (time bin  $T_1$ ), relaxation takes place whereby the qubit spontaneously transfers energy to the vacuum of the electromagnetic field in the form of a photonic field. This photonic field receives energy from the qubit, of coherent and incoherent nature : work  $\mathcal{W}$  and heat  $\mathcal{Q}$ . **The work and heat rate** from the qubit to the electromagnetic field in absence of dephasing are defined as :

$$\dot{\mathcal{W}}_{q,f} = \hbar\omega_0\gamma |\langle \hat{\sigma}_-(t) \rangle|^2 \quad (5.1)$$

$$\dot{\mathcal{Q}}_{q,f} = \hbar\omega_0\gamma (\langle \hat{\sigma}_+(t)\hat{\sigma}_-(t) \rangle - |\langle \hat{\sigma}_-(t) \rangle|^2) \quad (5.2)$$

with  $\hat{\sigma}_\pm$  defined in Section 2.5.1, and where  $\gamma$  is the spontaneous emission rate of the qubit. We also note that  $|\langle \hat{\sigma}_-(t) \rangle|^2$  is equal to the atomic coherence in the energy basis squared :  $s^2 = p_g p_e$ . We emphasize that we are discussing here the work and heat rates, which are a function of time, hence the dot over  $\mathcal{W}$  and  $\mathcal{Q}$ , and whose rates are set by the emission rate of the atom,  $\gamma$  : the speed with which the atom releases energy into the electromagnetic field. Note : from now we drop the subscripts  $q, f$ , and we only consider the energetic transfers from the qubit to the field.

After time  $\Delta t$ , a second  $\pi/2$  pulse is applied (time bin  $P_2$ ), again providing work to the qubit :  $\Delta\mathcal{E}_f = \mathcal{W}_{P_2}$ . The second pulse has a **relative phase with respect to the first pulse of  $\phi_R$ , where R indicates we are referring to the Ramsey phase**. For  $\phi_R = 0(\phi_R = \pi)$ , the sequence is constructive (destructive), meaning the second pulse brings the qubit closer to the excited (ground) state in terms of population. At the end of the pulse (time bin  $T_2$ ), the qubit relaxes back to the ground state, through spontaneous emission. The photonic field receives again energy from the qubit in the form of work and heat. Finally, we can write down the energy balance describing a single Ramsey sequence in a closed system in terms of time bin-integrated energies :

$$\mathcal{W}_{P_1} + \mathcal{W}_{P_2} = \mathcal{W}_{T_1} + \mathcal{Q}_{T_2} + \mathcal{W}_{T_2} + \mathcal{Q}_{T_2},$$

$$\mathcal{E}_{\text{abs}} = \mathcal{W}_{T_1} + \mathcal{Q}_{T_2} + \mathcal{W}_{T_2} + \mathcal{Q}_{T_2},$$

where we see that the total energy absorbed ( $\mathcal{E}_{\text{abs}}$ ) is equal to the sum of the total work and heat emitted by the qubit at the end of the sequence. To study the thermodynamics of the Ramsey sequence thus requires us to look at the output

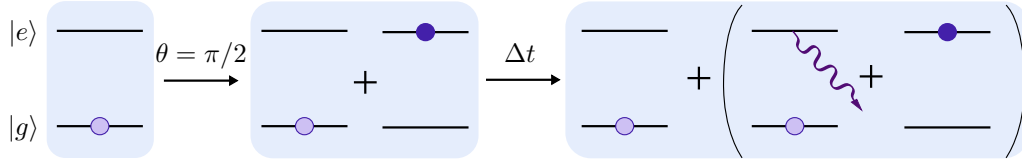


Figure 5.2 – **Light-matter entanglement** In between two  $\pi/2$  pulses in a Ramsey sequence, entanglement between field and qubit builds up. A first pulse creates an equal superposition between the ground and excited state in the qubit. During time  $\Delta t$ , the excited state has time to decay, resulting in an entangled qubit-field state.

state of light along the whole pulse sequence, subdividing time into two bins : the interval between pulses ( $P_1 + T_1$ ) and the interval between the second pulse and the end of the spontaneous emission ( $P_2 + T_2$ ).

### 5.2.2 . Time bin entanglement with Ramsey sequences

The photonic state after the Ramsey sequence can be determined by considering the schematic in Fig. 5.2, where we start with the two-level system in the ground state  $|g\rangle$ . A  $\pi/2$  pulse then creates an equal superposition. The joint field-qubit state at this point in time is given by

$$|\Psi_{2\text{LS}}\rangle \otimes |\Psi_{\text{field}}\rangle = \frac{1}{\sqrt{2}}(|g\rangle + |e\rangle) |0\rangle \quad (5.3)$$

During time  $\Delta t$  the state of the two-level system evolves, creating the state (141) :

$$|\Psi\rangle = \frac{1}{\sqrt{2}} |g0\rangle + \frac{\alpha |e0\rangle + \beta |g1\rangle}{\sqrt{2}}, \quad (5.4)$$

where the amplitudes  $\alpha = e^{-\gamma\Delta t/2}$  and  $\beta = \sqrt{1 - \alpha^2}$ . At this point we notice that the field and qubit are entangled, and we rewrite the state as :

$$|\Psi\rangle = \frac{1}{\sqrt{2}}(|0_{T_1}\rangle + \beta |1_{T_1}\rangle) |g\rangle + \frac{\alpha}{\sqrt{2}} |0_{T_1}\rangle |e\rangle, \quad (5.5)$$

where the subscript indicates that we consider the photonic field in time bin  $T_1$ . A second  $\pi/2$  pulse with Ramsey phase  $\phi_R$  changes the atomic state of the joint system

$$|\Psi\rangle = \frac{1}{\sqrt{2}}(|0_{T_1}\rangle + \beta |1_{T_1}\rangle) \frac{|g\rangle + e^{i\phi_R} |e\rangle}{\sqrt{2}} + \frac{\alpha}{\sqrt{2}} |0_{T_1}\rangle \frac{|e\rangle - e^{-i\phi_R} |g\rangle}{\sqrt{2}}. \quad (5.6)$$

In time bin  $T_2$  we let the atomic state fully decay, i.e.  $|g\rangle \rightarrow |0\rangle$  and  $|e\rangle \rightarrow |1\rangle$ , and the photonic field acquires the properties of the entangled qubit-field state :

$$|\Psi\rangle = \frac{1}{2}[(1 - e^{-i\phi_R}\alpha) |00\rangle + (e^{i\phi_R} + \alpha) |01\rangle + \beta |10\rangle + e^{i\phi_R}\beta |11\rangle], \quad (5.7)$$

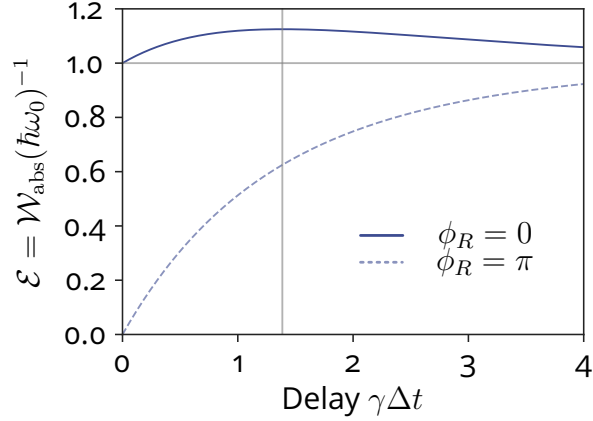


Figure 5.3 – **Absorbed energy in a Ramsey sequence.** The total energy absorbed by a qubit in a Ramsey sequence as a function of pulse separation normalized by the lifetime of the qubit  $\gamma^{-1}$ , for constructive (destructive) phase  $\phi_R = 0(\pi)$  between pulses. Grey vertical line indicates the delay for which we expect a maximum energy absorbed :  $2\ln(2)/\gamma$ . Here the energy absorbed is  $9/8$  times higher than expected from two  $\pi/2$  pulses, see grey horizontal line.

where  $|ij\rangle = |i_{T_1}j_{T_2}\rangle$  with  $i, j \in [0, 1]$ . The total photon number at the end of the Ramsey sequence for constructive phase  $\phi_R = 0$  is given by

$$\mu = \frac{1}{4}[(1 + \alpha)^2 + \beta^2 + 2\beta^2] = 1 + \frac{\alpha}{2}(1 - \alpha). \quad (5.8)$$

The total photon-number emission  $\mu$  is optimized for  $\phi_R = 0$ , and  $\alpha = e^{-\gamma\Delta t/2} = 1/2$ , resulting in  $\mu = 9/8$ . For a quantum emitter with lifetime  $\gamma^{-1}$ , this thus scenario corresponds to a pulse separation of  $\gamma\Delta t = 2\ln(2)$ .

The expected average photon-number in emission  $\mu$  is equal to the amount of energy absorbed by the qubit  $\mathcal{E}$  (i.e. work  $\mathcal{W}_{\text{abs}}$ ) normalized to the qubit transition energy  $\hbar\omega_0$ , which we plot in Fig. 5.3 as a function of pulse separation  $\gamma\Delta t$  for constructive phase  $\phi_R = 0$  and destructive phase  $\phi_R = \pi$ . As expected, for two  $\pi/2$ -pulses **driving simultaneously ( $\Delta t \rightarrow 0$ ) in-phase ( $\phi_R = 0$ ) the qubit, we effectively generate a  $\pi$ -pulse**, resulting in a single-photon Fock state  $|1\rangle$ . However, as we increase the delay between the two pulses, we see an **enhancement in the work absorbed, manifested by an increase in average photon-number released at the end of the sequence, with an expected maximum for  $\gamma\Delta t = 2\ln(2) = 9/8$** . For a Ramsey phase  $\phi_R = \pi$ , two pulses simultaneously arriving at the qubit ( $\Delta t \rightarrow 0$ ), bring the qubit back to the ground state. As we change the delay, the qubit starts to decay between pulses, and in the limit of  $\Delta t \gg \gamma^{-1}$ , the qubit is fully decayed by the time the second pulse arrives. As a result, in this limit the energy absorbed by the qubit is equivalent to

twice a  $\pi/2$ -pulse, and we retrieve  $\mu = 1$ .

### 5.3 . Experimental study of enhancement in work absorption

To investigate the energetic of Ramsey interferometry, we use a charged QD state, a four-level system (see Section 2.5.2), which is placed inside a cryostation kept at 5K. We resonantly excite the QD using a pulsed laser field operating at 925nm. Initial benchmark measurements for single pulse excitation and pulse area  $\theta = \pi$ , reveal a high single-photon indistinguishability  $M_s = (93.43 \pm 0.39)\%$  (Section 2.4.3), and from the decay profile, see Fig. 5.4, we extract a lifetime  $\gamma^{-1} = 202.4 \pm 5.1$  ps from a mono-exponential decay.

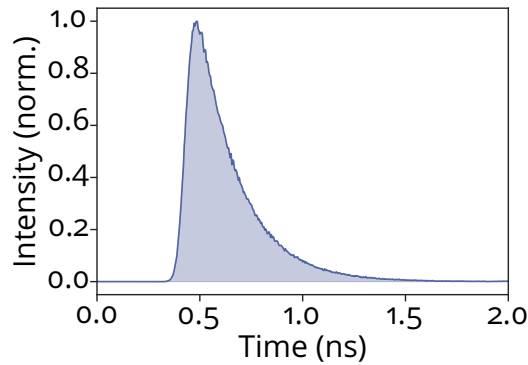


Figure 5.4 – **Decay profile of a charged QD state.** Spontaneous decay profile of a charged QD state under resonant excitation with pulse area  $\theta = \pi$ .

To apply Ramsey interferometry to the QD, the pulsed laser field is first sent into a Michelson interferometer, allowing us to generate pulse sequences with variable delay  $\Delta t$  between two output pulses of pulse area  $\theta = \pi/2$ , see Fig. 5.5. The Michelson interferometer contains a 50 : 50 beam splitter that splits the input field into two arms containing mirrors. The mirrors reflect the light back towards the beam splitter, where 50% of the light is sent into the output of the Michelson interferometer (here the excitation path). One of the mirrors is mounted onto a variable delay stage; we refer to this interferometer arm as the delay arm. This delay stage allows us to coarsely tune the pulse delay  $\Delta t$  in the range 0 – 334 ps.

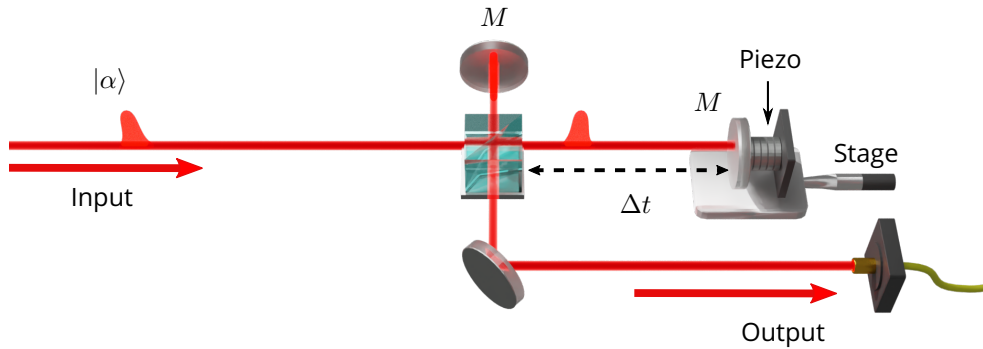


Figure 5.5 – **The Michelson interferometer to generate pulse sequences.** A pulsed coherent laser field  $|\alpha\rangle$  is input to a 50 : 50 beam splitter which divides the classical field into two pulses, one in each port containing a reflective mirror. One mirror is mounted on a coarse delay stage which is used to adjust the pulse separation between the two reflected pulses within a 0 – 334ps range. Applying a voltage to a piezoelectric actuator changes the delay with  $\approx 20\text{nm}$  precision, resulting in a change in the relative phase between the two excitation pulses output to the interferometer.

We are able to change the relative phase  $\phi_R$  between the two excitation pulses by using a piezoelectric actuator attached to the back of the mirror in the delay arm. The actuator (PK25LA2P2, Thorlabs) has a maximum displacement of  $12\ \mu\text{m} \pm 15\%$  for a drive voltage of 200 V, and can be electrically tuned with  $\approx 10\ \text{nm}$  precision. A change in position on this scale creates a path length difference between the pulses, resulting in a relative phase  $\phi_R$ . As qualitatively explained in the previous section, this Ramsey phase in turn affects the photonic state emitted by the QD, with  $\phi_R = 0(\pi)$  leading to constructive (destructive) quantum interference in the excitation step.

We apply this Ramsey sequence to the QD repeated at the repetition rate of the laser  $(\tau_p)^{-1} = 81\ \text{MHz}$ , see Fig. 5.6. Here, the mirrors on both sides of the QD represent the cavity, thereby forming the four-level system indicated in inset. After one sequence, the QD fully decays whereby it emits a photonic field  $|\psi\rangle$ . This photonic field is separated from the driving field through cross-polarization (see Section 2.5.2), indicated by the two polarizers with orthogonal linear polarization  $V$  and  $H$ .

We record the QD emission intensity time trace whilst continuously changing the relative phase. In Fig. 5.7 we show the resulting time traces for two coarse

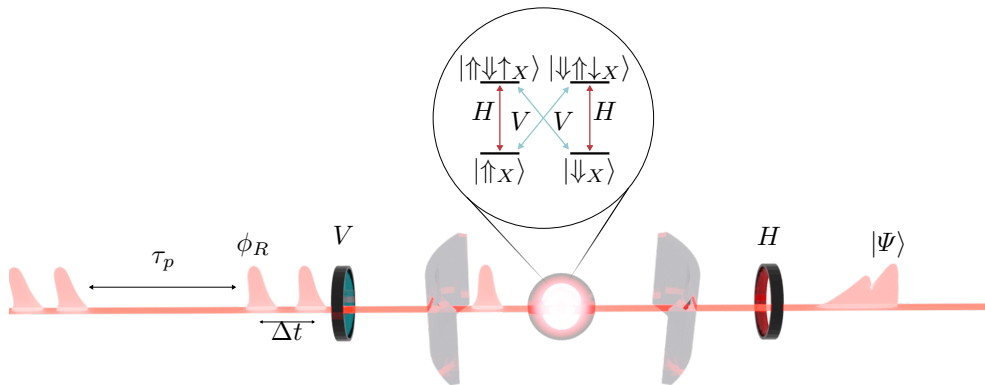


Figure 5.6 – **Experimental procedure.** A four-level system is coherently excited by two  $\pi/2$  pulses ( $V$  polarized) separated by time  $\Delta t$  at a repetition rate of  $\tau_p^{-1} = 81$  MHz. We separate the spontaneously emitted photonic field  $|\Psi\rangle$  from the drive using a cross-polarization configuration, here indicated by the two polarizers with orthogonal polarizations  $H$  and  $V$  before and after the QD-cavity system.

delays :  $\Delta t = 17$  ps and  $\Delta t = 167$  ps. As we scan the phase, we see constructive and destructive interference (i.e. Ramsey fringes) between the two  $\pi/2$  pulses used to excite the QD. When increasing the coarse delay, we notice a decrease in amplitude. This decrease in amplitude can be understood from the fact that as the coarse delay is increased, the qubit has time to decay between pulses. As a result, the second  $\pi/2$  pulse, in or out of phase, cannot fully excite the qubit.

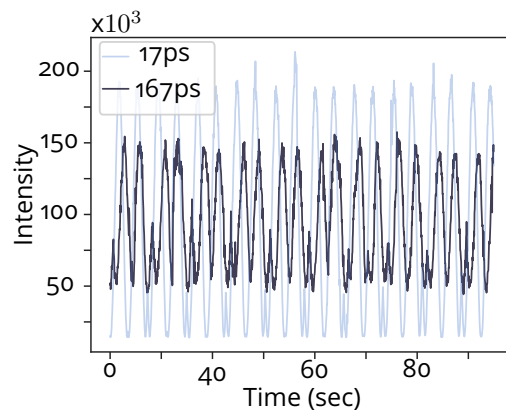


Figure 5.7 – **Ramsey fringes.** The QD emission intensity obtained with Ramsey sequences as a function of time when continuously changing the relative phase between excitation pulses  $\phi_R$ . For pulse delays  $\Delta t = 17$  ps and  $\Delta t = 167$  ps.

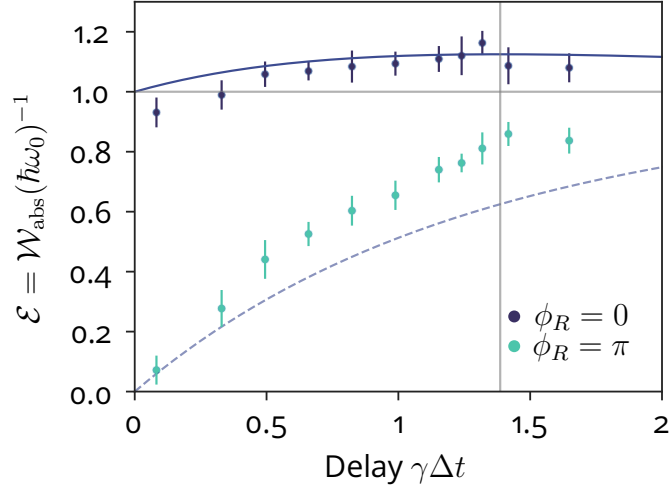


Figure 5.8 – **Energy absorbed by the qubit in a Ramsey sequence.** The energy normalized to the transition frequency of the qubit as a function of pulse delay between two  $\pi/2$  excitation pulses for constructive and destructive Ramsey phase. With  $\gamma^{-1} = 202.4 \pm 5.1$  ps.

From the Ramsey fringes we extract the average minimum ( $I_{\min}$ ) and maximum ( $I_{\max}$ ) emission intensity, corresponding to  $\phi_R = \pi$  and  $\phi_R = 0$ , respectively, which we repeat for several delays  $\Delta t$ . We normalize by the emission intensity measured when exciting the QD with a single  $\pi$ -pulse. These values represent the energy emitted by the qubit  $\Delta\mathcal{E}_q/(\hbar\omega_0)$  over the whole sequence, and are equal to the work absorbed  $\mathcal{E} = \mathcal{W}_{\text{abs}}$ . In Fig. 5.8, we plot the mean energy absorbed for Ramsey phase  $\phi_R = 0$  and  $\phi_R = \pi$ , together with their corresponding theoretical curves in solid and dashed, respectively, considering no dephasing. We indicate with a gray vertical line where the delay is corresponding to  $\gamma\Delta t = 2\ln(2)$ , and with the gray horizontal line the energy emitted for state preparation with a single  $\theta = \pi$  pulse.

Let us first examine the data for  $\phi_R = 0$ . Remarkably, we observe an increase in work absorption with a maximum around  $\gamma\Delta t = 2\ln(2)$  as theoretically predicted. Our observations nicely follow theoretical prediction within error bars. For the data corresponding to Ramsey phase  $\phi_R = \pi$ , the general behavior is in agreement with predictions : with almost no energy released into the electromagnetic field for  $\Delta t \rightarrow 0$  and a continuous increase with  $\Delta t$ . However, we observe an emission intensity consistently higher than expected and seemingly diverging from the theoretical curve for increasing delays. This trend could potentially be caused by memory effects in the charged quantum dot, induced when probing the quantum dot with pulse sequences. In a charged QD the central spin couples to a nuclear spin bath, which induces an effective magnetic field (Overhauser field) around

which the central spin precesses. This coupling is delay dependent and alters the spin relaxation time (139; 142; 143). As such, what we witness in Fig. 5.8 for  $\phi_R = \pi$  could be a signature of the spin dependence of the Ramsey sequence, not captured by our simple two-level model.

In the following sections we study the nature of the energy exchange between the QD and the electromagnetic field by the QD during the Ramsey sequence. We therefore focus on two delays :  $\gamma\Delta t = 0.33$  ( $\Delta t = 67$  ps) and  $\gamma\Delta t \approx 2\ln(2)$  ( $\Delta t = 287$  ps), corresponding to  $\mathcal{W}_{\text{abs}} \approx \hbar\omega_0$  and  $\mathcal{W}_{\text{abs}} \approx 9/8\hbar\omega_0$ , respectively.

#### 5.4 . Experimental study of temporally resolved energetic exchanges during spontaneous emission

We are interested in investigating the energetic exchanges during spontaneous emission along the Ramsey sequence, i.e. in time bins  $T_1$  and  $T_2$  (see Fig. 5.1). From Eq. 5.2 we see that this requires temporally resolving the coherence transfer along the qubit decay. Here, we propose a protocol to measure temporally resolved energetic exchanges in Ramsey sequences. It involves self-homodyne measurements with two detectors  $D_1$  and  $D_2$  whereby we compute the visibility of interference time-resolved over the temporal profile of the emitted photonic fields.

Indeed, a decay profile, such as in Fig. 5.4, measured by detector  $D_i$  is nothing more than the temporally resolved intensity over the spontaneous decay of an excited QD :  $\mu_i(t) = \langle \hat{a}^\dagger(t)\hat{a}(t) \rangle$ , see Section 2.4.1. As such, the profile contains information on the rate with which energy is given to the electromagnetic field, see Ref. (83) and Section 2.5.5. To temporally resolve the coherence transfer we perform homodyne measurements with the spontaneously emitted fields, see Section 4, and compute the decay profiles measured by detectors  $D_i$  after interference. From the decay profiles we extract the temporally resolved visibility of interference

$$v_{\text{max}}(t) = \max_{\phi} \frac{\mu_1(t) - \mu_2(t)}{\mu_1(t) + \mu_2(t)}, \quad (5.9)$$

with  $\phi$  the interferometer phase, and we find the first-order coherence transferred over the emission profile :  $v_{\text{max}}(t) \leq |\langle \hat{\sigma}_-(t) \rangle|^2$ . Experimentally, to build temporal profiles – and thus extract energetic quantities – requires integration over longer measurement times, whereby we repeat the exact same Ramsey sequence. To do so, we need a stabilized Ramsey phase relation over several sequence repetitions.

##### 5.4.1 . Locking the Ramsey phase

To maintain a fixed phase relation between the two  $\theta = \pi/2$  excitation pulses we add to the Michelson interferometer a continuous wave laser (CW, Toptica), operating at 925 nm, and a photo diode, see Fig. 5.9. Because the CW laser has a comparable wavelength to the excitation laser, path length differences are similarly sensed. The CW laser also interferes at the beam splitter in the Michelson

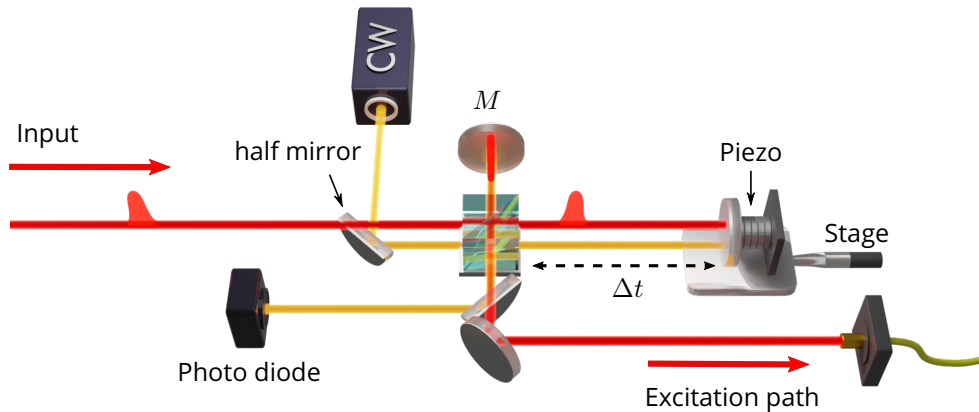


Figure 5.9 – **A phase-stabilized Michelson interferometer.** A continuous wave laser, a photo diode, and a voltage driven piezo are used in a Michelson interferometer to stabilize the phase between two pulses separated by time  $\Delta t$ . The pulses with fixed relative phase  $\phi_R$  are sent into the QD excitation path, which undergoes a Ramsey sequence.

interferometer. The interferometric signal imprinted on the amplitude of the CW field is registered by a photo diode in one of the output ports of the beam splitter. The photo diode transforms the intensity time trace of the CW field to an electrical signal. Using a PID (Proportional - Integral - Derivative) controller, the signal from the photo diode generates a feedback signal to stabilize the phase controlling a piezo. The PID controller takes an error signal, defined as the difference between the signal measured and the desired signal (called set point), and generates a feedback signal that can be described by the following formula :

$$u(t) = P \cdot e(t) + I \int_0^t e(\tau) d\tau + D \frac{de(t)}{dt}, \quad (5.10)$$

with  $e(t)$  the error signal at time  $t$ . The coefficients  $P, I, D$  are chosen such that the deviation over time from the set point is minimized. Basically, the  $P$  component is a proportional response to a deviation from the set point, i.e. if the deviation is large, the response is equally large. The integral part compensates for slow drift over time, whereas the derivative part generates a feedback signal in response to sudden changes in the signal. We calibrate the set point where to lock the phase based on the resulting QD emission intensity (i.e. maximum constructive or destructive interference). For every set point we find the optimal parameters  $P, I, D$  that allow us to minimize the deviation.

In Fig. 5.10 we show the time trace of the QD emission intensity for delay  $\Delta t = 67$  ps and indicate the measurement intervals where the locked

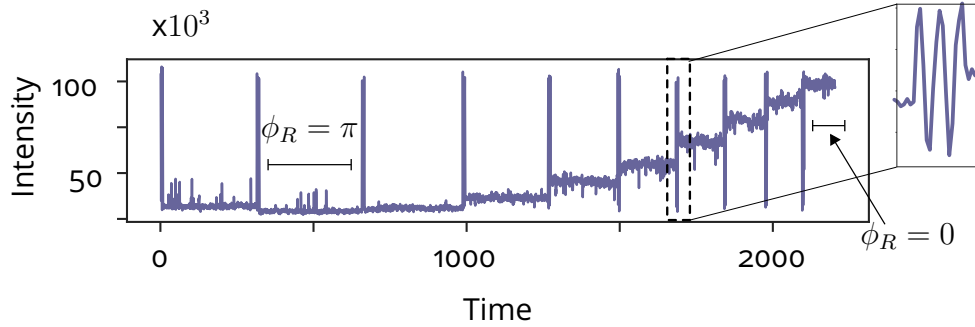


Figure 5.10 – **Locking the Ramsey phase.** The QD emission intensity as a function of time. The inset shows the Ramsey fringes visible when varying the path length difference on the order of the wavelength of the QD. In between scanning of the phase (witnessed here as spikes) the relative phase  $\phi_R$  between two excitation pulses is locked, resulting in a stable emission intensity.

Ramsey phase corresponds to  $\phi_R = \pi$  and  $\phi_R = 0$ . We scan the phase before locking it, as indicated by the Ramsey fringes visible in the inset. In between those scans, the phase is locked and the small residual fluctuations are caused by acoustic noise coming from the lab environment and charge noise in the QD sample.

With the PID controller we can thus prepare excitation pulses of  $\theta = \pi/2$  with relative phases locked to  $\phi_R = 0$  and  $\phi_R = \pi$  – corresponding to maximum emission intensity and minimum emission intensity in Fig. 5.10, respectively – and pulse delay  $\Delta t$ . We apply the prepared excitation sequence to the charged QD at repetition rate  $(\tau_p)^{-1}$ . The resulting photonic field is sent to a detector where we measure the temporally resolved emission intensity. Fig. 5.11 shows an example of the temporal profile of a photonic field acquired with  $\phi_R = 0(\pi)$  and  $\Delta t = 287$  ps in solid (dashed). The rising slopes of the two peaks coincide with the two excitation pulses. We witness a decrease in intensity when the pulses have opposite phase, as expected when considering the evolution of the Bloch vector in Ramsey sequences.

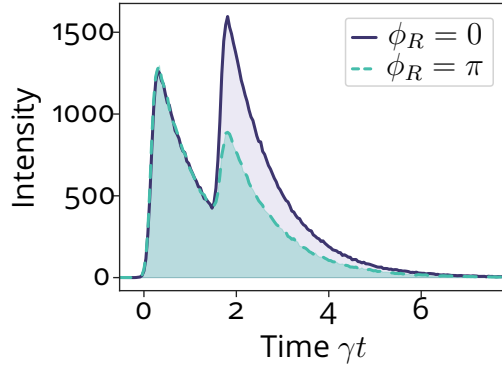


Figure 5.11 – **Lifetimes of the photonic field emitted during the whole Ramsey sequence.** The temporal profile of the spontaneous emission of a quantum emitter when excited by two  $\theta = \pi/2$  pulses separated by  $\Delta t = 287$  ps. For pulses arriving in phase  $\phi_R = 0$  (solid) or out of phase  $\phi_R = \pi$  (dashed). The x-axis is normalized to the lifetime of the emitter  $\gamma^{-1}$ .

#### 5.4.2 . Experimental protocol

In order to quantify the work and heat exchanges during spontaneous emission, we need to measure the first-order coherence present at each point in time in the wavepacket emitted by the QD. We do so by sending the wavepacket  $|\Psi\rangle$ , the resulting emitted field from the Ramsey sequences with locked phase  $\phi_R$ , into an unbalanced Mach-Zehnder interferometer, see Fig. 5.12. Here, two consecutively generated wavepackets – with equal  $\phi_R$  – interfere at BS<sub>2</sub> constructively or destructively depending on the interferometer phase  $\phi$ . **We determine the amount of coherence in the photonic field by probing interferometer phase  $\phi = 0$  (equivalent to  $\phi = \pi$ ), corresponding to maximum constructive (destructive) interference in output port containing detectors  $D_1$  ( $D_2$ ).** In practice, this means that we let the interferometer phase  $\phi$  freely evolve and perform post-selection on the data.

With the two detectors we register the photon arrival times. In addition, we register the laser clock signal, allowing us to build a histogram of photon arrival time after two wavepacket interference, i.e. decay profiles, see Section 2.4.1. At the end of each measurement, we obtain two lists of photon arrival times (one per detector), which we cut into 500ms chunks. For each time chunk we compute the integrated intensity and the decay profiles measured by detector  $D_1$  and  $D_2$  during that time chunk. With the integrated intensities we determine the optical phase  $\phi$  per time chunk, i.e. for each decay profile, according to :  $\phi = \arccos(v(t)/v_{\max})$ .

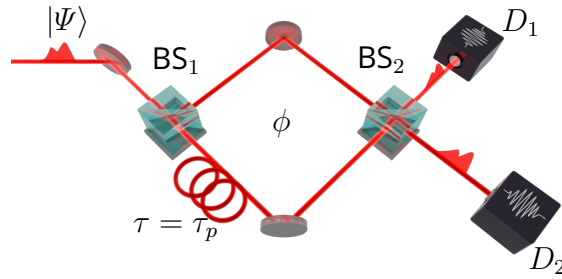


Figure 5.12 – **Extracting temporally resolved coherence transfer.** An unbalanced Mach-Zehnder interferometer where consecutive identical inputs  $|\Psi\rangle$ , taking different paths, interfere at  $BS_2$ . Detectors  $D_1$  and  $D_2$  register the photon events after interference.

Fig. 5.13(b) shows an example of such a visibility time trace for  $\Delta t = 67$  ps and  $\phi_R = \pi$  resulting from the anti-correlated intensities displayed in Fig. 5.13(a). Each time chunk (iteration), corresponding to two decay profile, is now assigned to an interferometer phase  $\phi$ . From this visibility time trace we determine the 5 highest and 5 lowest visibilities ( $\phi = 0(\pi)$ ) – i.e.  $v_{\max}$  – and save the corresponding decay profiles (20 in total). As a result, we have selected the decay profiles corresponding to a measurement where the interferometer phase was  $\phi = 0(\pi)$ . We repeat this procedure for several  $\phi_R$  and  $\Delta t$ .

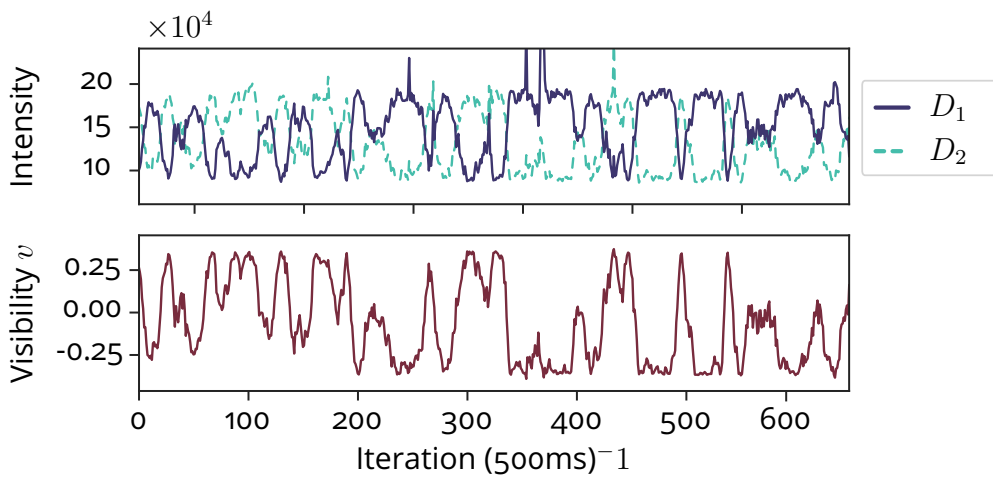


Figure 5.13 – **Extracting Hong-Ou-Mandel phase  $\phi$ .** (a) The integrated intensities measured by detector  $D_1$  and  $D_2$  as a function of time, where each point corresponds to 500ms integration time. (b) The corresponding visibility of interference from which we determine the interferometer phase  $\phi(t)$ .

### 5.4.3 . Heat and work transfer during spontaneous emission

Let us initially consider the delay  $\Delta t = 287$  ps ( $\gamma\Delta t \approx 2\ln(2)$ ). An example of two paired decay profiles – i.e. temporally resolved intensities  $\mu_1(t)$  and  $\mu_2(t)$  – measured with detectors  $D_1$  and  $D_2$  after HOM interference is shown in Fig. 5.14 for (a)  $\phi_R = 0$  and (b)  $\phi_R = \pi$ . We observe two emission peaks, corresponding to the arrival times of the two excitation pulses separated by  $\Delta t$ . For both Ramsey phases we witness constructive (destructive) interference in detector  $D_1$  ( $D_2$ ), indicating interferometer phase  $\phi = 0(\phi = \pi)$ . Moreover, we clearly see the effect of probing with different Ramsey phases :  $\phi_R = 0$  resulting in a second emission peak higher than the initial peak, and  $\phi_R = \pi$  resulting in a lower peak emission after the second pulse arrives.

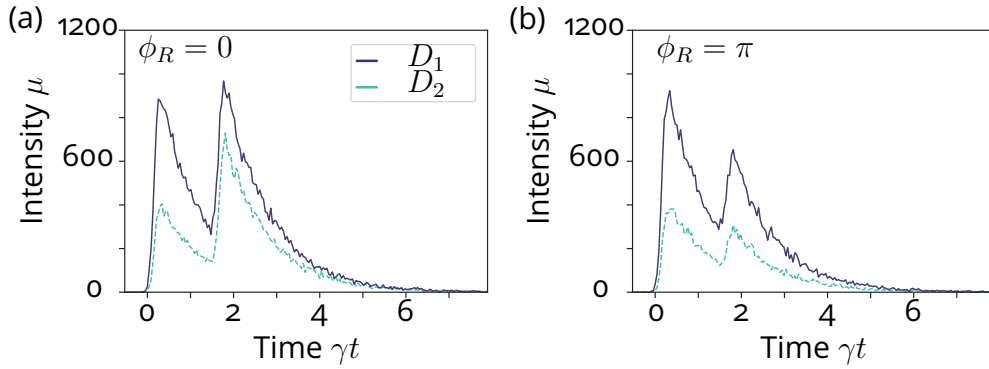


Figure 5.14 – **Temporal profiles after HOM interference.** The temporally resolved photonic wavepackets after interference in a Hong-Ou-Mandel interferometer measured with two detectors  $D_1$  and  $D_2$  monitoring the output ports of the beam splitter. For interferometer phase  $\phi = 0(\pi)$  measured by  $D_1$  ( $D_2$ ) for (a)  $\phi_R = 0$  (b)  $\phi_R = \pi$ .

We compute for both  $\phi_R = 0$  and  $\phi_R = \pi$  the sum of the two temporally resolved intensities  $\mu(t) = \mu_1(t) + \mu_2(t)$ . The sum of the detector intensities is equal to the total energy rate from the qubit to the vacuum of the electromagnetic field :  $\dot{\mathcal{E}}(t)$ , see Fig. 5.15(a) where we normalize each curve by considering that the initial peak corresponds to the energy given by a  $\theta = \pi/2$  pulse in the Ramsey sequence, thus setting the value of the first peak to  $\dot{\mathcal{E}} = \hbar\omega_0 \sin^2(\theta/2) = 1/2$ .

From the temporal profiles, we also calculate the absolute value of the temporally resolved visibility, which is given by :

$$v_{\max}(t) = \frac{|\mu_1(t) - \mu_2(t)|}{\mu_1(t) + \mu_2(t)} = \frac{\dot{\mathcal{W}}}{\dot{\mathcal{E}}}, \quad (5.11)$$

see Sec. 4.3, and is proportional to the efficiency of coherence transfer rate. Note that we explicitly write the time-dependence of  $v_{\max}$  to indicate that we consider

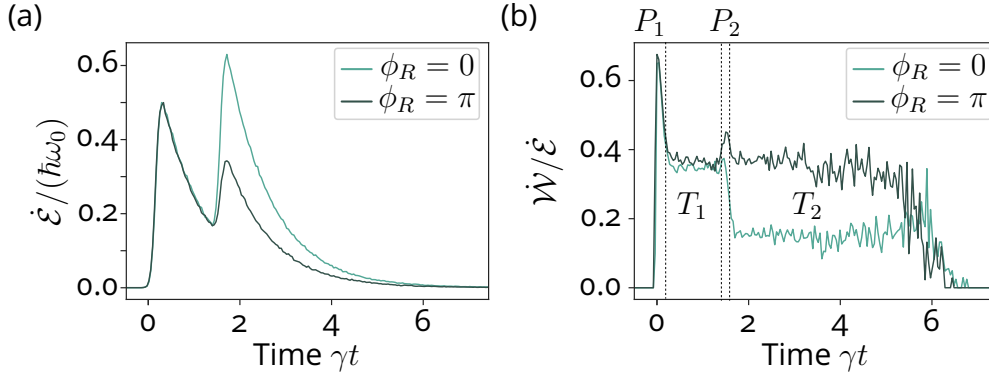


Figure 5.15 - **Temporally resolved energy transfer.** (a) The total energy  $\mathcal{E}$  transferred from the quantum emitter to the vacuum of the electromagnetic field (normalized by the transition energy of the qubit) as a function of time  $t$  (normalized by the lifetime of the emitter  $\gamma^{-1}$ ). (b) The coherence transfer rate as a function of time, where we also indicate the time bins in the Ramsey sequence :  $P_1, T_1, P_2, T_2$ . Both panels show the curves for constructive and destructive Ramsey phase :  $\phi_R = 0$ , and  $\phi_R = \pi$ , respectively.

the temporally resolved visibility of interference. The resulting temporally resolved visibilities of interference are shown in Fig. 5.15(b).

For both  $\phi_R = 0$  and  $\phi_R = \pi$ , we observe two spikes coinciding with the arrival times of the  $\theta = \pi/2$  excitation pulses in time bin  $P_1$  and  $P_2$  (i.e.  $t = 0, t = 287$  ps). These peaks are the direct evidence for the highly ideal emission taking place during the excitation pulses and arise from scattering of coherent laser light (144; 145).

At the end of the laser pulse in time bin  $P_1$  and  $P_2$ , the coherence transfer rate reaches a constant value, evidenced by the plateaus in  $\dot{\mathcal{W}}/\dot{\mathcal{E}}$ . This behavior is expected when considering the evolution of the density matrix of the quantum emitter in time bin  $T_1$  and  $T_2$ . During these time bins, the coherences in the qubit decay according to :

$$s = \sqrt{p_g p_e} e^{-\gamma t/2} = \frac{1}{2} e^{-\gamma t/2 - \gamma^* t}, \quad (5.12)$$

where  $\Gamma = \frac{\gamma}{2} + \gamma^*$  (see Section 2.5.1), and the excited state decays following :

$$P_e = \frac{1}{2} e^{-\gamma t}. \quad (5.13)$$

for  $\theta = \pi/2$ . Considering  $\mathcal{W} = \hbar\omega_0 s^2$  and  $\mathcal{E} = \hbar\omega_0 P_e$ , see Section 4.2, we get for  $\gamma^* \ll \gamma/2$  that the time-dependence in  $\dot{\mathcal{W}}/\dot{\mathcal{E}}$  cancels, resulting in a **constant**

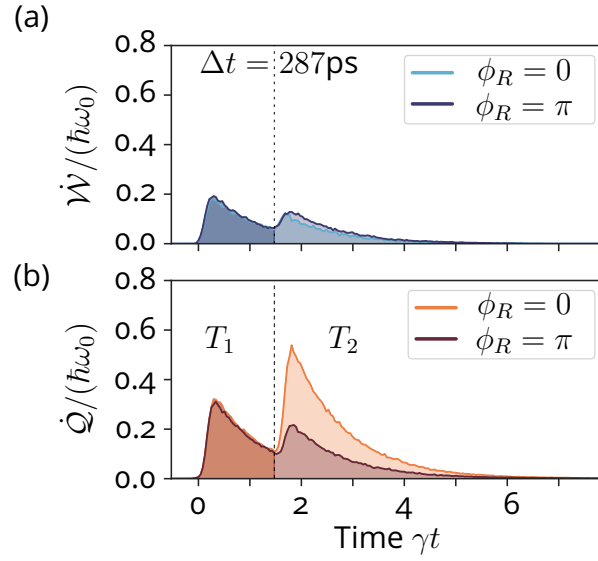


Figure 5.16 – **Temporally resolved work and heat transfer for  $\Delta t = 287$  ps.** (a) The temporally resolved work transfer normalized to the transition energy of the qubit as a function of time for two excitation pulses of pulse area  $\theta = \pi/2$  separated by  $\Delta t = 287$  ps and with relative Ramsey phase  $\phi_R = 0$  and  $\phi_R = \pi$ . (b) The temporally resolved heat transfer normalized to the transition energy of the qubit as a function of time. The dashed vertical line in both panels indicates the threshold between time bins  $T_1$  and  $T_2$ .

**coherence transfer rate** in time bin  $T_1$  and  $T_2$ . This measurement, whereby we measure the temporally resolved visibility in Ramsey sequences for a single delay  $\Delta t$ , thus potentially provides a new tool to quantify the dephasing rate of a quantum emitter.

From the temporally resolved normalized energy transfer and visibility in Fig. 5.15, we calculate the temporally resolved work and heat transfer according to :

$$\dot{W} = v_{\max}(t) \times \dot{\mathcal{E}}, \quad (5.14)$$

$$\dot{Q} = (1 - v_{\max}(t)) \times \dot{\mathcal{E}}, \quad (5.15)$$

where we remove the contribution in coherence coming from the scattered laser field in time bin  $P_1$  and  $P_2$  (spikes in Fig. 5.15(b)). Indeed, we need to discriminate between coherence transfer coming from spontaneous emission and scattered coherent light during the excitation pulse. We therefore extrapolate the plateau in time bin  $T_1$  and  $T_2$  into time bin  $P_1$  and  $P_2$  to include the coherence transfer attributed to spontaneous decay during the pulse. In time bin  $P_2$  the coherence transfer due to spontaneous emission can be attributed to both time bin  $T_1$

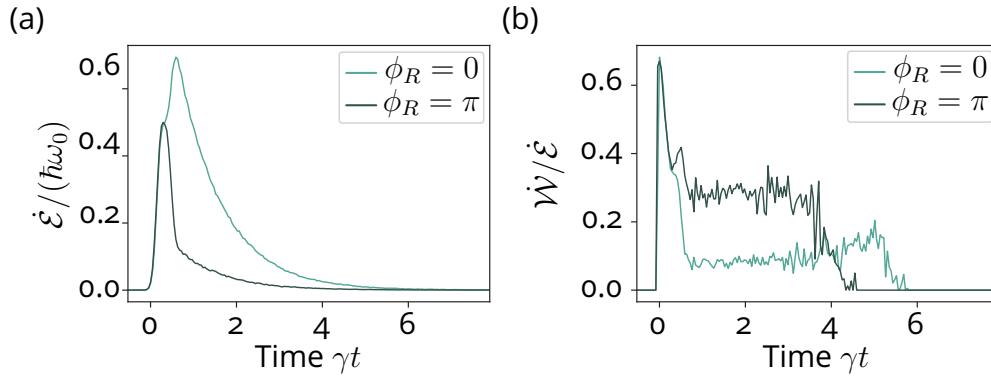


Figure 5.17 – **Temporally resolved energy transfer for  $\Delta t = 67$  ps.** (a) The total energy  $\dot{\mathcal{E}}$  transferred from the quantum emitter to the vacuum of the electromagnetic field (normalized by the transition energy of the qubit) as a function of time  $t$  (normalized by the lifetime of the emitter  $\gamma^{-1}$ ). (b) The coherence transfer rate as a function of time, where we also indicate the time bins in the Ramsey sequence :  $P_1, T_1, P_2, T_2$ . Both panels show the curves for constructive and destructive Ramsey phase :  $\phi_R = 0$ , and  $\phi_R = \pi$ , respectively.

and  $T_2$ , and therefore is divided into two. We calculate the error in work and heat transfer by considering the limiting cases where we attribute the coherence transfer in  $P_2$  fully to  $T_1$  or fully to  $T_2$ . The resulting temporally resolved work and heat transfer for  $\phi_R = 0$  and  $\phi_R = \pi$  are shown in Fig. 5.16 where the dashed vertical line indicates the end (beginning) of time bin  $T_1$  ( $T_2$ ), and corresponds to  $\Delta t = 287$  ps. Interestingly, **the work transfer during spontaneous decay is barely affected by the Ramsey phase, unlike the heat transfer where the second pulse is able to boost the heat transfer. Hence, the enhancement in work absorption for constructive phase  $\phi_R = 0$  mostly results in the generation of energy of correlation nature.**

We perform the same data analysis for pulse separation  $\Delta t = 67$  ps, and plot the temporally resolved total energy transfer and fraction of coherence transfer ( $v_{\max}$ ) as a function of time  $\gamma t$  in Fig. 5.17. We normalize the total energy transfer Fig. 5.17(a) by setting the height of the first peak to  $\dot{\mathcal{E}} = 1/2$ . Although the excitation pulses are separated shortly in time, we can identify the first excitation pulse for  $\phi_R = 0$  as the shoulder in the temporal profile, and normalize it to  $\dot{\mathcal{E}} = 1/2$ . In the temporal profile for  $\phi_R$  we see the effect of driving the qubit with two  $\theta = \pi/2$  pulses of opposite phase : the second pulse brings the qubit closer to the ground state, reducing the emission intensity. Similar to the visibility for  $\Delta t = 287$  ps, we observe in Fig. 5.17(b) a plateau in the coherence transfer in time bin  $T_2$ , indicating no dephasing  $\gamma^* \ll \gamma/2$ .

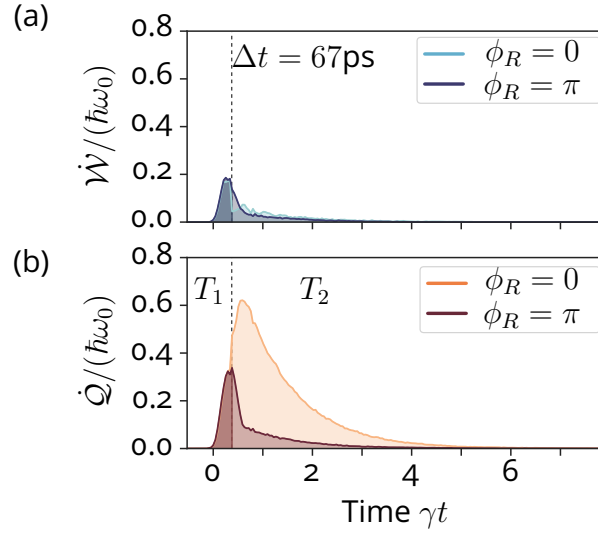


Figure 5.18 – **Temporally resolved work and heat transfer for  $\Delta t = 67$  ps.** (a) The temporally resolved work transfer normalized to the transition energy of the qubit as a function of time for two excitation pulses of pulse area  $\theta = \pi/2$  separated by  $\Delta t = 67$  ps and with relative Ramsey phase  $\phi_R = 0$  and  $\phi_R = \pi$ . (b) The temporally resolved heat transfer normalized to the transition energy of the qubit as a function of time. The dashed vertical lines in both panels indicate the threshold between time bins  $T_1$  and  $T_2$ .

Using Eqs. 5.14 and 5.15, we plot the temporally resolved work and heat transfer for  $\phi_R = 0$  and  $\phi_R = \pi$ , see Fig. 5.18. We see that the main contribution to energy transfer over the decay profile is of heat nature, which is further increased by the second excitation pulse at  $t = 67$  ps (dashed vertical line). Comparable to the temporally resolved work and heat for  $\Delta t = 287$  ps, we find that the work transfer is not affected by the Ramsey phase, whereas the heat transfer is. We can expect such behavior in heat transfer with Ramsey phase, considering that **for  $\phi_R = 0$  we create more entanglement between the qubit and the light field**, which ties in with the nature of the Ramsey sequence : a tool to measure coherence and the ability to maintain the atom-field quantum superposition.

To fully appreciate the differences in work and heat transfer between  $\Delta t = 67$  ps and  $\Delta t = 287$  ps, we calculate the time integrated work  $\mathcal{W}$  and heat  $\mathcal{Q}$  transfer for each time bin and Ramsey phase, Fig. 5.19. We normalize the work and heat in each time bin (per  $\phi_R$ ) by the total energy emitted  $\mathcal{E}(\phi_R = 0) = \mathcal{W} + \mathcal{Q}$  for delay  $\Delta t = 67$  ps. This  $\mathcal{E}$  should be proportional to  $\hbar\omega_0$ , see Fig. 5.3, and thus allows us to visualize the enhancement in energy absorption expected for  $\Delta t = 287$  ps. The largest difference between  $\Delta t = 67$  ps

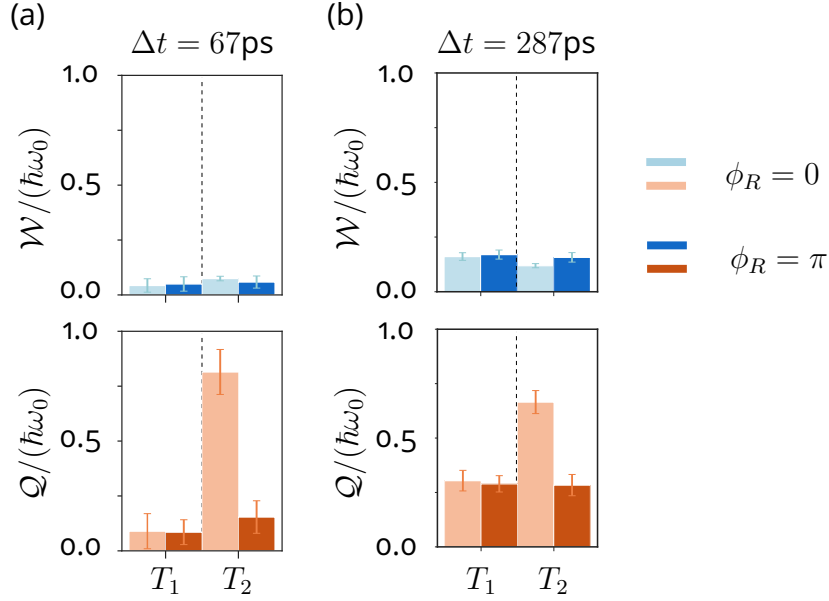


Figure 5.19 – **Integrated work and heat transfer.** The work  $\mathcal{W}$  and heat  $Q$  transferred from the qubit to the vacuum of the electromagnetic field, integrated over time bin  $T_1$  and  $T_2$  and normalized by the transition energy of the qubit. For (a)  $\Delta t = 67$  ps, and (b)  $\Delta t = 287$  ps. Colors indicate the different Ramsey phases  $\phi_R$ .

and  $\Delta t = 287$  ps is indeed observed in the heat transfer, where we witness a larger increase (across time bins) than in the work transfer. From these integrated work and heat we find the total energy (equal to the work absorbed) integrated over  $T_1$  and  $T_2$  for  $\phi_R = 0$  :  $\mathcal{E}(\Delta t = 67\text{ps}) = (1.02 \pm 0.13)\hbar\omega_0$  and  $\mathcal{E}(\Delta t = 287\text{ ps}) = (1.25 \pm 0.09)\hbar\omega_0$ . This latter value is slightly above the theoretically expected maximum achievable work absorbed by the qubit, i.e.  $\mathcal{E} = \mathcal{W}_{\text{abs}} = 9/8\hbar\omega_0$ .

## 5.5 . Signatures of memory effects

While most our observations are qualitatively in agreement with our simple picture presented in Sec. 5.2, we observe interesting deviations arising from the specific nature of our four-level system.

We note that for both  $\Delta t = 67$  ps and  $\Delta t = 287$  ps, the (onset of the) visibility plateau in time bin  $T_1$  (Figs. 5.15, 5.17) reaches a value of  $\dot{\mathcal{W}}/\dot{\mathcal{E}} \approx 0.4$ , a value lower than expected for a  $\theta = \pi/2$  pulse. Indeed, for a pulse of  $\theta = \pi/2$ , we expect the coherence brought to the qubit to be equal to :  $s(\theta = \pi/2) = \cos(\theta/2)\sin(\theta/2) = 1/2$ . We suspect this discrepancy is – similarly

to the data in Sec. 5.3 – due to the build-up of a fluctuating magnetic field caused by nuclear spin noise in the charged quantum dot, **induced when performing two-pulse excitation**, and leading to dephasing and decoherence of the optical states (146; 147). As a result, nuclear spin noise reduces the purity in coherence and thereby the maximum obtainable coherence transfer.

This observation shows that spin memory effects are probably at play in our measurements, and cause reduced coherence transfer and discrepancies between theory – for a two-level system – and experiment in emission intensity  $\mathcal{E} = \mathcal{W}_{\text{abs}}$ . At the time of measurement, we studied various delays  $\Delta t$ , and witnessed another phenomenon which potentially can be explained with this hypothesis, but needs further investigation.

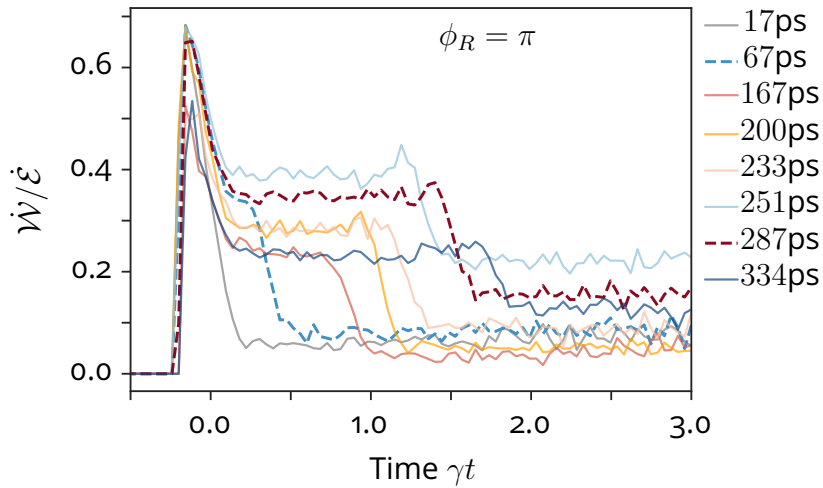


Figure 5.20 – **Delay-dependent coherence transfer.** The temporally resolved visibility of interference  $v = \dot{\mathcal{W}}/\dot{\mathcal{E}}$  as a function of time (normalized by the decay rate of the emitter), shows delay-dependent plateaus, indicating decoherence mechanisms at play.

Fig. 5.20 shows the temporally resolved visibility of interference  $v_{\text{max}}(t) = \dot{\mathcal{W}}/\dot{\mathcal{E}}$  for all probed delays with  $\phi_R = \pi$ , where we highlight the previously studied delays in dashed. We witness a delay-dependent coherence transfer rate, indicated by the varying height of the initial plateau (i.e. time bin  $T_1$ ), which, in addition, never reaches the expected value  $s = 1/2$ . These results led us to choose delays  $\Delta t = 67$  ps and 287 ps for our initial study, since these delays have comparable plateau heights in time bin  $T_1$ , and whose values are closest to the ideal case of  $\dot{\mathcal{W}}/\dot{\mathcal{E}} = 1/2$ , thus allowing us to compare energetics. Indeed, with exception of  $\Delta t = 251$  ps, all other delays seem to suffer more from the unknown source of noise with plateau heights varying between  $\dot{\mathcal{W}}/\dot{\mathcal{E}} = 0.25 - 0.3$ .

## 5.6 . Conclusion and perspectives

In this chapter we have revisited excitation of a four-level system with Ramsey sequences in terms of quantum thermodynamics. Firstly, we discussed how excitation with Ramsey sequences ( $\theta = \pi/2$ ) can lead to an enhanced work absorption of  $\mathcal{W}_{\text{abs}} = 9/8\hbar\omega_0$  when two pulses are delayed by  $\gamma\Delta t = 2\ln(2)$ . Subsequent measurements with out four-level system indeed reveal this enhanced work absorption, witnessed by the increase in emission intensity from our qubit with respect to a single  $\pi$ -pulse.

To understand the nature of the energy emitted by the qubit – and how the enhanced work absorption influences it – we performed homodyne measurements with the wavepackets resulting from Ramsey sequences for  $\Delta t = 67$  ps and  $\Delta t = 287$  ps, where we expect the latter to be close to the delay of maximum work absorption ( $\gamma\Delta t = 2\ln(2)$ ) and the first to be energetically equivalent to excitation with a single  $\pi$ -pulse. After interference, we computed the visibility from the temporally resolved emission intensities (i.e. decay profiles). The resulting visibilities allowed us to temporally resolve the work and heat transfer from the qubit to the vacuum of the electromagnetic field during spontaneous emission. This procedure not only gives us a powerful tool to understand the time resolved energetics of spontaneous emission, but also potentially gives us a new method to measure the dephasing rate of a quantum emitter. Indeed, we qualitatively explained that the observation of plateaus in the temporally resolved visibilities (or coherence transfer rates) can be related to a dephasing rate of  $\gamma^* \ll \gamma/2$ . Hence, any slope observed in between Ramsey excitation could reveal  $\gamma^* \neq 0$ .

The temporally resolved work and heat transfers indicate that the energy emitted by the qubit is mostly of heat nature. Moreover, regardless of delay, the heat is the only quantity that is impacted by the relative phase between the two excitation pulses. The work transfer, on the other hand, is not affected by this phase and remains more or less constant between excitation pulses. This is consistent with the picture that for  $\Delta t \approx 2\ln(2)\gamma^{-1}$  the second pulse with  $\phi_R = 0$  generates additional entanglement between the atom and the emitted field.

The work presented here in this chapter is, however, not finished yet. More analysis needs to be done to understand the data presented, and the potential implications. Different questions need to be addressed, such as whether spin memory effects explain the discrepancy between theory and experiment in work absorption or coherence transfer, or the potential usefulness of the state of light generated by Ramsey sequences.

Finally, one can also imagine a possibility to connect the amount of entanglement between the field and the qubit to the fraction of heat emitted by the qubit

in between, or at the end of a Ramsey sequence. However, to do so requires the ability to distinguish between "quantum" heat and "classical" heat, which is not always possible. Indeed, qubit dephasing also increases the heat transfer efficiency. More theory research needs to be performed to understand if there is a figure of merit which could potentially be used as a witness for entanglement in these protocols, and others.

## 6 - General conclusion and perspectives

In this thesis, we studied the role of photon-number coherence in optical quantum schemes and in the energetics of basic building blocks of photon-based quantum technologies. We conducted experimental studies making use of QD-cavity devices based on deterministic and mature technology.

We first used the QD-cavity system to explore the impact of photon-number coherence in optical quantum schemes. To exemplify the impact, we performed Hong-Ou-Mandel experiments – a pillar of linear quantum information processing – with photon-number superpositions. We showed that the presence of photon-number coherence strongly modifies interference in correlation measurements, compared to the use of single-photon Fock state inputs. We subsequently revealed this strong modification through phase-resolved correlation measurements, and demonstrated that the way of extracting the wavepacket indistinguishability adopted so far in the quantum emitter community should be revisited. Moreover, we showed that phase-resolved correlation measurements can then reveal the presence of a new quantum interference phenomenon, which lead to errors in heralded quantum gate schemes.

In a second part of the thesis, we investigated the role of quantum coherence in the energetic transfers between two systems. We first explained in Chapter 4 how considering a closed bipartite quantum system, allows us to define notions such as work and heat in the quantum regime. Using this framework we then explored the energetic transfers between a qubit and the vacuum of the electromagnetic field that takes place during spontaneous emission, in absence and presence of decoherence. In a second step of our protocol, we measured the energetic exchanges between two light fields interfering at a beam splitter. We showed that we were able to transfer energy from a quantum field onto a classical field, and quantify the nature of the energy transfer, i.e. work or heat. Finally, in our conclusion and perspectives we discussed ways to optimize the discharging process in our protocol.

Finally, we used the energetic framework to revisit another pillar of quantum optics : the Ramsey sequence. We revealed, theoretically and experimentally, how applying a Ramsey sequence to a qubit results in an enhanced energy absorption with respect to a single  $\pi$ -pulse. Moreover, we demonstrated that we were able to temporally resolve the energetic transfers between the qubit and the vacuum of the electromagnetic field in between excitation pulses. Lastly, we discussed the questions to be addressed in the next steps of this study, such as possible spin-based memory effects, or the possibility to define a metric to quantify qubit-field entanglement.

In the following, I will briefly summarize a few possible directions of research, exploiting photon-number coherence.

## 6.1 . On the use of photon-number superpositions

Many optical quantum schemes, such as quantum key distribution, quantum computation or quantum networks for example, rely on the use of single-photon Fock states. However, photon-number superpositions can potentially bring interesting features to established protocols where correlations between the vacuum and one-photon component of the photonic field, can be exploited.

### 6.1.1 . Twin-field quantum key distribution

One interesting approach to quantum key distribution, is the so-called twin-field QKD scheme, which makes use of photon-number superpositions. First proposed in 2018 by Lucamarini et al. (148), the scheme constitutes pairs of optical fields generated at two distant locations (A and B) that are combined at a measuring station (C), where the latter consists of a 50 : 50 beam splitter with two photon detectors monitoring two output ports. In the original proposal, the states generated at station A and B are two attenuated laser fields, both carrying an optical phase. If the two coherent fields, arriving at the beam splitter, carry the same ('twin') phase, they are used to generate a quantum key. The authors predict that the key rate – i.e. the amount of information (bits) per unit time – is comparable to other QKD schemes, which is given by the square root of the channel transmittance :  $\sqrt{\eta}$ . However, as the authors mention, this scheme could potentially drastically outperform other schemes and extend the distance of secure quantum key distribution. This better scaling over distance is due to mainly the fact that twin-field QKD uses a central station "C" that mitigates the exponential losses into fiber links. Additionally, even though it requires two sources at stations A and B, the principle relies on the detection of a single click by the detectors, thus, making twin-field QKD more robust against losses.

Since the first publication, other proposals have been put forward whereby the authors consider changes to the original protocol such as removing the requirement of post-selection on the 'twin' phase (149), changing the combination of input states into station A and B (150; 151), or considering different network structures (152). These changes, the authors predict, possibly can increase the key rate over long distances, and help scaling the technologies to realistic multi-users network infrastructures. Subsequently, researchers were able to implement the protocol suggested by Ref. (149) and achieve twin-field key distribution between two cities separated by more than 500 km, with key rates orders of magnitudes larger than other schemes (3).

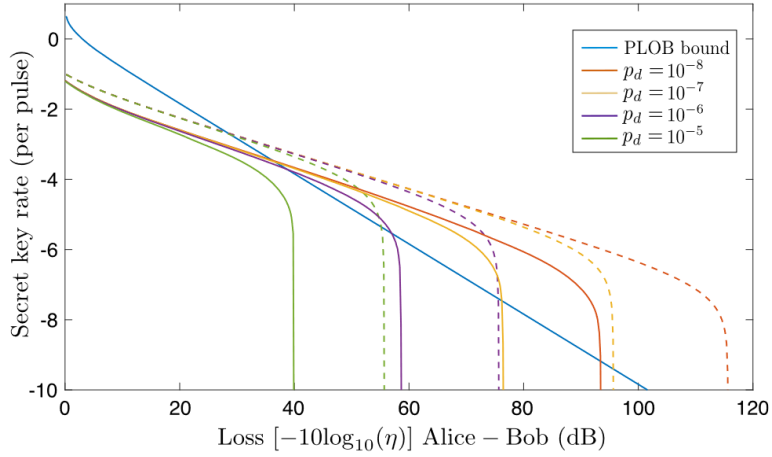


Figure 6.1 – **Twin-field QKD with different sources.** The key rate as a function of overall channel losses between stations A (Alice) and B (Bob) for different light sources, attenuated laser (solid) or photon-number superposition states (dashed). Color-coded is the dark counts noise ( $p_d$ , colors), together with the fundamental PLOB bound (blue). Taken from Ref. (149). See main text for details.

Crucially, all twin-field QKD experiments so far have been based on the use of attenuated coherent fields. Contrastingly, the authors of Refs. (95; 149) predict that the use of photon-number superpositions of the form

$$|\pm\rangle = \sqrt{p_0} |0\rangle \pm e^{i\phi} \sqrt{p_1} |1\rangle, \quad (6.1)$$

as input states, can potentially outperform attenuated laser fields in twin-field QKD by tens of dB. This prediction can be understood by considering that for attenuated laser pulses, the photon statistics are those of a coherent source. Therefore, suppressing the two-photon component (which is vulnerable to photon splitting attacks) requires a strong attenuation and the usage of additional states (decoy states) to prevent eavesdropping. Fig. 6.1, taken from Ref. (149), shows the predicted key rates as a function of overall loss between A (Alice) and B (Bob) for different scenarios where the colors ( $p_d$ ) indicate the different dark counts, and blue the PLOB bound (153), which is a fundamental limit to the secret key rate obtained in repeaterless schemes (i.e. no additional measurements, nodes needed). The two protocols studied here either consider attenuated laser fields as input to A and B (solid lines), or a photon-number superposition according to Eq. 6.1 input to A(B) and  $|0\rangle$  or  $|1\rangle$  input to A(B) (dashed lines). As seen in Fig. 6.1, the authors predict that under certain conditions, implementing photon-number superpositions can surpass the PLOB bound and outperform the use of coherent fields, showing the potential photon-number superpositions in twin-field QKD.

The demonstration of coherent control over the photon-number superposition state (83), and the capability to interfere two different sources (Section 4), potentially opens up the road to the use of QD-cavity systems in twin-field QKD protocols. Additionally, the first demonstration of active phase stabilization in our lab (Section 5), can also remove the requirement of post-selection on the 'twin' phase. As a result, recently, Dr. Dario Fioretto started to implement twin-field QKD protocols using our QD-cavity systems as sources to test whether we can reach the theoretical predicted curves, and perhaps extend the schemes by using two different QD sources.

### 6.1.2 . Compensating for photon-number coherence in quantum gates

In Chapter 3 we discussed the impact of photon-number coherence on the performance and fidelity of quantum gates. At Quandela, researchers are currently looking into ways to overcome the negative impact of coherent photon-number superpositions using the Perceval platform (104). In the past, researchers already studied ways to compensate for source inefficiencies (i.e. brightness) or detector inefficiencies (154), or for imperfect beam splitters (155) in heralded CNOT gates. Both Ref. (154) and Ref. (155) predict that one can compensate for these imperfections and increase the fidelity by changing gate parameters (e.g. beam splitter ratios). In Ref. (155), the authors test this hypothesis by simulating a reconfigurable photonic processor (an integrated photonic circuit) that allows to tune the gate parameters. Based on the results of the simulation the authors predict that a reconfigurable chip could form a solution to errors in quantum gate performance due to losses. Such a chip was simultaneously experimentally fabricated and tested by the authors of Ref. (156), demonstrating the feasibility of such a scheme.

These studies, so far, only discussed changing gate parameters to overcome photon losses. New methods should be developed to overcome the effects of photon-number coherence leading to single-photon interference effects.

### 6.1.3 . Towards continuous variable quantum computation

In Sec. 5.2 we have shown that the photonic state resulting from double pulse excitation is of the form :

$$|\Psi\rangle = \frac{1}{2}[(1 - e^{-i\phi_R}\alpha)|0_e0_l\rangle + (e^{i\phi_R} + \alpha)|0_e1_l\rangle + \beta|1_e0_l\rangle + e^{i\phi_R}\beta|1_e1_l\rangle], \quad (6.2)$$

a state which is partially entangled in the time bin basis with a photon emitted in the early (*e*) time bin  $T_1$  and/or in the late (*l*) time bin  $T_2$ , and a state which is partially coherent since most energy arises from correlations (of heat nature).

Our experimental setup in Chapter 5 also allowed to perform time-resolved intensity correlation measurements whereby we collect time tags of coincidences in an HOM measurement with respect to a laser clock signal. With this data

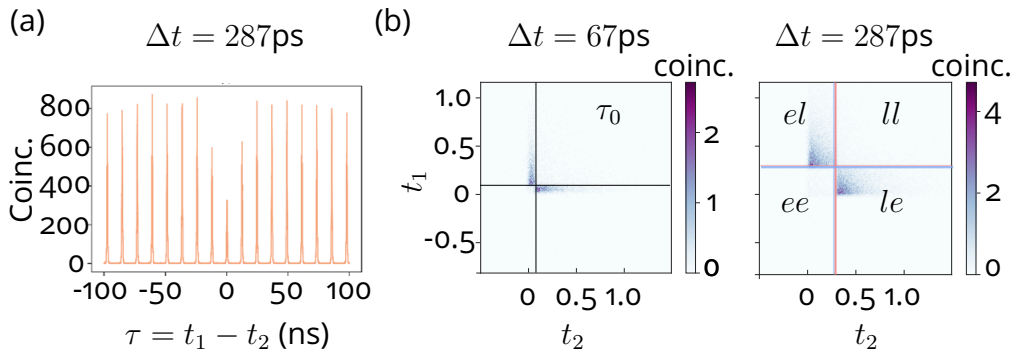


Figure 6.2 – **Time bin entanglement.** (a) A coincidence histogram as a function of delay  $\tau$  obtained with HOM measurements with the photonic state generated in Ramsey sequences for  $\Delta t = 287$  ps. (b) The two-time coincidence map of the zero delay peak ( $\tau = 0 = \tau_0$  in coincidence histograms) for  $\Delta t = 67$  ps and 287 ps, with  $\tau = t_1 - t_2$ , divided into quadrants corresponding to the early  $e$  and late  $l$  time bins of Eq. 6.2.

we can not only compute coincidence histograms such as the one shown in Fig. 6.2(a) for  $\Delta t = 287$  ps, but also two-time coincidence maps  $G^{(2)}(t_1, t_2)$ , Fig. 6.2(b). Essentially, such a map is created by considering that any coincidence in a histogram is related to two detection event times :  $\tau = t_1 - t_2$ . Hence, once  $t_1$  and  $t_2$  are known, we can visualize the correlations between clicks in a 2D coincidence map with  $t_1$  and  $t_2$  on the x,y-axes.

In Fig. 6.2(b) we plot the two-time coincidence maps of the zero delay peak  $\tau_0$  for  $\Delta t = 67$  ps and 287 ps, where the latter map corresponds to the zero delay peak in the histogram in Fig. 6.2(a). We can divide both maps into quadrants based on the early ( $e$ ) and late ( $l$ ) time bins. We observe for the zero delay peaks that we only obtain coincidences between different time bins (i.e.  $el$  and  $le$ ), indicating that the two photons in Eq. 6.2 are indeed temporally separated. These two-time coincidence maps reveal interesting entangled states of light generated with Ramsey sequences, which potentially can be extended by multiple  $\pi/2$ -pulses to generate more complex states of light, and could be of great interest for continuous variable quantum computing.

In our group, within the PhD of Hubert Lam, different types of quantum light states for quantum computing are currently investigated, exploring their potential use in continuous variable schemes. Further research can focus on characterization of these output states of light produced in Ramsey interferometry or other common excitation protocols (36), and the potential possibility to produce high-dimensional entanglement by extending the protocol to include spin-photon entanglement for example.

## 6.2 . On the energetics of optical quantum computing

As discussed in Chapter 4, quantum thermodynamics is a relatively young field whose focus so far has mainly been on theory. As such, much experimental research is needed for testing proposed theories and push them further towards realistic systems.

### 6.2.1 . Energetic exchanges at a beam splitter

In Chapter 4 we demonstrated how self-homodyne and homodyne measurements between quantum fields and between a quantum field and a coherent field allow to measure the work and heat transferred from one field to another. It would be interesting, for the field of quantum optics and quantum thermodynamics, to explore more variations of input states to a beam splitter and push further the energetics of a beam splitter. Possible scenarios to study would be the interference between two different quantum fields, for a variety of input states. Additionally, one could investigate ways of optimizing work transfer at the beam splitter. Such an extensive study could potentially reveal methods of mitigating the energetic footprint of optical quantum technologies (157).

### 6.2.2 . Energetics of entangling states

Another possibility could be to investigate the energetics of the generation of entangled photonic states of light. Such states, GHZ (158) or cluster (159) states for example, are at the core of measurement-based quantum computing and quantum networks and anticipated to overcome the difficulties encountered when performing quantum logical gates with single-photons (Section 3) (160; 161). From a thermodynamic point-of-view, it would thus be interesting to compare the energetics of spin-based (cluster) to post-selection-based (GHZ) entanglement, and potentially predict the energetic benefit of using one scheme over the other.

## Bibliographie

- [1] Nobel Prize Outreach AB 2023. Press Release (2023). URL <https://www.nobelprize.org/prizes/physics/2022/press-release/>.
- [2] Basset, F. B. *et al.* Quantum key distribution with entangled photons generated on demand by a quantum dot. *Science Advances* **7**, eabe6379 (2021). URL <https://www.science.org/doi/abs/10.1126/sciadv.abe6379>.
- [3] Chen, J.-P. *et al.* Twin-field quantum key distribution over a 511km optical fibre linking two distant metropolitan areas. *Nature Photonics* **15**, 570–575 (2021). URL <https://doi.org/10.1038/s41566-021-00828-5>.
- [4] Childress, L. & Hanson, R. Diamond NV centers for quantum computing and quantum networks. *MRS Bulletin* **38**, 134–138 (2013). URL <https://doi.org/10.1557/mrs.2013.20>.
- [5] Lu, C.-Y. & Pan, J.-W. Quantum-dot single-photon sources for the quantum internet. *Nature Nanotechnology* **16**, 1294–1296 (2021). URL <https://doi.org/10.1038/s41565-021-01033-9>.
- [6] Ulanov, A. E., Fedorov, I. A., Sychev, D., Grangier, P. & Lvovsky, A. I. Loss-tolerant state engineering for quantum-enhanced metrology via the reverse Hong-Ou-Mandel effect. *Nature Communications* **7**, 1–6 (2016).
- [7] Dowling, J. P. Quantum optical metrology – the lowdown on high-N00N states. *Contemporary Physics* **49**, 125–143 (2008). URL <https://doi.org/10.1080/00107510802091298>.
- [8] Pezzè, L., Smerzi, A., Oberthaler, M. K., Schmied, R. & Treutlein, P. Quantum metrology with nonclassical states of atomic ensembles. *Reviews of Modern Physics* **90** (2018).
- [9] Zhong, H.-S. *et al.* Quantum computational advantage using photons. *Science* **370**, 1460–1463 (2020). URL <https://www.science.org/doi/abs/10.1126/science.abe8770>.
- [10] Kwiat, P. G. *et al.* New High-Intensity Source of Polarization-Entangled Photon Pairs. *Phys. Rev. Lett.* **75**, 4337–4341 (1995). URL <https://link.aps.org/doi/10.1103/PhysRevLett.75.4337>.
- [11] Ou, Z. Y., Pereira, S. F., Kimble, H. J. & Peng, K. C. Realization of the Einstein-Podolsky-Rosen paradox for continuous variables. *Phys. Rev. Lett.* **68**, 3663–3666 (1992). URL <https://link.aps.org/doi/10.1103/PhysRevLett.68.3663>.

- [12] Turchette, Q. A., Hood, C. J., Lange, W., Mabuchi, H. & Kimble, H. J. Measurement of Conditional Phase Shifts for Quantum Logic. *Phys. Rev. Lett.* **75**, 4710–4713 (1995). URL <https://link.aps.org/doi/10.1103/PhysRevLett.75.4710>.
- [13] Somaschi, N. *et al.* Near-optimal single-photon sources in the solid state. *Nature Photonics* **10**, 340–345 (2016). URL <https://doi.org/10.1038/nphoton.2016.23>.
- [14] Tomm, N. *et al.* A bright and fast source of coherent single photons. *Nature Nanotechnology* **16**, 399–403 (2021). URL <http://dx.doi.org/10.1038/s41565-020-00831-x>.
- [15] Schell, A. W. *et al.* Single defect centers in diamond nanocrystals as quantum probes for plasmonic nanostructures. *Opt. Express* **19**, 7914–7920 (2011). URL <https://opg.optica.org/oe/abstract.cfm?URI=oe-19-8-7914>.
- [16] Sipahigil, A. *et al.* Indistinguishable Photons from Separated Silicon-Vacancy Centers in Diamond. *Phys. Rev. Lett.* **113**, 113602 (2014). URL <https://link.aps.org/doi/10.1103/PhysRevLett.113.113602>.
- [17] Tchernij, S. D. *et al.* Single-Photon-Emitting Optical Centers in Diamond Fabricated upon Sn Implantation. *ACS Photonics* **4**, 2580–2586 (2017). URL <https://doi.org/10.1021/acsp Photonics.7b00904>.
- [18] Bradac, C., Gao, W., Forneris, J., Trusheim, M. E. & Aharonovich, I. Quantum nanophotonics with group IV defects in diamond. *Nature Communications* **10**, 5625 (2019). URL <https://doi.org/10.1038/s41467-019-13332-w>.
- [19] Kiraz, A. *et al.* Indistinguishable Photons from a Single Molecule. *Phys. Rev. Lett.* **94**, 223602 (2005). URL <https://link.aps.org/doi/10.1103/PhysRevLett.94.223602>.
- [20] Rezus, Y. L. A. *et al.* Single-Photon Spectroscopy of a Single Molecule. *Phys. Rev. Lett.* **108**, 93601 (2012). URL <https://link.aps.org/doi/10.1103/PhysRevLett.108.093601>.
- [21] Zhang, L. *et al.* Electrically driven single-photon emission from an isolated single molecule. *Nature Communications* **8**, 580 (2017). URL <https://doi.org/10.1038/s41467-017-00681-7>.
- [22] Kuhn, A., Hennrich, M. & Rempe, G. Deterministic Single-Photon Source for Distributed Quantum Networking. *Phys. Rev. Lett.* **89**, 67901 (2002). URL <https://link.aps.org/doi/10.1103/PhysRevLett.89.067901>.

- [23] Hijlkema, M. *et al.* A single-photon server with just one atom. *Nature Physics* **3**, 253–255 (2007). URL <https://doi.org/10.1038/nphys569>.
- [24] Ripka, F., Kübler, H., Löw, R. & Pfau, T. A room-temperature single-photon source based on strongly interacting Rydberg atoms. *Science* **362**, 446–449 (2018). URL <https://doi.org/10.1126/science.aau1949>.
- [25] Santori, C., Fattal, D., Vučković, J., Solomon, G. S. & Yamamoto, Y. Indistinguishable photons from a single-photon device. *Nature* **419**, 594–597 (2002). URL <https://doi.org/10.1038/nature01086>.
- [26] Claudon, J. *et al.* A highly efficient single-photon source based on a quantum dot in a photonic nanowire. *Nature Photonics* **4**, 174–177 (2010). URL <https://doi.org/10.1038/nphoton.2009.287x>.
- [27] Purcell, E. M., Torrey, H. C. & Pound, R. V. Resonance Absorption by Nuclear Magnetic Moments in a Solid. *Phys. Rev.* **69**, 37–38 (1946). URL <https://link.aps.org/doi/10.1103/PhysRev.69.37>.
- [28] Solomon, G. S., Pelton, M. & Yamamoto, Y. Single-mode Spontaneous Emission from a Single Quantum Dot in a Three-Dimensional Microcavity. *Phys. Rev. Lett.* **86**, 3903–3906 (2001). URL <https://link.aps.org/doi/10.1103/PhysRevLett.86.3903>.
- [29] Pelton, M. *et al.* Efficient Source of Single Photons : A Single Quantum Dot in a Micropost Microcavity. *Phys. Rev. Lett.* **89**, 233602 (2002). URL <https://link.aps.org/doi/10.1103/PhysRevLett.89.233602>.
- [30] Senellart, P., Solomon, G. & White, A. High-performance semiconductor quantum-dot single-photon sources. *Nature Nanotechnology* **12**, 1026–1039 (2017). URL <http://dx.doi.org/10.1038/nnano.2017.218>.
- [31] Knill, E., Laflamme, R. & Milburn, G. J. A scheme for efficient quantum computation with linear optics. *Nature* **409**, 46–52 (2001). URL <https://doi.org/10.1038/35051009>.
- [32] Hong, C. K., Ou, Z. Y. & Mandel, L. Measurement of subpicosecond time intervals between two photons by interference. *Phys. Rev. Lett.* **59**, 2044–2046 (1987). URL <https://link.aps.org/doi/10.1103/PhysRevLett.59.2044>.
- [33] Hong, S. *et al.* Quantum enhanced multiple-phase estimation with multi-mode N00N states. *Nature Communications* **12** (2021).
- [34] Flissikowski, T., Betke, A., Akimov, I. A. & Henneberger, F. Two-Photon Coherent Control of a Single Quantum Dot. *Phys. Rev. Lett.* **92**, 227401

- (2004). URL <https://link.aps.org/doi/10.1103/PhysRevLett.92.227401>.
- [35] Rabi, I. I. Space Quantization in a Gyating Magnetic Field. *Phys. Rev.* **51**, 652–654 (1937). URL <https://link.aps.org/doi/10.1103/PhysRev.51.652>.
- [36] Wein, S. C. *et al.* Photon-number entanglement generated by sequential excitation of a two-level atom. *arXiv* **2106.02049** (2021).
- [37] Monsel, J., Fellous-Asiani, M., Huard, B. & Auffèves, A. The Energetic Cost of Work Extraction. *Physical Review Letters* **124**, 1–6 (2020).
- [38] Maffei, M., Camati, P. A. & Auffèves, A. Probing nonclassical light fields with energetic witnesses in waveguide quantum electrodynamics. *Phys. Rev. Research* **3**, L032073 (2021). URL <https://link.aps.org/doi/10.1103/PhysRevResearch.3.L032073>.
- [39] Renema, J. J. Simulability of partially distinguishable superposition and Gaussian boson sampling. *Phys. Rev. A* **101**, 63840 (2020). URL <https://link.aps.org/doi/10.1103/PhysRevA.101.063840>.
- [40] Thomas, S. E. *et al.* Bright Polarized Single-Photon Source Based on a Linear Dipole. *Phys. Rev. Lett.* **126**, 233601 (2021). URL <https://link.aps.org/doi/10.1103/PhysRevLett.126.233601>.
- [41] Gérard, J. M. *et al.* Enhanced Spontaneous Emission by Quantum Boxes in a Monolithic Optical Microcavity. *Phys. Rev. Lett.* **81**, 1110–1113 (1998). URL <https://link.aps.org/doi/10.1103/PhysRevLett.81.1110>.
- [42] Giesz, V. *et al.* Coherent manipulation of a solid-state artificial atom with few photons. *Nature Communications* **7** (2016).
- [43] Ollivier, H. *et al.* Reproducibility of High-Performance Quantum Dot Single-Photon Sources. *ACS Photonics* **7**, 1050–1059 (2020). URL <https://doi.org/10.1021/acsp Photonics.9b01805>.
- [44] Michler, P. *et al.* A Quantum Dot Single-Photon Turnstile Device. *Science* **290**, 2282–2285 (2000). URL <https://www.science.org/doi/abs/10.1126/science.290.5500.2282>.
- [45] Moreau, E. *et al.* Single-mode solid-state single photon source based on isolated quantum dots in pillar microcavities. *Applied Physics Letters* **79**, 2865–2867 (2001). URL <http://aip.scitation.org/doi/10.1063/1.1415346>.

- [46] Kupko, T. *et al.* Tools for the performance optimization of single-photon quantum key distribution. *npj Quantum Information* **6**, 29 (2020). URL <https://doi.org/10.1038/s41534-020-0262-8>.
- [47] Wang, H. *et al.* High-efficiency multiphoton boson sampling. *Nature Photonics* **11**, 361–365 (2017). URL <https://doi.org/10.1038/nphoton.2017.63>.
- [48] Auffèves-Garnier, A., Simon, C., Gérard, J.-M. & Poizat, J.-P. Giant optical nonlinearity induced by a single two-level system interacting with a cavity in the Purcell regime. *Phys. Rev. A* **75**, 53823 (2007). URL <https://link.aps.org/doi/10.1103/PhysRevA.75.053823>.
- [49] Muller, A. *et al.* Resonance Fluorescence from a Coherently Driven Semiconductor Quantum Dot in a Cavity. *Phys. Rev. Lett.* **99**, 187402 (2007). URL <https://link.aps.org/doi/10.1103/PhysRevLett.99.187402>.
- [50] Cosacchi, M. *et al.* On-demand generation of higher-order Fock states in quantum-dot-cavity systems. *Phys. Rev. Research* **2**, 33489 (2020). URL <https://link.aps.org/doi/10.1103/PhysRevResearch.2.033489>.
- [51] Marzin, J. Y., Gérard, J. M., Izraël, A., Barrier, D. & Bastard, G. Photoluminescence of Single InAs Quantum Dots Obtained by Self-Organized Growth on GaAs. *Phys. Rev. Lett.* **73**, 716–719 (1994). URL <https://link.aps.org/doi/10.1103/PhysRevLett.73.716>.
- [52] Baskaran, A. & Smereka, P. Mechanisms of Stranski-Krastanov growth. *Journal of Applied Physics* **111**, 044321 (2012). URL <http://aip.scitation.org/doi/10.1063/1.3679068>.
- [53] Goldstein, L., Glas, F., Marzin, J. Y., Charasse, M. N. & Le Roux, G. Growth by molecular beam epitaxy and characterization of InAs/GaAs strained-layer superlattices. *Applied Physics Letters* **47**, 1099–1101 (1985). URL <http://aip.scitation.org/doi/10.1063/1.96342>.
- [54] Madelung, O. *Semiconductors : data handbook* (Springer, 2004).
- [55] de Santis, L. *Single photon generation and manipulation with semiconductor quantum dot devices*. Ph.D. thesis, Université Paris Saclay (COMUE) (2018). URL <https://tel.archives-ouvertes.fr/tel-01783546>.
- [56] Solomon, G. S., Trezza, J. A. & Harris, J. S. Effects of monolayer coverage, flux ratio, and growth rate on the island density of InAs islands on GaAs. *Applied Physics Letters* **66**, 3161–3163 (1995). URL <http://aip.scitation.org/doi/10.1063/1.113709>.

- [57] Stier, O., Grundmann, M. & Bimberg, D. Electronic and optical properties of strained quantum dots modeled by 8-band  $k \cdot p$  theory. *Phys. Rev. B* **59**, 5688–5701 (1999). URL <https://link.aps.org/doi/10.1103/PhysRevB.59.5688>.
- [58] Reimann, S. M. & Manninen, M. Electronic structure of quantum dots. *Rev. Mod. Phys.* **74**, 1283–1342 (2002). URL <https://link.aps.org/doi/10.1103/RevModPhys.74.1283>.
- [59] Bester, G. Electronic excitations in nanostructures : an empirical pseudopotential based approach. *Journal of Physics : Condensed Matter* **21**, 023202 (2009). URL <https://iopscience.iop.org/article/10.1088/0953-8984/21/2/023202>.
- [60] Lodahl, P., Mahmoodian, S. & Stobbe, S. Interfacing single photons and single quantum dots with photonic nanostructures. *Rev. Mod. Phys.* **87**, 347–400 (2015). URL <https://link.aps.org/doi/10.1103/RevModPhys.87.347>.
- [61] Franceschetti, A., Wang, L., Fu, H. & Zunger, A. Short-range versus long-range electron-hole exchange interactions in semiconductor quantum dots. *Physical Review B - Condensed Matter and Materials Physics* **58**, R13367–R13370 (1998).
- [62] Luo, J. W., Bester, G. & Zunger, A. Long- And short-range electron-hole exchange interaction in different types of quantum dots. *New Journal of Physics* **11** (2009).
- [63] Tong, H. & Wu, M. W. Theory of excitons in cubic III-V semiconductor GaAs, InAs and GaN quantum dots : Fine structure and spin relaxation. *Phys. Rev. B* **83**, 235323 (2011). URL <https://link.aps.org/doi/10.1103/PhysRevB.83.235323>.
- [64] Ollivier, H. *Quantum purity and symmetry control of single-photon sources based on semiconductor quantum dots*. Ph.D. thesis, Université Paris-Saclay (2021). URL <https://tel.archives-ouvertes.fr/tel-03378446>.
- [65] Seguin, R. *et al.* Size-Dependent Fine-Structure Splitting in Self-Organized InAs/GaAs Quantum Dots. *Phys. Rev. Lett.* **95**, 257402 (2005). URL <https://link.aps.org/doi/10.1103/PhysRevLett.95.257402>.
- [66] Hilaire, P. *et al.* Deterministic assembly of a charged-quantum-dot-micropillar cavity device. *Phys. Rev. B* **102**, 195402 (2020). URL <https://link.aps.org/doi/10.1103/PhysRevB.102.195402>.

- [67] Drexler, H., Leonard, D., Hansen, W., Kotthaus, J. P. & Petroff, P. M. Spectroscopy of Quantum Levels in Charge-Tunable InGaAs Quantum Dots. *Phys. Rev. Lett.* **73**, 2252–2255 (1994). URL <https://link.aps.org/doi/10.1103/PhysRevLett.73.2252>.
- [68] Gerry, C. & Knight, P. *Introductory Quantum Optics* (Cambridge University Press, 2004).
- [69] Haroche, S. & Kleppner, D. Cavity quantum electrodynamics. *Physics Today* **42**, 24–30 (1989). URL <https://doi.org/10.1063/1.881201>.
- [70] Gerard, J.-M. & Gayral, B. Strong Purcell effect for InAs quantum boxes in three-dimensional solid-state microcavities. *Journal of Lightwave Technology* **17**, 2089–2095 (1999).
- [71] Auffèves, A. *et al.* Controlling the dynamics of a coupled atom-cavity system by pure dephasing. *Phys. Rev. B* **81**, 245419 (2010). URL <https://link.aps.org/doi/10.1103/PhysRevB.81.245419>.
- [72] Andreani, L. C., Panzarini, G. & Gérard, J.-M. Strong-coupling regime for quantum boxes in pillar microcavities : Theory. *Phys. Rev. B* **60**, 13276–13279 (1999). URL <https://link.aps.org/doi/10.1103/PhysRevB.60.13276>.
- [73] Dousse, A. *et al.* Controlled Light-Matter Coupling for a Single Quantum Dot Embedded in a Pillar Microcavity Using Far-Field Optical Lithography. *Phys. Rev. Lett.* **101**, 267404 (2008). URL <https://link.aps.org/doi/10.1103/PhysRevLett.101.267404>.
- [74] Nowak, A. K. *et al.* Deterministic and electrically tunable bright single-photon source. *Nat. Commun.* **5**, 1–7 (2014).
- [75] Antón, C. *et al.* Tomography of the optical polarization rotation induced by a single quantum dot in a cavity. *Optica* **4**, 1326–1332 (2017). URL <https://opg.optica.org/optica/abstract.cfm?URI=optica-4-11-1326>.
- [76] Mandel, L. & Wolf, E. *Optical Coherence and Quantum Optics* (Cambridge University Press, 1995).
- [77] Ralph, T. C., Langford, N. K., Bell, T. B. & White, A. G. Linear optical controlled-NOT gate in the coincidence basis. *Physical Review A - Atomic, Molecular, and Optical Physics* **65**, 5 (2002). [0112088v1](https://doi.org/10.1103/PhysRevA.65.052301).
- [78] O’Brien, J. L., Pryde, G. J., White, A. G., Ralph, T. C. & Branning, D. Demonstration of an all-optical quantum controlled-NOT gate. *Nature* **426**, 264–267 (2003). URL <https://doi.org/10.1038/nature02054>.

- [79] Kiraz, A., Atatüre, M. & Imamoglu, A. Quantum-dot single-photon sources : Prospects for applications in linear optics quantum-information processing. *Phys. Rev. A* **69**, 32305 (2004). URL <https://link.aps.org/doi/10.1103/PhysRevA.69.032305>.
- [80] Trivedi, R., Fischer, K. A., Vučković, J. & Müller, K. Generation of Non-Classical Light Using Semiconductor Quantum Dots. *Advanced Quantum Technologies* **3**, 1900007 (2020). URL <https://onlinelibrary.wiley.com/doi/abs/10.1002/qute.201900007>.
- [81] Ollivier, H. *et al.* Hong-Ou-Mandel Interference with Imperfect Single Photon Sources. *Physical Review Letters* **126**, 1–9 (2021).
- [82] Fischer, K. A. *et al.* Pulsed Rabi oscillations in quantum two-level systems : beyond the area theorem. *Quantum Science and Technology* **3**, 014006 (2018). URL <https://iopscience.iop.org/article/10.1088/2058-9565/aa9269>.
- [83] Loredó, J. C. *et al.* Generation of non-classical light in a photon-number superposition. *Nature Photonics* **13**, 803–808 (2019). URL <https://doi.org/10.1038/s41566-019-0506-3>.
- [84] Reiserer, A. & Rempe, G. Cavity-based quantum networks with single atoms and optical photons. *Rev. Mod. Phys.* **87**, 1379–1418 (2015). URL <https://link.aps.org/doi/10.1103/RevModPhys.87.1379>.
- [85] Jaynes, E. T. & Cummings, F. W. Comparison of quantum and semiclassical radiation theories with application to the beam maser (1962).
- [86] Wein, S. C. Modelling Markovian light-matter interactions for quantum optical devices in the solid state (2021). URL <http://arxiv.org/abs/2105.06580>.
- [87] Manzano, D. A short introduction to the Lindblad master equation. *AIP Advances* **10** (2020). URL <https://doi.org/10.1063/1.5115323>.
- [88] Senellart, P., Giesz, V. & Lanco, L. Ultrabright single-photon sources. *Photoniques* 23–26 (2017).
- [89] Uppu, R. *et al.* Scalable integrated single-photon source. *Science Advances* **6**, eabc8268 (2022). URL <https://doi.org/10.1126/sciadv.abc8268>.
- [90] Santis, L. D. *et al.* A solid-state single-photon filter. *Nature Nanotechnology* **12**, 663–667 (2017).

- [91] Ding, X. *et al.* On-Demand Single Photons with High Extraction Efficiency and Near-Unity Indistinguishability from a Resonantly Driven Quantum Dot in a Micropillar. *Phys. Rev. Lett.* **116**, 20401 (2016). URL <https://link.aps.org/doi/10.1103/PhysRevLett.116.020401>.
- [92] Teets, R., Eckstein, J. & Hänsch, T. W. Coherent Two-Photon Excitation by Multiple Light Pulses. *Phys. Rev. Lett.* **38**, 760–764 (1977). URL <https://link.aps.org/doi/10.1103/PhysRevLett.38.760>.
- [93] Koong, Z. X. *et al.* Coherent Dynamics in Quantum Emitters under Dichromatic Excitation. *Phys. Rev. Lett.* **126**, 47403 (2021). URL <https://link.aps.org/doi/10.1103/PhysRevLett.126.047403>.
- [94] Liu, J. *et al.* A solid-state source of strongly entangled photon pairs with high brightness and indistinguishability. *Nature Nanotechnology* **14**, 586–593 (2019). URL <https://doi.org/10.1038/s41565-019-0435-9>.
- [95] Bozzio, M. *et al.* Enhancing quantum cryptography with quantum dot single-photon sources. *npj Quantum Information* **8**, 104 (2022). URL <https://doi.org/10.1038/s41534-022-00626-z>.
- [96] Fischer, K. *et al.* Signatures of two-photon pulses from a quantum two-level system. *Nature Physics* **13**, 649–654 (2017). URL <https://doi.org/10.1038/nphys4052>.
- [97] Hanschke, L. *et al.* Quantum dot single-photon sources with ultra-low multiphoton probability. *npj Quantum Information* **4**, 43 (2018). URL <https://doi.org/10.1038/s41534-018-0092-0>.
- [98] Özdemir, K., Miranowicz, A., Koashi, M. & Imoto, N. Pulse-mode quantum projection synthesis : Effects of mode mismatch on optical state truncation and preparation. *Physical Review A* **66**, 53809 (2002).
- [99] Loredo, J. C. *et al.* Scalable performance in solid-state single-photon sources. *Optica* **3**, 433–440 (2016). URL <http://opg.optica.org/optica/abstract.cfm?URI=optica-3-4-433>.
- [100] Da Lio, B. *et al.* A Pure and Indistinguishable Single-Photon Source at Telecommunication Wavelength. *Advanced Quantum Technologies* **5**, 2200006 (2022). URL <https://onlinelibrary.wiley.com/doi/abs/10.1002/qute.202200006>.
- [101] He, Y.-M. *et al.* Deterministic implementation of a bright, on-demand single-photon source with near-unity indistinguishability via quantum dot imaging. *Optica* **4**, 802–808 (2017). URL <https://opg.optica.org/optica/abstract.cfm?URI=optica-4-7-802>.

- [102] Matthiesen, C. *et al.* Phase-locked indistinguishable photons with synthesized waveforms from a solid-state source. *Nature Communications* **4**, 1600 (2013). URL <https://doi.org/10.1038/ncomms2601>.
- [103] Gerhardt, S. *et al.* Polarization-dependent light-matter coupling and highly indistinguishable resonant fluorescence photons from quantum dot-micropillar cavities with elliptical cross section. *Phys. Rev. B* **100**, 115305 (2019). URL <https://link.aps.org/doi/10.1103/PhysRevB.100.115305>.
- [104] Heurtel, N. *et al.* Perceval : A Software Platform for Discrete Variable Photonic Quantum Computing 1–31 (2022). URL <http://arxiv.org/abs/2204.00602>.
- [105] Okamoto, R., O'Brien, J. L., Hofmann, H. F. & Takeuchi, S. Realization of a Knill-Laflamme-Milburn controlled-NOT photonic quantum circuit combining effective optical nonlinearities. *Proceedings of the National Academy of Sciences* **108**, 10067–10071 (2011). URL <https://www.pnas.org/doi/abs/10.1073/pnas.1018839108>.
- [106] Zeuner, J. *et al.* Integrated-optics heralded controlled-NOT gate for polarization-encoded qubits. *npj Quantum Information* **4**, 13 (2018). URL <https://doi.org/10.1038/s41534-018-0068-0>.
- [107] Gottesman, D. & Chuang, I. L. Demonstrating the viability of universal quantum computation using teleportation and single-qubit operations. *Nature* **402**, 390–393 (1999).
- [108] Gustin, C. & Hughes, S. Efficient Pulse-Excitation Techniques for Single Photon Sources from Quantum Dots in Optical Cavities. *Advanced Quantum Technologies* **3**, 1900073 (2020). URL <https://doi.org/10.1002/qute.201900073>.
- [109] Kammerlander, P. & Anders, J. Coherence and measurement in quantum thermodynamics. *Sci. Rep.* **6**, 1–7 (2016). URL <http://dx.doi.org/10.1038/srep22174>.
- [110] Lostaglio, M., Jennings, D. & Rudolph, T. Description of quantum coherence in thermodynamic processes requires constraints beyond free energy. *Nature Communications* **6**, 1–9 (2015).
- [111] Andolina, G. M. *et al.* Extractable Work, the Role of Correlations, and Asymptotic Freedom in Quantum Batteries. *Phys. Rev. Lett.* **122**, 47702 (2019). URL <https://link.aps.org/doi/10.1103/PhysRevLett.122.047702>.

- [112] Horodecki, M. & Oppenheim, J. Fundamental limitations for quantum and nanoscale thermodynamics. *Nature Communications* **4**, 2059 (2013). URL <https://doi.org/10.1038/ncomms3059>.
- [113] Alicki, R. & Kosloff, R. Introduction to Quantum Thermodynamics : History and Prospects. 1–33 (2018).
- [114] Vinjanampathy, S. & Anders, J. Quantum thermodynamics. *Contemporary Physics* **57**, 545–579 (2016). URL <https://doi.org/10.1080/00107514.2016.1201896>.
- [115] Kosloff, R. Quantum Thermodynamics : A Dynamical Viewpoint. *Entropy* **15**, 2100–2128 (2013). URL <https://www.mdpi.com/1099-4300/15/6/2100>.
- [116] Alicki, R. A quantum mechanical open system as a model of a heat engine. *J. Chem. Phys.* **12** (1979).
- [117] Kosloff, R. A quantum mechanical open system as a model of a heat engine. *The Journal of Chemical Physics* **80**, 1625–1631 (1984). URL <http://aip.scitation.org/doi/10.1063/1.446862>.
- [118] Skrzypczyk, P., Short, A. J. & Popescu, S. Work extraction and thermodynamics for individual quantum systems. *Nat. Commun.* **5** (2014).
- [119] Bäumer, E., Lostaglio, M., Perarnau-Llobet, M. & Sampaio, R. Fluctuating Work in Coherent Quantum Systems : Proposals and Limitations. *Fundamental Theories of Physics* **195**, 275–300 (2018).
- [120] Gemmer, J. & Anders, J. From single-shot towards general work extraction in a quantum thermodynamic framework. *New Journal of Physics* **17**, 085006 (2015). URL <https://iopscience.iop.org/article/10.1088/1367-2630/17/8/085006>.
- [121] Korzekwa, K., Lostaglio, M., Oppenheim, J. & Jennings, D. The Extraction of Work from Quantum Coherence. *New J. Phys.* **18**, 23045 (2016).
- [122] Alipour, S. *et al.* Correlations in quantum thermodynamics : Heat, work, and entropy production. *Sci. Rep.* **6**, 1–14 (2016). URL <http://dx.doi.org/10.1038/srep35568>.
- [123] Ali, M. M., Huang, W.-M. & Zhang, W.-M. Quantum thermodynamics of single particle systems. *Scientific Reports* **10**, 13500 (2020). URL <https://doi.org/10.1038/s41598-020-70450-y>.

- [124] Esposito, M., Ochoa, M. A. & Galperin, M. Nature of heat in strongly coupled open quantum systems. *Phys. Rev. B* **92**, 235440 (2015). URL <https://link.aps.org/doi/10.1103/PhysRevB.92.235440>.
- [125] Hänggi, P. & Talkner, P. The other QFT. *Nature Physics* **11**, 108–110 (2015). URL <https://doi.org/10.1038/nphys3167>.
- [126] Bergmann, N. & Galperin, M. A Green's function perspective on the nonequilibrium thermodynamics of open quantum systems strongly coupled to baths. *The European Physical Journal Special Topics* **230**, 859–866 (2021). URL <https://doi.org/10.1140/epjs/s11734-021-00067-3>.
- [127] Hossein-Nejad, H., O'Reilly, E. J. & Olaya-Castro, A. Work, heat and entropy production in bipartite quantum systems. *New J. Phys.* **17**, 75014 (2015). URL <https://iopscience.iop.org/article/10.1088/1367-2630/17/7/075014>.
- [128] Weimer, H., Henrich, M. J., Rempp, F., Schröder, H. & Mahler, G. Local effective dynamics of quantum systems : A generalized approach to work and heat. *EPL* **83**, 30008 (2008). URL <https://iopscience.iop.org/article/10.1209/0295-5075/83/30008>.
- [129] Schröder, H. & Mahler, G. Work exchange between quantum systems : The spin-oscillator model. *Phys. Rev. E* **81**, 21118 (2010). URL <https://link.aps.org/doi/10.1103/PhysRevE.81.021118>.
- [130] Ciccarello, F., Lorenzo, S., Giovannetti, V. & Palma, G. M. Quantum collision models : open system dynamics from repeated interactions. *arXiv* **2106.11974** (2021).
- [131] Fan, S., Kocabaş, E. & Shen, J.-T. Input-output formalism for few-photon transport in one-dimensional nanophotonic waveguides coupled to a qubit. *Phys. Rev. A* **82**, 63821 (2010). URL <https://link.aps.org/doi/10.1103/PhysRevA.82.063821>.
- [132] Rodrigues, F., De Chiara, G., Paternostro, M. & Landi, G. Thermodynamics of Weakly Coherent Collisional Models. *Physical Review Letters* **123** (2019).
- [133] Barra, F. Dissipative Charging of a Quantum Battery. *Phys. Rev. Lett.* **122**, 210601 (2019). URL <https://link.aps.org/doi/10.1103/PhysRevLett.122.210601>.
- [134] Besombes, L., Kheng, K., Marsal, L. & Mariette, H. Acoustic phonon broadening mechanism in single quantum dot emission. *Physical Review B - Condensed Matter and Materials Physics* **63**, 1–5 (2001).

- [135] Favero, I. *et al.* Acoustic phonon sidebands in the emission line of single InAs/GaAs quantum dots. *Physical review. B, Condensed matter* **68**, 233301 (2003).
- [136] Reigue, A. *et al.* Probing Electron-Phonon Interaction through Two-Photon Interference in Resonantly Driven Semiconductor Quantum Dots. *Phys. Rev. Lett.* **118**, 233602 (2017). URL <https://link.aps.org/doi/10.1103/PhysRevLett.118.233602>.
- [137] Denning, E. V., Iles-Smith, J., Gregersen, N. & Mork, J. Phonon effects in quantum dot single-photon sources. *Opt. Mater. Express* **10**, 222–239 (2020). URL <https://opg.optica.org/ome/abstract.cfm?URI=ome-10-1-222>.
- [138] Hu, D. *et al.* Ramsey interferometry with trapped motional quantum states. *Communications Physics* **1**, 29 (2018). URL <https://doi.org/10.1038/s42005-018-0030-7>.
- [139] Bechtold, A. *et al.* Three-stage decoherence dynamics of an electron spin qubit in an optically active quantum dot. *Nature Physics* **11**, 1005–1008 (2015). URL <https://doi.org/10.1038/nphys3470>.
- [140] Kuhr, S. *et al.* Analysis of dephasing mechanisms in a standing-wave dipole trap. *Phys. Rev. A* **72**, 23406 (2005). URL <https://link.aps.org/doi/10.1103/PhysRevA.72.023406>.
- [141] Nielsen, M. A. & Chuang, I. L. *Quantum Computation and Quantum Information* (Cambridge University Press, 2012). URL <https://www.cambridge.org/core/product/identifier/9780511976667/type/book>.
- [142] Ladd, T. D. *et al.* Pulsed Nuclear Pumping and Spin Diffusion in a Single Charged Quantum Dot. *Phys. Rev. Lett.* **105**, 107401 (2010). URL <https://link.aps.org/doi/10.1103/PhysRevLett.105.107401>.
- [143] Stockill, R. *et al.* Quantum dot spin coherence governed by a strained nuclear environment. *Nature Communications* **7**, 12745 (2016). URL <https://doi.org/10.1038/ncomms12745>.
- [144] Nguyen, H. S. *et al.* Ultra-coherent single photon source. *Applied Physics Letters* **99**, 261904 (2011). URL <http://aip.scitation.org/doi/10.1063/1.3672034>.
- [145] Matthiesen, C., Vamivakas, A. N. & Atatüre, M. Subnatural Linewidth Single Photons from a Quantum Dot. *Phys. Rev. Lett.* **108**, 93602 (2012). URL <https://link.aps.org/doi/10.1103/PhysRevLett.108.093602>.

- [146] Kuhlmann, A. V. *et al.* Charge noise and spin noise in a semiconductor quantum device. *Nature Physics* **9**, 570–575 (2013).
- [147] Yoneda, J. *et al.* A quantum-dot spin qubit with coherence limited by charge noise and fidelity higher than 99.9%. *Nature Nanotechnology* **13**, 102–106 (2018). URL <https://doi.org/10.1038/s41565-017-0014-x>.
- [148] Lucamarini, M., Yuan, Z. L., Dynes, J. F. & Shields, A. J. Overcoming the rate–distance limit of quantum key distribution without quantum repeaters. *Nature* **557**, 400–403 (2018). URL <https://doi.org/10.1038/s41586-018-0066-6>.
- [149] Curty, M., Azuma, K. & Lo, H.-K. Simple security proof of twin-field type quantum key distribution protocol. *npj Quantum Information* **5**, 64 (2019). URL <https://doi.org/10.1038/s41534-019-0175-6>.
- [150] Liu, Y. *et al.* Experimental Twin-Field Quantum Key Distribution through Sending or Not Sending. *Phys. Rev. Lett.* **123**, 100505 (2019). URL <https://link.aps.org/doi/10.1103/PhysRevLett.123.100505>.
- [151] Li, B.-H. *et al.* Long-distance twin-field quantum key distribution with entangled sources. *Opt. Lett.* **46**, 5529–5532 (2021). URL <https://opg.optica.org/ol/abstract.cfm?URI=ol-46-22-5529>.
- [152] Park, C. H. *et al.*  $2 \times N$  twin-field quantum key distribution network configuration based on polarization, wavelength, and time division multiplexing. *npj Quantum Information* **8**, 48 (2022). URL <https://doi.org/10.1038/s41534-022-00558-8>.
- [153] Pirandola, S., Laurenza, R., Ottaviani, C. & Banchi, L. Fundamental limits of repeaterless quantum communications. *Nature Communications* **8**, 15043 (2017). URL <https://doi.org/10.1038/ncomms15043>.
- [154] Lund, A. P., Bell, T. B. & Ralph, T. C. Comparison of linear optics quantum-computation control-sign gates with ancilla inefficiency and an improvement to functionality under these conditions. *Phys. Rev. A* **68**, 22313 (2003). URL <https://link.aps.org/doi/10.1103/PhysRevA.68.022313>.
- [155] Mower, J., Harris, N. C., Steinbrecher, G. R., Lahini, Y. & Englund, D. High-fidelity quantum state evolution in imperfect photonic integrated circuits. *Phys. Rev. A* **92**, 32322 (2015). URL <https://link.aps.org/doi/10.1103/PhysRevA.92.032322>.
- [156] Carolan, J. *et al.* Universal linear optics. *Science* **349**, 711–716 (2015). URL <https://doi.org/10.1126/science.aab3642>.

- [157] Auffèves, A. Quantum technologies need a quantum energy initiative. *arXiv :2111.09241* (2021).
- [158] Greenberger, D. M., Horne, M. A. & Zeilinger, A. Going Beyond Bell's Theorem BT - Bell's Theorem, Quantum Theory and Conceptions of the Universe. 69–72 (Springer Netherlands, Dordrecht, 1989). URL [https://doi.org/10.1007/978-94-017-0849-4\\_10](https://doi.org/10.1007/978-94-017-0849-4_10).
- [159] Briegel, H. J. & Raussendorf, R. Persistent Entanglement in Arrays of Interacting Particles. *Phys. Rev. Lett.* **86**, 910–913 (2001). URL <https://link.aps.org/doi/10.1103/PhysRevLett.86.910>.
- [160] Raussendorf, R., Browne, D. E. & Briegel, H. J. Measurement-based quantum computation on cluster states. *Phys. Rev. A* **68**, 22312 (2003). URL <https://link.aps.org/doi/10.1103/PhysRevA.68.022312>.
- [161] Azuma, K., Tamaki, K. & Lo, H.-K. All-photon quantum repeaters. *Nature Communications* **6**, 6787 (2015). URL <https://doi.org/10.1038/ncomms7787>.



## 7 - Appendix : Hong-Ou-Mandel interference with photon-number superpositions – theory

In this appendix, we present theory developed by Dr. Stephen Wein<sup>1</sup> to describe all the experimental work presented in this manuscript relying on a Mach-Zehnder-based Hong-Ou-Mandel (HOM) interferometer.

### 7.1 . General description

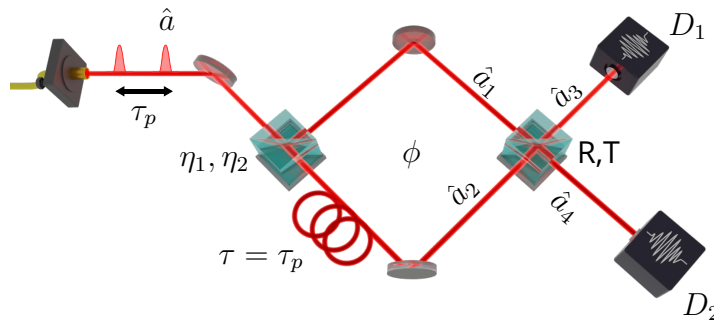


Figure 7.1 – **General Hong-Ou-Mandel interferometer** An unbalanced Mach-Zehnder interferometer with input mode  $\hat{a}$  and two beam splitters with transmission and reflection coefficients  $R, T$  and efficiencies  $\eta_1, \eta_2$ . Two detectors  $D_1$  and  $D_2$  with efficiencies  $\eta_3$  and  $\eta_4$  monitor the output ports of the final beam splitter.

We consider the Hong-Ou-Mandel interferometer in Fig. 7.1 where the input is a stream of identical pulses  $\hat{a}(t)$  impinging the first beam splitter. We neglect the other beam splitter input as it is in a vacuum state and considered uncorrelated with the main input mode. We define detector  $D_1$  ( $D_2$ ) monitoring output mode  $\hat{a}_3$  with an efficiency  $\eta_3$  ( $\hat{a}_4, \eta_4$ ). Moreover, we introduce efficiencies  $\eta_1, \eta_2$  capturing the possible intensity imbalance in the two arms of the HOM, and reflection (transmission) coefficient  $R$  ( $T$ ) of the second beam splitter. Finally, we label the time  $t_1$  ( $t_2$ ) as the time at which detector  $D_1$  ( $D_2$ ) clicks, and we assume parallel polarization ( $\parallel$ ) configuration for the fields in  $\hat{a}_1$  and  $\hat{a}_2$  unless otherwise stated.

1. Previously : Université Grenoble Alpes, CNRS, Grenoble INP, Institut Néel, 38000 Grenoble, France.

Currently : Quandela SAS, 7 Rue Léonard de Vinci, 91300 Massy, France.

To express the intensity correlation  $G_{D_1, D_2}^{(2)} = \eta_3 \eta_4 \langle \hat{a}_3^\dagger(t_1) \hat{a}_4^\dagger(t_2) \hat{a}_3(t_1) \hat{a}_4(t_2) \rangle$  in terms of the input mode  $\hat{a}$ , we work our way back from the detector level to the interferometer input.

We introduce the superoperators  $\mathcal{J}$ ,  $\mathcal{S}$  and  $\mathcal{R}$ , which are defined as

$$\begin{aligned}\mathcal{J}\hat{\rho} &= \hat{a}\hat{\rho}\hat{a}^\dagger \\ \mathcal{S}\hat{\rho} &= \hat{a}\hat{\rho} \\ \mathcal{R}\hat{\rho} &= \hat{\rho}\hat{a}^\dagger,\end{aligned}$$

and define the expectation value as

$$\langle \langle \mathcal{A}_1(t_1) \mathcal{A}_2(t_2) \cdots \mathcal{A}_n(t_n) \rangle \rangle = \text{Tr} \{ \mathcal{T}[\mathcal{A}_1(t_1) \mathcal{A}_2(t_2) \cdots \mathcal{A}_n(t_n)] \hat{\rho}(t_0) \}, \quad (7.1)$$

with time-ordering superoperator  $\mathcal{T}$  and  $t_0 \leq t_n$  for all  $n$ . Defining the expectation value in this fashion, shows that  $\mathcal{R}$  and  $\mathcal{S}$  commute and thus can be time-ordered. Consequently, the correlation function  $G_{34}^{(2)}$  can be written as  $\langle \langle \mathcal{R}_3(t_1) \mathcal{R}_4(t_2) \mathcal{S}_4(t_2) \mathcal{S}_3(t_1) \rangle \rangle$ , which in turn can be written as  $\langle \langle \mathcal{J}_4(t_2) \mathcal{J}_3(t_1) \rangle \rangle$ .

The beam splitter relations for the second beam splitter in Fig. 7.1 with reflection and transmission coefficients  $R, T$  are

$$\begin{aligned}\hat{a}_3(t) &= T\hat{a}_1(t) - R\hat{a}_2(t) \\ \hat{a}_4(t) &= R\hat{a}_1(t) + T\hat{a}_2(t)\end{aligned} \quad (7.2)$$

resulting in a second-order correlation function in terms of beam splitter input modes  $\hat{a}_1, \hat{a}_2$ . If we then also apply the relative time delay  $\tau_p$  and the phase  $\phi$  shift induced by the interferometer through

$$\begin{aligned}\hat{a}_1(t) &= \sqrt{\frac{\eta_1}{2}} \hat{a}(t) \\ \hat{a}_2(t) &= \sqrt{\frac{\eta_2}{2}} \hat{a}(t - \tau_p) e^{i\phi},\end{aligned} \quad (7.3)$$

where we take into account the possible intensity imbalance in the arms of the interferometer with  $\eta_1, \eta_2$ , we can express the second-order correlation function in terms of a general input mode  $\hat{a}$ .

The derivation of  $G_{D_1, D_2}^{(2)}$  in terms of the input mode  $\hat{a}$  follows a 3 step procedure, which we do not detail here<sup>2</sup>.

---

## 2. Quantum interferences with photon-number superposition states emitted by coherently driven quantum emitters (2023)

I. Maillette de Buy Wenniger, D. Fioretto, S.C. Wein, J. Senellart, C. Antón-Solanas, S. E. Thomas, N. Belabas, and P. Senellart

*In preparation*

We find

$$\begin{aligned}
\frac{4G_{D_1, D_2}^{(2)}(t_1, t_2)}{\eta_3 \eta_4} = & \frac{1}{2} \eta_1 \eta_2 (R^4 + T^4) [\langle \langle \mathcal{J}(t_2) \mathcal{J}(t_1 - \tau) \rangle \rangle + \langle \langle \mathcal{J}(t_2 - \tau) \mathcal{J}(t_1) \rangle \rangle] \\
& + R^2 T^2 [\eta_1^2 \langle \langle \mathcal{J}(t_2) \mathcal{J}(t_1) \rangle \rangle + \eta_2^2 \langle \langle \mathcal{J}(t_2 - \tau) \mathcal{J}(t_1 - \tau) \rangle \rangle] \\
& - 2\eta_1 \eta_2 R^2 T^2 \text{Re}\{\langle \langle \mathcal{S}(t_2) \mathcal{R}(t_2 - \tau) \mathcal{R}(t_1) \mathcal{S}(t_1 - \tau) \rangle \rangle\} \\
& - 2\eta_1 \eta_2 R^2 T^2 \text{Re}\{\langle \langle \mathcal{S}(t_2) \mathcal{R}(t_2 - \tau) \mathcal{S}(t_1) \mathcal{R}(t_1 - \tau) \rangle \rangle\} \cos(2\phi) \\
& + 2\sqrt{\eta_1 \eta_2} R T (R^4 - T^4) [\text{Re}\{B^+(t_1, t_2)\} \cos(\phi) \\
& - \text{Im}\{B^+(t_1, t_2)\} \sin(\phi)]
\end{aligned} \tag{7.4}$$

where

$$\begin{aligned}
B^+(t_1, t_2) = & \frac{1}{2} (B(t_1, t_2) + B(t_2, t_1)) \\
= & \frac{1}{2} [\langle \langle \mathcal{R}(t_2) \mathcal{S}(t_2 - \tau) [\eta_1 \mathcal{J}(t_1) - \eta_2 \mathcal{J}(t_1 - \tau)] \rangle \rangle \\
& + \langle \langle \mathcal{R}(t_1) \mathcal{S}(t_1 - \tau) [\eta_1 \mathcal{J}(t_2) - \eta_2 \mathcal{J}(t_2 - \tau)] \rangle \rangle],
\end{aligned} \tag{7.5}$$

and

$$\begin{aligned}
B(t_1, t_2) = & \langle \langle \mathcal{R}(t_2) \mathcal{S}(t_2 - \tau) [\eta_1 T^2 \mathcal{J}(t_1) + \eta_2 R^2 \mathcal{J}(t_1 - \tau)] \rangle \rangle \\
& - \langle \langle \mathcal{R}(t_1) \mathcal{S}(t_1 - \tau) [\eta_1 R^2 \mathcal{J}(t_2) + \eta_2 T^2 \mathcal{J}(t_2 - \tau)] \rangle \rangle.
\end{aligned} \tag{7.6}$$

We see that when  $R \neq T$ , the last two lines of Eq. 7.4 become non-zero, which correspond to single-photon interference effects that occur in the presence of one or more photons and are captured by two-time correlation function  $B(t_1, t_2)$ .

With Eq. 7.4, we can analyze the coincidences for different delays  $\tau_k = k\tau_p$  as defined in Section 3.2.3, and examine the effect of phase on the peak areas in correlation histograms. We restrict ourselves to a time-ordered scenario  $t_2 \geq t_1$ , and set  $t_2 = t_1 + \tau$  to probe specific histogram peaks, where the detection delay  $\tau$  is in the vicinity of  $n\tau_p$  with  $n \geq 0$ .

### 7.1.1 . Zero delay peak

To analyze the central peak ( $k = 0$ ), we restrict ourselves to  $\tau = \tau_p$ . We then factor correlation functions separated by delays  $t_2 - t_1 \geq \tau_p$ , followed by applying the periodic condition to eliminate  $\tau_p$  from the resulting expression. This would entail that if we have the term  $\langle \langle \mathcal{J}(t_2 - \tau_p) \mathcal{J}(t_1) \rangle \rangle$ , we get  $\langle \langle \mathcal{J}(t_2 - \tau_p) \rangle \rangle \langle \langle \mathcal{J}(t_1) \rangle \rangle = \langle \langle \mathcal{J}(t_2) \rangle \rangle \langle \langle \mathcal{J}(t_1) \rangle \rangle = I(t_1)I(t_2)$ , with  $I(t)$  the intensity of the input mode at time  $t$ .

If we apply these steps to Eq. 7.4, we get

$$\begin{aligned} \frac{4G_{D_1, D_2, 0}^{(2)}(t_1, t_2)}{\eta_3 \eta_4} = & \eta_1 \eta_2 (R^4 + T^4) I(t_1) I(t_2) + (\eta_1^2 + \eta_2^2) R^2 T^2 G^{(2)}(t_1, t_2) \\ & - 2\eta_1 \eta_2 R^2 T^2 \left[ |G^{(1)}(t_1, t_2)|^2 + |C^{(2)}|^2 \cos(2\phi) \right] \\ & + \sqrt{\eta_1 \eta_2} RT (R^4 - T^4) [(\eta_1 - \eta_2) \text{Re}\{B_0(t_1, t_2)\} \cos(\phi) \\ & - (\eta_1 + \eta_2) \text{Im}\{B_0(t_1, t_2)\} \sin(\phi)], \end{aligned} \quad (7.7)$$

with

$$B_0(t_1, t_2) = \langle \hat{a}(t_2) \rangle \langle \hat{a}^\dagger(t_2) \hat{a}^\dagger(t_1) \hat{a}(t_1) \rangle + \langle \hat{a}(t_1) \rangle \langle \hat{a}^\dagger(t_1) \hat{a}^\dagger(t_2) \hat{a}(t_2) \rangle. \quad (7.8)$$

To get the peak areas, we integrate  $t_1$  and  $t_2$  over all time. Using a normalization factor  $N = \eta_1 \eta_2 \eta_3 \eta_4 \mu^2 / 4$ , where  $\mu = \int I(t) dt$ , the average photon number of the interferometer input. As a result we obtain the central peak area :

$$\begin{aligned} 2g_{D_1, D_2}^{(2)}(k=0) = & (R^4 + T^4) + \frac{(\eta_1^2 + \eta_2^2)}{\eta_1 \eta_2} R^2 T^2 \left( M + c^{(2)} \cos(2\phi) \right) \\ & + RT (R^4 - T^4) \left[ \frac{(\eta_1 - \eta_2)}{\sqrt{\eta_1 \eta_2}} \text{Re}\{b_0\} \cos(\phi) - \right. \\ & \left. \frac{(\eta_1 + \eta_2)}{\sqrt{\eta_1 \eta_2}} \text{Im}\{b_0\} \sin(\phi) \right] \end{aligned} \quad (7.9)$$

where  $g^{(2)}$ ,  $M$ ,  $c^{(2)}$  are the intensity correlation, mean wavepacket overlap, and second-order coherence between Fock states  $|n\rangle$  and  $|n+2\rangle$ , given by :

$$g^{(2)} = \frac{1}{\mu^2} \iint \langle \hat{a}^\dagger(t) \hat{a}^\dagger(t') \hat{a}(t') \hat{a}(t) \rangle dt dt' \quad (7.10)$$

$$M = \frac{1}{\mu^2} \iint |\langle \hat{a}^\dagger(t') \hat{a}(t) \rangle|^2 dt dt' \quad (7.11)$$

$$c^{(2)} = \frac{1}{\mu^2} \iint |\langle \hat{a}(t') \hat{a}(t) \rangle|^2 dt dt', \quad (7.12)$$

respectively, where the integrals are taken over a single pulse of the input mode for both  $t$  and  $t'$ . Moreover, we have normalized the two-time correlation function according to  $b_0 = (1/\mu^2) \iint B(t_1, t_2) dt_1 dt_2$ .

For a balanced interferometer where  $R = T = 1/\sqrt{2}$  and  $\eta_1 = \eta_2 = 1$  we find

$$g_{D_1, D_2}^{(2)}(k=0) = \frac{1}{2} + \frac{1}{2} g^{(2)} - \frac{1}{2} M - \frac{1}{2} c^{(2)} \cos(2\phi). \quad (7.13)$$

which in the case of  $g^{(2)} = 0$  becomes :

$$g_{D_1, D_2}^{(2)}(k=0) = \frac{1}{2} (1 - M), \quad (7.14)$$

with  $M = M_s$ , see Section 2.4.3 and Section 3.2.1 for definition  $M_s$ .

### 7.1.2 . First delay peak

We find the phase dependence of the first delay ( $|k| = 1$ ) peak area by setting  $t_2 \rightarrow t_2 + \tau_p$ , shifting the correlation function to have the delay  $\tau$  centered around the first delay peaks of a coincidence histogram. Consequently, some terms with factor  $\tau_p$  cancels, changing the factorization of the correlation functions. We find :

$$\begin{aligned}
\frac{4G_{D_1, D_2, 1}^{(2)}(t_1, t_2)}{\eta_3 \eta_4} &= \frac{1}{2} \eta_1 \eta_2 (R^4 + T^4) \left[ I(t_1) I(t_2) + G^{(2)}(t_1, t_2) \right] \\
&+ R^2 T^2 \left[ \eta_1^2 + \eta_2^2 \right] I(t_1) I(t_2) \\
&- 2 \eta_1 \eta_2 R^2 T^2 \left[ S_{\{1|2\}}^{(2)}(t_1, t_2) + S_{\{1|M\}}^{(2)}(t_1, t_2) \cos(2\phi) \right] \\
&+ 2 \sqrt{\eta_1 \eta_2} R T (R^4 - T^4) \left[ \text{Re}\{B_1(t_1, t_2)\} \cos(\phi) \right. \\
&- \left. \text{Im}\{B_1(t_1, t_2)\} \sin(\phi) \right] \\
&+ 2 \sqrt{\eta_1 \eta_2} R T (R^4 - T^4) \left[ \eta_1 |\langle \hat{a}(t_1) \rangle|^2 I(t_2) \right. \\
&- \left. \eta_2 I(t_1) |\langle \hat{a}(t_2) \rangle|^2 \right] \cos(\phi),
\end{aligned} \tag{7.15}$$

with  $B_1(t_1, t_2) = \eta_1 \langle \hat{a}^\dagger(t_2) \rangle \langle \hat{a}^\dagger(t_1) \hat{a}(t_2) \hat{a}(t_1) \rangle - \eta_2 \langle \hat{a}(t_1) \rangle \langle \hat{a}^\dagger(t_1) \hat{a}^\dagger(t_2) \hat{a}(t_2) \rangle$ . Integrating over time and normalizing by  $N = \eta_1 \eta_2 \eta_3 \eta_4 \mu^2 / 4$ , we obtain :

$$\begin{aligned}
g_{D_1, D_2}^{(2)}(|k| = 1) &= \frac{1}{2} (R^4 + T^4) (1 + g^{(2)}) + \frac{(\eta_1^2 + \eta_2^2)}{\eta_1 \eta_2} R^2 T^2 \\
&- 2 R^2 T^2 \left( s_{\{1|2\}}^{(2)} + s_{\{1|M\}}^{(2)} \cos(2\phi) \right) \\
&+ \frac{2}{\sqrt{\eta_1 \eta_2}} R T (R^4 - T^4) \left[ \left( \text{Re}\{b_1\} + (\eta_1 + \eta_2) c^{(1)} \right) \cos(\phi) \right. \\
&- \left. \text{Im}\{b_1\} \sin(\phi) \right],
\end{aligned} \tag{7.16}$$

where we have  $b_1 = (1/\mu^2) \iint B_1(t_1, t_2) dt_1 dt_2$ , and the first-order coherence  $c^{(1)}$  between Fock states  $|n\rangle$  and  $|n+1\rangle$ , the temporal overlap between first- and second-order coherence  $s_{\{1|2\}}^{(2)}$ , and the temporal overlap between the first-order coherence and first-order two-time correlation function, or temporal coherence,  $s_{\{1|M\}}^{(2)}$ , defined as :

$$c^{(1)} = \frac{1}{\mu} \int |\langle \hat{a}(t) \rangle|^2 dt \tag{7.17}$$

$$s_{\{1|2\}}^{(2)} = \frac{1}{\mu^2} \iint \text{Re}\{ \langle \hat{a}^\dagger(t) \rangle \langle \hat{a}^\dagger(t') \rangle \langle \hat{a}(t') \hat{a}(t) \rangle \} dt dt' \tag{7.18}$$

$$s_{\{1|M\}}^{(2)} = \frac{1}{\mu^2} \iint \text{Re}\{ \langle \hat{a}^\dagger(t) \rangle \langle \hat{a}(t') \rangle \langle \hat{a}^\dagger(t') \hat{a}(t) \rangle \} dt dt'. \tag{7.19}$$

The latter term only arises when two photons from different pulses interfere. In the absence of a two-photon component in the pulsed input field ( $g^{(2)} = 0$ ), the latter term becomes :

$$s_{\{1,M\}}^{(2)} = c^{(1)} \left( \frac{2M}{1+M} \right), \quad (7.20)$$

where  $M = M_s$ .

For a balanced beam splitter,  $\eta_1 = \eta_2$  and  $R = T = 1/\sqrt{2}$ , we finally obtain :

$$g_{D_1, D_2}^{(2)}(|k| = 1) = \frac{3}{4} + \frac{1}{4}g^{(2)} - \frac{1}{2}s_{\{1,2\}}^{(2)} - \frac{1}{2}s_{\{1,M\}}^{(2)} \cos(2\phi). \quad (7.21)$$

### 7.1.3 . Far delay peaks

The second delay peaks and higher ( $|k| \geq 2$ ) are commonly referred to as the *uncorrelated* side peaks in literature and used for normalization of coincidence histograms. We show here that by deriving the peak area for the second delay peak, which we extend to further delays, that we can no longer consider these peaks uncorrelated and therefore are not a reliable reference for normalization.

To show the phase dependence of these peaks, we set  $t_2 \rightarrow t_2 + 2\tau_p$  and follow the same procedure as detailed in the previous two sections. We obtain :

$$\begin{aligned} \frac{4G_{D_1, D_2, 2}^{(2)}(t_1, t_2)}{\eta_3 \eta_4} &= [\eta_1 \eta_2 (R^4 + T^4) + (\eta_1^2 + \eta_2^2) R^2 T^2] I(t_1) I(t_2) \\ &\quad - 2\eta_1 \eta_2 R^2 T^2 |\langle \hat{a}(t_1) \rangle|^2 |\langle \hat{a}(t_2) \rangle|^2 (1 + \cos(2\phi)) \\ &\quad + \sqrt{\eta_1 \eta_2} (\eta_1 - \eta_2) RT (R^4 - T^4) [I(t_1) |\langle \hat{a}(t_2) \rangle|^2 \\ &\quad + |\langle \hat{a}(t_1) \rangle|^2 I(t_2)] \cos(\phi), \end{aligned} \quad (7.22)$$

where we write the index 2 in  $G_{D_1, D_2, 2}^{(2)}$  but this applies to any further delay.

Integrating and normalizing results in the peak area :

$$\begin{aligned} g_{D_1, D_2}^{(2)}(|k| \geq 2) &= (R^4 + T^4) + \frac{\eta_1^2 + \eta_2^2}{\eta_1 \eta_2} R^2 T^2 \\ &\quad - 2R^2 T^2 [c^{(1)}]^2 (1 + \cos(2\phi)) \\ &\quad + 2 \frac{(\eta_1 - \eta_2)}{\sqrt{\eta_1 \eta_2}} RT (R^4 - T^4) c^{(1)} \cos(\phi), \end{aligned} \quad (7.23)$$

which for  $R = T = 1/\sqrt{2}$  and  $\eta_1 = \eta_2 = 1$  becomes

$$g_{D_1, D_2}^{(2)}(|k| \geq 2) = 1 - \left( c^{(1)} \cos(\phi) \right)^2, \quad (7.24)$$

where we recognize the self-homodyne signal used to define interferometer phase.

## 7.2 . Normalization second-order correlation histograms

To understand the normalization procedure proposed in Section 3.3.1 let us consider a normalization of phase dependent coincidences by a factor proportional to  $(\mu_3 + \mu_4)^2/4 \simeq \mu^2/4$ , a factor which is phase independent. If we write this normalization factor in terms of the jump operators we get  $(1/4)[\int \langle \langle \mathcal{J}_3(t) + \mathcal{J}_4(t) \rangle \rangle dt]^2$ . Adding the two jump operators ideally cancels the phase-dependent terms. However, whenever  $\eta_3 \neq \eta_4$ , the terms do not fully cancel. In practice,  $\eta_3 \neq \eta_4$  can arise from differences in losses before detection, or difference in detection efficiencies.

We can potentially overcome this experimental difficulty by measuring the efficiency ratio  $r_\eta = \eta_3/\eta_4$ . This ratio can be measured by taking the ratio of phase-averaged counts at each detector :  $r_\eta = (\int \mu_3 d\phi)/(\int \mu_4 d\phi)$ , or by taking the ratio of maximum (or minimum) counts at each detector :

$$r_\eta = \frac{\max_\phi \mu_3}{\max_\phi \mu_4}. \quad (7.25)$$

In both cases,  $1 \pm c^{(1)} \cos(\phi)$ , becomes identical for  $\mu_3$  and  $\mu_4$ .

Knowing  $r_\eta$ , the phase-independent normalization factor becomes

$$\frac{1}{4r_\eta}(\mu_3 + r_\eta \mu_4)^2 = \frac{1}{4} \eta_3 \eta_4 \mu^2. \quad (7.26)$$

This normalization method holds as long as the inputs at the final beam splitter are balanced, i.e.  $\mu_1 = \mu_2 = \mu$  ( $\eta_1 = \eta_2 = 1$ ).

To obtain a phase- and loss-robust normalization factor, we consider the quantity  $\langle \langle (\mathcal{J}_3(t_2) + r_\eta \mathcal{J}_4(t_2))(\mathcal{J}_3(t_1) + r_\eta \mathcal{J}_4(t_1)) \rangle \rangle / (4r_\eta)$ . Applying  $\tau = \tau_p$ , and taking  $t_2 \gg t_1$ , we obtain

$$\begin{aligned} \frac{1}{4r_\eta} \langle \langle (\mathcal{J}_3(t_2) + r_\eta \mathcal{J}_4(t_2))(\mathcal{J}_3(t_1) + r_\eta \mathcal{J}_4(t_1)) \rangle \rangle &= \\ \frac{\eta_3^2}{16r_\eta} \langle \langle [\eta_1 \mathcal{J}(t_2) + \eta_2 \mathcal{J}(t_2 - \tau_p)][\eta_1 \mathcal{J}(t_1) + \eta_2 \mathcal{J}(t_1 - \tau_p)] \rangle \rangle & \quad (7.27) \\ = \frac{1}{4} \eta_3 \eta_4 \frac{(\eta_1 + \eta_2)^2}{4} I(t_1) I(t_2). & \end{aligned}$$

Secondly, we can expand the first line in Eq. 7.27 in terms of  $G_{D_1, D_2}^{(2)}$  and autocorrelations  $G_{D_1, D_1}^{(2)}(t_1, t_2)$  and  $G_{D_2, D_2}^{(2)}(t_1, t_2)$ , where the autocorrelations are defined as :

$$\begin{aligned} G_{D_1, D_1}^{(2)}(t_1, t_2) &= \eta_3^2 \langle \langle \mathcal{J}_3(t_1) \mathcal{J}_3(t_2) \rangle \rangle \\ G_{D_2, D_2}^{(2)}(t_1, t_2) &= \eta_4^2 \langle \langle \mathcal{J}_4(t_1) \mathcal{J}_4(t_2) \rangle \rangle. \end{aligned} \quad (7.28)$$

After integrating over the entire uncorrelated peak and normalizing by the factor  $N = \eta_1\eta_2\eta_3\eta_4\mu^2/4$ , we get :

$$\frac{1}{4r_\eta}(g_{D_1,D_1}^{(2)} + 2r_\eta g_{D_1,D_2}^{(2)}(|k| \geq 2) + r_\eta^2 g_{D_2,D_2}^{(2)}) = 1 + \frac{(\eta_1 - \eta_2)^2}{4}, \quad (7.29)$$

where  $g_{D_i,D_i}^{(2)}$  is the average peak area of the auto-correlation histogram obtained with detector  $i$ .

## 8 - Appendix : Photonic field

The theory presented in this appendix has been developed by the group of Prof. Alexia Auffèves<sup>1</sup> with Dr. Maria Maffei<sup>2</sup>, and Dr. Stephen Wein<sup>3</sup>. It describes formally the field emitted by a quantum emitter subject to pure dephasing.

### 8.1 . General form of the emitted field

In our experiments we consider the decoherence witnessed by the qubit to mainly perturb the spontaneous emission process, an assumption which we experimentally justify in Section 4.3.4. With this assumption we can describe the photonic (or battery) field containing at most one photon in the pulse operator formalism (98) as

$$\begin{aligned}\hat{\rho} &= p_0 |0\rangle \langle 0| + p_1 \iint dt dt' \xi(t, t') \hat{a}^\dagger(t) |0\rangle \langle 0| \hat{a}(t') \\ &\quad + \sqrt{p_0 p_1} \int dt \zeta(t) \hat{a}^\dagger(t) |0\rangle \langle 0| + \text{h.c.} \\ &= p_0 \hat{\rho}_0 + p_1 \hat{\rho}_1 + \sqrt{p_0 p_1} (\hat{\rho}_{01} + \hat{\rho}_{10}),\end{aligned}\tag{8.1}$$

where  $\hat{\rho}_{i(j)} = |i\rangle \langle i(j)|$  is the photonic density operator, and  $\hat{a}(t)$  is the propagating mode, and the photon-number probabilities  $p_0, p_1$  satisfy  $p_0 + p_1 = 1$ . Additionally, we introduce two parameters : the Hermitian function  $\xi(t, t') = \xi^*(t', t)$  describing the temporal shape and coherence of the pulse, and the complex amplitude  $\zeta(t)$  describing the temporal dynamics of the photon-number coherence. Considering the photon-number probabilities  $p_0$  and  $p_1$  satisfy  $p_0 + p_1 = 1$ , we have  $\text{Tr}[\hat{\rho}] = 1$  implies  $\int \xi(t, t) dt = 1$ .

For a state described by Eq. 8.1 the total purity of the state is given by

$$\mathcal{P} = \text{Tr}[\hat{\rho}^2] = p_0^2 + p_1^2 M_s + 2p_0 p_1 \mathcal{C}\tag{8.2}$$

with the single-photon indistinguishability, or purity in the temporal domain,

$$M_s = \text{Tr}[\hat{\rho}_1^2] = \iint |\xi(t, t')|^2 dt dt' .\tag{8.3}$$

1. Université Grenoble Alpes, CNRS, Grenoble INP, Institut Néel, 38000 Grenoble, France.

2. Université Grenoble Alpes, CNRS, Grenoble INP, Institut Néel, 38000 Grenoble, France.

3. Previously : Université Grenoble Alpes, CNRS, Grenoble INP, Institut Néel, 38000 Grenoble, France.

Currently : Quandela SAS, 7 Rue Léonard de Vinci, 91300 Massy, France.

Finally, we can write the purity in number coherence, between the vacuum and the single photon Fock state :

$$C = \text{Tr}[\hat{\rho}_{01}\hat{\rho}_{10}] = \int |\zeta(t)|^2 dt. \quad (8.4)$$

## 8.2 . Purely dephased emitter

Ideally, upon excitation of our two-level system we do not generate a two-photon component,  $g^{(2)} \ll 1$ , and thus  $\rho_{2,j} = 0$ , implying  $c^{(2)} = 0$ ,  $s_{\{1|2\}}^{(2)} = 0$  (see Appendix 7.1). Generating photonic states with high single-photon purity is desired in many optical quantum technologies. Hence, we want to predict how the peak areas of coincidence histograms are affected in absence of re-excitation, or emission of a two-photon component of our emitter.

We can analytically predict the phase dependence of the coincidence peak areas by considering a perfectly-prepared two-level system affected by pure dephasing. Instantaneous excitation (with pulse duration  $\tau_{\text{exc}} \rightarrow 0$ ) generates a photonic field described by the density operator :

$$\begin{aligned} \hat{\rho} = & p_0 |0\rangle \langle 0| + p_1 \iint dt dt' \xi(t, t') \hat{a}^\dagger(t) |0\rangle \langle 0| \hat{a}(t') \\ & + \sqrt{p_0 p_1} \int dt \zeta(t) \hat{a}^\dagger(t) |0\rangle \langle 0| + \text{h.c.} \end{aligned}$$

where

$$\begin{aligned} \xi(t, t') &= f(t) f^*(t') e^{-\gamma^* |t-t'|} \\ \zeta(t) &= \lambda f(t) e^{i\phi - \gamma^* t}, \end{aligned}$$

with the pure-state wavefunction  $f(t) = \sqrt{\gamma} e^{-i\omega t - \gamma t/2}$ , the spontaneous emission rate  $\gamma$ , the pure dephasing rate  $\gamma^*$ , and  $\lambda$  a parameter tuning the photon-number purity (83). Combined with  $c^{(2)} = 0$ ,  $s_{\{1|2\}}^{(2)} = 0$  and  $g^{(2)} = 0$  we get  $M = M_s$  and :

$$\begin{aligned} M_s &= \frac{\gamma}{\gamma + 2\gamma^*} \\ c^{(1)} &= \lambda^2 p_0 \left( \frac{\gamma}{\gamma + 2\gamma^*} \right) = \lambda^2 p_0 M_s \\ s_{\{1|M\}}^{(2)} &= \lambda^2 p_0 \left( \frac{\gamma^2}{(\gamma + \gamma^*)(\gamma + 2\gamma^*)} \right) = c^{(1)} \left( \frac{2M_s}{1 + M_s} \right). \end{aligned} \quad (8.5)$$

Thus, we see that in the absence of a two-photon component the overlap between temporal coherence and first-order coherence simply is a product of the two.

### 8.3 . Relation between $M_s$ and $\mathcal{C}$

For a two-level system spontaneously emitting a field under influence of pure dephasing and spectral diffusion we can relate  $M_s$  to  $\mathcal{C}$ . First, we consider the emission of a single photon in absence of pure dephasing. The temporal wave function associated with this field is given by  $f(t, \omega_0) = \sqrt{\gamma}e^{-\gamma t/2 - i\omega_0 t}$ , with the emitter transition frequency  $\omega_0$ . Such a field has some temporal coherence, which in the presence of pure dephasing undergoes an exponential decay in the time interval  $(t - t')$  captured by the temporal density function and coherence function, respectively :

$$\begin{aligned}\xi(t, t', \omega_0) &= f(t, \omega_0)f^*(t', \omega_0)e^{-\gamma^*|t-t'|} \\ \zeta(t, \omega_0) &= f(t, \omega_0)e^{-\gamma^*t}.\end{aligned}\quad (8.6)$$

This decay over time interval  $(t - t')$  prevents the temporal density function from being factored further. As a result, the single-photon component of a state subject to pure dephasing can no longer be considered as temporally pure.

In between successive excitations of the emitter, the transition frequency can change by an amount  $\delta\omega$ , although we consider the frequency fixed during each emission of a photonic field. Hence, when performing Hong-Ou-Mandel measurements the spectral diffusion between successive emitted photons will reduce the single-photon indistinguishability :

$$M_s(\delta\omega) = \iint dt dt' \text{Re}[\xi(t, t', \omega_0)\xi^*(t, t', \omega_0 + \delta\omega)]. \quad (8.7)$$

For the photonic field described in Eq. 8.1 subject to pure dephasing, this latter expression becomes :

$$M_s(\delta\omega) = \frac{\gamma(\gamma + 2\gamma^*)}{(\gamma + 2\gamma^*)^2 + \delta\omega^2}, \quad (8.8)$$

with  $\gamma + 2\gamma^* = 2/T_2$ , where  $T_2$  the total decoherence rate. This decoherence creates homogeneous broadening of the emission linewidth, which is broadened further by averaging over the spectral diffusion of the emitter  $\delta\omega$ .

Symmetrically, we see how the purity in photon-number basis between the vacuum and single-photon component is affected by pure dephasing and spectral diffusion :

$$\mathcal{C}(\delta\omega) = \int dt \text{Re}[\zeta(t, \omega_0)\zeta^*(t, \omega_0 + \delta\omega)]. \quad (8.9)$$

Evaluating this expression for our two-level system, we again find :

$$\mathcal{C}(\delta\omega) = \frac{\gamma(\gamma + 2\gamma^*)}{(\gamma + 2\gamma^*)^2 + \delta\omega^2} = M_s(\delta\omega). \quad (8.10)$$

Thus, pure dephasing affects the photon-number purity and single-photon indistinguishability identically :  $\mathcal{C} = M_s$ .

As a side note, the equality  $\mathcal{C} = M_s$  does not hold for all dephasing phenomena. In Ref. (83) they find the photon-number purity to be upperbounded by

$$\mathcal{C} \leq \sqrt{M_s}. \quad (8.11)$$

This upper bound shows that the photonic state will contain no photon number coherence in the limit of the temporal purity going to zero, but we can have a high temporal coherence without photon number coherence. Eq. 8.11 allows us to define the parameter  $\lambda^2 = \mathcal{C}\sqrt{M_s}$  with  $0 \leq \lambda \leq 1$  quantifying the **decoherence in photon number basis not arising from loss in temporal coherence**.

## 9 - Appendix : Discharging a quantum battery – theory

The theory provided in this appendix has been developed by Prof. Alexia Auffèves<sup>1</sup>, Dr. Maria Maffei<sup>2</sup>, and Dr. Stephen Wein<sup>3</sup>. It describes the experiments of Section 4.4 where we interfere the field emitted by the qubit with a classical field (discharging step of the protocol).

### 9.1 . Energy transfers in discharging

In the second step of the protocol presented in Section 4.4 we discharge the quantum battery through interference with a classical receiver. We consider the beam splitter depicted in Fig. 4.20 where we have the coherent field (c),  $|\beta\rangle$ , in input port  $\hat{a}_1(t) = \hat{a}_c^{(in)}(t)$  and the battery field (b) in input port  $\hat{a}_2(t) = \hat{a}_b^{(in)}(t)$ , with  $\langle \hat{a}_b^{(in)}(t) \rangle = \sin(\theta/2) \cos(\theta/2) \zeta(t)$  and  $\langle \hat{a}_c^{(in)}(t) \rangle = \beta(t)$ .

We consider constructive interference in output  $\hat{a}_4(t)$ , the energy received by the classical receiver in this output port is

$$\begin{aligned} \mathcal{E}_c^{(out)} &= \frac{1}{2} \left[ \mathcal{E}_c^{(in)} + \mathcal{E}_b^{(in)} \right] + \hbar\omega_0 \text{Re} \left[ \int dt \langle \hat{a}_b^{(in)}(t) \rangle \langle \hat{a}_c^{(in)}(t) \rangle^* \right] \\ &= \frac{\hbar\omega_0}{2} \left[ \int dt |\beta(t)|^2 + \sin^2 \left( \frac{\theta}{2} \right) \right] \\ &\quad + \hbar\omega_0 \cos \left( \frac{\theta}{2} \right) \sin \left( \frac{\theta}{2} \right) \text{Re} \left[ \int dt \zeta(t) \beta(t)^* \right], \end{aligned} \quad (9.1)$$

where the second term  $\hbar\omega_0 \text{Re} \left[ \int dt \langle \hat{a}_b^{(in)}(t) \rangle \langle \hat{a}_c^{(in)}(t) \rangle^* \right]$  is the energy exchange from interference between the coherent parts of the fields. Because of energy conservation, the addition of this energy in one output of the beam splitter must entail that the energy in the other output port  $\hat{a}_3(t)$  is reduced by the same amount of energy.

We can define an efficiency of energy transfer in discharging, denoted by the letter  $G$ , which is equal to the energy received by the classical field  $\mathcal{E}_c^{(out)}$  divided

---

1. Université Grenoble Alpes, CNRS, Grenoble INP, Institut Néel, 38000 Grenoble, France.

2. Université Grenoble Alpes, CNRS, Grenoble INP, Institut Néel, 38000 Grenoble, France.

3. Previously: Université Grenoble Alpes, CNRS, Grenoble INP, Institut Néel, 38000 Grenoble, France.

Currently: Quandela SAS, 7 Rue Léonard de Vinci, 91300 Massy, France.

by the total energy into the beam splitter  $\mathcal{E}_c^{(in)} + \mathcal{E}_b^{(in)}$ . Using the expression for  $\mathcal{E}_c^{(out)}$  in Eq. 9.1 we find a maximum energy transfer for  $\int dt |\beta(t)|^2 = \sin^2(\theta/2)$  (i.e.  $\beta(t) = \sin(\theta/2)\sqrt{\xi(t,t')}e^{-i\phi(t)}$ ) : when both fields impinging the beam splitter have the same input energy.

With equal input intensities we find that the energy exchanged, second term in Eq. 9.1, can be written as :

$$\Delta\mathcal{E}_c = \hbar\omega_0 \cos\left(\frac{\theta}{2}\right) \sin^2\left(\frac{\theta}{2}\right) \mathcal{C}_{b,c} = -\Delta\mathcal{E}_b, \quad (9.2)$$

where we define the parameter capturing the classical and quantum coherence exchanged  $\mathcal{C}_{b,c} = \text{Re} \left[ \int dt \zeta(t) \sqrt{\xi(t,t')} e^{i\phi(t)} \right]$ .

The energy exchanged in Eq. 9.2 can be split into a work and heat contribution, similar to the charging step :

$$\Delta\mathcal{E}_c = \mathcal{W}_{b,c} + \mathcal{Q}_{b,c}, \quad (9.3)$$

where the work component is equal to the coherent part of the field and the heat equal to the incoherent part. Following the analysis method introduced in Refs. (38; 122; 127–129), we find for the work

$$\begin{aligned} \mathcal{W}_{b,c} &= \hbar\omega_0 \left( \int dt |\langle \hat{a}_c^{out}(t) \rangle|^2 - \int dt |\langle \hat{a}_c^{in}(t) \rangle|^2 \right) \\ &= \hbar\omega_0 \text{Re} \left[ \int dt \langle \hat{a}_c^{(in)}(t) \rangle \langle \hat{a}_b^{(in)}(t) \rangle^* \right] \\ &\quad + \frac{\hbar\omega_0}{2} \left( \int dt |\langle \hat{a}_b^{(in)}(t) \rangle|^2 - \int dt |\langle \hat{a}_c^{(in)}(t) \rangle|^2 \right) \\ &= \hbar\omega_0 \sin^2\left(\frac{\theta}{2}\right) \left[ \cos\left(\frac{\theta}{2}\right) \mathcal{C}_{b,c} + \frac{1}{2} \left( \cos^2\left(\frac{\theta}{2}\right) \mathcal{C} - 1 \right) \right]. \end{aligned} \quad (9.4)$$

Finally, by combining this expression for work with the energy balance in Eq. 9.3 we obtain the heat transfer in discharge :

$$\mathcal{Q}_{b,c} = \frac{1}{2} \hbar\omega_0 \sin^2\left(\frac{\theta}{2}\right) \left( 1 - \cos^2\left(\frac{\theta}{2}\right) \mathcal{C} \right) = \mathcal{Q}_{q,b}/2. \quad (9.5)$$

## 9.2 . Relating visibility of interference and energetic exchanges

As before, we can access the first-order coherence  $c^{(1)}$  in photon-number basis by performing homodyne-type measurements and extracting the visibility  $v$  from the average photon-number  $\mu_i = \int \langle \hat{a}_i^\dagger(t) \hat{a}_i(t) \rangle dt$  measured at the output of a beam splitter :

$$v = \frac{\mu_3 - \mu_4}{\mu_3 + \mu_4}. \quad (9.6)$$

For a beam splitter with input modes  $\hat{a}_1(t), \hat{a}_2(t)$  and output modes  $\hat{a}_3(t), \hat{a}_4(t)$ , the beam splitter relations are given by :

$$\begin{pmatrix} \hat{a}_3(t) \\ \hat{a}_4(t) \end{pmatrix} = \frac{1}{\sqrt{2}} \begin{pmatrix} 1 & e^{i\phi} \\ -e^{i\phi} & 1 \end{pmatrix} \begin{pmatrix} \hat{a}_1(t) \\ \hat{a}_2(t) \end{pmatrix}, \quad (9.7)$$

with  $\phi = \phi(t)$  the freely evolving relative phase between the interfering fields originating from a path length difference.

In the discharging step, the input fields are a quantum battery field (b)  $\hat{a}_1(t) = \hat{a}_b^{(in)}(t)$  and a classical coherent field (c)  $\hat{a}_2(t) = \hat{a}_c^{(in)}(t)$ , with  $\langle \hat{a}_b^{(in)}(t) \rangle = \sin(\theta/2) \cos(\theta/2) \zeta(t)$  and  $\langle \hat{a}_c^{(in)}(t) \rangle = \beta(t)$ . From the normalization condition we impose on the experiment,  $\mathcal{E}_b^{(in)} = \mathcal{E}_c^{(in)} = \hbar\omega_0 \sin^2(\theta/2)$  we find that the visibility in the discharge process is given by :

$$\begin{aligned} v &= \frac{1}{\mu_b} \text{Re} \left[ \int dt \langle \hat{a}_c^{(in)}(t) \rangle \langle \hat{a}_b^{(in)}(t) \rangle^* \right] \\ &= \cos\left(\frac{\theta}{2}\right) \text{Re} \left[ \int dt \zeta(t) \sqrt{\xi(t, t')} e^{i\phi} \right] = \cos\left(\frac{\theta}{2}\right) C_{b,c}, \end{aligned} \quad (9.8)$$

where again we have  $C_{b,c} = \text{Re} \left[ \int dt \zeta(t) \sqrt{\xi(t, t')} e^{i\phi} \right]$ .

### 9.3 . Pure dephasing in energy transfer

#### 9.3.1 . Work and heat equations in presence of pure dephasing

To demonstrate the validity of our theoretical framework in the presence of pure dephasing, we start from the main results reported in Refs. (122; 127; 128). Let us consider the bipartite system containing a qubit  $q$  coupled to a battery field  $b$ . This frame can be generalized to any pair of systems ( $\mathcal{A}$  and  $\mathcal{B}$ ) coupled by an Hamiltonian interaction  $V_{\mathcal{A},\mathcal{B}}$ . At time  $t$  we can write the joint state as  $\rho(t) = \rho^{\mathcal{A}}(t) \otimes \rho^{\mathcal{B}}(t) + \chi_{\mathcal{A},\mathcal{B}}(t)$ , with  $\rho^{\mathcal{A}(\mathcal{B})}(t) = \text{Tr}_{\mathcal{B}(\mathcal{A})}\{\rho(t)\}$  and the correlation matrix  $\chi_{\mathcal{A},\mathcal{B}}(t)$  containing all classical and quantum correlations. Through this separation of dynamics we can find the definitions of work and heat transfer in terms of the bare Hamiltonians of the two systems  $H_{\mathcal{A}(\mathcal{B})}$  :

$$\dot{\mathcal{W}}_{\mathcal{A}(\mathcal{B})} = -\frac{i}{\hbar} \text{Tr}_{\mathcal{A},\mathcal{B}} \{ [H_{\mathcal{A}(\mathcal{B})}, V_{\mathcal{A},\mathcal{B}}] \rho^{\mathcal{A}}(t) \otimes \rho^{\mathcal{B}}(t) \}, \quad (9.9)$$

$$\dot{\mathcal{Q}}_{\mathcal{A}(\mathcal{B})}(t) = -\frac{i}{\hbar} \text{Tr}_{\mathcal{A},\mathcal{B}} \{ [H_{\mathcal{A}(\mathcal{B})}, V_{\mathcal{A},\mathcal{B}}] \chi_{\mathcal{A},\mathcal{B}}(t) \}. \quad (9.10)$$

For these coupled systems we can write a "quantum version" of the first law of thermodynamics, where for each system undergoing a change in internal energy  $\Delta\mathcal{E}$  we can write  $\Delta\mathcal{E}_{\mathcal{A}(\mathcal{B})} = \mathcal{W}_{\mathcal{A}(\mathcal{B})} + \mathcal{Q}_{\mathcal{A}(\mathcal{B})}$ . If the average coupling energy is constant ( $d/dt \text{Tr}\{V_{\mathcal{A},\mathcal{B}}\rho(t)\} = 0$ ), we find  $\dot{\mathcal{W}}_{\mathcal{A}}(t) = -\dot{\mathcal{W}}_{\mathcal{B}}(t)$  and

$$\dot{Q}_A(t) = -\dot{Q}_B(t).$$

Next, we want to include pure dephasing in the framework. When introducing pure dephasing we can no longer consider a bipartite system. We now consider a three-body system comprising the qubit ( $A$ ), electromagnetic field ( $B$ ), and phonons ( $C$ ). In this tripartite system, the phonons do not couple to the electromagnetic field, leaving us with the Hamiltonian  $H_{A,B,C} = H_A + H_B + H_C + V_{A,B} + V_{A,C}$ , and the joint system state written as  $\rho(t) = \rho^A(t) \otimes \rho^B(t) \otimes \rho^C(t) + \chi_{A,B,C}(t)$ . The work and heat transfers to the qubit are now given by :

$$\begin{aligned} \dot{W}_A = & -\frac{i}{\hbar} \text{Tr}_{A,B} \{ [H_A, V_{A,B}] \rho^A(t) \otimes \rho^B(t) \} \\ & -\frac{i}{\hbar} \text{Tr}_{A,C} \{ [H_A, V_{A,C}] \rho^A(t) \otimes \rho^C(t) \}, \end{aligned} \quad (9.11)$$

$$\begin{aligned} \dot{Q}_A(t) = & -\frac{i}{\hbar} \text{Tr}_{A,B} \{ [H_A, V_{A,B}] \chi_{A,B}(t) \} \\ & -\frac{i}{\hbar} \text{Tr}_{A,C} \{ [H_A, V_{A,C}] \chi_{A,C}(t) \}. \end{aligned} \quad (9.12)$$

The work and heat transfers towards the electromagnetic field ( $B$ ), and/or the phonon bath ( $C$ ) read :

$$\dot{W}_{B(C)} = -\frac{i}{\hbar} \text{Tr}_{A,B(C)} \{ [H_{B(C)}, V_{A,B(C)}] \rho^A(t) \otimes \rho^{B(C)}(t) \}, \quad (9.13)$$

$$\dot{Q}_{B(C)}(t) = -\frac{i}{\hbar} \text{Tr}_{A,B(C)} \{ [H_{B(C)}, V_{A,B(C)}] \chi_{A,B(C)}(t) \}, \quad (9.14)$$

with  $\chi_{A,C}(t) = \text{Tr}_B\{\chi(t)\}$  and  $\chi_{A,B}(t) = \text{Tr}_C\{\chi(t)\}$ . The internal energy change of the qubit and electromagnetic field are still governed by  $\Delta\mathcal{E}_{A(B)} = \mathcal{W}_{A(B)} + \mathcal{Q}_{A(B)}$ . However, now the average coupling energy is given by  $\text{Tr}\{V_{A,B}\rho(t)\} + \text{Tr}\{V_{A,C}\rho(t)\}$ , which, if constant, results in  $\dot{W}_A(t) + \dot{W}_B(t) + \dot{W}_C(t) = 0$ , and symmetrically for the heat flow :  $\dot{Q}_A(t) + \dot{Q}_B(t) + \dot{Q}_C(t) = 0$ . Because the phonon bath does not exchange energy with the qubit we can set  $\dot{W}_C(t) = 0$ ,  $\dot{Q}_C(t) = 0$ , and  $\text{Tr}\{V_{A,C}\rho(t)\} = 0$ . Moreover, as we are considering spontaneous emission, the field is initially in a vacuum state resulting in a Lorentzian-shaped light spectrum centered at the qubit wavelength, giving  $\text{Tr}\{V_{A,B}\rho(t)\} = 0$ . As a result, as long as the phonon bath does not exchange energy with the other two systems, we find that the work and heat exchanged between the qubit and field are equal and opposite in sign. Finally we note that the expressions for the heat and work transfer to the electromagnetic field in Eqs. 9.13, 9.14 are identical to Eqs. 9.11, 9.12. Therefore, following the derivation in Ref. (122) we obtain for the tripartite system Eq. 4.25 in the main text.

### 9.3.2 . Relation between $M_{b,c}$ and $\mathcal{C}_{b,c}$

We can derive a relation between  $\mathcal{C}_{b,c}$  and  $M_{b,c}$  when only the qubit emission is affected by pure dephasing and spectral diffusion. In the discharging step we have a photonic state described by temporal density function  $\xi$  and coherence function  $\zeta$ , and a classical field described by amplitude  $\beta(t) = \sin(\theta/2)\sqrt{\xi(t,t)}e^{-i\phi(t)}$ . The mean wavepacket overlap, prone to spectral diffusion, between the two fields is given by :

$$\begin{aligned} M_{b,c}(\delta\omega) &= \iint dt dt' \text{Re} \left[ \sqrt{\xi(t,t,\omega_0)\xi(t',t',\omega_0)} e^{-i\omega_0(t-t')} \zeta^*(t,t',\omega_0 + \delta\omega) \right] \\ &= \frac{\gamma(\gamma + \gamma^*)}{(\gamma + \gamma^*)^2 + \delta\omega^2}, \end{aligned} \quad (9.15)$$

where  $\phi(t) = \omega_0 t$ .

We find for  $\mathcal{C}_{b,c}$  :

$$\begin{aligned} \mathcal{C}_{b,c}(\delta\omega) &= \int dt \text{Re} \left[ \sqrt{\xi(t,t,\omega_0)} e^{-i\omega_0 t} \zeta^*(t,t,\omega_0 + \delta\omega) \right] \\ &= \frac{\gamma(\gamma + \gamma^*)}{(\gamma + \gamma^*)^2 + \delta\omega^2}, \end{aligned} \quad (9.16)$$

which gives  $\mathcal{C}_{b,c}(\delta\omega) = M_{b,c}(\delta\omega)$ , showing both parameters are equally affected by pure dephasing and spectral diffusion. For completeness, a more general bound using a Cauchy-Schwarz inequality can be found if the decoherence is not only due to pure dephasing :

$$\mathcal{C}_{b,c} \leq \sqrt{M_{b,c}}. \quad (9.17)$$

## 9.4 . Field amplitude and work transfer

Let us consider the matrix describing beam splitter interaction between two plane waves of the same frequency (i.e.  $\omega = \omega_0$ ) :

$$\begin{pmatrix} \hat{a}_3 \\ \hat{a}_4 \end{pmatrix} = \begin{pmatrix} \cos(\frac{\varphi}{2}) & e^{i\varphi} \sin(\frac{\varphi}{2}) \\ -e^{i\varphi} \sin(\frac{\varphi}{2}) & \cos(\frac{\varphi}{2}) \end{pmatrix} \begin{pmatrix} \hat{a}_1 \\ \hat{a}_2 \end{pmatrix}, \quad (9.18)$$

with  $\varphi$  the beam splitter angle. Input channel  $\hat{a}_2$  carries the battery field  $b$ , and input channel  $\hat{a}_1$  carries the work receiver  $w$ . The Hamiltonian describing the bipartite system is given by :

$$H = \hbar\omega_0(\hat{w}^\dagger \hat{w} + \hat{b}^\dagger \hat{b}) + \frac{i\hbar\Omega}{2}(\hat{w}^\dagger \hat{b} - \hat{b}^\dagger \hat{w}), \quad (9.19)$$

where  $\Omega$  corresponds to the coupling strength between the two fields. In the interaction picture we can remove the bare Hamiltonians of the work receiver and the battery field, leaving us :

$$H = \frac{i\hbar\Omega}{2}(\hat{w}^\dagger \hat{b} - \hat{b}^\dagger \hat{w}). \quad (9.20)$$

The two fields interact for time  $\tau = \Omega\tau = \varphi$ , resulting in the density matrix  $\rho(t)$  describing the joint state :

$$\rho(\tau) = U(\tau)\rho(0)U^\dagger = e^{\varphi(\hat{w}^\dagger\hat{b}-\hat{b}^\dagger\hat{w})/2}\rho(0)e^{-\varphi(\hat{w}^\dagger\hat{b}-\hat{b}^\dagger\hat{w})/2}, \quad (9.21)$$

where

$$\begin{aligned} U^\dagger(\tau)\hat{b}U(\tau) &= \cos\left(\frac{\varphi}{2}\right)\hat{b} - \sin\left(\frac{\varphi}{2}\right)\hat{w}, \\ U^\dagger(\tau)\hat{w}U(\tau) &= \cos\left(\frac{\varphi}{2}\right)\hat{w} + \sin\left(\frac{\varphi}{2}\right)\hat{b}. \end{aligned}$$

We can now derive the energy exchanged among two system and decompose the energy into a work and heat component. The energetic exchanges in this closed bipartite system are equal and opposite. As such, we will only write down the explicit expressions for the work receiver  $w$ . For the work receiver, the energy change reads :

$$\begin{aligned} \Delta\mathcal{E}_w &\equiv \mathcal{E}_w(\tau) - \mathcal{E}_w(0) = \hbar\omega_0 \left[ \sin^2\left(\frac{\varphi}{2}\right) (\langle\hat{b}^\dagger\hat{b}\rangle_0 - \langle\hat{w}^\dagger\hat{w}\rangle_0)2 + \sin(\varphi)\text{Re}[\langle\hat{b}\hat{w}^\dagger\rangle_0] \right] \\ &= \hbar\omega_0 \left[ \sin^2\left(\frac{\varphi}{2}\right) (\langle\hat{a}_2^\dagger\hat{a}_2\rangle - \langle\hat{a}_1^\dagger\hat{a}_1\rangle)2 + \sin(\varphi)\text{Re}[\langle\hat{a}_2\hat{a}_1^\dagger\rangle] \right] \\ &= \mathcal{E}_3 - \mathcal{E}_1, \end{aligned} \quad (9.22)$$

where we use  $\langle\dots\rangle_0 \equiv \text{Tr}[\dots\rho(0)]$  and  $\rho(0) = \rho(1, 2)$ . Consequently, we find that the work transfer towards the work receiver reads :

$$\begin{aligned} \dot{\mathcal{W}}_w(t)/(\hbar\omega_0) &= \Omega\text{Re}\{\text{Tr}[\hat{w}\rho(t)]\text{Tr}[\hat{b}^\dagger\rho(t)]\} \\ &= \Omega\text{Re}\{\text{Tr}[U^\dagger(t)\hat{w}U(t)\rho(0)]\text{Tr}[U^\dagger(t)\hat{b}^\dagger U(t)\rho(0)]\} \\ &= \Omega\text{Re}\{(\cos(\Omega t/2)\langle\hat{w}\rangle_0 + \sin(\Omega t/2)\langle\hat{b}\rangle_0)(\cos(\Omega t/2)\langle\hat{b}^\dagger\rangle_0^* - \sin(\Omega t/2)\langle\hat{w}^\dagger\rangle_0^*)\} \\ &= \Omega(\cos^2(\Omega t/2) - \sin^2(\Omega t/2))\text{Re}\{\langle\hat{w}\rangle_0\langle\hat{b}^\dagger\rangle_0^*\} \\ &\quad - \cos(\Omega t/2)\sin(\Omega t/2)(|\langle\hat{w}\rangle_0|^2 - |\langle\hat{b}\rangle_0|^2). \end{aligned} \quad (9.23)$$

The total work received by  $w$  is then computed by integrating between 0 and  $\tau$  :

$$\begin{aligned} \mathcal{W}_w &\equiv \int_0^\tau dt\mathcal{W}(t) = \hbar\omega_0 \left[ \sin(\varphi)\text{Re}\{\langle\hat{w}\rangle_0\langle\hat{b}^\dagger\rangle_0^*\} + \sin^2(\varphi/2)(|\langle\hat{b}\rangle_0|^2 - |\langle\hat{w}\rangle_0|^2) \right] \\ &= \hbar\omega_0 \left[ \sin(\varphi)\text{Re}\{\langle\hat{a}_1\rangle\langle\hat{a}_2^\dagger\rangle^*\} + \sin^2(\varphi/2)(|\langle\hat{a}_2\rangle|^2 - |\langle\hat{a}_1\rangle|^2) \right], \end{aligned} \quad (9.24)$$

and the heat transfer to the work receiver is given by :

$$\begin{aligned} \mathcal{Q}_w &\equiv \Delta\mathcal{E}_w - \mathcal{W}_w \\ &= \hbar\omega_0 \left[ \sin(\varphi)\text{Re}\left\{\langle\hat{a}_2\hat{a}_1^\dagger\rangle - \langle\hat{a}_2\rangle\langle\hat{a}_1^\dagger\rangle^*\right\} + \sin^2(\varphi/2)\left(\langle\hat{a}_2^\dagger\hat{a}_2\rangle - |\langle\hat{a}_2\rangle|^2\right) \right] \\ &\quad - \hbar\omega_0 \left[ \sin^2(\varphi/2)\left(\langle\hat{a}_1^\dagger\hat{a}_1\rangle - |\langle\hat{a}_1\rangle|^2\right) \right]. \end{aligned} \quad (9.25)$$

Thus, the heat depends on the statistics of both input fields and their correlations.  
We can consider some examples :

$$\rho(0) = |\alpha\rangle \langle\alpha| \otimes |\beta\rangle \langle\beta| \rightarrow \mathcal{Q}_w = 0; \quad (9.26)$$

$$\rho(0) = |1\rangle \langle 1| \otimes |1\rangle \langle 1| \rightarrow \mathcal{W}_w = 0; \quad (9.27)$$

$$\rho(0) = |\alpha\rangle \langle\alpha| \otimes |1\rangle \langle 1| \rightarrow \mathcal{W}_w = -\hbar\omega_0|\alpha|^2 \sin^2(\varphi/2),$$

$$\mathcal{Q}_w = \hbar\omega_0 \sin^2(\varphi/2); \quad (9.28)$$

$$\rho(0) = |\alpha\rangle \langle\alpha| \otimes (c_1^* |1\rangle + c_0^* |0\rangle)(c_1 |1\rangle + c_0 |0\rangle) \rightarrow$$

$$\mathcal{W}_w = \hbar\omega_0[\text{Re}\{\alpha c_1 c_0^*\} \sin(\varphi) + (|c_1 c_0^*|^2 - |\alpha|^2) \sin^2(\varphi/2)]. \quad (9.29)$$



## List of publications

- **Measurement of coherence-powered work exchanges between a qubit and light fields**  
I. Maillette de Buy Wenniger, S. E. Thomas, M. Maffei, S. C. Wein, M. Pont, N. Belabas, S. Prasad, A. Harouri, A. Lemaître, I. Sagnes, N. Somaschi, A. Auffèves and P. Senellart  
*arXiv* 2202.01109
- **Quantum interferences with photon-number superposition states emitted by coherently driven quantum emitters**  
I. Maillette de Buy Wenniger, D. Fioretto, S.C. Wein, J. Senellart, C. Antón-Solanas, S. E. Thomas, N. Belabas, and P. Senellart  
*In preparation*
- **Hong-Ou-Mandel Interference with Imperfect Single Photon Sources**  
H. Ollivier, S. E. Thomas, S. C. Wein, I. Maillette de Buy Wenniger, N. Coste, J. C. Loredó, N. Somaschi, A. Harouri, A. Lemaître, I. Sagnes, L. Lanco, C. Simon, C. Anton, O. Krebs, and P. Senellart  
*Phys. Rev. Lett.* **126**, 063602 (2021)
- **Intermittency of CsPbBr<sub>3</sub> Perovskite Quantum Dots Analyzed by an Unbiased Statistical Analysis**  
I. M. Palstra, I. Maillette de Buy Wenniger, B. K. Patra, E. C. Garnett, A. F. Koenderink  
*J. Phys. Chem. C* **125**, 12061-12072 (2021)
- **Reproducibility of High-Performance Quantum Dot Single-Photon Sources**  
H. Ollivier, I. Maillette de Buy Wenniger, S. E. Thomas, S. C. Wein, A. Harouri, G. Coppola, P. Hilaire, C. Millet, A. Lemaître, I. Sagnes, O. Krebs, L. Lanco, J. C. Loredó, C. Antón, N. Somaschi, and P. Senellart  
*ACS Photonics* **7**, 4, 1050-1059 (2020)